Development of Affinity and Fluorescent Probes to Elucidate the Mechanism of Small Molecule Modulators of Neurogenesis

Thesis submitted for the degree of Doctor of Philosophy



Rachel Sim

St John's College, University of Oxford

Supervisor: Prof Angela Russell

Disclaimer

This thesis entitled 'Development of affinity and fluorescent probes to elucidate the mechanism of small molecule modulators of neurogenesis' submitted on 15 January 2021 by Rachel Sim contains material of confidential nature, specifically the disclosure of novel structures of small molecule modulators of neurogenesis. This report should be withheld from consultation and prevented from being reproduced or further disseminated until appropriate IP protection has been filed.

Declaration of Authorship

This thesis and the work of which it is a record, were carried out by myself unless otherwise acknowledged. No part of this thesis has been submitted in any other previous application for a higher degree.

Rachel Sim

15 January 2021, Oxford

Abstract

Neurogenesis is an endogenous neuroprotective mechanism that mainly occurs in two neurogenic niches of the adult mammalian brain. In neurodegenerative diseases, such as Parkinson's disease and Alzheimer's disease, adult neurogenesis is often impaired. For these diseases, pharmacological stimulation of the *de novo* production of neurons in the stem cell niches of the brain is a promising regenerative therapy. OXS-N1 was previously identified as a hit neurogenic compound through an *in vitro* phenotypic screen. It increased neurogenesis in murine neural stem cells (NSCs) *in vitro* and in wild-type mice *in vivo* after oral administration. The aim of this DPhil work is to identify the molecular target(s) of OXS-N1 and the mechanism of its neurogenic activity through a chemoproteomics approach.

A series of affinity probes was synthesised to assess the molecular interactions of OXS-N1 through affinity-based protein profiling (AfBPP). Vimentin was identified as the molecular target of OXS-N1 through pull-down studies and mass spectrometry analysis. Using fluorescent-tagged OXS-N1 derivatives, OXS-N1 was found to localise primarily in the cytoplasm, correlating to the known subcellular localisation of vimentin. It was found to directly bind to vimentin in live NSCs, without causing significant disassembly or aggregation of vimentin filaments. The protein-ligand binding was further validated using waterLOGSY and intact protein mass spectrometry. Reported literature vimentin binders also increased neurogenesis *in vitro*, showing that vimentin modulation could be used in future neuroregenerative therapies.

Acknowledgements

I would like to thank Angie for being a wonderful mentor and supervisor throughout my PhD. Thank you for being encouraging and for giving advice so that I could improve in many aspects of my research including experimental work, presentations and writing. Thank you for being supportive of my decision to return to Singapore during the pandemic and for the constant guidance through our video meetings.

I would also like to thank A*STAR for the PhD scholarship to support my time in Oxford, and for the support to attend many conferences to present my work.

Thank you to Francis and his group for advice on neurosphere culture and other biological experiments. Julie, thank you for the hard work in the initial discovery of OXS-N1. Mega and Blanca, thank you for kindly providing me with the primary neural stem cells from your dissections. Mega, thank you for being so patient in teaching me how to do the dissections for the first time and for sharing all your knowledge on neurosphere cultures with me! Anna, thank you for helping with the setup of organotypic cultures and for teaching me confocal imaging techniques.

Thank you to the AJR group for making the lab a fun and enriching place for me to learn and grow. Carole, thank you for helping and guiding me in the lab, especially in the early days of my PhD. Thank you for sharing your knowledge on the fluorescent tags and for helping to run waterLOGSY experiments! Liam, thank you for imparting all the NMR knowledge to me and for painstakingly checking all my NMRs. Seb, thank you for brainstorming ideas on my project together and for always being so encouraging when I want to try new experiments. Thank you for helping with the mass spec experiments and for running the SPR ones! Aini, thank you for teaching me the pull-down techniques and for being lots of fun on our conferences together. Kate, thank you for all the fun we had together at the pharmacology lab and for those crazy times when we were both in the lab at 6 am.

Thank you to Ed and Dan for the advice on the proteomics experiments and data analysis. Thank you to Val for running image analysis for the neurosphere assays. Thank you to Elisabete for the mass spec training and guidance.

Thank you to the best DPhil group for sharing many good times (and cakes) together! Isabel, you have always been so encouraging; thank you for being on the target identification journey with me. Alice, thank you for organising get-togethers and finding nice places for us to go! Ria, thank you for showing me how to use the equipment in Pharmacology and thank you for those lovely bakes. Purnima, thank you for the fun we had together sharing the fumehood at the start, and for hanging out together.

Thank you to my family and friends who supported me from afar and sent me constant words of encouragement on this journey. To my parents and my sister, thank you for keeping me company on video calls and taking turns to visit me in Oxford. To Choon Huat, thank you for giving me strength and for waiting 3 years for me – I'm so glad to be back home with you again.

Table of Contents

Disclaimer ii

Declaration of Authorship iii

Abstract iv

Acknowledgments v

Table of Contents vii

Abbreviations xiii

Chapter 1 Introduction 1

1.1 Neurogenesis 1

1.1.1 Evidence for Adult Neurogenesis 2

1.1.2 Importance of Adult Neurogenesis 2

1.1.3 Neurogenesis as a Response to Brain Injury 3

1.2 Molecular Mechanisms of Adult Neurogenesis 4

1.2.1 Intrinsic Factors 4

1.2.2 Extrinsic Factors 6

1.2.3 Signalling Pathways 9

1.3 Neurodegenerative Diseases 12

1.3.1 Alzheimer's Disease (AD) 12

1.3.2 Parkinson's Disease (PD) 13

1.3.3 Huntington's Disease (HD) 13

1.3.4 Therapeutic Strategies 14

1.3.5 Regenerative Medicine for Neurodegenerative Diseases 15

1.4 Small Molecule Modulators of Neurogenesis 16

1.4.1 Antidepressants 16

1.4.2 Modulators of Signalling Pathways associated with Neurogenesis 17
1.4.3 Scaffolds identified by Drug Discovery Programmes 18
1.5 In-House Phenotypic Screen for Proneurogenic Molecules 21
1.5.1 Pilot Screen 22
1.5.2 Hit Compound OXS-N1 23
1.5.3 *In vivo* Activity of OXS-N1 24
1.5.4 Preliminary Mechanism of Action Studies 25
1.6 Target Identification 28
1.6.1 Affinity-based Protein Profiling (AfBPP) 29
1.6.2 Photoaffinity Labelling 32
1.6.3 SILAC Approach 35
1.6.4 Label-free Approaches 35
1.6.5 Examples of Successful Target Identification Studies 36
1.7 Target Validation 40
1.7.1 Biophysical Methods 40
1.7.2 Genetic Methods 43
1.8 Project Aims 44
Chapter 2 Development of Affinity Probes 45
2.1 Overview 45
2.2 Synthesis and Testing of OXS-N1 and Analogues 45
2.2.1 Design and Synthesis of OXS-N1 and Analogues 45
2.2.2 *In vitro* Neurosphere Differentiation Assay 46
2.2.3 Activity of OXS-N1 and analogues 50
2.3 Design and Synthesis of Alkyne-tagged Probes 51

2.4 Design and Synthesis of Photoaffinity Building Block 54
2.5 In Vitro Testing of Probes 59
2.5.1 Activity of Probes 59
2.5.2 Labelling of Target Proteins 61
2.6 Design and Synthesis of Biotinylated Probes 62
2.7 Design and Synthesis of Dual-tagged Probes 63
2.8 Summary 66
Chapter 3 Development of Fluorescent Probes 67
3.1 Overview 67
3.2 Rhodamine-tagged Derivatives 67
3.3 BODIPY-tagged Derivatives 69
3.3.1 Synthesis and Testing of BODIPY-tagged OXS-N1 69
3.4 Cellular Imaging 70
3.4.1 *In vitro* Cellular Uptake of Fluorescent Probe 70
3.4.2 Confocal Imaging 72
3.4.3 Competition Study with Parent Compound 73
3.4.4 Quantification of Fluorescence Signal 73
3.5 Slice Culture Imaging 75
3.5.1 Organotypic Slice Cultures 75
3.6 Summary 78
Chapter 4 Target Identification 79
4.1 Overview 79
4.2 AfBPP using Biotinylated Probes 79

4.2.1 Chemoproteomics Workflow 79
4.2.2 Protein Identification from In-gel Digest 81
4.3 AfBPP using Dual-Tagged Probes 82
4.3.1 Chemoproteomics Workflow 82
4.3.2 Protein Identification from In-gel Digest 84
4.3.3 Protein Identification from In-solution Digest 86
4.4 Protein Hits from AfBPP 91
4.4.1 Vimentin (Vim) 91
4.4.2 Mitochondrial proteins (Atp5a1, Atp1a2, Slc25a5) 92
4.4.3 Transketolase (Tkt) 93
4.4.4 Elongation factor 1-gamma (Eef1g) 93
4.5 Validation of Pull-down Hits 93
4.5.1 Immunoblotting of Putative Targets 93
4.5.2 Competition with Parent Compound 95
4.6 Summary 96
Chapter 5 Target Validation 97
5.1 Overview 97
5.2 Vimentin as a Molecular Target 97
5.2.1 Expression of Vimentin in Cells and Tissues 97
5.2.2 Structure of Vimentin Filaments 99
5.2.3 Functions of Vimentin 101
5.2.4 Links to Diseases 101
5.2.5 Links to Neurogenesis 102
5.2.6 Vimentin-binding Small Molecules 103

5.2.7 Related Intermediate Filament Proteins 105

5.3 Biophysical Methods for Probing Protein-Ligand Interaction 106

5.3.1 WaterLOGSY 107

5.3.2 In-gel Fluorescence & Protein Mass Spectrometry (MS) 109

5.3.3 Surface Plasmon Resonance (SPR) 114

5.3.4 Thermal Shift Assay (TSA) 116

5.4 Target Visualisation 118

5.4.1 Co-localisation with Fluorescent Probe 118

5.4.2 Effects of Compound Treatment on Assembly of Vimentin Filaments 120

5.5 Investigation of Vimentin Post-Translational Modifications 121

5.5.1 Phosphorylation of Vimentin 121

5.6 Summary 123

Chapter 6 Conclusion 124

6.1 Overview 124

6.2 Research Findings 124

6.3 Future Work 127

6.3.1 Investigation of Vimentin Modulation 127

6.3.2 Investigation of Protein-protein Interactions & Affected Pathways 128

6.3.3 Investigation of Vimentin as a Therapeutic Target 129

6.4 Summary 131

Chapter 7 Experimental 132

7.1 Chemistry Methods 132

7.1.1 General Experimental 132

7.1.2 Analytical Procedures 132
7.1.3 General Synthetic Procedures 133
7.1.4 Experimental Procedures and Characterisation Data 134
7.2 Biology Methods 164
7.2.1 Materials 164
7.2.2 Experimental Procedures 164
Chapter 8 References 171
Appendices 182
Appendix 1: List of Enriched Proteins in LFQ Experiments 182
Appendix 2: List of Enriched Proteins in TMT Experiments 189
Appendix 3: Western Blots of Putative Hits 212
Appendix 4: WaterLOGSY Spectra of Compound 28 213
Appendix 5: Confocal Images of Vimentin Filaments in DG-derived NSCs 214

Abbreviations

δ	Chemical shift
Aβ	β-amyloid
Ac	Acetyl
ACN	Acetonitrile
AD	Alzheimer's disease
APCI	Atmospheric pressure chemical ionisation
aq.	Aqueous
AfBPP	Affinity-based proteomic profiling
Boc	*tert*-Butyloxycarbonyl
BODIPY	4-Bora-3a,4a-diaza-s-indacene
br.	Broad
BrdU	Bromodeoxyuridine
BSA	Bovine serum albumin
CAA	2-Chloroacetamide
CETSA	Cellular thermal shift assay
COSY	Correlation spectroscopy
CuAAC	Copper(I)-catalysed alkyne-azide cycloaddition
CyJohnPhos	2-(Dicyclohexylphosphino)biphenyl
DAPI	4′,6-Diamidino-2-phenylindole
DAPT	*N*-[*N* -(3,5-difluorophenacetyl)-L-alanyl]-S-phenylglycine t-butyl ester
DBU	1,8-Diazabicyclo[5.4.0]undec-7-ene
DCX	Doublecortin
DG	Dentate gyrus
DIPEA	*N,N*-Diisopropylethylamine
DMA	Dimethylacetamide
DMAP	4-Dimethylaminopyridine
DME	Dimethoxyethane
DMF	Dimethylformamide
DMSO	Dimethyl sulfoxide
dppf	1,1′-Ferrocenediyl-bis(diphenylphosphine)
EC_{50}	Half maximal effective concentration
EGF	Epidermal growth factor
EI	Electron ionisation
eq	Equivalents
ESI	Electron spray ionisation
Et	Ethyl
FGF2	Fibroblast growth factor-2
FP	Fluorescence polarisation
FT-IR	Fourier transform infrared spectroscopy
GFAP	Glial fibrillary acidic protein
GFP	Green fluorescent protein
GO	Gene ontology
h	Hour(s)
HATU	1-[Bis(dimethylamino)methylene]-1*H*-1,2,3-triazolo[4,5-b]pyridinium 3-oxide hexafluorophosphate

HD	Huntington's disease
HMBC	Heteronuclear multiple bond correlation spectroscopy
HPLC	High performance liquid chromatography
HRMS	High resolution mass spectrometry
HSQC	Heteronuclear single quantum coherence spectroscopy
IF	Intermediate filament
K_D	Dissociation constant
LC-MS	Liquid-chromatography mass spectrometry
liq.	Liquid
M	Molar
MALDI-TOF	Matrix assisted laser desorption ionization-time of flight mass spectrometry
Me	Methyl
MIDA	*N*-Methyliminodiacetic acid
min	Minute(s)
MK2	Mitogen-activated protein kinase-activated protein kinase 2
mp	Melting point
Ms	Methanesulfonyl
MS	Molecular sieves
MW	Microwave
NAMPT	Nicotinamide phosphoribosyltransferase
NMR	Nuclear magnetic resonance
NeuN	Neuronal nuclei
NOE	Nuclear Overhauser effect
NSC	Neural stem cells
OB	Olfactory bulb
PAL	Photoaffinity labelling
PBS	Phosphate-buffered saline
PD	Parkinson's disease
PEG	Polyethylene glycol
Ph	Phenyl
PTM	Post-translational modification
RA	Retinoic acid
RFU	Relative fluorescence units
RGL	Radial glia-like
RMS	Rostral migratory stream
rt	Room temperature
s	Second(s)
sat.	Saturated
SAR	Structure-activity relationship
SDS-PAGE	Sodium dodecyl sulfate polyacrylamide gel electrophoresis
SILAC	Stable isotope labelling by amino acids in cell culture
siRNA	Small-interfering RNA
SPAAC	Strain-promoted alkyne-azide cycloaddition
SGZ	Subgranular zone
SPhos	2-Dicyclohexylphosphino-2′,6′-dimethoxybiphenyl
SPR	Surface plasmon resonance
SVZ	Subventricular zone
TAMRA	Tetramethylrhodamine

TBI	Traumatic brain injury
TBTA	Tris((1-benzyl-4-triazolyl)methyl)amine
*t*BuBrettPhos	2-(Di-*tert*-butylphosphino)-2′,4′,6′-triisopropyl-3,6-dimethoxy-1,1′-biphenyl
*t*BuXPhos	2-Di-*tert*-butylphosphino-2′,4′,6′-triisopropylbiphenyl
TCEP	Tris (2-carboxyethyl)phosphine
Tf	Trifluoromethanesulfonate
THF	Tetrahydrofuran
TGF-β	Transforming growth factor-β
TLC	Thin layer chromatography
TMS	Trimethylsilyl
TMT	Tandem mass tags
TPD	3-Trifluoromethyl-3-phenyldiazirine
TrixiePhos	*rac*-2-(Di-*tert*-butylphosphino)-1,1′-binaphthyl
Ts	Toluenesulfonyl
TSA	Thermal shift assay
Tuj1	Beta-tubulin-III
UTR	3'-Untranslated region
UV	Ultraviolet
Vim	Vimentin
XantPhos	4,5-Bis(diphenylphosphino)-9,9-dimethylxanthene
XPhos	2-Dicyclohexylphosphino-2′,4′,6′-triisopropylbiphenyl
waterLOGSY	Water-ligand observed via gradient spectroscopy
WFA	Withaferin A
WT	Wild-type

Chapter 1 Introduction

1.1 Neurogenesis

Neurogenesis is the process by which new neurons are generated in the brain. This process is crucial during embryonic development and continues in restricted regions in postnatal and adult brains. In the adult mammalian brain, neurogenesis is an endogenous neuroprotective mechanism that mainly occurs in the subventricular zone (SVZ) along the lateral ventricles and the subgranular zone (SGZ) of the dentate gyrus (DG) in the hippocampus (Figure 1).[1]

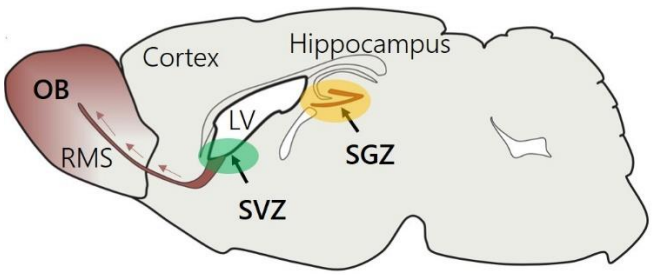


Figure 1. Schematic showing the neurogenic niches of a mammalian brain: the subventricular zone (SVZ) and the subgranular zone (SGZ); OB, olfactory bulb; RMS, rostral migratory stem; LV, lateral ventricle.[1]

Neural stem cells (NSCs) found in these neurogenic niches are self-renewing and multipotent, possessing the ability to differentiate into various cell types such as astrocytes, oligodendrocytes or neurons.[2,3] NSCs in the SVZ are type B cells which possess astrocyte-like features and express glial fibrillary acidic protein (GFAP). They give rise to rapidly proliferating type C interneuron progenitors which divide to form neuroblasts. The key stages of the neurogenesis process are illustrated in detail in Figure 2 (Section 1.2). The neuroblasts migrate along the rostral migratory stream (RMS) to the olfactory bulb (OB), where they mature and are incorporated into the synaptic circuitry as different classes of interneurons.[4]

NSCs in the SGZ are radial glia-like (RGL) type 1 cells with astrocyte-like features. They give rise to transient amplifying type 2 progenitor cells which then give rise to neuroblasts. The

neuroblasts migrate into the granule cell layer and are incorporated as dentate granule neurons of the DG.[5]

1.1.1 Evidence for Adult Neurogenesis

While there has been some debate in the field on whether neurogenesis occurs beyond adolescence,[6] recent literature has provided more evidence that hippocampal neurogenesis continues throughout adulthood, at lower levels as compared to a young brain.[7] Hippocampal neurogenesis was found to persist even in patients above 79 years of age,[8] and even in patients suffering from mild cognitive impairments and Alzheimer's disease.[9]

Early reports of adult neurogenesis were based on birth-dating methods, by tracking the incorporation of the thymine analogues, such as bromodeoxyuridine (BrdU) and iododeoxyuridine (IdU), into cellular DNA during the S phase of the cell cycle. Immunohistochemical staining of BrdU, along with staining for specific neuronal markers, allows for newborn neurons to be identified. A study by Eriksson *et al.* reported the presence of BrdU+ neurons in the adult hippocampus after administration of BrdU to the patients, indicating that the neurons were newly formed.[10] This finding was further supported by Spalding *et al.* who used the ^{14}C concentration in genomic DNA to birth-date mature neurons and showed that 0.004% of the hippocampal neurons in adult humans are replaced daily.[11] Roy *et al.* isolated hippocampal progenitor cells from the adult human brain and demonstrated their ability to mature into functional neurons *in vitro*.[12]

1.1.2 Importance of Adult Neurogenesis

Adult neurogenesis has been reported to contribute to specific brain functions, including memory formation, olfactory learning and cognitive function. The integration of new neurons into the olfactory circuitry of the OB is thought to play a role in olfactory function and memory.[13] Similarly, neurogenesis in the DG is reported to contribute to synaptic plasticity, spatial learning, memory and trace conditioning.[14,15] Wojtowicz reported on the use of ionising

radiation to reduce the number of young neurons by more than 50% without affecting the population of mature neurons in the hippocampus.[16] This reduction in adult hippocampal neurogenesis led to a reduction in contextual fear conditioning and long-term memory retention in rats.[17]

Adult hippocampal neurogenesis can be affected by a variety of factors such as stress,[18] exercise,[19] hormones[20] and antidepressants.[21] Various studies involving environment enrichment and genetic manipulations[22] have shown correlations between neurogenesis and performance in spatial memory tests.[14,23] Exercise enhances adult hippocampal neurogenesis, leading to improved spatial learning and reversing the age-dependent reduction in hippocampal cell proliferation in mice models.[24,25] Using ionising radiation to disrupt hippocampal neurogenesis, Santarelli *et al.* showed that the stimulation of neurogenesis was necessary for bringing about the behavioural effects of chronic antidepressants.[26]

1.1.3 Neurogenesis as a Response to Brain Injury

The adult brain responds to damage caused by traumatic brain injury (TBI) and cerebral ischemic brain injury by stimulating neurogenesis. Arvidsson *et al.* reported that cerebral ischemia in rats induced NSC proliferation in the SVZ and the newly born neurons migrate into the injury site in the ischemic striatum, where they mature into functional neurons.[27] TBI in rats induced the proliferation of neural progenitor cells in the SVZ and the DG, and this increase persisted for at least a year when compared to non-injured controls.[28,29] New dentate granule neurons survive and integrate into the existing hippocampal circuitry, contributing to innate cognitive recovery.[30] These findings are supported by further studies in adult human brains after TBI, which showed a similar increase in the proliferation of endogenous NSCs.[31] Enhanced neurogenesis induced by injury contributes to functional repair of the damaged site and brain recovery.

1.2 Molecular Mechanisms of Adult Neurogenesis

The general neurogenesis process involves the proliferation of neural progenitor cells, and neuronal differentiation, maturation and integration into existing neuronal circuitry.[32] Neurogenesis is regulated by a balance between the proliferation of neural progenitor cells, the differentiation of neuroblasts and the survival rate of newly differentiated neurons. These stages are modulated by a variety of intrinsic and extrinsic factors, and by a complex network of signalling transduction pathways[33] (Figure 2). NSCs and progenitor cells when grafted from a neurogenic niche to non-neurogenic areas of the brain differentiate into glial cells instead of neurons, showing that the microenvironments of the SVZ and SGZ regions are crucial for adult neurogenesis.[34]

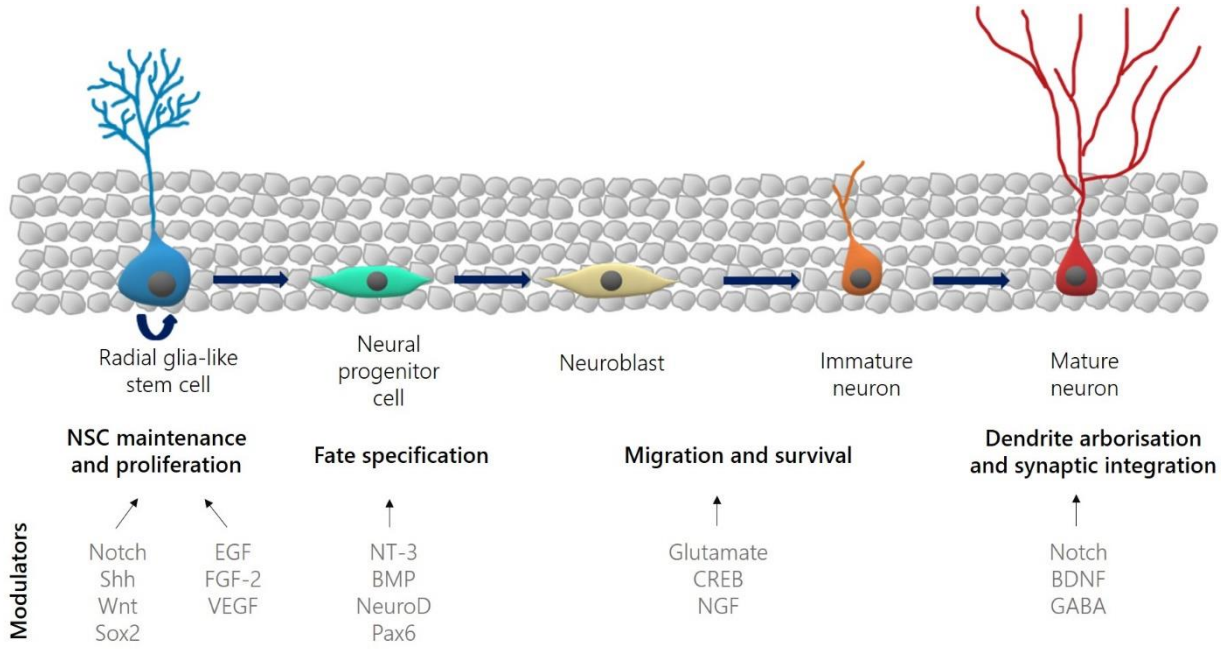


Figure 2. Schematic showing the key stages of neurogenesis, modulated by various transcription factors, signalling pathways and intrinsic and extrinsic factors.

1.2.1 Intrinsic Factors

A variety of intrinsic factors contribute to the renewal and differentiation of NSCs, including transcription factors, epigenetic modifications and non-coding RNAs. Pax6 is a neurogenic transcription factor which promotes differentiation of neuroblasts towards a neuronal fate in the RMS. Its action is opposed by Olig2, which promotes oligodendrogenesis.[35] Recombination

signal sequence-binding protein J (RBPJ) regulates neuronal differentiation partly through the transcriptional repression of Olig2.[36] Another transcription factor, cAMP response element-binding protein (CREB), serves as a final phosphorylation substrate for several signalling pathways involved in neurogenesis. cAMP-mediated phosphorylation of CREB stimulates proliferation of progenitor cells and promotes the survival of immature hippocampal neurons.[37] The loss of CREB signalling resulted in reduced maturation of progenitor cells and impaired dendritic development, along with decreased expression of Pax6.[38]

Sox2 is a transcription factor that is expressed in NSCs in the neurogenic niches and required for their maintenance. In adult Sox2-deficient mice, the proliferation of NSCs and progenitor cells and their ability to differentiate into neurons were both greatly impaired.[39] Sox2 is especially important for priming the epigenetic landscape in hippocampal neural progenitor cells to activate genes that are essential for neuronal differentiation, including proneural genes such as NeuroD1, and neurogenic genes such as BDNF, Sox21 and Gadd45b.[40]

Epigenetic mechanisms, such as DNA methylation and histone modifications, also contribute to the regulation of adult neurogenesis. Petrik *et al.* showed that Brahma-related gene 1 (Brg1), the central catalytic ATPase subunit of various chromatin-modifying enzymatic complexes, is important for the proliferation and maintenance of NSCs in the adult hippocampus, and coordinates with Pax6 in the SVZ to keep progenitor cells in the neurogenic lineage.[41] The *de novo* DNA methyltransferase Dnmt3a is highly expressed in postnatal NSCs of the SVZ and DG, and promotes the expression of neurogenic genes. Wu *et al.* used Dmnt3a-knockout mice to show that the deletion of Dmnt3a reduced neuronal differentiation and resulted in impaired neurogenesis in both neurogenic niches.[42]

More recent work has also shown crucial roles for non-coding regulatory RNA, including microRNA (miRNA) and long non-coding RNA (lncRNA), in regulating adult neurogenesis.[43] miRNAs regulate transcriptional pathways by binding to the 3'-untranslated region (UTR) of target mRNA and recruiting the RNA-inducible silencing complex (RISC), leading to the

degradation of the targeted transcript.[44] The importance of miRNAs for maturation of adult-born neurons was demonstrated using a conditional knockout of RISC, which led to decreased levels of differentiation and maturation of neural progenitor cells in the SVZ and DG. Specific miRNAs, such as miR-124 and miR-410, were found to regulate genes contributing to neuronal lineage specificity.[45,46] lncRNAs interact with DNA, RNA and protein to form complexes that modify chromatin and regulate gene transcription. Lineage-specific lncRNAs are activated during neuronal differentiation in the SVZ and contribute to the regulation of glial-neuronal lineage specification of NSCs in neurogenesis.[47]

1.2.2 Extrinsic Factors

Endogenous extrinsic factors in the SVZ and SGZ microenvironment play an important role in regulating the fate of the NSCs in these niches.

1.2.2.1 Neurotrophic Factors

Neurotrophic factors are a family of pleiotropic molecules that are crucial for key stages of the nervous system maintenance, including proliferation, differentiation, migration and synaptic plasticity. Neurotrophins have been implicated in the modulation of adult neurogenesis in both the SVZ and SGZ at different stages.[48] Their effects depend on two receptor classes, the tropomyosin receptor kinase (Trk)[49] and the p75 neurotrophin receptor.[50]

Brain-derived neurotrophic factor (BDNF) is highly expressed in the brain and has a crucial role in the maintenance of neurons. Through dynamic imaging, Bagley and Belluscio have shown that BDNF modulates neuroblast mobility through the TrkB receptor and that elevated levels of BDNF increases the migration of neuroblasts within the RMS.[51] BDNF was also found to be essential for dendrite development of newborn dentate granule cells in the DG of adult mice.[52] A site-specific knockdown of BDNF by RNA interference *in vivo* resulted in reduced hippocampal neurogenesis and delayed spatial learning.[53] Increased BDNF levels have been associated with increased neurogenesis due to exercise.[54]

Neurotrophin-3 (NT-3) supports the survival and differentiation of immature neurons and promotes neurite growth. NT-3 is highly expressed in the DG of the adult brain, most notably in the neurons. The differentiation of neural progenitor cells was significantly impaired in NT-3 conditional knock-out mice, leading to deficits in long-term potentiation and spatial memory.[22] NT-3 was found to play a role in cell fate determination and maturation of the progenitor cells, processes which are pivotal in adult neurogenesis. In the SVZ, NT-3 secreted by the endothelial cells regulates the quiescence state and long-term maintenance of the NSCs through nitric oxide induction.[55]

Nerve growth factor (NGF) is important for the maintenance and proliferation of the cholinergic neurons in the forebrain. It has a proliferative effect on NSCs and induces differentiation through the TrkA receptor, by activating the phosphorylation of ERK1/2 and the P13K/Akt pathway.[56] NGF also promotes the survival of immature hippocampal neurons and administration of exogenous NGF enhances cognitive performance in adult rodents.[57] The neuroprotective effect of NGF contributes to regeneration processes after injury, leading to restoration of neuronal networks in injury sites of the brain.[58]

1.2.2.2 Neurotransmitters

Gamma aminobutyric acid (GABA) is an inhibitory neurotransmitter that plays an important role in regulating the excitability of neurons in the adult brain. The inhibitory action of GABA is primarily mediated by $GABA_A$ and $GABA_B$ receptors ($GABA_AR$ and $GABA_BR$), which are ligand-gated chloride channels.[59] GABAergic excitation modulates the proliferation and maturation of neural progenitor cells and the synaptic integration of new mature neurons.[60] Depolarisation of progenitor cells due to $GABA_AR$ activation induces calcium ion signalling[61] and leads to an increased expression of NeuroD, required for neuronal differentiation.[62] Earnheart *et al.* demonstrated that the lack of a functional γ-subunit in $GABA_AR$ reduced the survival of immature neurons and led to decreased hippocampal neurogenesis in mice.[63]

Glutamate is the main excitatory neurotransmitter that is responsible for the plasticity of the nervous system.[64] Glutamate signalling induces the expression of neurotrophic factors such as BDNF and NGF. The *N*-methyl D-aspartate (NMDA) glutamate receptor is important for modulating the potentiation of synapses and long-term changes in neuronal circuits. Tashiro *et al.* used a retrovirus-mediated, single-cell gene knockout method to demonstrate that the NMDA receptor is essential for the survival of new neurons in the DG of mice.[65] Glutamate signalling, together with GABAergic signalling, provides homeostatic control on activity-dependent neuronal differentiation in adult neurogenesis.[66]

1.2.2.3 Growth Factors

Growth factors are extracellular proteins that bind to a specific tyrosine kinase receptor, leading to subsequent activation of downstream signalling pathways such as the PI-3 kinase(PI3K)/Akt pathway.[67] Fibroblast growth factor-2 (FGF2) is a multifunctional growth factor which has angiogenic effects and plays crucial roles in regulating the proliferation and differentiation of NSCs and progenitor cells in the neurogenic niches through FGFR1 signalling.[68] FGF2 knockout mice showed decreased proliferation of NSCs in the SVZ and a corresponding reduction in the size of their olfactory bulbs.[69] Epidermal growth factor (EGF) plays a similar role in regulating the proliferation of NSCs in the SVZ and SGZ via EGFR signalling.[70] Both FGF2 and EGF are important growth factors that allow NSCs to retain their self-renewal potential.[71] NSCs harvested from the SVZ and DG require the addition of EGF and FGF2 for long-term survival and continued proliferation *in vitro*.[72] EGF and FGF2 treatment promoted the proliferation of neural progenitor cells in adult rats after transient focal ischemia.[73]

Vascular endothelial growth factor (VEGF) is an angiogenic protein that also has neurotrophic and neuroprotective effects. VEGF was found to promote proliferation of neural progenitor cells *in vitro* and in adult rat brains *in vivo*.[74] Palmer *et al.* identified links between neurogenesis and angiogenesis in adult rat SGZ, where neurogenesis occurs in close proximity to blood capillaries. The high expression of VEGF in this niche promotes angiogenesis and provides trophic support

to support survival of immature neurons.[75] Fabel *et al.* showed that VEGF was required for the positive effects of exercise on hippocampal neurogenesis. Blockade of VEGF using a soluble Flt-1 fusion protein (sFlt) prevented the running-induced proliferation of neural progenitors in the hippocampus of mice.[76] Expression of VEGF is upregulated after cerebral hypoxia, contributing to brain repair progresses via regulation of angiogenesis and neurogenesis.[77]

1.2.3 Signalling Pathways

Along with extrinsic factors, signalling pathways also contribute to the regulation of proliferation, differentiation, maturation, and survival stages of neurogenesis. A schematic by Johnson *et al.* illustrates how different components in the cells act on various aspects of neurogenesis (Figure 3).[78]

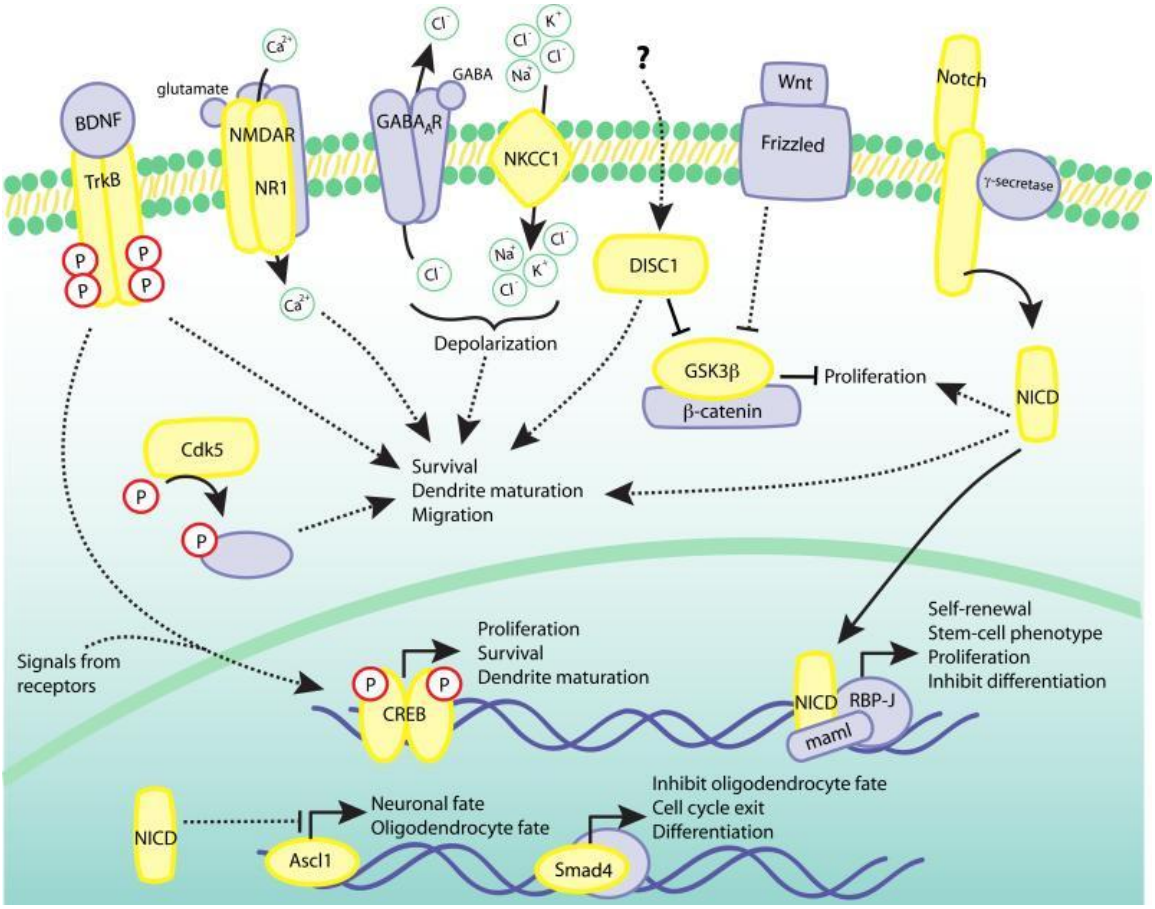


Figure 3. Schematic of a single cell (with cellular membrane, cytoplasm, and nucleus containing DNA and transcriptional elements) to depict how intrinsic factors and signalling pathways are involved in regulating the stages of adult neurogenesis.[78] Direct signalling is indicated by solid lines, while indirect signalling is indicated by dashed lines. Components labelled in yellow: Tropomyosin receptor kinase B (TrkB), N-methyl-D-aspartate receptor (NMDAR), Glutamate receptor (NR1), Na-K-Cl cotransporter (NKCC1), Disrupted in schizophrenia 1 (DISC1), Glycogen synthase kinase-3β (GSK3β), Notch intracellular domain (NCID), cAMP response element-binding protein (CREB), Cyclin-dependent kinase 5 (Cdk5), Achaete-Scute family BHLH transcription factor 1 (Ascl1), SMAD Family Member 4 (Smad4).

1.2.3.1 Wnt Signalling

The Wnt/β-catenin signalling pathway regulates the maintenance and proliferation of NSCs and the differentiation of neural progenitor cells.[79] Using a lentiviral vector expressing Wnt3, Lie *et al.* demonstrated that the activation of the Wnt signalling pathway *in vivo* increased the percentage of new immature neurons found in the SGZ. Inhibition of the Wnt signalling pathway using a mutant Wnt1 protein resulted in a drastic decrease in adult hippocampal neurogenesis, showing that this signalling pathway is key regulator of neurogenesis.[80] The loss of Wnt7a impaired the dendritic arborisation of dentate granule neurons *in vivo*, showing that Wnt signalling also contributes to the terminal differentiation and maturation of new neurons.[81]

1.2.3.2 Notch Signalling

The Notch signalling pathway has a key role in maintaining NSCs in their proliferative and undifferentiated state.[82] Notch receptors are activated upon binding of ligands such as Delta and Jagged, resulting in the cleavage of Notch by the γ-secretase complex to release the Notch intracellular domain (NICD). NICD translocates to the nucleus and forms a transcriptional complex with the DNA-binding protein RBPJ.[83] This complex activates the transcription of repressor genes such as Hes and Hey, which inhibit neuronal differentiation by suppressing the expression of proneural genes.[84] Notch signalling promotes adult NSC self-renewal, with NSCs in the SVZ and the SGZ having higher levels of Notch activity as compared to intermediate neural progenitors.[85]

A loss of function in Notch receptors led to a rapid depletion of NSCs and increased levels of neuronal differentiation. Inhibition of Notch signalling has also been associated with increased NSC differentiation *in vitro* and *in vivo*. Borghese *et al.* used DAPT, a γ-secretase inhibitor, to block Notch signalling in human embryonic stem cell-derived NSCs (hESNSCs) and reported a significant decrease in transcriptional levels of Notch, Hes5 and Hey1 genes, along with an increase in expression of proneural genes. The DAPT-mediated Notch inhibition shifted the cell fate of the hESNSCs towards neuronal lineages, resulting in increased neurogenesis.[86]

1.2.3.3 Sonic Hedgehog (Shh) Signalling

Shh is an extracellular signalling protein that mediates its action via the transmembrane receptor protein Patched (Ptc) and transducer protein Smoothened (Smo).[87] Ptc and Smo are expressed in the neurogenic niches, and support the role of Shh in regulating the stem cell niche and structural plasticity in the adult brain.[88] Binding with Shh inactivates Ptc and activates Smo, allowing for the transcription of Gli genes, which are important for regulating the survival and migration of immature neurons.[89] Using a conditional Smo knockout model, Balordi and Fishell showed that the absence of Shh signalling resulted in a depletion of NSCs in the SVZ and a overproduction in neuroblasts, which exhibited significant loss of ability to migrate to the OB.[90] An upregulation of Shh after traumatic or ischemic injury contributes to the regenerative response of the adult brain, by stimulating neurogenesis, axon elongation and synaptogenesis.[91,92]

1.2.3.4 Bone Morphogenic Protein (BMP) Signalling

BMPs constitute ligands of the transforming growth factor β (TGF- β) superfamily of cytokines and regulate important cellular processes including proliferation, neurogenesis and gliogenesis.[93] They are recognised by cell-surface serine-threonine kinase receptors, mainly BMP type I and type II receptors (BMPRI, BMPRII). BMPs modulate adult NSC proliferation and differentiation in the neurogenic niches. The BMP target gene Id1, which inhibits differentiation, is highly expressed in the NSCs in the SVZ and contributes to NSC self-renewal.[94] BMPs affect the cell fate speciation, by promoting an astroglial fate and blocking oligodendrocyte specification.[95] The activity of BMPs is modulated by their natural antagonists, Noggin, Chordin and Follistatin.[96] Overexpression of Noggin in the hippocampus of transgenic mice inhibited BMP signalling in the SGZ, leading to an increase in proliferation of the NSCs and expansion of the neural progenitor pool.[97] An age-associated increase in BMP signalling in mice was observed to contribute to reduced levels of hippocampal neurogenesis.[98]

1.3 Neurodegenerative Diseases

Alterations in neurogenesis have been reported in a range of neurodegenerative diseases including Alzheimer's disease (AD), Parkinson's disease (PD) and Huntington's disease (HD). While the underlying mechanisms involving dysregulated proteins differ between the various neurodegenerative diseases, progressive neuronal cell death is commonly exhibited by patients suffering from these diseases. Impaired adult neurogenesis in these diseases reduces the ability of NSCs to self-renew and generate new neurons to replace damaged ones. Such neurodegeneration leads to a decline in brain functions and cognitive functions over time.

1.3.1 Alzheimer's Disease (AD)

AD is an age-related, neurodegenerative disease that is characterised by massive neuronal and synaptic loss and a progressive decline of cognitive functions. The majority of AD cases are sporadic forms, while some rarer familial forms are caused by mutations in genes encoding for amyloid precursor protein (APP), presenilin-1 (PS1) and presenilin-2 (PS2). AD's key pathological features are the deposition of β-amyloid (Aβ) plaques and the hyperphosphorylation of tau proteins leading to neurofibrillary tangles in the brain.[99] Neuronal atrophy is observed as the disease progresses, leading to tissue loss and brain shrinkage in AD patients.[100]

Studies with transgenic animal AD models have reported compromised adult SVZ and DG neurogenesis in the early stages of the disease. Scopa et al. demonstrated that such defects were associated with the presence of toxic Aβ oligomers in the NSCs, which resulted in reduced NSC proliferation and impaired terminal differentiation into mature neurons.[101] Dysregulation in the morphology and function of immature neurons in APP transgenic mice suggested that there was an imbalance in GABAergic and glutamatergic neurotransmission.[102] Similar reductions in the number of progenitor cells in the SVZ and DG of AD patients have been observed, along with impaired hippocampal-dependent memory and olfactory functions.[103,104] The maturation of newly born neurons declined progressively as the disease progressed to late-stage in AD

patients.[9] Impaired neurogenesis is linked to cognitive decline and thought to play an important role in the disease progression of AD.[105]

1.3.2 Parkinson's Disease (PD)

PD is a progressive neurodegenerative disorder that is characterised by the accumulation of alpha-synuclein (α-syn) and the selective loss of dopaminergic neurons in the substantia nigra of the brain, resulting in motor dysfunction and other non-motor symptoms. Dysfunction of serotonergic neurons projecting to the hippocampus is also thought to contribute to depression and anxiety in the early phase of the disease. Kohl *et al.* developed a α-syn transgenic rat model to show that the overexpression of α-syn leads to key pathological features of PD including dopamine loss and progressive loss of motor functions. They reported a severe impairment in dendritogenesis of neuroblasts in the DG of four months old rats, leading to the reduced survival of immature neurons and decreased hippocampal neurogenesis.[106] In PD patients, a decrease in the proliferation of neural progenitor cells in the SVZ was observed, attributed to a reduction in EGF production due to the loss of dopamine signalling.[70] Alterations in hippocampal neurogenesis have also been observed, and the resulting hippocampal dysfunction contributed to depression and cognitive impairment in PD patients.[107]

1.3.3 Huntington's Disease (HD)

HD is an autosomal-dominant neurodegenerative disorder that results from the fusion of a cytomegalovirus enhancer to the chicken β-actin promoter (CAG) trinucleotide-repeat expansion within the huntingtin (HTT) gene. Aggregation of the toxic mutant HTT protein causes neuronal damage predominantly in the striatum, leading to motor and cognitive impairments.[108] Ernst *et al.* showed that the turnover of striatal neurons was reduced significantly in HD patients.[109] Impaired hippocampal neurogenesis has also been observed in the early stages of the disease in R6/1 and R6/2 transgenic HD mouse models.[110] Kohl *et al.* reported a reduction in newly generated neurons in the OB of adult R6/2 mice, suggesting that HTT aggregation has a negative impact on neuronal maturation.[111] In the hippocampus of

YAC128 transgenic HD mice, the reduction in progenitor cell proliferation and neuronal differentiation continued throughout the disease progression.[112]

1.3.4 Therapeutic Strategies

Long-term therapies for these neurodegenerative diseases have been lacking. Most of the available treatment options offer symptomatic relief to modestly slow the rate of cognitive impairment but are ineffective at halting the disease progression. Currently available therapeutic treatments for AD include acetylcholinesterase inhibitors such as rivastigmine, galantamine, tacrine, and donepezil, and *N*-methyl D-aspartate (NMDA) receptor antagonists such as memantine.[113] Treatment for PD focuses on alleviating symptoms of motor dysfunction by increasing dopamine signalling. This is usually done by using a dopamine precursor, such as levodopa, or dopamine receptor agonists, such as carbergoline, pergolide and ropinirole.[114] While they are effective at controlling motor symptoms in the early stages, a reduced benefit is observed in PD patients as the disease progresses.[115] Therapeutic treatments for HD focus on alleviating hyperkinetic movement disorders. These include acetylcholinesterase inhibitors, NMDA receptor antagonists, dopamine antagonists and glutamate antagonists.[116]

More recent efforts are being directed towards the discovery of disease-modifying therapies that can block the progress of the disease by targeting the various molecular pathways involved. In particular, the dysregulation of Aβ peptides production and clearance has been a target of interest in the development of therapeutics for AD.[99] An aggregation of Aβ42 monomers into oligomers and fibrils is thought to trigger inflammatory responses leading to formation of neurofibrillary tangles characteristic of AD.[117] In 2019, 40% of disease-modifying agents in clinical trials for AD have amyloid as their primary target.[118] Small molecule anti-amyloid agents are mainly Aβ precursor protein cleaving enzyme (BACE) inhibitors and γ-secretase inhibitors.[119] Unfortunately, many BACE inhibitors including CNP520 and elenbecestat have failed to show cognitive or behavioural benefits in mild to moderate AD patients, leading to failures in clinical trials.[120] Clinical trials of Aβ antibodies such as solanezumab, crenezumab and

aducanumab have also been conducted in patients with mild cognitive impairment or mild AD.[121] While aducanumab treatment reduced levels of Aβ plaques, solanezumab treatment did not show significant impact on Aβ plaque or paired helical filament tau (PHF-tau) deposition and failed to sufficiently slow cognitive decline.[122] The lack of success in developing disease-modifying therapies for AD is possibly due to the complexity of the disease mechanism biology and the poor predictive ability of animal models.

For PD treatment, many of the pharmacological agents aimed at reducing protein aggregation and reducing inflammation have failed to achieve their end points in clinical trials.[123] The heterogeneity of the PD patient population and lack of clear biomarkers to identify preclinical PD are some challenges contributing to the lack of success over the past few decades.[124] Currently, therapies that focus on reducing of the levels of pathological forms of α-syn are being developed to alter the disease progression. B2-adrenergic receptor agonists such as clenbuterol have been shown to reduce α-syn gene expression, but further studies in humans are required.[125] Similar strategies aimed at reducing the expression of the htt gene are being developed for HD, involving the use of RNA interference and antisense oligonucleotides.[126] However, there are no approved disease-modifying therapies for PD and HD to date.

1.3.5 Regenerative Medicine for Neurodegenerative Diseases

Since neuronal loss contributes to disease progression in neurodegenerative diseases, there is an interest in developing regenerative treatments that can compensate for this loss. The transplantation of NSCs, genetically altered or stimulated with proneurogenic factors, was reported to rescue spatial and memory deficits in several AD animal models.[127] Dopaminergic cells grafted into a rodent model of PD survived long-term and maintained their functional efficiency.[128] This cell replacement effect can also be achieved and sustained for a longer period by stimulating the endogenous neurogenic niches of the adult brain. Impaired adult neurogenesis has been observed in pre-symptomatic stages of neurodegenerative diseases, representing an opportunity to use this as biomarker for early diagnosis and treatment.[101] With

increasing evidence that adult neurogenesis responds to environmental factors and injuries,[19] using small molecules to enhance the *de novo* production of neurons in the brain could be a therapeutic strategy to replace lost neurons in pathological conditions.

1.4 Small Molecule Modulators of Neurogenesis

1.4.1 Antidepressants

Administrating antidepressants has been found to increase neurogenesis in various animal models and human studies.[129] This effect was observed across various classes of antidepressants (Figure 4), including selective serotonin reuptake inhibitors (SSRIs), specific norepinephrine reuptake inhibitors (SNRIs), monoamine oxidase inhibitors (MAOIs) and tricyclic antidepressants.

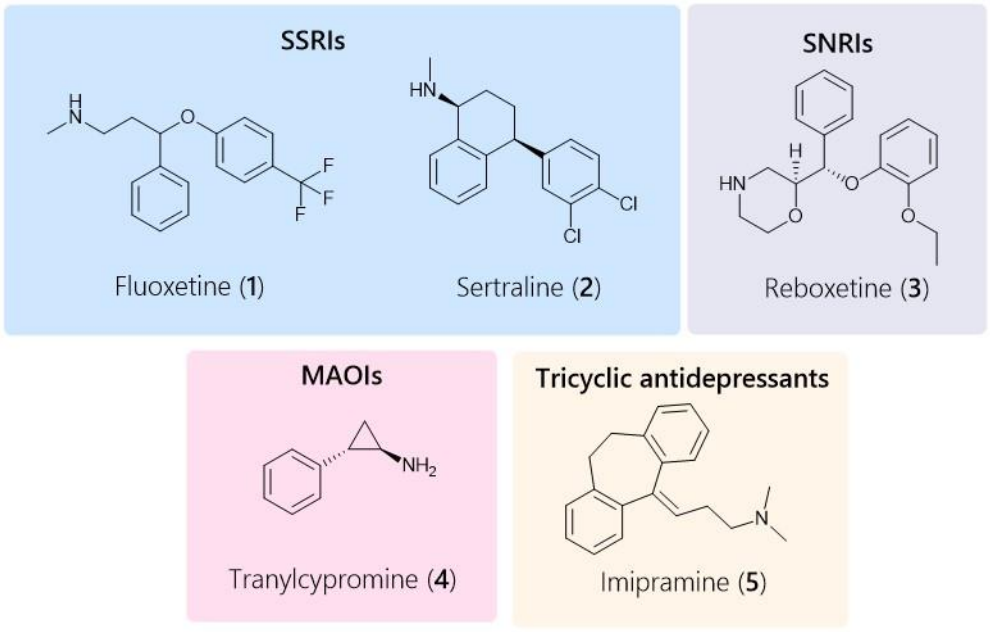


Figure 4. Figure showing the chemical structures of various classes of antidepressants.[26,129,130]

Chronic administrations of fluoxetine, reboxetine and tranylcypromine were found to increase neurogenesis in the DG of adult rats after 14 days, a time course consistent with that required to observe the therapeutic effects of antidepressants.[130] The increase in proliferation and maturation of hippocampal cells was suggested to contribute to the mechanism of action of

antidepressants. Disrupting neurogenesis in mice using X-ray irradiation was found to inhibit the positive behavioural effects exerted by antidepressants such as imipramine and fluoxetine.[26] Treatment with antidepressants, but not treatment with other psychotropic drugs, increased the expression of neurotrophic factors such as FGF2, BDNF and VEGF in cortical astrocyte cultures.[131]

1.4.2 Modulators of Signalling Pathways associated with Neurogenesis

Small molecules discovered for other therapeutic applications have been shown to also modulate neurogenesis by acting on related signalling pathways (Figure 5).

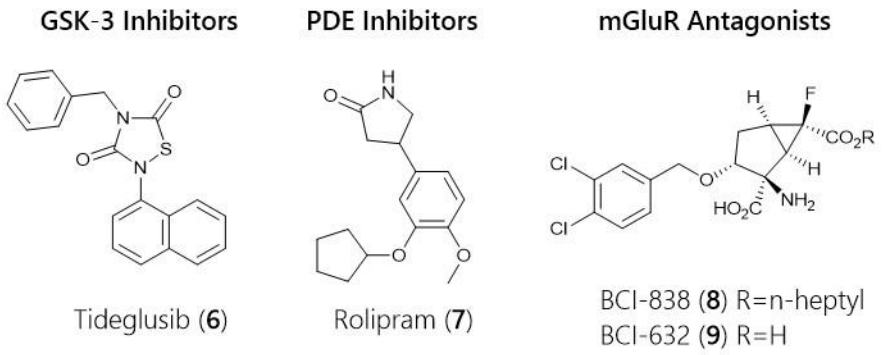


Figure 5. Chemical structures of small molecules shown to have neurogenic effects by modulating pathways associated with neurogenesis.[132-134]

1.4.2.1 Activators of Wnt Signalling

The enzyme glycogen synthase kinase-3 (GSK-3) is a key component of the Wnt signalling pathway. Inhibition of GSK-3 activity stabilises and activates β-catenin and subsequently activates Wnt signalling. Morales-Garcia *et al.* demonstrated that a chemically diverse library of GSK-3 inhibitors increased the proliferation and differentiation of DG-derived NSCs towards a neuronal phenotype *in vitro*. A 7-day treatment of tideglusib significantly increased the number of newborn neurons in the DG of adult rats.[132]

1.4.2.2 Activators of CREB Signalling

As CREB phosphorylation contributes to the survival of newborn neurons, inhibiting the degradation enzyme phosphodiesterase (PDE) activates CREB signalling and promotes

neuronal survival. PDE inhibitors Cilostazol and Rolipram were found to increase neurogenesis in the SVZ and SGZ of adult mice after ischemia by increasing levels of phosphorylated CREB.[135,136] PDE7 inhibitors promoted proliferation in neurosphere cultures and induced differentiation of NSCs *in vitro*. With long-term treatment of PDE7 inhibitors in mice, there was a significant increase in the number of newborn neurons in the OB and the DG, contributing to improvements in spatial learning and memory tasks.[133]

1.4.2.3 Glutamate Receptor Antagonists

Glutamate receptor signalling is involved in critical stages of proliferation and maturation in the neurogenesis process. Blockade of these receptors have been found to stimulate neurogenesis and contribute to improvements in spatial memory.[137,138] A range of metabotropic glutamate receptor (mGluR) antagonists have been reported to increase proliferation of progenitor cells in the DG.[139] BCI-838, an investigational prodrug that metabolises to the active Group II mGluR antagonist BCI-632, was found to reduce levels of Aβ peptides and stimulate hippocampal neurogenesis in transgenic APP mouse models.[134] The increase in hippocampal cell proliferation reversed APP transgene-associated learning and memory deficits, suggesting that pharmacological inhibition of glutamate receptors could be useful in AD treatment.

1.4.3 Scaffolds identified by Drug Discovery Programmes

Phenotypic screening uses a disease-driving phenotype to screen for molecules that change the outcome of biological pathways rather than activity at a specific target. It has been used as an approach by several groups to find proneurogenic molecules for development into drug candidates (Figure 6).[140]

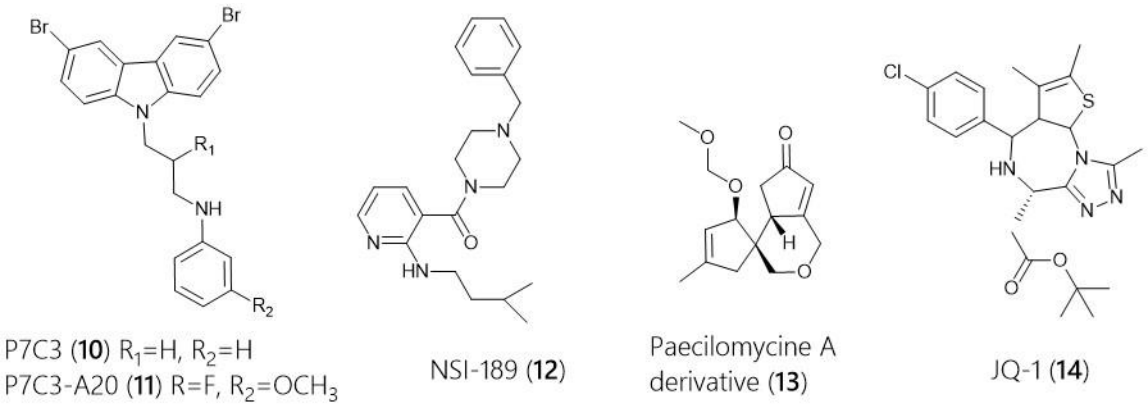


Figure 6. Chemical scaffolds that have been discovered through drug discovery programmes for neurogenic compounds.[141-144]

1.4.3.1 Aminopropyl Carbazole P7C3 Derivatives

P7C3 (**10**), an aminopropyl carbazole, was identified by Pieper *et al.* as a proneurogenic compound based on *in vivo* screening in Npas3 knockout mice with impaired hippocampal neurogenesis.[141] 1,000 compounds were initially screened for BrdU incorporation in the SGZ after 7 days of administration in mice by intracerebroventricular (ICV) infusion. The most pharmacologically favourable hit, P7C3, was found to inhibit the apoptosis of newborn neurons and enhance hippocampal neurogenesis in the aged mice.[145] Yoon *et al.* did further work to synthesise various aminopropyl carbazole derivatives, and improved the activity and neuroprotective effects of P7C3 by modification of the aniline ring. The dibromocarbazole group was noted to be essential for neurogenic activity.[146]

A chemical probe based on P7C3, P7C3-S326, was designed by Wang *et al.* to identify the intracellular molecular targets for the elucidation of its mechanism.[147] P7C3-S326 had a benzophenone moiety for photo-crosslinking and an alkyne moiety for attachment of affinity tags using click chemistry. The target identification strategy is described in detail in Section 1.6.5.1. The molecular target of P7C3 was found to be nicotinamide phosphoribosyltransferase (NAMPT), the rate-limiting enzyme involved in converting nicotinamide into nicotinamide adenine dinucleotide (NAD). NAMPT activation by P7C3 leads to increased intracellular NAD levels, which contributes to enhancing cell survival and hence promotes neurogenesis.

Optimised variants of P7C3, such as P7C3-S243 and P7C3-A20, have been reported to have a similar mechanism of action by activating NAMPT and enhancing the flux of intracellular NAD.[147] Administration of P7C3-S243 in a rat model of PD blocked dopaminergic neuron cell death and protected the animals from motor deficits.[148] The neuroprotective effects were also reported in transgenic TgF344-AD rats when P7C3-S243 was administered over a long period of 24 months. While amyloid plaque deposition was not altered, the rate of neurodegeneration was slowed and the rats were protected from cognitive deficits.[149] Treatment with P7C3-A20 was found to stimulate postnatal SVZ and SGZ neurogenesis in a cerebral ischemia model in rats, improving spatial learning and memory 4 weeks after the stroke.[150] The efficacy of P7C3-A20 was also demonstrated in TBI models, with the increases in adult neurogenesis contributing to protection from injury-induced deficits and improved functional recovery.[151] Together, these studies suggest that increasing neurogenesis using a small molecule is a viable therapeutic strategy for neurodegenerative diseases, traumatic and ischemic injuries.

1.4.3.2 NSI-189

NSI-189 (**12**) is a benzylpiperizine-aminopyridine discovered by NeuralStem Inc. through an *in vitro* phenotypic drug screen using human fetal hippocampal NSCs.[152] The neurogenic activity of the compound was also observed *in vivo*, resulting in an increase in hippocampal cell proliferation and hippocampal volume in young mice. Oral administration of NSI-189 after cranial radiotherapy prevented neurocognitive complications in rats.[142] NSI-189 was tested in Phase 1B, double blind clinical trials as a treatment for major depressive disorder (MDD). An increase in hippocampal volume and a reduction in depressive and cognitive symptoms were observed with a 28-day drug treatment.[153] While the Phase 2 clinical trial failed to meet the clinical outcome on the clinician-rated depression severity scales, treatment with NSI-189 resulted in significant improvements in multiple cognitive tests.[154] As the exact mechanism contributing to the neurogenic effects of NSI-189 is not yet well understood, there are some challenges in interpreting the results of the clinical trials.

1.4.3.3 Spiro Derivatives

Chakravarty *et al.* generated a series of neurotrophic compounds using a 2-oxa-spiro[5.5]-undecane scaffold, identified based on a natural product, Paecilomycine A.[143] Joshi *et al.* further optimised the scaffold to 2-oxo-spiro[5.4]decane (**13**), which was found to show improved neurogenic properties *in vitro* and *in vivo*.[155] The neurogenic and neuroprotective properties of these derivatives was found to be associated with the activation of TrkB-PI3K-AKT pathway.

1.4.3.4 BET-Bromodomain Inhibitors

Li *et al.* carried out an *in vitro* differentiation phenotypic screen of 8000 compounds in murine neural progenitor cells.[144] 21 out of 30 confirmed hits were identified as BET-bromodomain(BRD) inhibitors. The neurogenic activity of the BET-BRD inhibitors corresponded with biochemical binding affinity of BET proteins. Treatment with BRD4 inhibitor JQ-1 (**14**) resulted in a two-fold increase in neurons formed, and a transcriptional activation of proneural genes. shRNA knockdown of BRD2, BRD3 and BRD4 in the cells enhanced differentiation of neural progenitor cells towards neurons, and blocked gliogenesis. The genetic validation suggests BET-BRD as a novel target for neurogenesis. Benito *et al.* showed that JQ-1 enhanced cognitive functions and synaptic plasticity in both WT and transgenic APP mice, suggesting that BET-BRD inhibitors could be developed as a therapeutic treatment for AD.[156]

1.5 In-House Phenotypic Screen for Proneurogenic Molecules

As neurogenesis is a complex process regulated by many factors highlighted in Section 1.2, identifying a specific target for a drug discovery programme is very challenging. A phenotypic screen would allow for identification of small molecules that increase neurogenesis in cellular or animal models irrespective of underlying mechanisms. This approach is especially more advantageous as the phenotypic outcome captures key aspects of physiological processes such as cell-cell interactions and interactions across multiple signalling pathways.[157] The successful discovery of P7C3 as a neurogenic compound led to the identification of NAMPT activation as a

mechanism for increasing neurogenesis, showing that a phenotypic drug discovery approach is also promising for identifying novel drug targets.

1.5.1 Pilot Screen

In collaboration with Prof. Francis Szele's group (Department of Physiology, Anatomy and Genetics, University of Oxford), an in-house phenotypic screen (Figure 7) was employed to discover small molecules that could modulate neurogenesis in SVZ- and DG-derived murine NSCs *in vitro*.

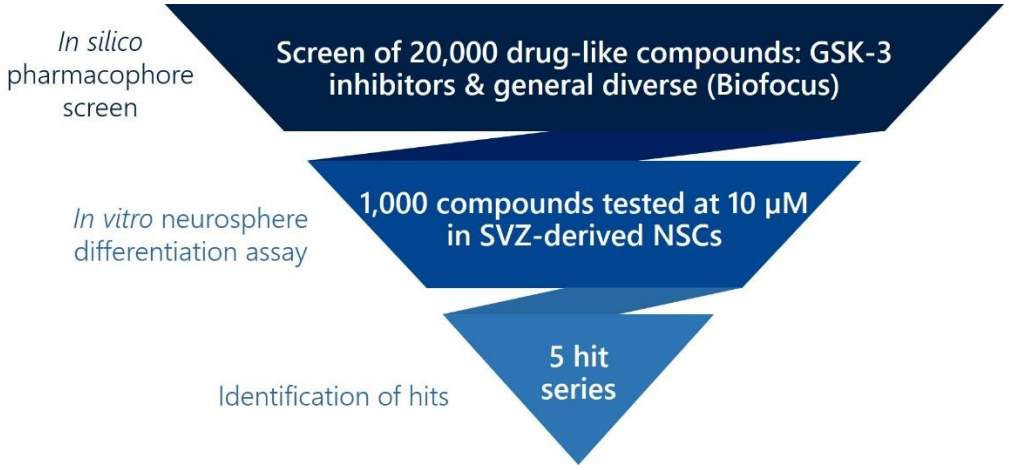


Figure 7. Schematic showing the pilot screening cascade for proneurogenic compounds.

A pilot screen was conducted using a Biofocus library comprising 20,000 compounds. *In silico* pharmacophore modelling was used to shortlist 200 compounds with structural similarities to known neurogenic compounds such as GSK3 inhibitors, which have been shown to act on the Wnt signalling pathway. Together with 800 randomly selected compounds, a total of 1,000 compounds were tested at single concentration of 10 µM in SVZ-derived NSCs in the *in vitro* neurosphere differentiation assay. Immunohistochemical staining was used to identify cells expressing neuronal markers MAP2 and Tuj1, and the percentage of MAP2+Tuj1+ cells was used as the phenotypic readout. Retinoic acid was used as a positive control. 30 compounds were identified as compounds of interest which increased the percentage of neurons formed after 6 days of differentiation. A concentration response study of these compounds was conducted in

both SVZ- and DG-derived NSCs. 5 distinct compound classes displaying neurogenic effects were identified as hits, one of which is OXS-N1.

1.5.2 Hit Compound OXS-N1

OXS-N1 was resynthesised and confirmed as a hit that increased neurogenesis *in vitro*, after 6-days of treatment in SVZ- and DG-derived NSCs (Figure 8). Treatment of the cells with OXS-N1 increased the percentage of cells expressing neuronal markers Tuj1 and MAP2 by up to 2-fold as compared to the vehicle control, DMSO.

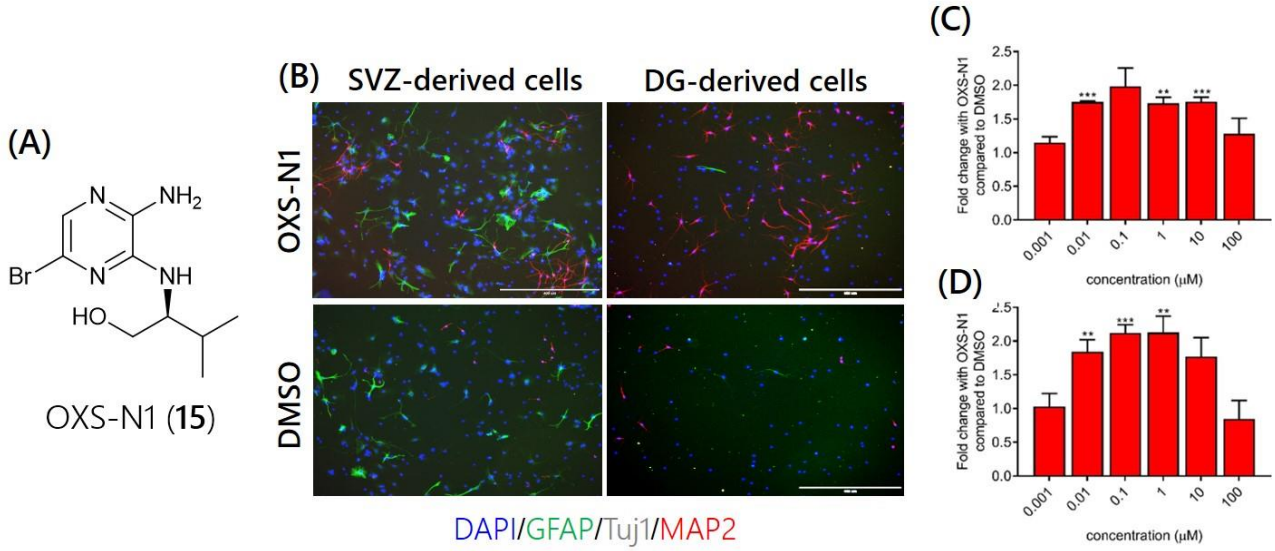


Figure 8. (A) Chemical structure of OXS-N1; (B) confocal images showing SVZ- and DG-derived cells with immunohistochemical staining after 6 days of compound treatment. Images taken by Dr Julie Davies (DPAG, Oxford). Graphs showing OXS-N1 concentration-dependent fold-change in percentage of neurons compared to DMSO control in (C) DG-derived and (D) SVZ-derived cells. Graphs kindly provided by Dr Julie Davies (DPAG, Oxford).

The pharmacokinetics and pharmacodynamics of OXS-N1 were examined through absorption, distribution, metabolism and excretion (ADME) studies. ADME properties of OXS-N1 indicated good absorption through the gut and permeability through the blood brain barrier (Figure 9). While the liver microsomal stability study indicated relatively good metabolic stability, the whole hepatocyte study highlighted possible issues with poor half-life and rapid clearance. A pharmacokinetic study showed that an oral dosage of 25 mg/kg was sufficient to give a good profile of compound concentration in the plasma and brain for up to 8 hours.

(A) ADME Properties of OXS-N1

Aqueous solubility/ µM	> 100
$T_{1/2}$ S9 liver microsomes/ min	1380
$T_{1/2}$ whole hepatocytes/ min	12
Plasma protein binding/ mean fu	0.544
Caco2 permeability/ mean efflux ratio	1.15
MDCK efflux/ mean efflux ratio	2.60

(B) *In Vivo* Pharmacokinetic Study of OXS-N1

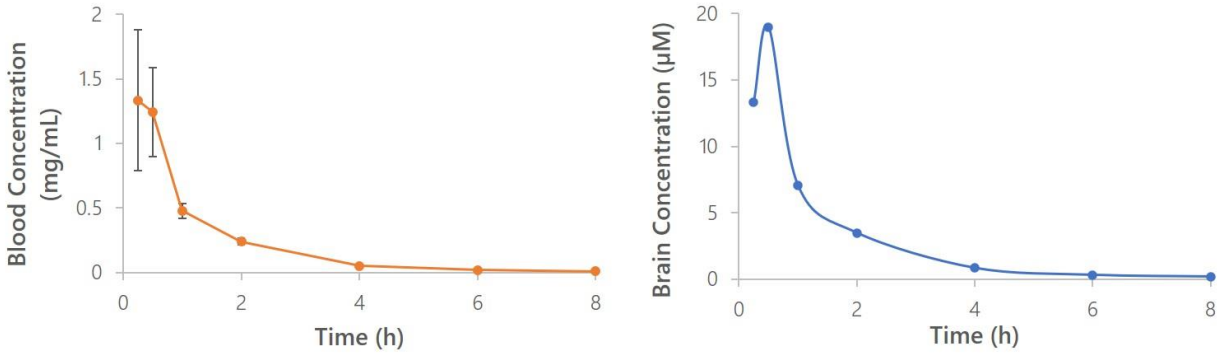


Figure 9. (A) Table showing ADME properties of OXS-N1. (B) Graphs showing plasma and brain concentrations of OXS-N1 against time after oral dosing (25 mg/kg). $T_{1/2}$, half-life; S9, liver microsomal fraction obtained after centrifugation at 9000 g; fu, fraction unbound; Caco2, human colorectal adenocarcinoma cell line; MDCK, Madin-Darby canine kidney cell line. Graphs kindly provided by Dr Julie Davies (DPAG, Oxford).

1.5.3 *In vivo* Activity of OXS-N1

Oral administration of OXS-N1 was found to increase SVZ and DG neurogenesis in wild-type (WT) mice. BrdU+Dcx+ and BrdU+NeuN+ double labelling was used to identify newly born immature and mature neurons respectively. There was a significantly higher density of BrdU+Dcx+ and BrdU+NeuN+ cells in both the ventral and dorsal DG of mice treated with OXS-N1 for one week compared to vehicle controls (Figure 10). A similar increase in the density of BrdU+Dcx+ and BrdU+NeuN+ cells in the OB after a 3-week treatment, but not 1-week, suggested that additional time was required for the newly born cells to migrate from the SVZ to the OB. The animals also spent more time in the novel arm in the novelty Y maze after 3-week treatment with OXS-N1, suggesting an improvement in spatial memory.

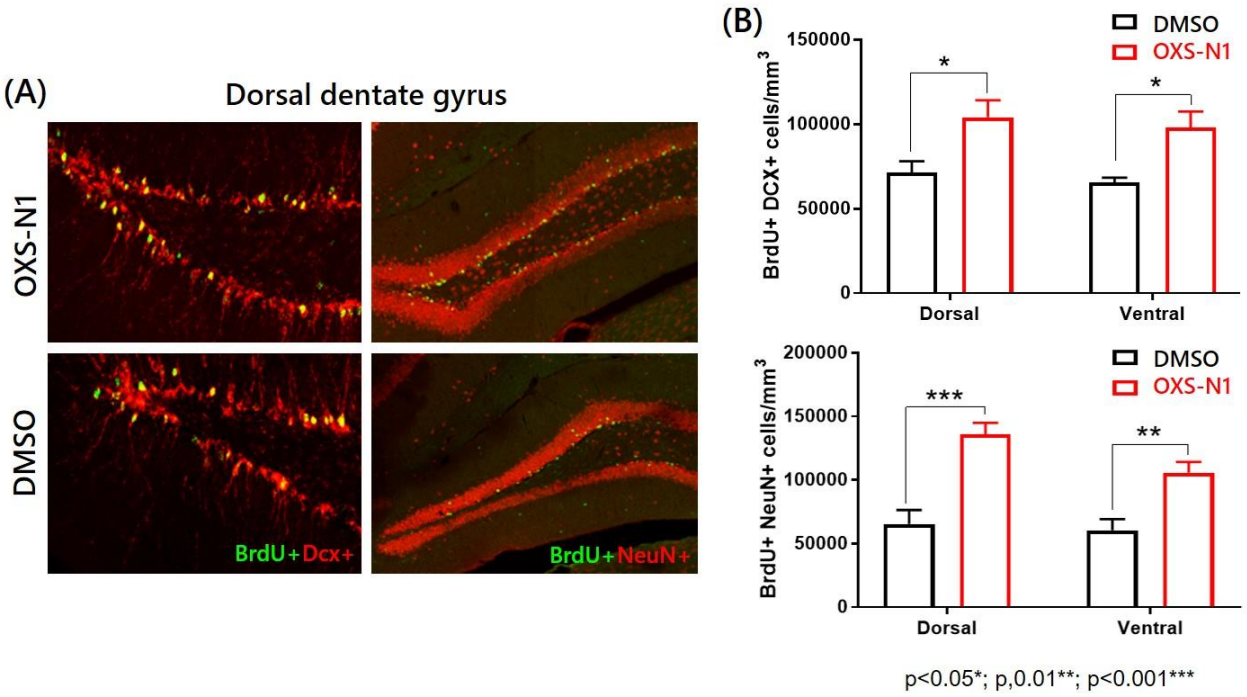


Figure 10. (A) Confocal images taken in the dorsal (anterior) DG of brains immunofluorescentlly labelled for either BrdU and Dcx for immature neurons or BrdU and NeuN for mature neurons. Images taken by Dr Julie Davis (DPAG, University of Oxford). (B) Graphs showing the quantification of the density of BrdU+Dcx+ and BrdU+NeuN+ cells in dorsal and ventral DG after the mice were treated with DMSO and OXS-N1 for one week. Graphs kindly provided by Dr Julie Davies (DPAG, Oxford).

1.5.4 Preliminary Mechanism of Action Studies

The *in vitro* and *in vivo* activity of OXS-N1 is promising, but its mechanism of action remains unknown. Knowing its molecular target would help the development of the hit compound to a lead candidate. Preliminary mechanism of action studies were carried out to understand if OXS-N1 was targeting known drug targets such as kinases, and to profile transcriptional changes associated with OXS-N1 treatment.

1.5.4.1 Kinome Screen

OXS-N1 contains an aminopyrazine ring, a motif which is commonly encountered in ATP-competitive hinge-binding kinase inhibitors. Scaffolds containing hydrogen bond donor-acceptor moieties can bind to the catalytic domain of kinases by forming hydrogen bonds with the residues in the hinge region. Aminopyrazine and aminopyrimidine moieties have been identified in inhibitors of kinases including tyrosine kinase and MK2.[158,159]

To investigate if kinase inhibition is linked to the mechanism of action of 2-aminopyrazine derivative OXS-N1, a screen against diverse kinases was conducted as part of the preliminary studies. A DiscoverX scanEDGE™ assay panel of 97 kinases was used to evaluate the kinase binding ability of OXS-N1. The assay quantitatively measured interactions between the compound and various kinases, using competitive binding to indicate thermodynamic interaction affinity. The readout (% ctrl) indicates the percentage of kinases captured on the solid supported substrate after compound treatment, compared to a DMSO control. OXS-N1 was tested at a single concentration of 1 μM, as this concentration provided at least a 1.5-fold increase in the percentage of neurons formed in both the SVZ- and DG-derived cells (Figure 8C & D). Binding of OXS-N1 to a kinase would result in a lower % ctrl value. Kinases which were identified as possible targets of OXS-N1, inhibiting kinase substrate binding by >70%, are shown in Table 1. To further investigate the potential inhibitory potency of OXS-N1 on the putative hits identified from the kinome screen, 10 different concentrations of OXS-N1 were tested against the 5 kinases to determine IC_{50} values. Staurosporine was used as a positive control and the IC_{50} values are compared in Table 1.

Table 1. Table showing % ctrl values (Kinome screen) for selected kinases after OXS-N1 treatment. The % ctrl indicates the percentage of kinases captured on the solid supported substrate after compound treatment, compared to a DMSO control. Kinases with % ctrl value below 30 were identified as potential hits. IC_{50} values of OXS-N1 and the positive control (staurosporine) against these 5 kinases were determined. The most significant hit, FLT3, is highlighted in blue.

Kinase	% Ctrl (with 1 μM OXS-N1)	IC_{50} (μM) for Positive Control (Staurosporine)	IC_{50} (μM) for OXS-N1
ABL1	28	0.196	-
AXL	13	0.0080	-
FLT3	0.2	0.0014	9.40
LKB1	9.6	0.083	-
SPRK3/MSSK1	6.9	2.95	-

Among the 5 kinases identified from the kinome screen, the most significant hit is FLT3. No IC_{50} values could be determined for OXS-N1 against the 4 kinases, ABL1, AXL, LKB1 and SPRK3, as no inhibitory effect was noted up to the highest concentration tested (30 μM). OXS-N1 has an

IC_{50} value of 9.40 μM against FLT3, a type III receptor tyrosine kinase. A third of acute myeloid leukemia patients have mutations of the FLT3 gene, which cause downstream oncogenic effects on myeloid transcription factors.[160] FLT3 knockout mice were found to have severe abnormalities in hematopoietic tissues but not in the central nervous system, suggesting that FLT3 does not play a significant role as a trophic factor for development of nervous tissues.[161] However, Brazel *et al.* suggested that FLT3 offers trophic support to NGF, with a role to play in NSC proliferation and maturation.[162] The IC_{50} of OXS-N1 for FLT3 is quite high compared to the positive control, suggesting that it only exhibits a weak inhibitory effect on FLT3. The hits generated from the kinome screen were hence insufficient to identify a clear target to pursue in target validation studies, and more detailed target identification studies have to be carried out.

1.5.4.2 RNA Sequencing

RNA sequencing was done on RNA harvested from SVZ- and DG-derived cells after treatment with OXS-N1 under proliferating and differentiating conditions. This was used to evaluate the transcriptional effects of OXS-N1 (1 μM) treatment on the NSCs. OXS-N1 was found to result in differential expression of around 7,000 genes, particularly enriching for the Gene Ontology (GO) cellular components pathways. Figure 11 shows the processes enriched by OXS-N1, ranked by the p-values. Compared to the DMSO control, OXS-N1 treatment induced an upregulation of genes associated with synapse and cellular respiration, which corresponds with reported changes in metabolic processes of activated stem cells. Significant changes in cellular metabolism have been associated with the differentiation of NSCs and subsequent maturation into neurons.[163] There was also a downregulation of genes involved in translational and mitotic machinery after OXS-N1 treatment. This suggests that OXS-N1 treatment induced changes in translational control, which is typically observed during neuronal differentiation.[164]

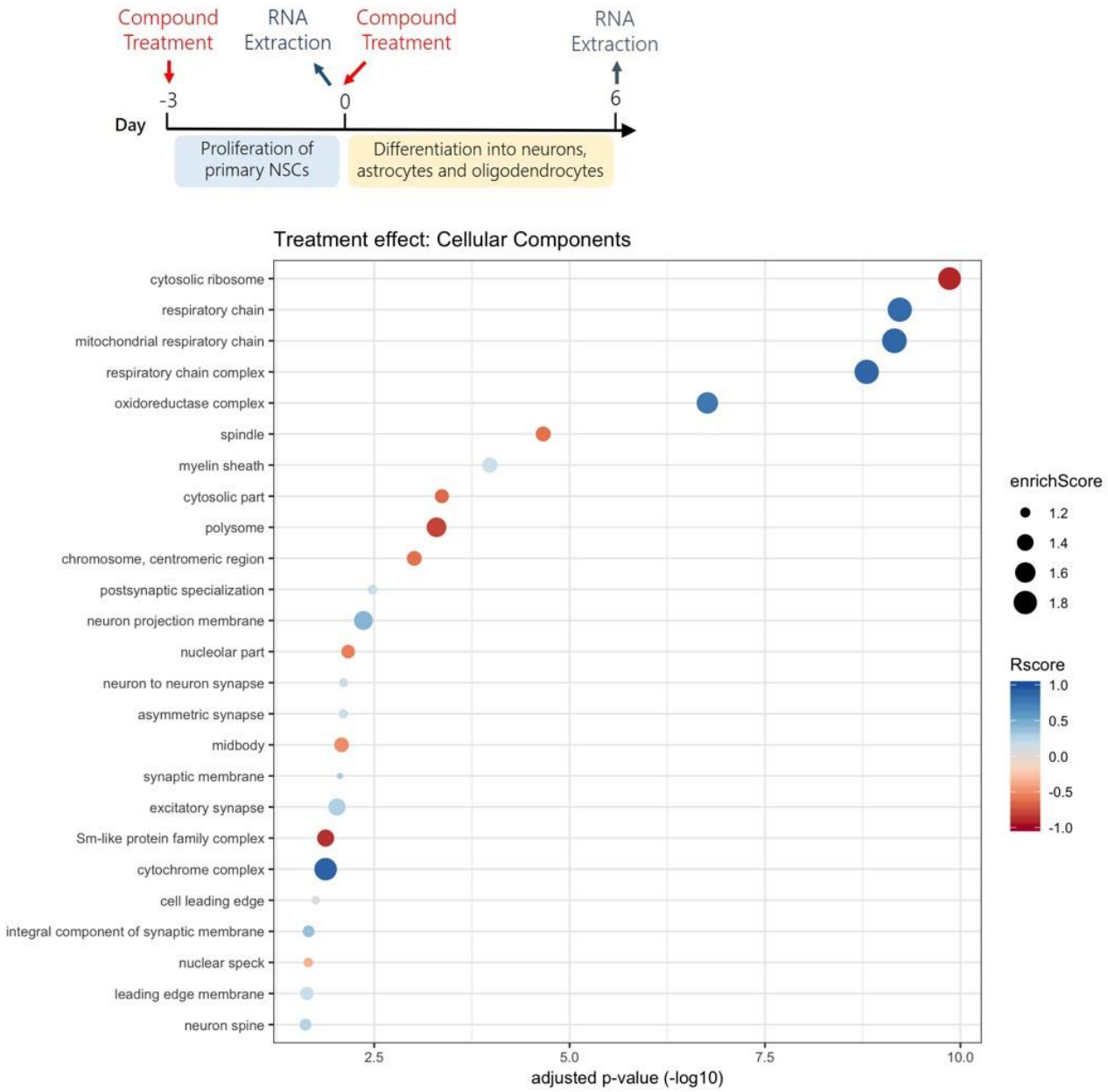


Figure 11. Figure showing processes in the GO cellular components pathway affected by OXS-N1 treatment. Rscore reflects the proportion of up/downregulated genes in that process, with dark blue indicating a higher proportion of upregulated genes. The enrichScore is an indication of the number of observed over expected genes in that process. Cell treatment and RNA extraction experiments were done by Dr Julie Davis (DPAG, Oxford) and RNA-sequencing analysis was done by Dr Jesse Dabney (DPAG, Oxford).

1.6 Target Identification

For diseases that are complex and poorly understood, phenotypic screening has been useful to identify biologically active agents. While such approaches allow for initial screening of therapeutic compounds, understanding of the molecular targets affected by the hit compounds is important for identifying the mechanism of action and for improving activity and efficacy. Any off-target effects can also be addressed to optimise the drug candidate. Target identification

involves elucidating the direct molecular target, for example a protein, which the small molecule interacts with. Diverse approaches to target identification include (i) proteomics involving probing of protein-small molecule interactions, (ii) genetic screening methods involving identification of small molecule-resistant genes in genetically engineered species,[165] and (iii) bioinformatic methods involving computational analysis of drug targets based on chemical similarities and analysis of interacting networks.[166] The focus of this DPhil work will be on chemoproteomics, a commonly used direct approach involving small chemical probes to investigate the interactions with protein targets in pull-down assays.

1.6.1 Affinity-based Protein Profiling (AfBPP)

A common approach in protein profiling is the use of affinity resins to isolate cellular protein targets.[167] Structure-activity relationship (SAR) studies of the small molecule are crucial to identify suitable positions for the attachment of the affinity moieties. The small molecule can be covalently attached to a solid support via a linker, or it can be bound to avidin-agarose beads via a biotin moiety (Figure 12). Proteins that bind non-specifically to the small molecule are removed by stringent washing steps. Target proteins that interact with the small molecule can be captured from the cell lysates by affinity purification, separated by sodium dodecyl sulfate polyacrylamide gel electrophoresis (SDS-PAGE) and isolated from the gel. The proteins can be then identified by liquid-chromatography mass spectrometry (LC-MS).

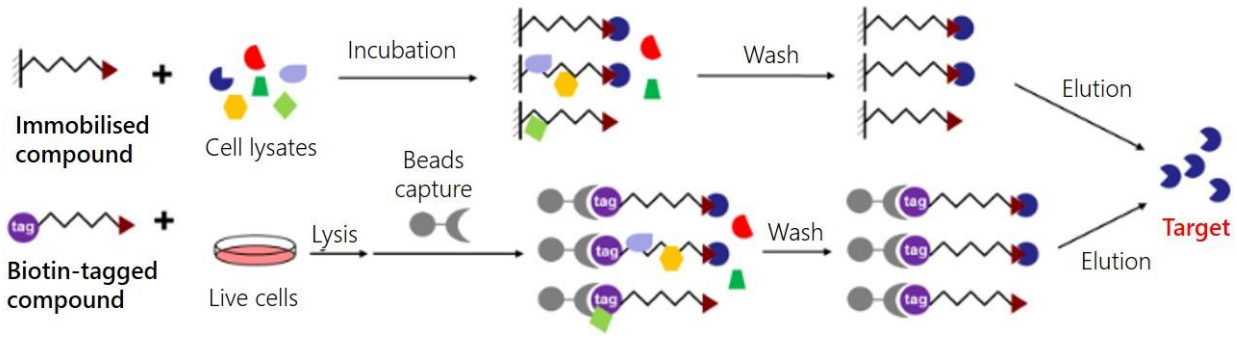


Figure 12. Schematic showing general workflow of affinity-based protein profiling using small molecules immobilised onto a resin or tagged with an affinity tag such as biotin.[167]

1.6.1.1 Bioorthogonal Reactions

The addition of a bulky biotin tag to the small molecule of interest often results in loss of activity or decrease in cell permeability. Affinity purification is hence often done in cell lysates, which is not ideal as it does not mimic the actual environment that the small molecules bind to their targets in. To overcome this problem, two-step tag-and-capture approaches are increasingly used to capture proteins in live cells.[168] A small tag such as a terminal alkyne, azide or cyclopropane, is incorporated into the molecule instead of a biotin group. The small functionality introduced is likely to better retain biological activity, and reduce problems of cellular uptake. This allows the probe to be used in live cells, which is a more biologically relevant setting than cell lysates. The reactive functionality can then be subsequently transformed in a bioorthogonal reaction (Figure 13) to introduce various reporter groups, such as biotin and fluorophores, into the small molecule under biocompatible conditions.[169]

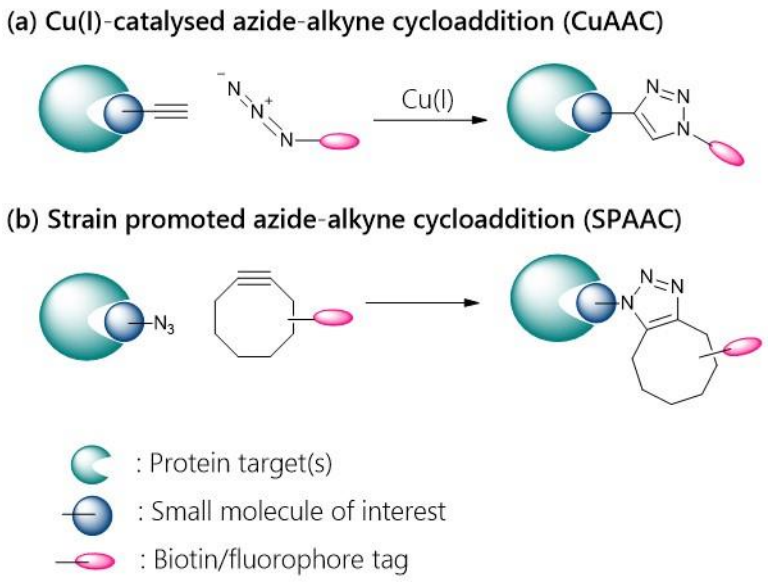


Figure 13. Schematic showing the use of CuAAC and SPAAC as biorthogonal reactions in proteomics applications.

The most commonly used bioorthogonal reaction is a copper (I) catalysed alkyne-azide cycloaddition (CuAAC) reported by Sharpless and Meldal.[170,171] Along with improvements in ligands used to increase copper reactivity,[172] this 'click' chemistry strategy has been applied as a bioconjugation strategy in many protein profiling applications.[173] Alkynes are advantageous as tags due to their small size and low chemical reactivity. Speers and Cravatt have reported that

the use of the azide on the reporter group partner during CuAAC can minimise the background labelling.[174] Incorporation of the alkyne into the probe instead of the reporter group avoids problems of background signal that arise due to the formation of reactive copper acetylides in presence of excess alkyne.

Due to the toxicity of the copper catalyst, CuAAC has to be conducted in fixed cells or in cell lysates.[175] A copper-free alternative would be a strain-promoted alkyne-azide cycloaddition (SPAAC), with a cyclooctyne containing a reporter tag reacting with an azide-tagged probe.[176] This reaction occurs under physiological conditions, without the need for a catalyst. However, the reaction occurs at a slower rate than CuAAC, and the cyclooctyne reagents generally have poorer solubility, limiting their applicability.[177] A side-by-side comparison of CuAAC and SPAAC by Li et al. suggested that CuAAC gave higher protein identification levels and better accuracy compared to SPAAC for proteomics experiments.[178]

1.6.1.2 Probe Design

In designing the probes, the alkyne handle should be incorporated at a position that minimises perturbation to the biological activity of the molecule. A linker group, usually a polyethylene glycol (PEG) spacer, can be used to project the alkyne handle away from the core of the molecule, to minimise steric effects between the molecule and reporter groups.[179] The biological activity of the probes can be validated in comparison to the parent compound in cellular assays, to ensure that the probe has a similar mechanism of action as the parent compound. While alkynes are rare in biological systems, it is still important to consider the reactivity of terminal alkynes with biological molecules. Terminal alkynes are found in several enzyme inhibitors, such as *N*-propargylamines, which inhibit FAD-dependent enzymes.[180] Reaction of the alkynes with enzymes such as p450 enzymes and FAD-dependent enzymes can potentially reduce the amount of probe available in the living cells.

1.6.1.3 Controls

Well-designed controls are required to remove false positives in the target binding experiments. An inactive analogue could serve as a control to identify proteins that are binding non-specifically to the probe. However, the inactivity of the analogues could be due to solubility or cell permeability issues. The inactive analogues may be able to bind to target proteins in cell lysates where such issues are not so prominent, leading to false negative results. It is hence important to ensure that the inactive analogue used as the control retains similar chemical and physical properties to the active compound. For example, the inactive enantiomer of the active compound could be used as enantiomers should bind non-specifically to the same proteins via electrostatic interactions. Only the active enantiomer should bind specifically to the target protein by stereospecific interactions.[167] The parent compound can also be used in competition experiments, where an excess of the parent compound competes with the probe for the target proteins, lowering the amount of target protein identified in the pull-down experiments.

1.6.2 Photoaffinity Labelling

The incorporation of photoaffinity labelling is a useful approach to enhance the identification of weakly bound or lowly abundant protein target.[181] Photoaffinity labelling requires a chemical probe that bears a photoactivatable moiety. The photoreactive group generates a reactive species upon ultraviolet (UV) irradiation and forms covalent linkages with adjacent molecules, ideally the target proteins. The covalent binding improves recovery of proteins even for small molecules with low efficacy and weak affinity binding, and minimises the loss of the probe-protein binding interactions through multiple washing steps of affinity purification.[182] An ideal photoaffinity probe should be stable in the dark, retain biological activity as compared to the small molecule, and should not interfere with the binding to the target protein. Activation of the probe should also be above wavelengths that proteins absorb at, namely 200 and 280 nm, to prevent degradation of the proteins.

General photoaffinity probes involve three functionalities, namely the small molecule of interest, the photoreactive moiety and the bioorthogonal reaction handle. The photoreactive moiety should generate highly reactive intermediates that can form stable adducts with various functionalities, and be isolated in the purification step. Commonly used photoactivatable moieties include benzophenones, aryl azides and diazirines, which form diradicals, nitrenes and carbenes respectively as the reactive intermediates (Figure 14). The bioorthogonal reaction handle allows for the later stage incorporation of the reporter tag using click chemistry.

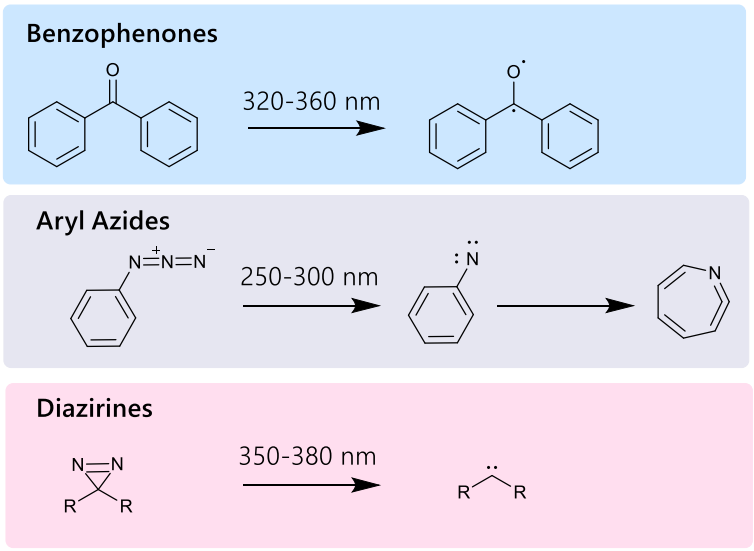


Figure 14. Figure showing the commonly used photoactivable groups and the reactive species formed upon UV irradiation. Aryl azide forms the singlet nitrene, which undergoes ring expansion to 1,2-didehydrozepine and reacts with nucleophiles.[183] Benzophenone forms a reactive triplet diradical while diazirine forms a singlet carbene upon photoactivation.[181]

1.6.2.1 Benzophenones

Benzophenones are readily synthesised by Friedel-Crafts acylation of arenes with benzoyl chloride. They show low reactivity to water and are activated by long wavelengths of 320-360 nm, making it suitable for use in biological systems. Increased length of irradiation improves the crosslinking yield as benzophenones can be repeatedly photoactivated. However, the long irradiation time to generate the reactive triplet diradical may increase non-specific protein binding. The hydroxyl group in the labelling product may also be involved in dehydration reactions, leading to problems in MS analysis.[184] Disadvantages of the benzophenone group include its bulkiness and preferential reaction with methionine residues.[185]

1.6.2.2 Aryl Azides

Aryl azides are readily synthesised and can be incorporated into compounds using aromatic substitution or amide coupling reactions. However, their short activation wavelength of 260 nm may cause damage to nucleic acids and proteins in biological systems. Low labelling yields have also been attributed to the low reactivity of the nitrene species form and the rearrangement of nitrene to benazirines and ketenimines.[182]

1.6.2.3 Diazirines

Diazirines form carbenes when activated at 365 nm, minimising damage to biological molecules. They are highly reactive and can form covalent bonds with the target proteins rapidly by insertion into neighbouring C-H or heteroatom-H bonds. They are easily quenched in water, which reduces the labelling efficiency but also minimises non-specific protein binding.[186]

Diazirines have been increasingly chosen as photoaffinity labels for small molecule probes. Alkyl diazirines are especially attractive due to their compact size, which causes minimal perturbations to chemical structure and activity of the small molecule. Li *et al.* introduced a 'minimalist' linker which contains both a diazirine and an alkyne on a single alkyl chain to detect small molecule-protein interactions through protein profiling and cellular imaging *in vitro*.[187] Aromatic diazirines, such as trifluoromethylphenyldiazirine (TPD) derivatives, have better cross-linking efficiencies compared to alkyl diazirines, as carbenes from alkyl diazirines tend to rapidly isomerise into diazo isomers.[188] However, the TPD group is bulky and requires a longer synthetic route, making it less attractive in comparison to the smaller alkyl diazirine linkers.

1.6.2.4 Controls

Issues of non-specific cross-linking are common as photoaffinity probes cross-link to highly abundant or 'sticky' proteins. Control experiments have to be conducted to remove background labelling from specific cross-linking. The amount of labelling which occurs in the absence of a photoaffinity probe and without UV radiation should be determined. A competition experiment, using an excess of the unmodified parent compound, can identify specific cross-linking to

proteins as the parent compound should have greater affinity toward its target than the photoaffinity probe. A dose-dependent decrease of signal from the reporter tag in the presence of the parent compound would indicate specific labelling of proteins.

1.6.3 SILAC Approach

Stable isotope labelling with amino acids in cell culture (SILAC) is a useful method for quantification in chemoproteomics. It relies on the metabolic incorporation of an isotope label, such as ^{15}N, into the amino acid residues of proteins through media supplementation in cell culture.[189] Protein incorporating 'light' chains and 'heavy' chains can be quantified in the pull-down samples using MS analysis. Ong *et al.* combined SILAC with affinity enrichment for target identification in a study with kinase inhibitors and immunophilin binders.[190] Small molecule-loaded beads were used in heavy and light affinity pull-down experiments, and in one experimental condition, an excess of small molecule was used to displace target proteins. Proteins interacting with the small molecule were enriched in the heavy state and were identified through SILAC ratios determined by MS. The known protein targets of the small molecules tested were successfully identified by Ong *et al.* with great specificity by using this method. The SILAC approach provides an unbiased and robust identification of proteins interacting with small molecules. However, SILAC is limited by the need to label cells efficiently, requiring at least 3 generations of the cells for high labelling efficiency. This approach is hence not suitable for primary cells which can only be cultured for limited passages.

1.6.4 Label-free Approaches

Label-free approaches are advantageous as they do not require the incorporation of reporter groups or other modifications on the small molecule. Drug affinity responsive target stability (DARTS) is a label-free method that uses the protease susceptibility of the proteins to identify the target proteins. As proteins that are bound to small molecules are more stable towards proteolysis, they can be identified after proteolysis of the cell lysates and affinity enrichment. Lomenick *et al.* used the DARTS approach to identify a new target of resveratrol, and validated

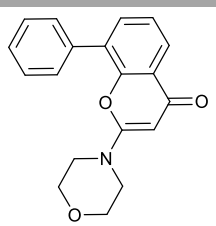
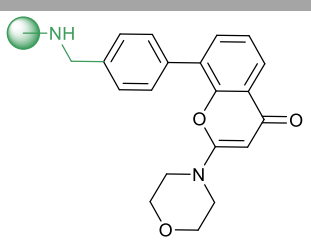
known targets of small molecules like rapamacyin.[191] However, this approach might be limited to probe targets of low abundance and weak binding affinities to the drug.

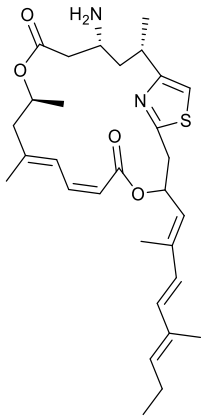
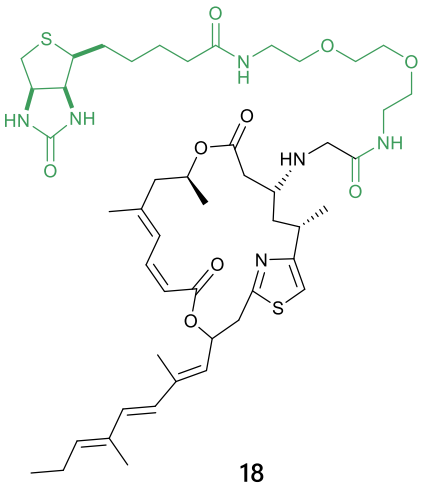
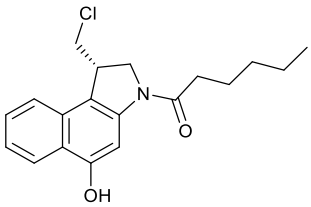
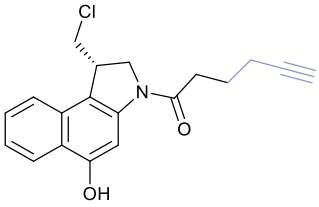
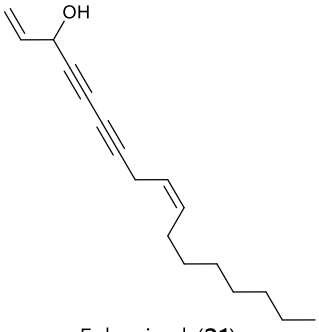
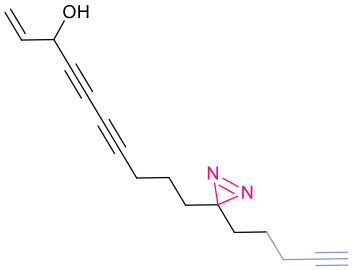
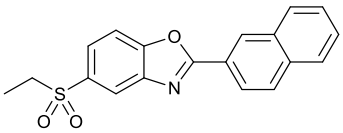
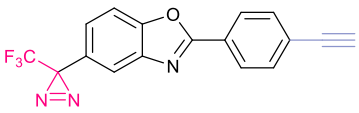
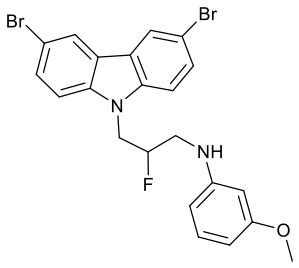
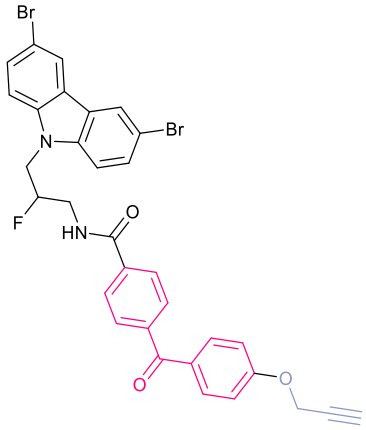
Stability of proteins from rates of oxidation (SPROX) is another label-free method that probes the thermodynamic stability of the proteins during chemical denaturation by using hydrogen peroxide, which oxidises methionine residues irreversibly. Thermodynamic measurements of protein-folding reactions are used to detect protein-small molecule interactions. West at al. used the SPROX approach to investigate the protein targets of cyclosporine A (Cs A), resulting in the identification of 2 previously known targets and 8 other new targets.[192] While there are advantages to identifying protein targets directly using this method, there are also several limitations, such as the need for a methionine-containing peptide in the target protein, and the possibility that the oxidative reaction might have influences on ligand binding and protein folding.

1.6.5 Examples of Target Identification Studies

Several methodologies for target identification have been discussed, including AfBPP, photoaffinity labelling and label-free approaches. Chemoproteomics approaches for target deconvolution for small molecules often integrate these methodologies in complementary ways. Some examples highlighting the variety of affinity, clickable and photoaffinity probes used in target identification studies are presented in Table 2.

Table 2. Examples of probes developed to identify targets for literature compounds. Colours in chemical structures indicate various modifications made to the parent compound to incorporate groups for chemoproteomic experiments: Resin/biotin tags highlighted in green, biorthogonal handles highlighted in blue and photoreactive groups highlighted in pink.

Parent Compound	Probe	Control	Target ID Methods	Target(s)
 LY294002 (**16**)	 **16b**	Inactive analogue	Isotopic labelling, LC-MS/MS	PI3K (on-target), BET-BRD (off-target)[193]

 Pateamine A (**17**)	 **18**	Competition with parent compound	SDS-PAGE gel band excision, MALDI-TOF	Eukaryotic translation initiator-4A (eIF4A)[194]
 Duocarmycin seco drug (**19**)	 **20**	Vehicle (DMSO)	SDS-PAGE gel band excision, LC-MS/MS	Aldehyde dehydrogenase (ALDH1A1)[195]
 Falcarinol (**21**)	 **22**	Vehicle (DMSO)	SILAC	Aldehyde dehydrogenase (ALDH2)[196]
 Ezutromid (**23**)	 **24**	Inactive analogue, Competition with active analogues	In-solution tryptic digestion, LC-MS/MS	Aryl hydrocarbon receptor (AhR)[197]
 P7C3-A20 (**11**)	 P7C3-S326 (**25**)	Competition with parent compound	2D gel spot excision, Shotgun MS	Nicotinamide phosphoribosyl-transferase (NAMPT)[147]

1.6.5.1 Chemoproteomic Profiling of LY294002

LY294002 (**16**) is a phosphoinositide 3-kinase (PI3K) inhibitor which is used to study the role of PI3K signalling in cell migration, proliferation and survival.[198] PI3K inhibitors are promising therapeutic agents for cancer treatment and resolved crystal structures of PI3Kγ with LY294002 has accelerated the drug discovery process to develop more potent PI3K inhibitors.[199] While LY294002 showed good antitumour activity *in vivo*, it was not taken into clinical trials due to dermal toxic side effects.[200] Dittmann *et al.* carried out quantitative chemoproteomic profiling of LY294002 to validate its selectivity for PI3K.[193] LY294002 was immobilised on beads and PI3K-inactive compound LY3030511 was used as a negative control. After affinity enrichment, tandem mass tag (TMT) labelling was used to quantify the captured proteins from the samples. Competition with the parent compound LY294002 was used to determine IC_{50} values for each competed protein. The IC_{50} values of LY294002 for PI3Kα, PI3Kβ and PI3Kδ were in the sub-micromolar range, which corresponded to reported values in literature.[201] The chemoproteomics profiling also confirmed that PI3K-inactive compound LY3030511 did not interact with PI3K. Surprisingly, both LY294002 and LY3030511 was found to have IC_{50} values in the micromolar range for bromo and BET family proteins BRD2, BRD3 and BRD4. X-ray crystal structures of the compounds with the BET proteins confirmed the binding mode to be novel and selective for the N-terminal bromodomain. The polypharmacology of the chromen-4-one scaffold suggests that the widely used LY294002 is promiscuous and this could have contributed to the toxicity effects observed *in vivo*. This highlights the importance of using chemoproteomics to profile the molecular targets of therapeutic agents and establish any off-target binding that might led to adverse toxicity effects in the later stages of drug development.

1.6.5.2 Target Identification of Ezutromid

Ezutromid (**23**) is a utrophin modulator discovered through phenotypic screening for the treatment of Duchenne muscular dystrophy (DMD). To identify the molecular interactions responsible for the phenotypic effect of Ezutromid, Wilkinson *et al.* developed a dual-tagged probe (**24**) comprising of a trifluoromethyl-phenyldiazirine as a photoaffinity label and an

alkyne as a click handle.[197] An inactive analogue containing the naphthyl substituent at the 1'-position instead of the 2'-position was used as a control to identify non-specific interactions with proteins. Active variants of the parent compound were also selected as competition controls to facilitate the identification of therapeutically relevant targets. Proteome-wide target identification was conducted following affinity enrichment, and enriched proteins were identified using LC-MS/MS. Potential targets were shortlisted by combining differences in proteins identified by the active probe and not in the 2 controls. Target validation using immunoblotting in live muscle cells and K_D determination using a fluorescence quenching assay subsequently confirmed aryl hydrocarbon receptor (AhR) as the molecular target of ezutromid. RT-PCR experiments showed that ezutromid treatment decreased the expression of AhR-responsive genes, indicating that ezutromid is an AhR antagonist. While AhR gene silencing studies were not performed, structurally distinct AhR antagonists were shown to also increase utrophin expression in muscle cells. This provided pharmacological validation that AhR antagonism contributes to the phenotypic effect observed and could be a novel mechanism to modulate utrophin modulation.

1.6.5.3 Target Identification of P7C3

Various methods have been used to identify the molecular target of proneurogenic compound P7C3, including affinity purification with biotinylated probes and radiolabelling. Among the strategies employed, the most successful one was a photo-crosslinking approach combined with AfBPP. The chemical probe reported by Wang *et al.*, P7C3-S326 (**25**), has a benzophenone moiety for photo-crosslinking and an alkyne moiety for attachment of affinity tags using click chemistry.[147] This probe was found to retain activity in both the *in vitro* doxorubicin toxicity (dox:tox) assay and the *in vivo* neurogenesis assay. Upon UV irradiation, P7C3-S326 was covalently bound to many proteins from cultured cells. Coincubation with a 30x excess of the parent compound P7C3-A20 resulted in one of the protein bands at 55 kDa being outcompeted, highlighting it as a possible molecular target. Click chemistry was used to append fluorescent tags on the probe-protein complexes. A red fluorescent dye was attached onto P7C3-S326-bound

proteins in presence of excess P7C3-A20, and a green fluorescent dye was attached onto P7C3-S326-bound proteins in absence of P7C3-A20. The proteins were resolved by 2D gel electrophoresis and green-only spots indicated proteins of interest that were outcompeted by the parent compound. The relevant spots were excised from the gel and identified by shotgun mass spectrometry. NAMPT was identified from all four of the spots excised at 55 kDa. P7C3-S326 binds to the recombinant NAMPT enzyme in a manner that can be outcompeted by other active variants of P7C3, validating it as a molecular target of P7C3-A20 and its derivatives. By agonising the activity of NAMPT, P7C3-A20 enhances the intracellular production of nicotinamide adenine dinucleotide (NAD) from nicotinamide. Increased level of NAD protects the cells from doxorubicin-mediataed toxicity and contributes to overall neuroprotective effect. However, the exact mechanism in which P7C3-A20 activates NAMPT is not yet clear. The P7C3-A20 binding site on NAMPT is unknown and effects of P7C3-A20 binding on post-translational modifications of NAMPT have not been explored.

1.7 Target Validation

Target identification strategies identify putative targets, which must then be validated through target-specific experiments. A key objective of target validation is to verify that the interaction with the molecular target mediates the biological response in the cellular or disease models. This is crucial to show that the small molecule-target interactions are physiologically relevant. Quantitative measurements of the binding affinity between the small molecule and protein target are also important. This can be done by testing on recombinant or purified proteins using various biophysical methods. The binding affinity of the small molecule can be then correlated to its biological activity in cellular assays.

1.7.1 Biophysical Methods

A correlation study relating the affinity of the small molecule for the target protein and its potency of causing the cellular phenotype is a common method of target validation. This can be tested using analogues of the small molecule demonstrating varying potency, in a SAR-type

study. The binding affinity and kinetics of the small molecule can be tested using a variety of biophysical methods, such as thermal shift assays, surface plasmon resonance and NMR methods.

1.7.1.1 Cellular Thermal Shift Assay (CETSA)

CETSA is a method developed by Martinez Molina *et al.* to monitor drug target engagement in cells and tissue samples.[202] This technique makes use of the biophysical principle that the binding of a small molecule induces thermal stabilisation of the protein. Typically, thermal shift assays (TSAs) are used to characterise ligand binding by observing shifts in the protein melting curves with compound addition.[203] Techniques to monitor protein unfolding include ThermoFluor, which measures the fluorescence when a fluorophore binds to exposed hydrophobic residues of the unfolded proteins,[204] and differential static light scattering, which measures the amount of precipitated protein.[205] However, these methods can only be used with purified or recombinant proteins and do not allow for probing in a cellular context. Using the CETSA method, melting curves of proteins in cell lysates can be calculated from the levels of soluble proteins obtained after the heat treatment. By varying the concentration of the compound treatment and monitoring changes in the melting curves, levels of cellular target engagement can be quantified. This method covers the whole cellular proteome in an unbiased manner and can be adapted into a high-throughput screen.[206]

1.7.1.2 Fluorescence Polarisation Assay

Fluorescence polarisation (FP) is a technique that can be used to study molecular interactions by measuring the polarisation of the light emitted by a fluorescent ligand binding to a protein. Small molecules rotate rapidly in the solution and when excited with polarised light, they emit depolarised light. When the fluorophore binds to a large molecule such as a protein, the whole complex rotates slowly and emits plane polarised light upon excitation. FP assays are useful for detection of interactions with fast dissociation rates, as quantification of ligand binding can be

done without perturbing the equilibrium. The measurements are done using a microplate reader, allowing for rapid high-throughput screening of ligands.[207]

1.7.1.3 Surface Plasmon Resonance (SPR)

SPR is an efficient method used for studying protein interactions, measuring binding affinities and binding kinetics. It can be employed for a high-throughput ligand screen against a target protein.[208] The protein of interest is immobilised on the chip using various methods such as amide coupling and His-tagging. A solution containing the ligand is pumped across the chip, and as the ligand binds to the protein, the mass of the material bound to the surface increases. This difference in mass is reflected in the angle of polarised light reflected from the chip, allowing for the quantification of binding affinities. A key challenge of this method is to immobilise the protein on the chip without affecting its biological activity or restricting binding of ligands.[209]

1.7.1.4 WaterLOGSY

Water-ligand observed via gradient spectroscopy (waterLOGSY) is an NMR method for identifying compounds which interact with macromolecules such as proteins and DNA fragments. This method has been used in screening of ligands and is partly useful for screening fragments in early stages of the drug discovery processes.[210] It relies on the transfer of bulk water magnetisation to the ligand via the nuclear Overhauser effect (NOE) through different pathways, including via the protein-ligand complex to the free ligand.[211] The resonance of non-binding compounds appears opposite in sign compared to the interacting compounds. Ligand titration can be used to determine K_D through waterLOGSY and water-accessible protons of interacting ligands can be identified, giving some information on the ligand binding orientation.[212] However, a limitation of this method is the risk of false negatives, as ligands which are bound very strongly with slow dissociation rates would not show an opposite resonance in the waterLOGSY spectrum.[213]

1.7.2 Genetic Methods

Genetic methods of target validation are used to establish links between the modulation of the protein target of interest and the cellular phenotype observed. If a biologically active small molecule causes a cellular phenotype by binding to and inhibiting a specific protein, it is expected that (i) overexpression of the target protein will diminish the effects of the small molecule; (ii) deletion of the target protein will cause the same cellular phenotype as the treatment with the small molecule; (iii) a mutant target protein that no longer binds to the small molecule but retains cellular activity of WT protein will exhibit resistance to the small molecule. Genetic methods including overexpression, knockdown and knockout techniques, are used to address the aforementioned aspects.

1.7.2.1 Knockdown Models

The easiest and most widely used genetic method of target validation is to knock down the target protein through RNA interference.[214] Small-interfering RNA (siRNA) and short hairpin RNA (shRNA) are used to induce degradation of the target gene mRNA and knock down the expression of the target protein to varying levels.[215] If the binding of the small molecule to the protein target elicits or activates biological functions that result in a particular cellular phenotype, knockdown of the target would impair its biological activity.

Transfection of siRNA or shRNA constructs into cells can be done using chemical or physical methods. Chemical transfection methods typically involve the use of a lipid reagent, which can cause toxic side effects. Primary cells, especially neuronal cells, are difficult to transfect, and physical transfection methods such as electroporation are preferred.[216] The balance between transfection efficiency and cytotoxicity has to be optimised with each knockdown experiment.

1.7.2.2 Knockout Models

Clustered regularly interspaced short palindromic repeats (CRISPR)/Cas technology enables genetic manipulations for generating knockout models. Cas9 proteins can be programmed to cleave specific DNA sequences by custom guide RNAs (gRNAs), allowing for the genome to be

edited at a precise locus.[217] Cellular repair of the site-specific DNA breaks results in various outcomes, including mutation of a specific site through mutagenic non-homologous end-joining (NHEJ), insertions or deletions at the site. A mutation in the protein-coding region subsequently results in a functional gene knockout. The cellular phenotypic outcome of a complete loss of target gene function can be observed, compared to knockdown models which may still have remaining functional mRNAs. However, the use of primary cells with CRISPR/Cas technology remains a challenge, due to difficulty in delivering the components into the cells, and differences in exonuclease and promoter activities.[218] With increasing applications of CRISPR/Cas technology in animal models, it can also be useful for *in vivo* target validation.[219]

1.8 Project Aims

The aim of this DPhil work is to identify the molecular targets of OXS-N1 and elucidate its mechanism of action contributing to the proneurogenic activity observed *in vitro* and *in vivo*. Elucidation of these targets would aid the study of pathways associated with NSC fate speciation and neurogenesis and facilitate hit-to-lead optimisation in the drug design process.

The starting point of this work is to develop OXS-N1 into both an affinity probe and a fluorescent tagged derivative for use in chemical proteomics and other methods to assess its molecular interactions and localisation in NSCs. Identification of putative targets will be done using affinity-based protein profiling coupled with mass spectrometry analysis. Identified molecular targets will then be validated using a variety of orthogonal methods to pinpoint the therapeutically relevant target.

Chapter 2 Development of Affinity Probes

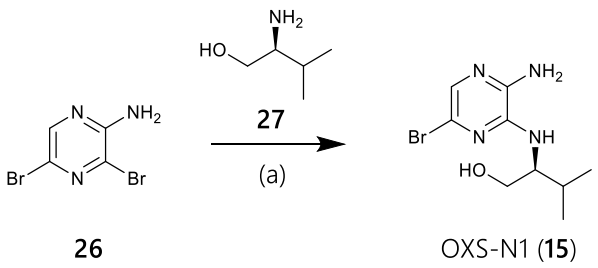
2.1 Overview

This chapter outlines the design and synthesis of affinity probes based on the hit compound OXS-N1. Structural-activity relationship (SAR) studies were carried out using analogues of OXS-N1 to identify a suitable position to append the modifications required for affinity enrichments. A variety of affinity linkers, including biotin, click handles and photoaffinity groups, were explored. To identify target proteins that are of biological significance, an inactive analogue was designed as a negative control. Optimisation of click reaction and UV irradiation conditions was carried out to ensure sufficient labelling of proteins for target identification studies.

2.2 Synthesis and Testing of OXS-N1 and Analogues

2.2.1 Design and Synthesis of OXS-N1 and Analogues

OXS-N1 was resynthesised to confirm its biological activity following the results from the compound screen. A nucleophilic aromatic substitution (S_NAr) between 2-amino-3,5-dibromopyrazine **26** and L-valinol **27** gave OXS-N1 in 56% yield (Scheme 1). Analogues can be synthesised by changing the pyrazine derivative or amino alcohol derivative in the S_NAr reaction.



*Scheme 1. Synthesis of OXS-N1 (**15**). Reagents and conditions: (a) DIPEA, nBuOH, 160 °C, 5 days, 56%.*

As mentioned in Section 1.6.1.3, a corresponding inactive analogue is important for identifying non-specific interactions in AfBPP experiments. As OXS-N1 was only tested as the *(S)*-

enantiomer, the activity of the *(R)*-enantiomer has not been properly investigated. The (*R*)-enantiomer was envisioned to be a potential inactive control as it would retain the same physical properties as OXS-N1. To test out possible scaffolds for developing an inactive control, the amino alcohol was changed to D-valinol to obtain the (*R*)-enantiomer **28** and 2,2-dimethylpropan-1-ol to obtain gem-dimethyl derivative **29** (Figure 15). In preliminary compound screenings (Dr Julie Davis, Department of Physiology, Anatomy and Genetics, University of Oxford), derivative **29** was identified to be inactive.

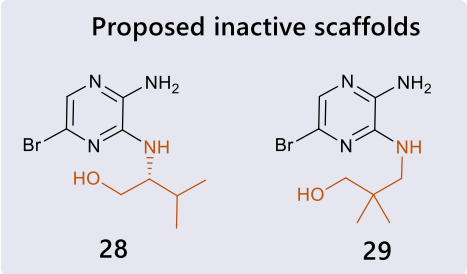


*Figure 15. Proposed inactive scaffolds enantiomer **28** and gem-dimethyl derivative **29**.*

2.2.2 *In vitro* Neurosphere Differentiation Assay

The neurogenic activities of OXS-N1 and its derivatives were assessed *in vitro* in a neurosphere differentiation assay using NSCs that were derived from the SVZ and DG regions of postnatal mice, with an age range of 2 to 6 days. The general workflow of the assay is outlined in Figure 16.

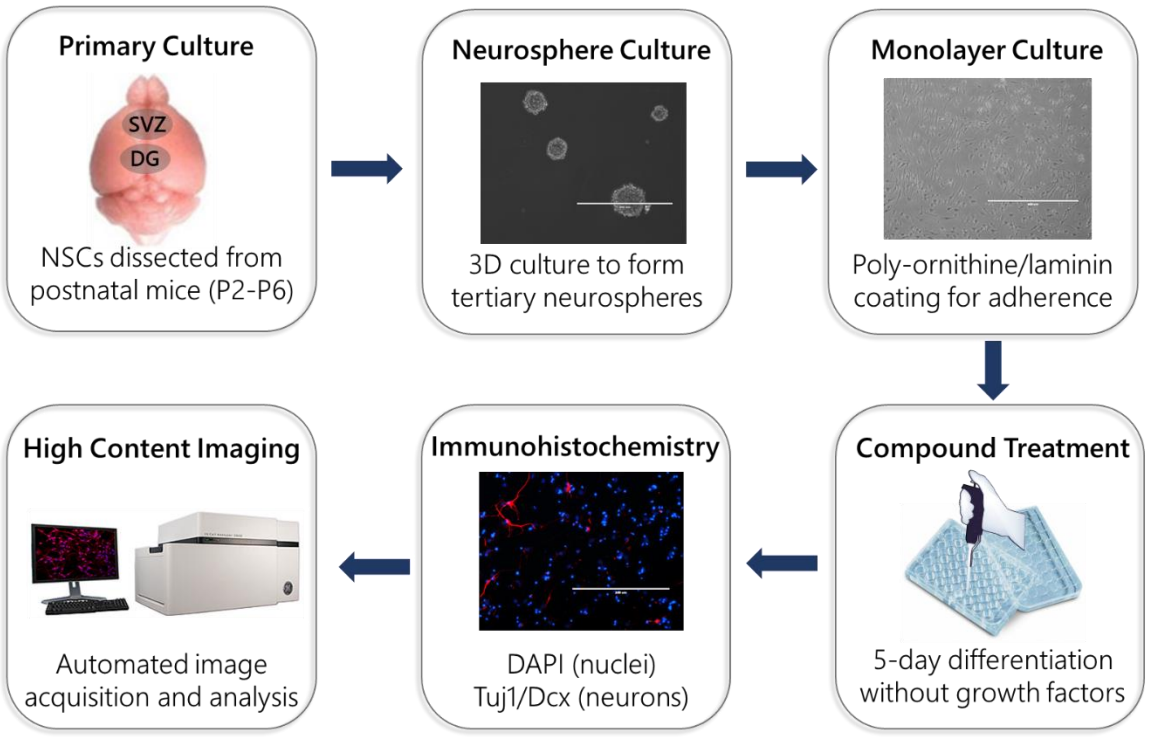


Figure 16. General workflow for the neurosphere differentiation assay used to assess the biological activity of the compounds.

Primary NSCs harvested from the neurogenic niches of the brain are cultured in serum-free conditions. The addition of growth factors EGF and FGF2 supports the expansion of the NSCs as free-floating clonal spheres known as neurospheres. The neurospheres are made up of a mix of NSCs and progenitor cells, surrounded by a rich extracellular matrix (ECM). The 3D culture provides a more physiologically relevant niche as compared to a 2D culture.[220] These cells retain the ability to self-renew and to differentiate into neurons, astrocytes and oligodendrocytes.

Tertiary neurospheres are dissociated to obtain single cells that are cultured as an adherent monolayer on plates pre-coated with poly-orthinine and laminin coating. Upon removal of EGF and FGF2 from the growth media, the cells are left to differentiate in the presence or absence of compounds for 5 days. Immunohistochemistry staining is performed to identify the cell types obtained through various markers. Antibodies specific for doublecortin (DCX) and beta-tubulin-III (Tuj1) are used to identify neurons. The individual wells are imaged using a fluorescence microscope and the percentage of DCX+ or Tuj1+ neurons among the living cells is used to assess the biological activity of the compounds.

2.2.2.1 Quantification of Phenotypic Outcome

An imaging-based assay poses some challenges for analysis of a large number of compounds, with bottlenecks observed in terms of (i) acquisition of images for each well, and (ii) quantification of cells in each channel.

Automated image acquisition of 96-well plates was set up with a fluorescence microscope (Evos Auto FL2), to ensure constant imaging parameters throughout the wells and unbiased selection of imaging areas within each well. However, the analysis of images for each well is still time-consuming and requires manual counting to quantify the neurons, the identification of which could be subjective to the person doing the counting.

In a collaboration with Dr Val Miller (Ebner Group, Target Discovery Institute, University of Oxford), a high content imaging protocol was set up on the GE InCell 1000 High Content Imager. An example of the automated quantification process is shown in Figure 17. Hoechst nuclear staining identifies all the cells in the image, and unviable cells stained with NucGreen Dead 488 are subtracted from the total number of cells to give a sum of the living cells. Living cells which also stain positive for DCX are counted as neurons and the ratio of neurons to living cells is computed as a percentage. The percentage obtained for each compound is then normalised against the percentage obtained from cells treated with DMSO (0.1% v/v), to give a fold-change of neurons formed with compound treatment.

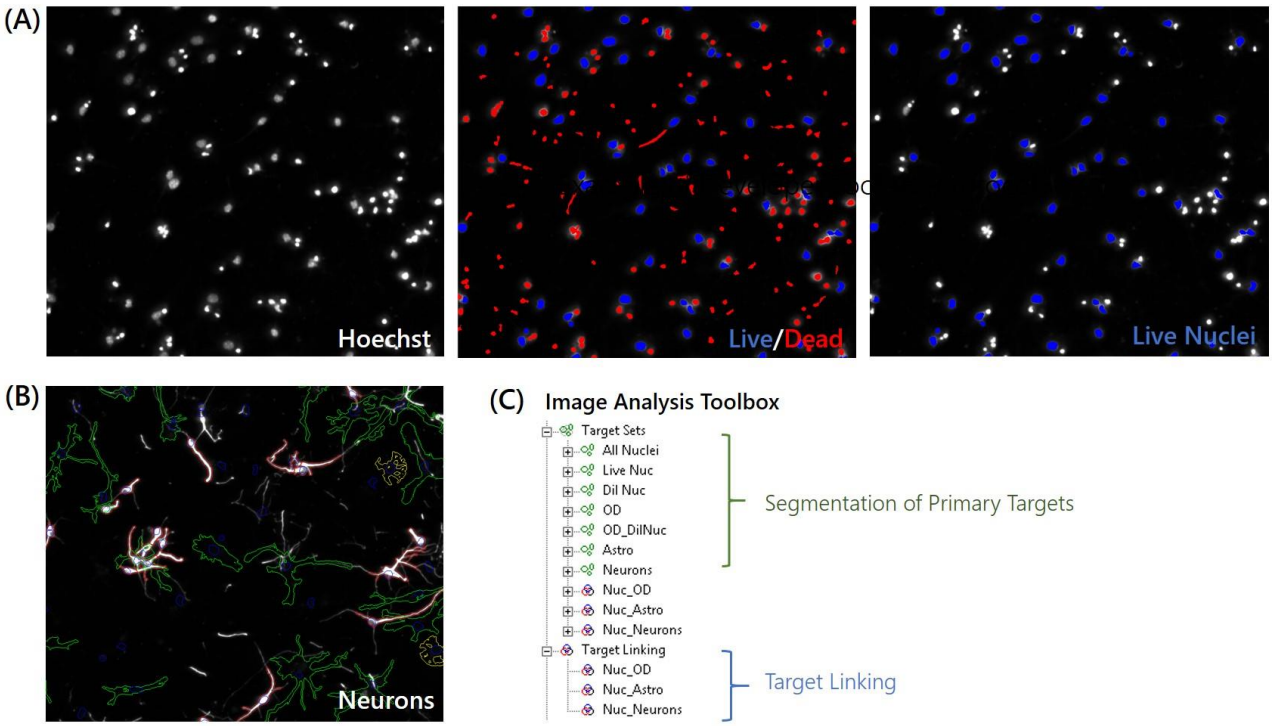


Figure 17. Images from automated quantification protocol using the InCell Analyzer. (A) Live nuclei selection: All nuclei are identified with Hoechst staining; dead cells are identified using NucGreen Dead 488 staining. Live nuclei are highlighted in blue. (B) Neuron segmentation: neurons are identified by DCX staining. Only neurons with live nuclei (in blue) are counted. (C) Developer toolbox, used to count different primary targets from various channels and link targets such as live nuclei and neurons. All Nuclei refers to count of all cells marked by Hoechst; Live Nuc refers to count of live cells after subtracting cells marked by NucGreen Dead 488 (Dil Nuc); Neurons refers to count of neurons marked by DCX staining; OD and Astro refers to counts of oligodendrocytes and astrocytes respectively.

2.2.2.2 Positive Controls

Proneurogenic compounds P7C3-A20 (**11**)[141] and retinoic acid (RA, **30**)[221] are used as positive controls in the neurosphere differentiation assay. Both positive controls resulted in a 2.0 – 2.5-fold increase in the percentage of neurons formed after 5 days of differentiation, normalised to DMSO (Figure 18). P7C3-A20 and RA are known to increase neurogenesis by differing mechanisms of action. P7C3-A20 provides a neuroprotective effect by activating NAMPT,[147] while RA induces an increase in neuronal differentiation by activating the retinoic acid receptors in the nucleus.[221] The activity of both positive controls in the assay confirms that the neurosphere differentiation assay is a suitable screening model for identifying a wide range of compounds exerting neuroprotective and neurogenic effects, regardless of mechanism.

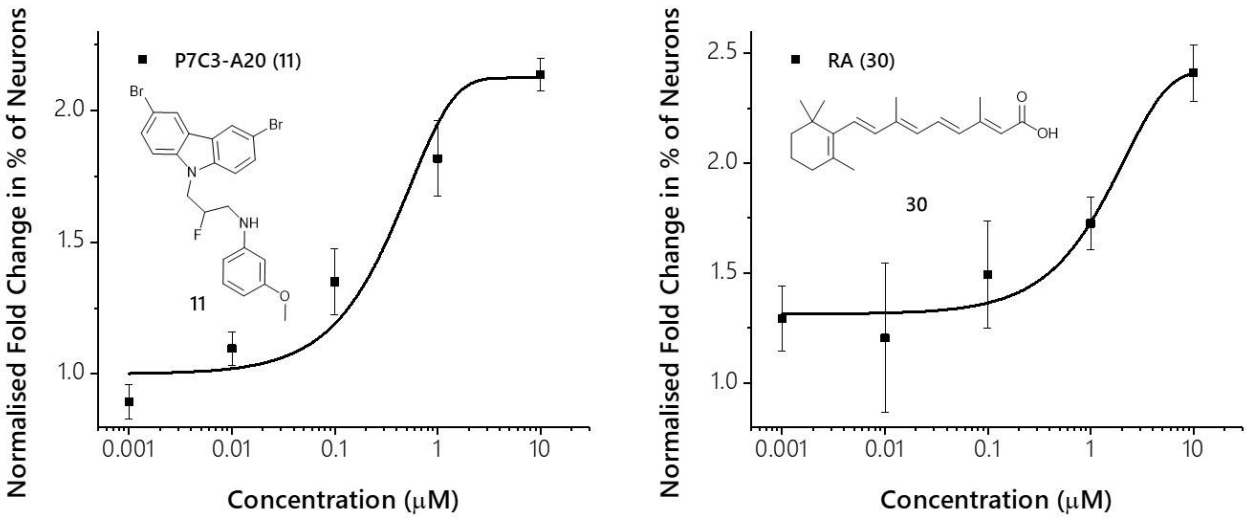


*Figure 18. Biological activity of P7C3-A20 (**11**) and retinoic acid (**30**) in the neurosphere differentiation assay in SVZ-derived murine neural stem cells. The fold-change of percentage of neurons present is normalised to the percentage of neurons present in vehicle(DMSO)-treated cells. Error bars are standard error of the mean; biological replicates, n = 3.*

2.2.3 Activity of OXS-N1 and analogues

OXS-N1 (**15**) and its proposed inactive analogues were tested *in vitro* in the neurosphere differentiation assay at 10 concentrations, ranging from 1 nM to 25 μM. OXS-N1 (**15**) increased the percentage of neurons formed by at least 2-fold in both SVZ- and DG-derived cells after 5 days of differentiation (Figure 19). The (*R*)-enantiomer **28** exhibited a drop in efficacy (EC_{max} ~1.5-fold) but was still moderately active. The gem-dimethyl derivative **29** was found to be inactive at the concentrations tested (EC_{50} > 25 μM) in both SVZ- and DG-derived cells. **29** was hence deemed to be a suitable scaffold for developing inactive probes for use as controls in pull-down experiments.

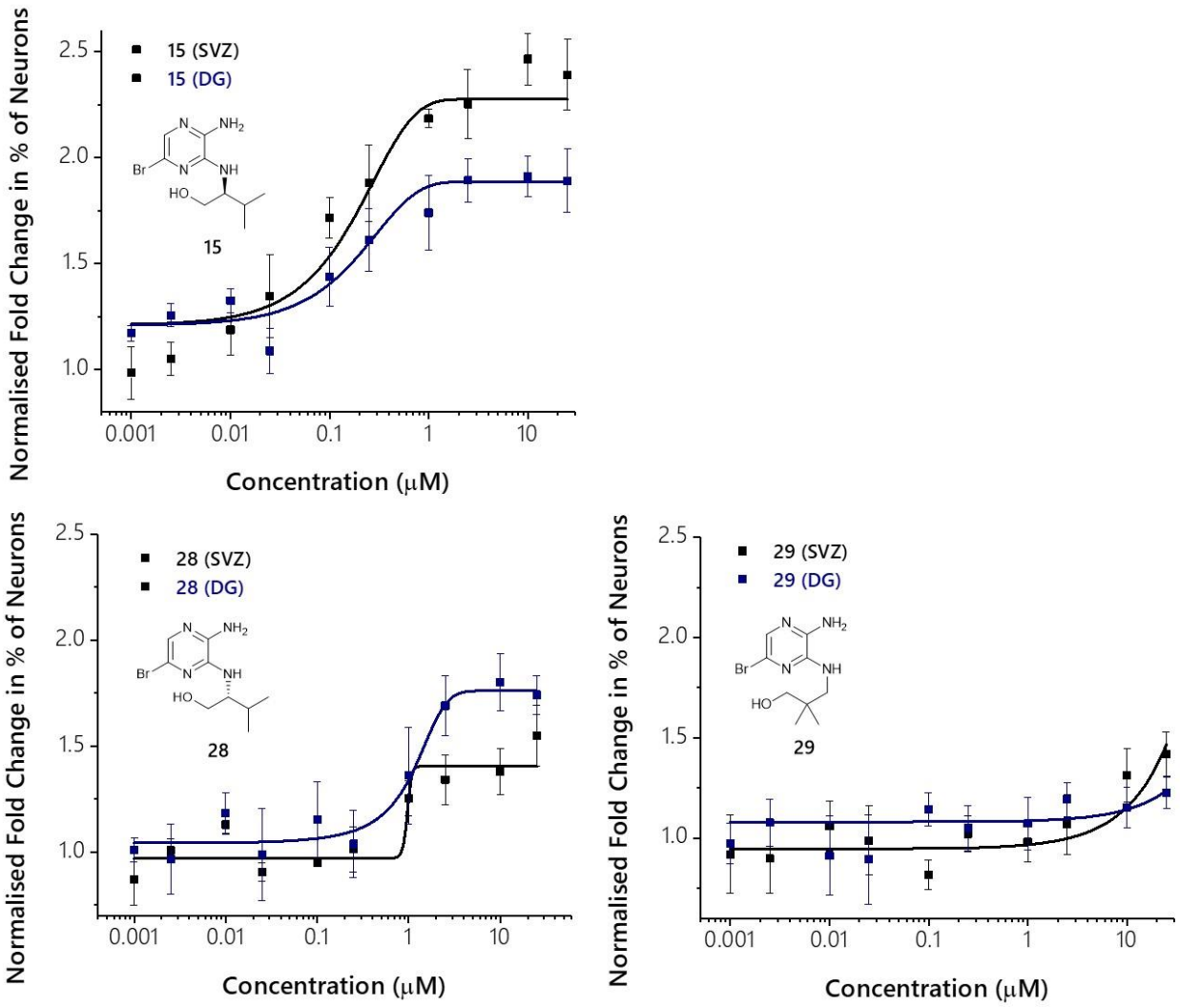
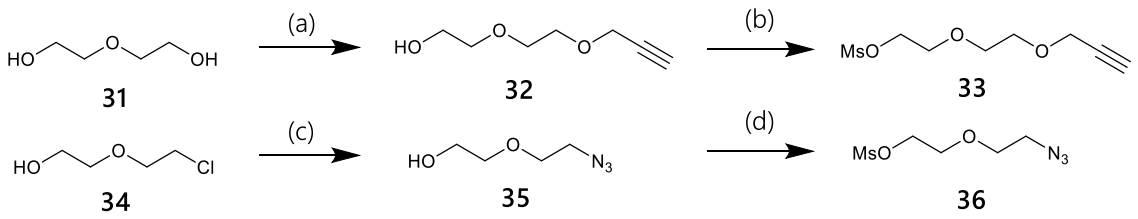


*Figure 19. Concentration-response curves of OXS-N1 (**15**) and analogues **28** and **29** assessed in SVZ- and DG-derived NSCs. Fold-change values are normalised to DMSO. Error bars are standard error of the mean; biological replicates, n = 3.*

2.3 Design and Synthesis of Alkyne-tagged Probes

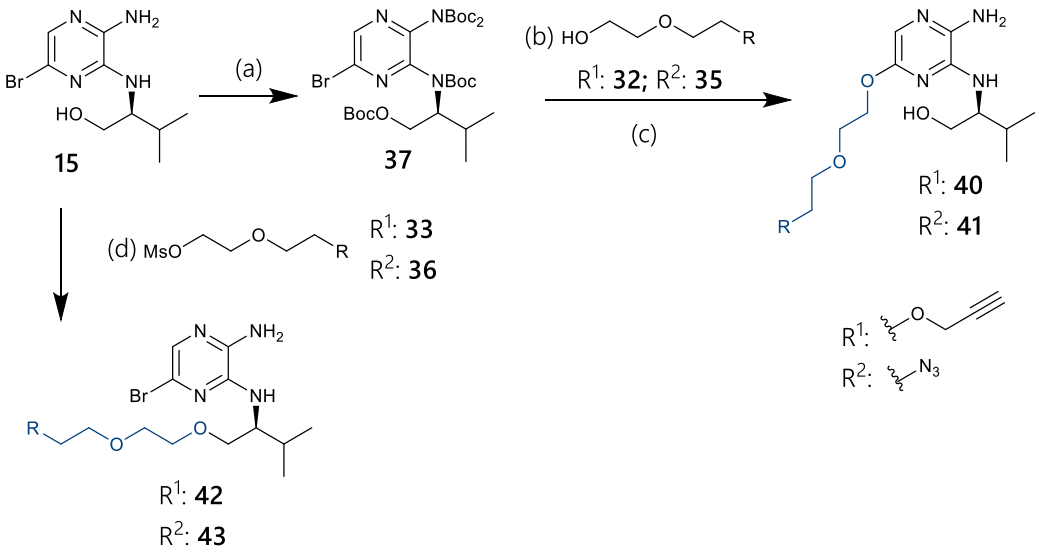
To develop OXS-N1 into a probe for AfBPP studies, a bioorthogonal handle was required as a site for the attachment of reporter groups for visualisation or enrichment. An alkyne tag was chosen to allow for ligation to azide partners bearing biotin or fluorophore labels in CuAAC click reactions. As the cytotoxicity of Cu(I) limits the click reactions to cell lysates and fixed cells, the use of SPAAC was explored in parallel by also synthesising the azide derivatives. Alkyne and azide tags were appended onto PEG linkers, which served as a hydrophilic spacer arm between the compound and bioorthogonal handle. The synthesis of the clickable PEG linkers from diethylene glycol **31** and 2-(2-chloro-ethoxy)-ethanol **34** is outlined in Scheme 2. Alkylation of

diethylene glycol using propargyl bromide gave the alkyne-tagged alcohol **32**, which was subsequently activated by mesylation.



Scheme 2. Synthesis of PEG chain alkyne- and azide-tagged linkers. Reagents and conditions: (a) Propargyl bromide, KOH, THF, 60 °C, 3 h, 37%; (b) Methanesulfonyl chloride, Et_3N, CH_2Cl_2, rt, 1 h, 83%; (c) NaN_3, H_2O, 90 °C, 73% ;(d) Methanesulfonyl chloride, Et_3N, CH_2Cl_2, rt, 1 h, 82%.

Due to the absence of detailed SAR information, our strategy was to develop multiple probes with alkyne or azide tags introduced at different positions to determine which would retain similar levels of activity to OXS-N1. The clickable PEG linkers were appended at the 5-bromo position and hydroxyl group of the parent compound **15** (Scheme 3).

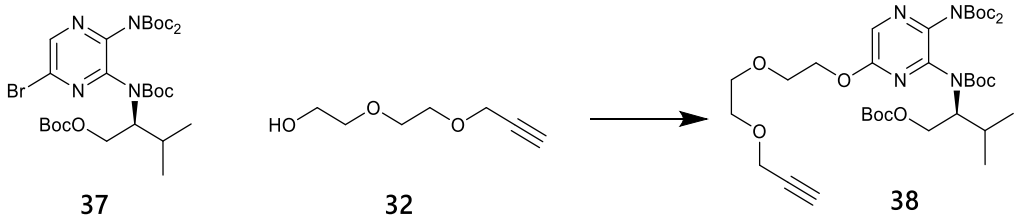


*Scheme 3. Synthesis of alkyne-tagged and azide-tagged clickable probes from **15**. Reagents and conditions: (a) Boc_2O, DIPEA, DMAP, THF, rt, 16 h, 70%; (b) $Pd(OAc)_2$, tBuXPhos, Cs_2CO_3, **32** or **35**, toluene, 90 °C, 16 h, 51% (**38**), 55% (**39**); (c) TFA, CH_2Cl_2, 3 h, 23% (**40**), 25% (**41**); (d) KOH, **33** or **36**, DMF, 60 °C, 16 h, 5% (**42**), 10% (**43**).*

The reactive hydroxyl and amino functionalities in **15** were masked by Boc-protecting groups to give tetra-Boc protected **37**. The bromo group on **15** was found to be unreactive to nucleophilic aromatic substitution with PEG-alkyne derivative **32**. A series of Buchwald-Hartwig coupling

reaction conditions was screened as an alternative (Table 3), with Entry 1 found to be optimal, giving **38** in 51% isolated yield. **40** was obtained in 23% yield following Boc deprotection.

*Table 3. Screen of reaction conditions for the Buchwald-Hartwig coupling between **37** and **32**. [a]Isolated yield; [b]starting material **37** recovered.*

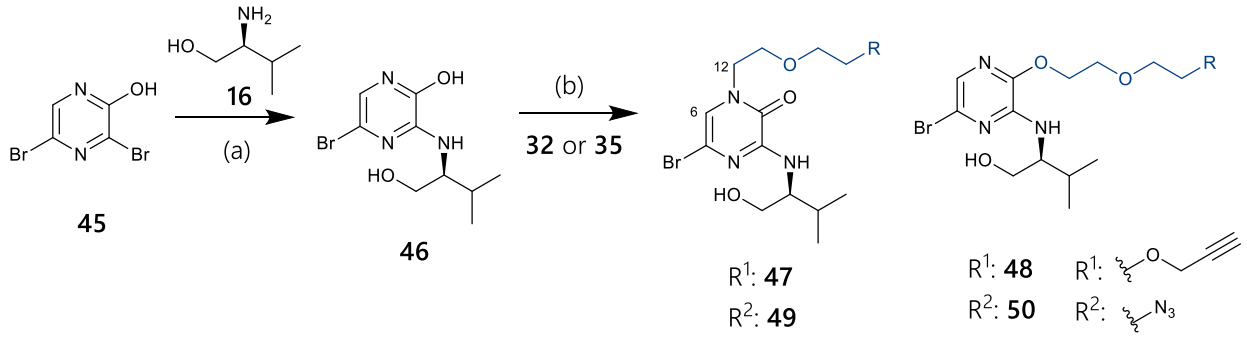


37 32 38

Entry	Pd Catalyst	Ligand	Base	Solvent	Yield (%)[a]
1	$Pd(OAc)_2$	*t*BuXPhos	Cs_2CO_3	Toluene	51
2	$Pd(OAc)_2$	*t*BuXPhos	K_3PO_4	Toluene	14
3	$Pd(OAc)_2$	TrixiePhos	Cs_2CO_3	Toluene	28
4	$Pd(OAc)_2$	XantPhos	K_2CO_3	Toluene	0[b]
5	$Pd(OAc)_2$	*t*BuBrettPhos	NaO*t*Bu	Toluene	0[b]

Alkylation of **15** using mesylate **33** allowed for the alkyne handle to be appended on the hydroxyl group to give **42**. Azide tags were appended via similar synthetic routes. Alkylation was selective for the hydroxyl group of the valinol side chain as it was more reactive than the amino group on the pyrazine ring.

To functionalise at the 2-position of the pyrazine ring, 2-hydroxypyrazine derivative **46** was used. Interestingly, alkylation of hydroxyl derivative **46** led to the isolation of both *N*-alkylated **47** and *O*-alkylated **48** isomers (3:1) (Scheme 4). The regioselectivity of the alkylation of 2-hydroxypyridines has been reported in literature to be affected by the solvent, nature of electrophile and base used.[222,223] The presence of a C=O stretch (1640 cm^{-1}) in the IR spectrum of **47** and the correlation observed between H6 and C12 in a HMBC experiment confirmed the *N*-alkylated product as the major regioisomer obtained. There was no correlation between the equivalent hydrogen on the alkyl chain and carbon on the pyrazine ring in the *O*-alkylated isomer **48**.

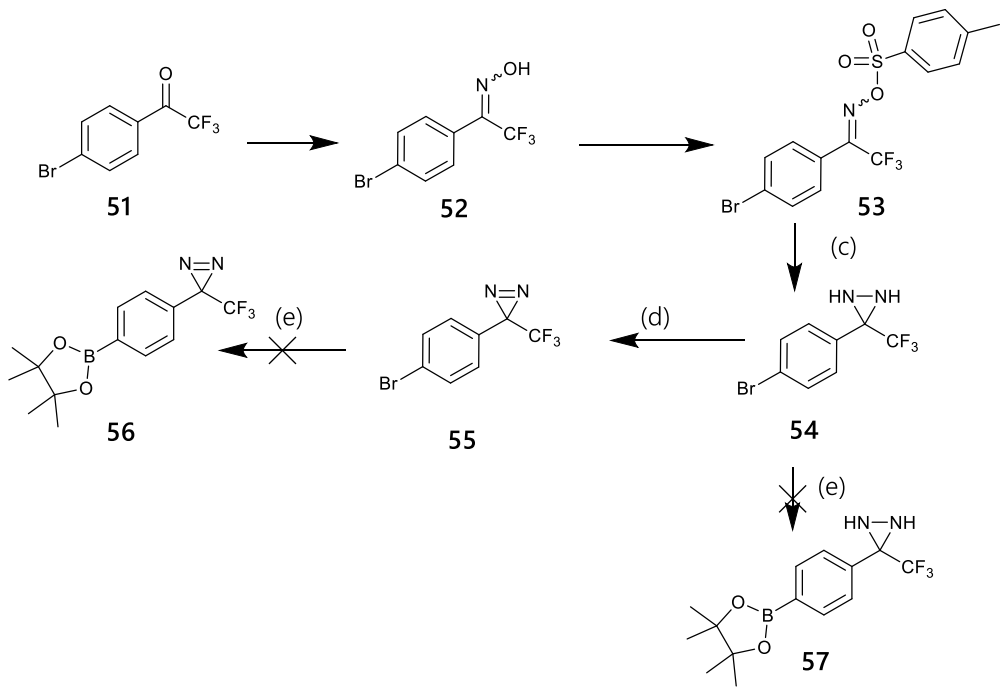


*Scheme 4. Synthesis of alkyne- and azide-tagged derivatives. Reagents and conditions: (a) DIPEA, nBuOH, 160 °C, 19 h, 39%; (b) K_2CO_3, DMF, **32** or **35**, 80 °C, 3 h, 38% (**47**), 12% (**48**), 34% (**49**), 12% (**50**).*

2.4 Design and Synthesis of Photoaffinity Building Block

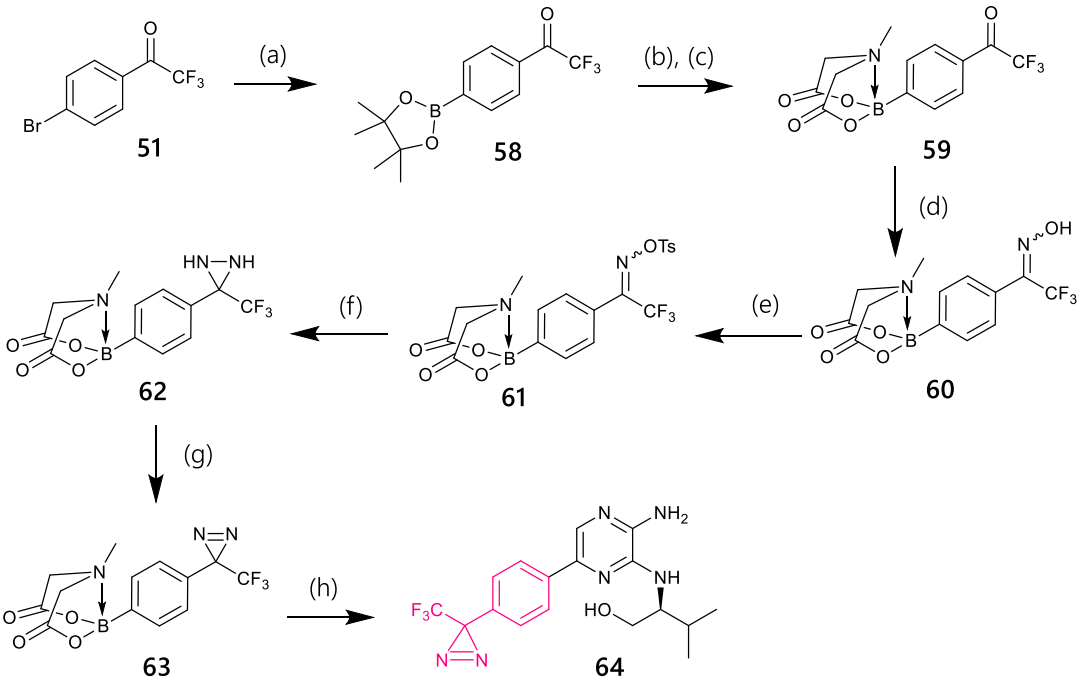
Photoaffinity labelling (PAL) involves introducing photoreactive groups that can covalently bind to proteins upon photoirradiation. This allows for the capture and identification of target proteins with low abundance and low binding affinity. Among the photoreactive groups discussed in Section 1.6.2, 3-Trifluoromethyl-3-phenyldiazirine (TPD) was chosen as a photoaffinity tag due to its rapid photolysis and high irradiation wavelength of 350 nm which results in less damage to biological systems. As the synthesis of the TPD moiety is lengthy and involves reaction conditions that are incompatible with functional groups on OXS-N1 and its analogues, the synthesis of a TPD derivative containing a boronic acid functionality for Suzuki coupling was explored.

Commercially available 4′-bromo-2,2,2-trifluoroacetophenone **51** was converted to oxime **52**, which was subsequently activated by *O*-tosylation (Scheme 5). Tosyl oxime **53** was transformed to diaziridine **54** by treatment with liquid ammonia, and oxidation using iodine gave diazirine **55**. With this 4-step procedure, diazirine **55** was formed with an overall yield of 36%. However, both the diaziridine and diazirine functionalities were found to be unstable to Miyaura borylation conditions, resulting in decomposition.



Scheme 5. Synthetic routes which were explored to obtain the TPD-boronic acid derivative. Reagents and conditions: (a) $NH_2OH.HCl$, pyridine, EtOH, 80 °C, 3 h, 87%; (b) p-TsCl, DMAP, NEt_3, CH_2Cl_2, rt, 1.5 h, 89%; (c) liq. NH_3, CH_2Cl_2, -78 °C → rt, 6 h, 89%; (d) I_2, NEt_3, MeOH, rt, 20 min, 52%; (e) $PdCl_2dppf$, B_2pin_2, KOAc, DMF, 90 °C, 16 h.

Introduction of the boronic acid functionality before diazirine formation was an alternative synthetic route that limited the exposure of the diazirine to prolonged heating conditions (Scheme 6).

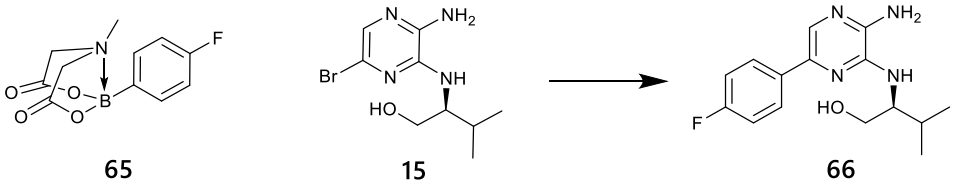


Scheme 6. Synthesis of TPD-MIDA boronate building block and TDP-labelled derivative. Reagents and conditions: (a) $PdCl_2dppf$, B_2pin_2, KOAc, DMF, 90 °C, 16 h, 75%; (b) $NaIO_4$, acetone, rt, 2 h; (c) MIDA, DMF, 90 °C, 16 h, 42% over 2 steps; (d) $NH_2OH.HCl$, pyridine, CH_3CN, 80 °C, 16 h, 32%; (e) p-TsCl, DMAP, NEt_3, CH_3CN, rt, 1.5 h, 71%; (f) liq. NH_3, CH_3CN/CH_2Cl_2 (1:2), –78 °C → rt, 6 h, 91%; (g) I_2, NEt_3, CH_3CN, rt, 20 min, 44%; (h) $Pd(OAc)_2$, SPhos, K_3PO_4, 1,4-dioxane, 60 °C, 6 h, 5%.

Bromide **51** was transformed to boronic ester **58** through Miyaura borylation. Attempted transformation of boronic ester directly led to decomposition, hence a protecting group strategy was employed. As boronic acids are known to be unstable to a range of conditions, this group was protected as the corresponding MIDA boronate.[224] Boronic ester **58** was hydrolysed and subsequently reacted with *N*-methylimidodiacetic acid (MIDA) to form MIDA boronate **59**. MIDA was chosen as a protecting group as the coordination of the nitrogen to the sp^3 boron centre provided increased stability and ease of handling compared to the pinacol ester derivative.[225] The ketone was transformed into diazirine **63**, through a high-yielding 4-step sequence. Pleasingly the MIDA protecting group survived this sequence despite the range of functional group transformations performed, including oxidative conditions. TPD-MIDA boronate **63** represents a useful building block that can be employed to incorporate the diazirine functionality into a range of compounds by Suzuki coupling for photoaffinity labelling.

TPD-MIDA boronate **63** was used in a Suzuki-Miyaura cross coupling reaction with **15** to obtain photoaffinity-labelled **64**. Employing the slow-release coupling reaction conditions reported by Burke,[224] **64** was obtained in a disappointingly low yield (5%) and was difficult to purify. We hence opted to screen reaction conditions using commercially available 4-fluorophenyl-MIDA boronate **65** as a substitute for screening purposes (Table 4).

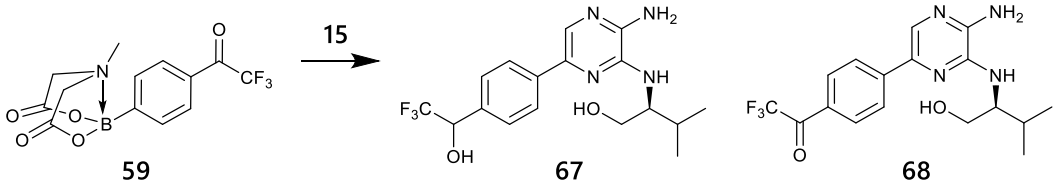
*Table 4. Screen of reaction conditions for the Suzuki-Miyaura cross-coupling of **15** and **65**. [a]Isolated yield; [b]analysis by LCMS, with 1,3,5-trimethoxybenzene as standard; [c]starting material **15** observed.*



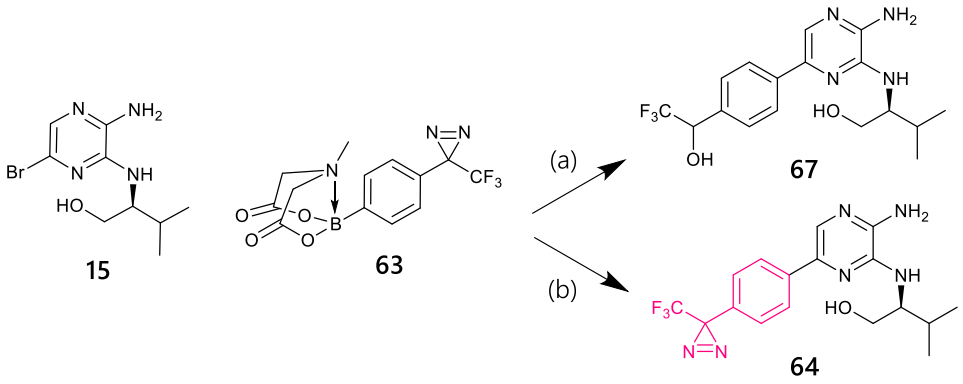
Entry	Pd Catalyst	Ligand	Base	$Cu(OAc)_2$	Solvent	Yield (%)
1	$Pd(dppf)Cl_2$	XPhos	K_2CO_3	0.5 eq	DMF	15[a, c]
2	$Pd(dppf)Cl_2$	XPhos	K_2CO_3	-	DMF	12[b, c]
3	$Pd(dppf)Cl_2$	SPhos	K_2CO_3	0.5 eq	DMF	5[b, c]
4	$Pd(OAc)_2$	XPhos	K_2CO_3	0.5 eq	DMF	10[b, c]
5	XPhos Pd G3	XPhos	K_2CO_3	-	DMF	21[a, c]
6	$Pd(OAc)_2$	*t*BuXPhos	Cs_2CO_3	-	DMF/H_2O	90[a]
7	$Pd(OAc)_2$	CyJohnPhos	$NaHCO_3$	-	DMF	0[b, c]
8	$Pd(OAc)_2$	PPh_3	K_2CO_3	-	DMF/H_2O	95[a]

The reaction was attempted again using trifluoro-MIDA boronate **63** with the optimised conditions (Scheme 7a). However, reduction of the trifluoromethyl diazirine functionality was observed, resulting in full conversion to secondary alcohol **67**. Thermal decomposition could have occurred, resulting in reactive carbene species being formed and quenched by water in the reaction solvent.[226] Further optimisation with **59** (Table 5) attributed the formation of the side product to the use of DMF as a solvent. While DMF has been reported in the literature as a reducing agent for metal salts, there have been few reports of DMF acting as a reductant in organic transformations.[227] Through a solvent screen, DME (Entry 8) was identified as the best solvent for the coupling reaction, allowing for trifluoromethyl ketone **68** to be obtained in 70% yield. The TPD-probe **64** was obtained with the same reaction conditions, but with much lower yield of 25% (Scheme 7b). The low yield could be attributed to the instability of the diazirine group when heated in Pd-catalysed reactions. As only a small quantity of the compound was required for biological evaluation, no further optimisation was done to improve the yield.

*Table 5. Screen of reaction conditions for the Suzuki-Miyaura cross-coupling of **59** and **15**. [a]Isolated yield; [b]analysis by ^{19}F NMR, with trifluorotoluene as standard; [c]starting material **15** observed.*



Entry	Pd Catalyst	Ligand	Base	Solvent	Conversion (%)[b]	
					67	68
1	XPhos Pd G3	XPhos	K_2CO_3	DMF (with 4Å MS)	0[c]	0[c]
2	XPhos Pd G3	XPhos	K_2CO_3	DMF	0[c]	0[c]
3	XPhos Pd G3	XPhos	K_2CO_3	DMF/H_2O	100	0
4	XPhos Pd G3	XPhos	K_2CO_3	DMA/H_2O	0[c]	0[c]
5	XPhos Pd G3	XPhos	K_2CO_3	Dioxane/H_2O	0	55
6	XPhos Pd G3	XPhos	K_2CO_3	CH_3CN/H_2O	0	57
7	XPhos Pd G3	XPhos	K_2CO_3	DME/H_2O	0	58
8	$Pd(OAc)_2$	PPh_3	K_2CO_3	DME/H_2O	0	70[a]



*Scheme 7. Suzuki-Miyaura coupling of MIDA-boronate **63** and **15** with optimised reaction conditions, leading to the formation of reduced product **67** and TPD-probe **64**. Reaction conditions: (a) $Pd(OAc)_2$, PPh_3, K_2CO_3, DMF/H_2O (2:1), 90 °C, 16 h, 95%; (b) $Pd(OAc)_2$, PPh_3, K_2CO_3, DME/H_2O (2:1), 90 °C, 16 h, 25%.*

2.5 In Vitro Testing of Probes

2.5.1 Activity of Probes

The probes with alkyne tags incorporated at various positions around the molecule were compared to determine the most appropriate position for appending affinity tags. The biological activity of the probes was evaluated in the neurosphere differentiation assay using SVZ-derived NSCs (Figure 20).

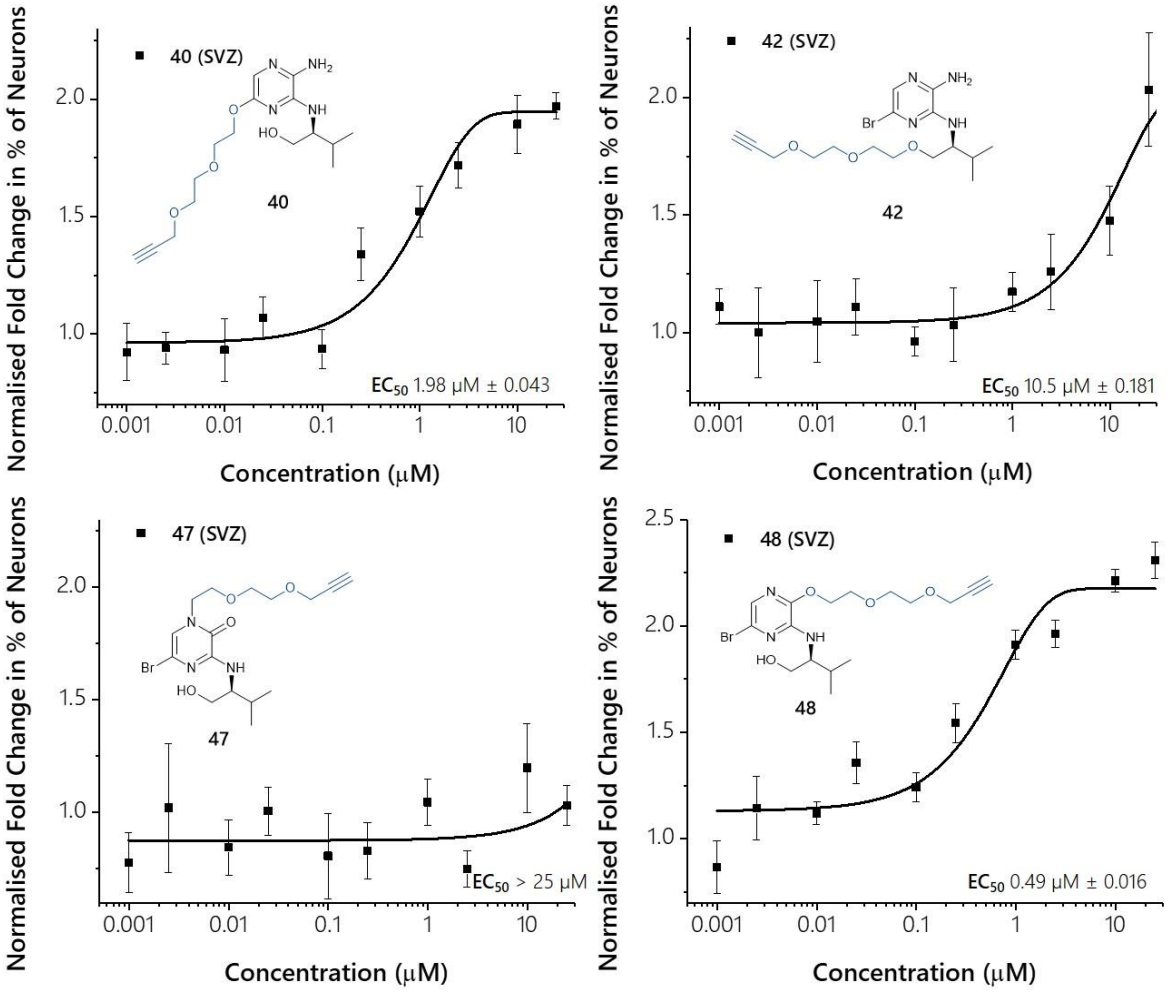
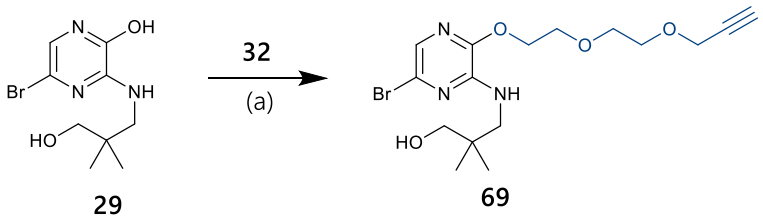


*Figure 20. Concentration-response curves of alkyne-tagged probes **40**, **42**, **47** and **48** assessed in SVZ-derived NSCs. Fold-change values are normalised to DMSO. Error bars are standard error of the mean; biological replicates, n = 2.*

N-Alkylated probe **47** was inactive (EC_{50} > 25 μM), indicating that the pyrazine ring was important for biological activity. Both **40** and **42** remained active, but with a drop in activity indicating that modifications on the 5-bromo group of the ring and the hydroxyl group of the

valinol side chain are only moderately tolerated. *O*-Alkylated probe **48** retained comparable activity (EC_{50} ~500 nM) to the parent compound **15**, and hence was chosen as the most suitable probe for use in AfBPP studies.

To obtain a corresponding negative control, gem-dimethyl analogue **69** was synthesised with the alkyne tag incorporated at the same position as **48** (Scheme 8).



*Scheme 8. Synthesis of corresponding inactive alkyne-tagged probe **69**. Reagents and conditions: (a) K_2CO_3, DMF, **32**, 80 °C, 3 h, 15%.*

This analogue was confirmed to be inactive at the concentrations tested (Figure 21). As it also bears an alkyne handle, inactive probe **69** is useful as a control for identifying non-specific labelling in the subsequent pull-down experiments. The TPD-tagged derivative **64** was found to be only moderately active (EC_{50} ~3 μM). The decrease in compound activity with modifications at the 5-position of the pyrazine ring indicates that the region is likely to be important for interacting with the molecular targets in the cells.

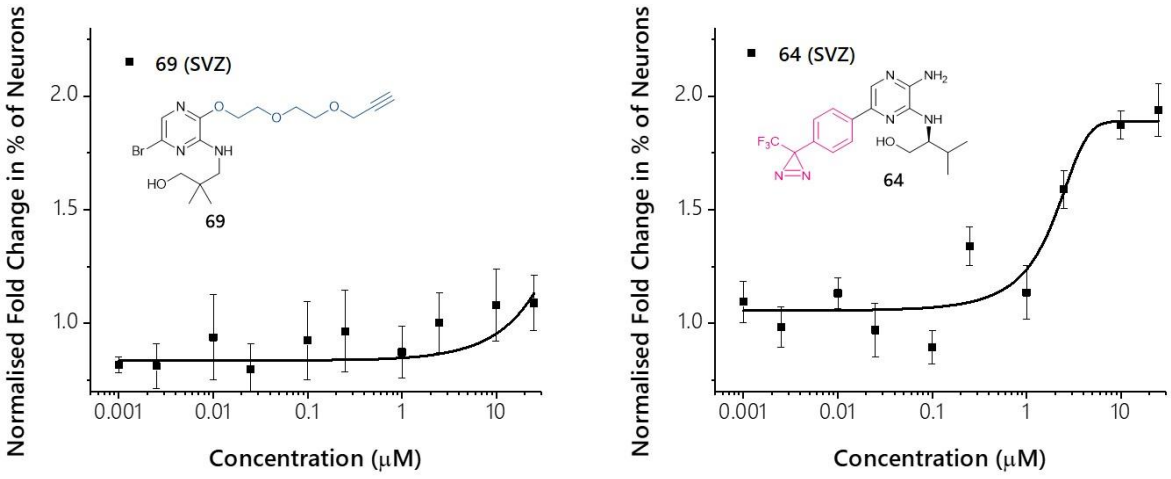


*Figure 21. Concentration-response curves of negative control **69** and TPD-tagged derivative **64** assessed in SVZ-derived NSCs. Fold-change values are normalised to DMSO. Error bars are standard error of the mean, biological replicates, n = 2.*

2.5.2 Labelling of Target Proteins

To optimise the concentration of probe needed for specific labelling of proteins, SVZ-derived NSCs were incubated with different concentrations of the alkyne-tagged probe **48** and compared to the vehicle-treated control (DMSO). Subsequent cell lysates obtained were subjected to a click reaction with TAMRA-azide, allowing for the visualisation of labelled proteins on a SDS-PAGE gel through fluorescence imaging (Figure 22).

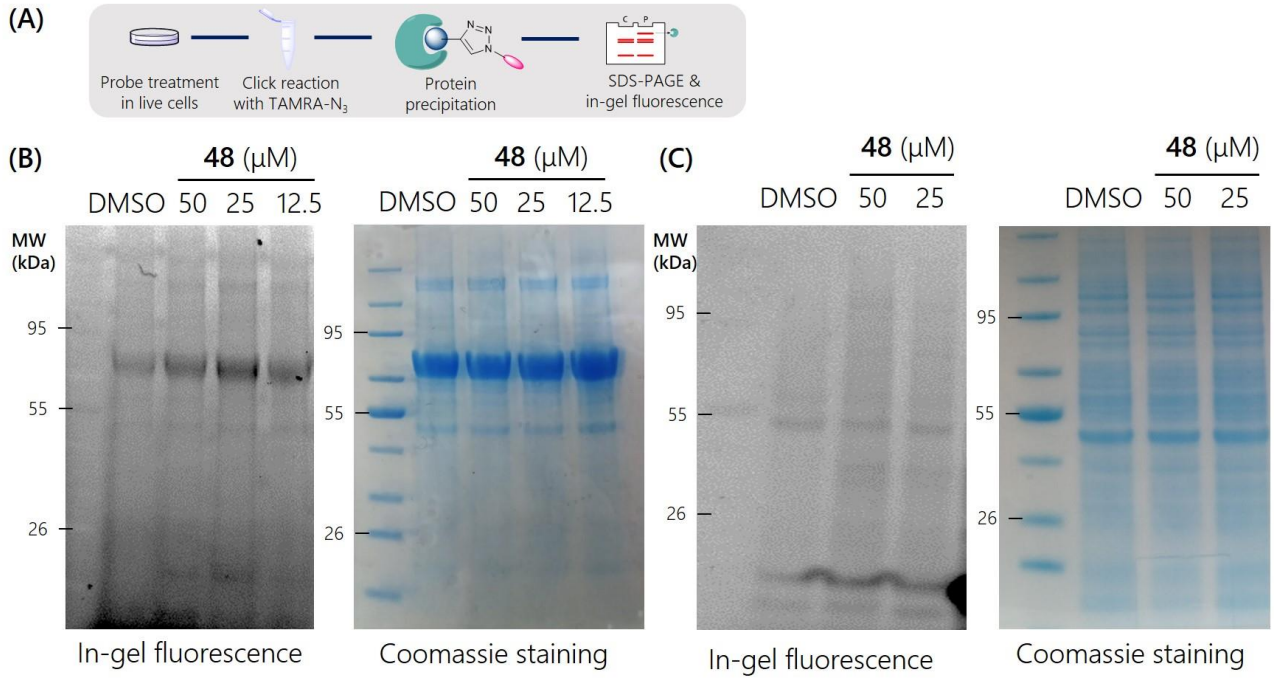


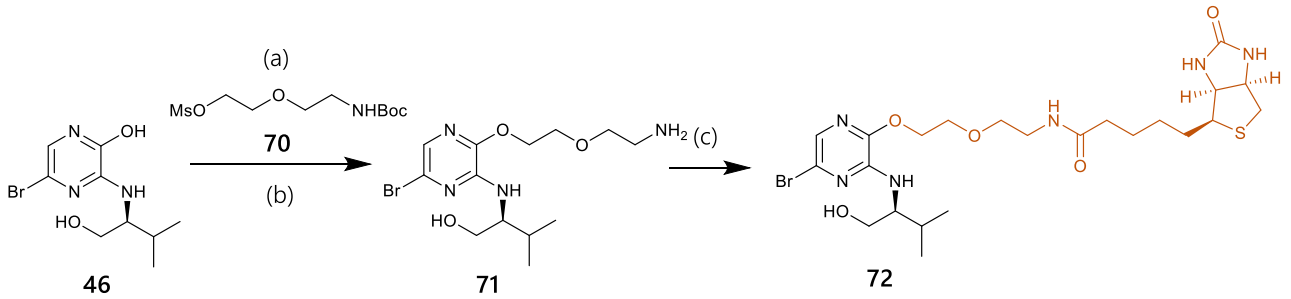
Figure 22. Images of SDS-PAGE gel after click reaction. (A) General workflow; (B) In-gel fluorescence showing proteins labelled after click reaction and Coomassie Blue staining to show even protein loading across the conditions; (C) In-gel fluorescence showing that the non-specific band was removed with more stringent washing of the cell pellet before cell lysis.

As shown in Figure 22B, for all the conditions tested, a thick band was observed at around 70 kDa, indicating significant non-specific labelling. The presence of this non-specific band even in the DMSO control indicated that the TAMRA-azide reagent was interacting non-specifically with a highly abundant protein in the cell lysates. This was suspected to be bovine serum albumin (BSA) which was present in the cell culture media. The cell lysis condition was optimised to include stringent washing of the cell pellet with phosphate buffered saline (PBS) multiple times before the cell lysis buffer was added. The optimised protocol successfully reduced the non-specific labelling as shown in Figure 22C. However, very few proteins were labelled through the

click reaction, even for cells treated with a high concentration (50 μM) of probe **48**. Poor labelling of proteins could be attributed to weak affinity binding of the small molecule to the target proteins. It could also be indicative of a loss in non-covalent binding of the probe to the target protein through protein precipitation and stringent washing steps.

2.6 Design and Synthesis of Biotinylated Probes

Preliminary results from testing alkyne-tagged probe **48** indicated poor labelling of proteins after the click reaction step. To improve the capture of target proteins, it was envisioned that direct pull-down of target proteins using affinity-tagged probes could bypass click reaction and protein precipitation steps and minimise loss of target proteins. Due to the strong interaction between biotin and avidin,[228] biotin was chosen as the affinity tag to be incorporated into OXS-N1. As it was demonstrated that modifications at the 2-position of the ring were well-tolerated, a probe containing the biotin moiety at the 2-position was synthesised. To minimise problems of poor solubility and low cell permeability, biotin was appended onto the **46** via a hydrophilic PEG linker **70**. The biotinylated probe **72** was obtained through amide coupling (Scheme 9). Using the inactive gem-dimethyl scaffold **29**, the corresponding inactive analogue **73** was synthesised by a similar route.



*Scheme 9. Synthesis of biotinylated probe **72**. Reagents and conditions: (a) K_2CO_3, DMF, **70**, 80 °C, 3 h, 15%; (b) TFA, CH_2Cl_2, 3 h, 80%; (c) D-Biotin, HATU, DIPEA, DMF, 16 h, 49%.*

The activity of biotinylated probe **72** was found to decrease by about 10-fold (EC_{50} ~3 μM) as compared to the parent compound, while the negative control **73** displayed no activity (Figure 23). At the highest concentration tested, probe **72** only increased the percentage of neurons

obtained by 1.5-fold, indicating an overall decrease in efficacy of the compound. This could be due to poor cell permeability of the biotinylated derivative, or weaker affinity binding in cells to the target proteins.

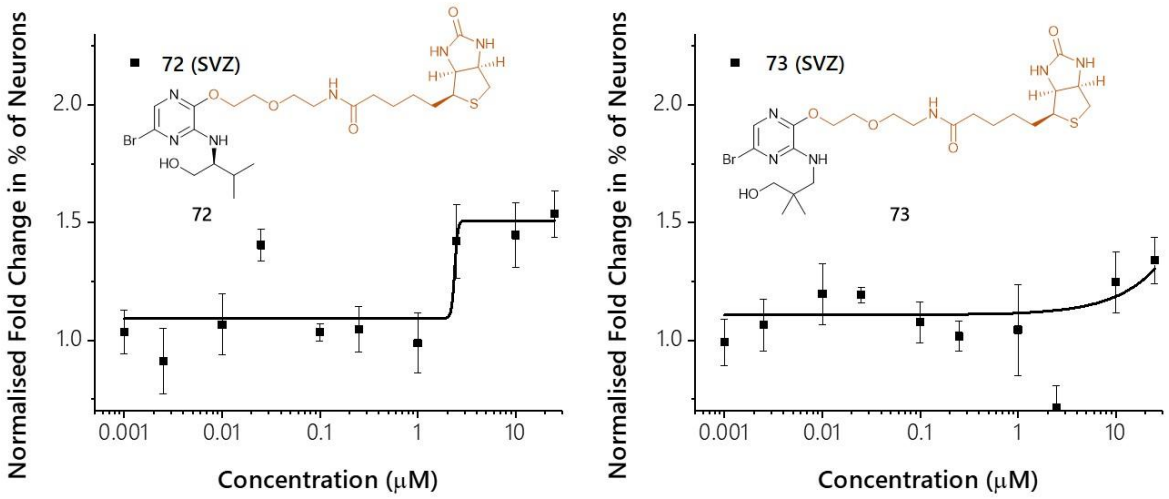
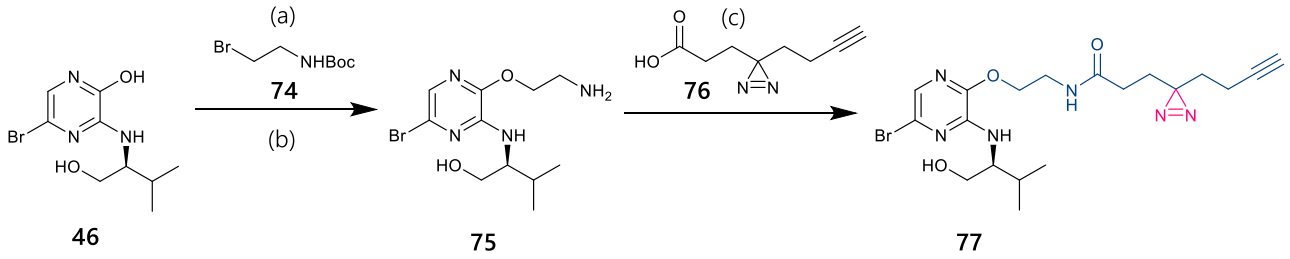


*Figure 23. Concentration-response curves of biotinylated probes **72** and **73** assessed in SVZ-derived NSCs. **72** shows weaker activity in vitro as compared to OXS-N1, while **73** shows no activity. Fold-change values are normalised to DMSO. Error bars are standard error of the mean; biological replicates, n = 2.*

2.7 Design and Synthesis of Dual-tagged Probes

As the addition of the bulky TPD group to OXS-N1 reduced the bioactivity of the compound, appending an additional alkyne handle at another position is likely to further reduce its bioactivity. It was envisioned that a minimalist linker with both the alkyne and diazirine on the same alkyl chain would be most appropriate for developing dual-tagged probes. This would minimise the modifications made to the compound and mimic the parent compound as closely as possible. The linker containing both an alkyne and a diazirine was appended via amide coupling to obtain the dual-tagged probe **77** (Scheme 10). As the incorporation of photocrosslinking is likely to increase background labelling of non-specifically bound proteins, it is important to have a negative control bearing the similar photoreactive group. Using the same linker **76**, the corresponding negative control **78** was synthesised via a similar route.



*Scheme 10. Synthesis of dual-tagged probe **77**. Reagents and conditions: (a) K_2CO_3, DMF, **74**, 80 °C, 3 h, 15%; (b) TFA, CH_2Cl_2, 3 h, 85%; (c) **76**, HATU, DIPEA, DMF, 16 h, 49%.*

The activity of the dual-tagged probes was assessed in SVZ-derived cells (Figure 24). 77 was found to retain good biological activity, confirming that modifications at the 2-position of the pyrazine ring caused minimal impact on the activity of the compound. **78** was confirmed to be inactive, and suitable for use as a negative control.

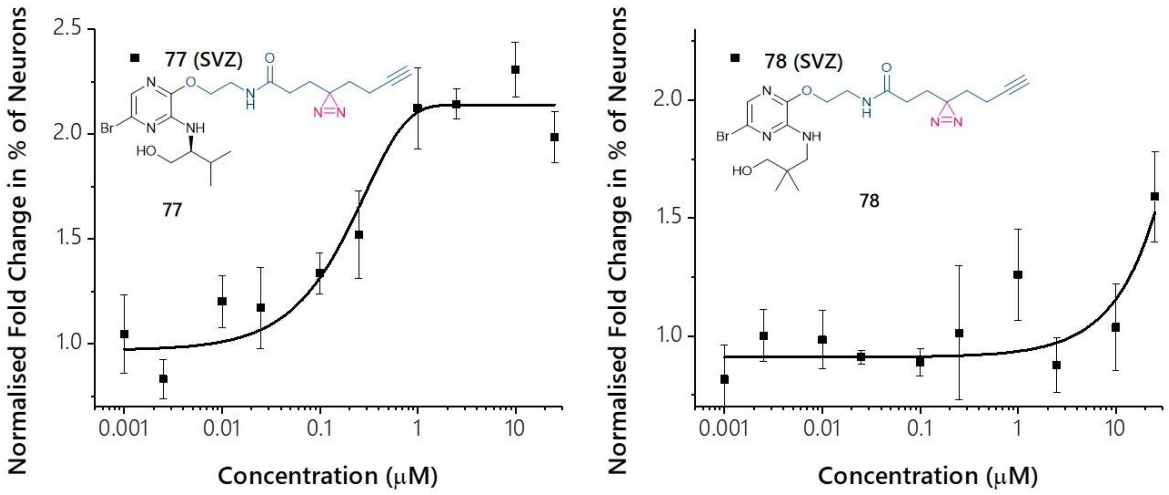


*Figure 24. Concentration-response curves of dual-tagged probes **77** and **78** assessed in SVZ-derived NSCs. **77** shows comparable activity in vitro as compared to OXS-N1, while **78** shows no activity. Fold-change values are normalised to DMSO. Error bars are standard error of the mean; biological replicates, n = 2.*

To test if the use of photocrosslinking improves the labelling of proteins in cells, SVZ-derived NSCs were incubated with dual-tagged 77 at various concentrations from 6.25 to 50 μM. Upon UV irradiation, the diazirine group forms a carbene, which readily inserts into neighbouring bonds. After cell lysis, the probe-protein complexes were subjected to click reaction with TAMRA-azide and visualised on a SDS-PAGE gel (Figure 25). Significant labelling of proteins was observed with 50 μM of 77, with many fluorescently-labelled bands observed on the SDS-

PAGE gel, as compared to the DMSO control. The intensity of the fluorescent bands decreases with the probe concentration, indicating that the labelling of the proteins is concentration-dependent. While the photolabeling approach increased the number of proteins labelled in cells, it also resulted in significant background labelling, which must be distinguished from the target protein labelling by using appropriate controls.

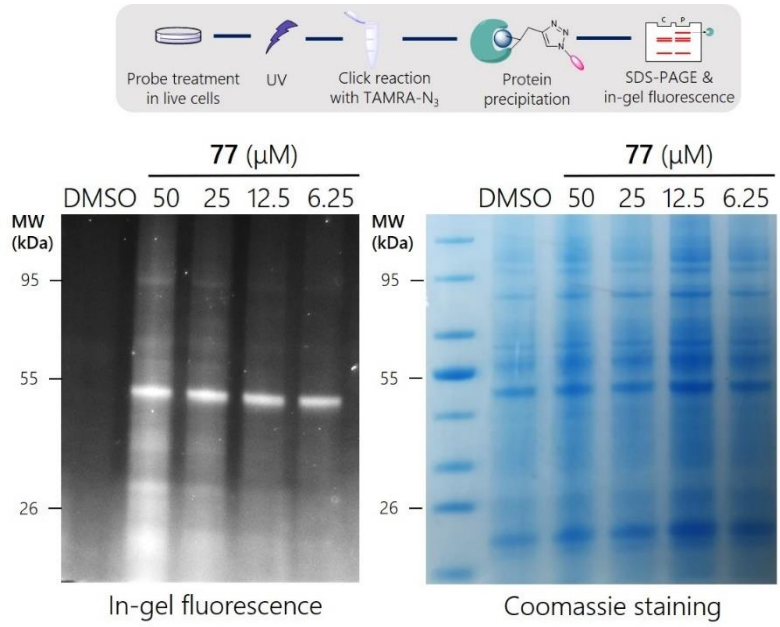


Figure 25. Images of SDS-PAGE gel after click reaction of cell lysates with TAMRA-azide. Probe-protein complexes are visualised as fluorescent bands in the rhodamine channel. Concentration-dependent labelling of proteins is observed. Coomassie Blue staining shows even protein loading across the conditions tested.

Apart from the inactive probe, a competition control could also be used as a negative control. As described in Section 1.6.5, the parent compound or a more active analogue can serve as a competitor during the probe treatment. It is assumed that the competition control binds with higher affinity to the target proteins in the cells as compared to the probe, and hence the band containing the target protein of interest would be absent in the competition control. To test out the use of OXS-N1 (**15**) as a competition control, the cells were treated with a fixed concentration of probe **77** along with increasing concentrations of **15** (Figure 26). The high intensity of some of the labelled proteins even in the presence of a high concentration of **15** indicates that these interactions are non-specific. A few weaker bands appeared to decrease in intensity with increasing concentrations of the parent compound and could indicate possible targets of interest.

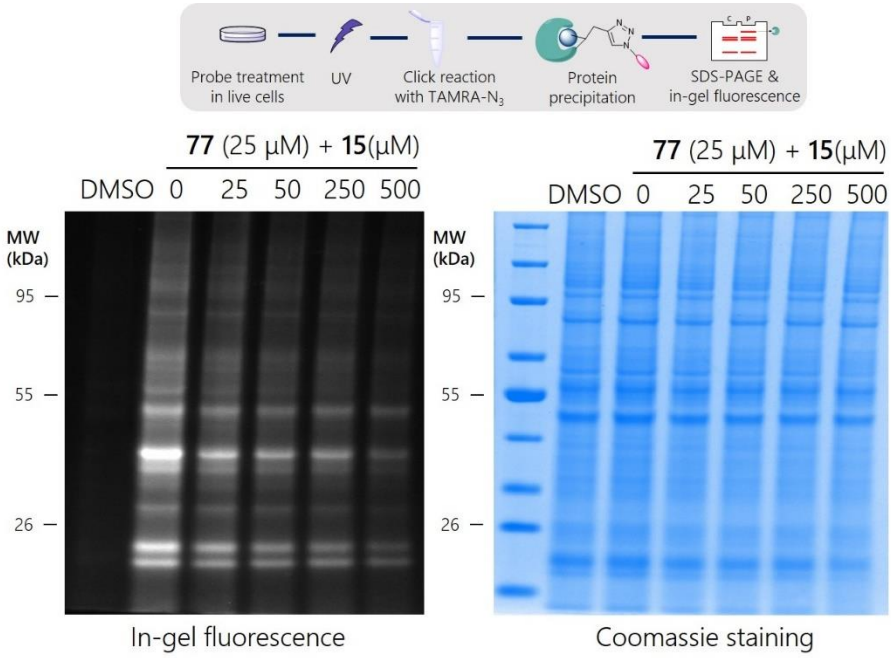


Figure 26. Labelled proteins visualised by in-gel fluorescence after click reaction with TAMRA-azide. Concentration-dependent out-competition of some protein bands observed. Coomassie Blue staining shows even loading of the samples.

2.8 Summary

Alkyne-tagged probes with the clickable handle incorporated at positions around the parent compound were used to establish probe SAR. Modifications at the 2-position of the pyrazine ring were most well-tolerated and probe **47** was selected as the active probe for target enrichment studies. A corresponding negative probe was synthesised from the inactive scaffold **28** with the alkyne tag incorporated at the same position. Preliminary optimisation of the click reaction using TAMRA-azide highlighted potential issues of weak affinity binding to target proteins in the cells. Biotinylated probes **72** and **73** were synthesised but the poor cell permeability and bulkiness of the biotin group decreased the efficacy of the active probe significantly. To minimise modifications to the parent compound, dual-tagged probes **77** and **78** incorporating a minimalist diazirine and alkyne linker on the same alkyl chain were synthesised. Using photoaffinity labelling, more labelled proteins could be visualised on the gel, but many of the protein bands were likely to be non-specific interactions. Having both the inactive probe and competitor as controls will be important to identify biologically relevant targets. The use of these probes for target identification studies by mass spectrometry will be described in detail in Chapter 4.

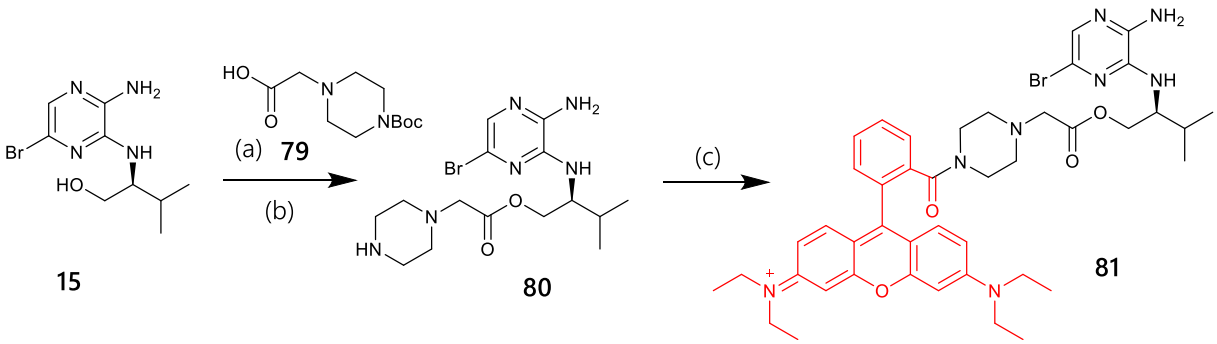
Chapter 3 Development of Fluorescent Probes

3.1 Overview

This chapter aims to describe the design and synthesis of fluorescent probes to visualise the subcellular localisation of OXS-N1 in NSCs. Knowing the subcellular location of the potential targets would aid target identification efforts, especially the optimisation of conditions for cell lysis and target enrichment. Due to the toxicity of the copper(I) catalyst, live cell imaging using alkyne-tagged probes was unfeasible. Rhodamine- and BODIPY-tagged derivatives were developed to obtain cell-permeable fluorophore-conjugated probes. Fluorescence microscopy was used to assess the localisation of the fluorophore-tagged probes, and a competition study with the parent compound was used to assess the specificity of the binding.

3.2 Rhodamine-tagged Derivatives

Rhodamine B was chosen as a label due to its high fluorescence quantum yield and photostability.[229] The cationic charge on the dye also contributes to its excellent uptake into cells. As secondary amide derivatives of rhodamine are known to rapidly cyclise to form non-fluorescent lactams,[230] piperazine was used as a linker to obtain a tertiary amide derivative (Scheme 11). The amino group on the pyrazine ring was unreactive to amide coupling, hence the conjugation of the piperazine linker to **15** resulted in ester formation at the hydroxyl group on the side chain instead. Subsequent deprotection gave the secondary amine **80**, which was then coupled to rhodamine B, affording the tertiary amide derivative **81**. As modifications at the hydroxyl group of the valinol side chain were previously tolerated, it was likely that the *O*-linked derivative **81** would also retain biological activity.



*Scheme 11. Synthesis of rhodamine-labelled derivative **81**. Reagents and conditions: (a) **79**, HATU, DIPEA, DMF, rt, 16 h, 81%; (b) TFA, CH_2Cl_2, rt, 16 h, 87%; (c) Rhodamine B, HATU, DMF, rt, 16 h, 12%.*

However, when tested in the neurosphere differentiation assay, rhodamine-labelled derivative **81** showed cytotoxic effects at concentrations above 100 nM (Figure 27). Significant staining was observed in the red channel for the cells treated with **81**, but the morphology of the cells was observed to be round instead of dendritic, indicating the labelled cells were not neurons. The staining was most likely due to non-specific labelling by the secondary antibodies for dead cells which have compromised membrane integrity.[231] Labelling by NucGreen confirmed that these labelled cells were not viable. Hence, the bioactivity of probe **81** could not be assessed in this assay.

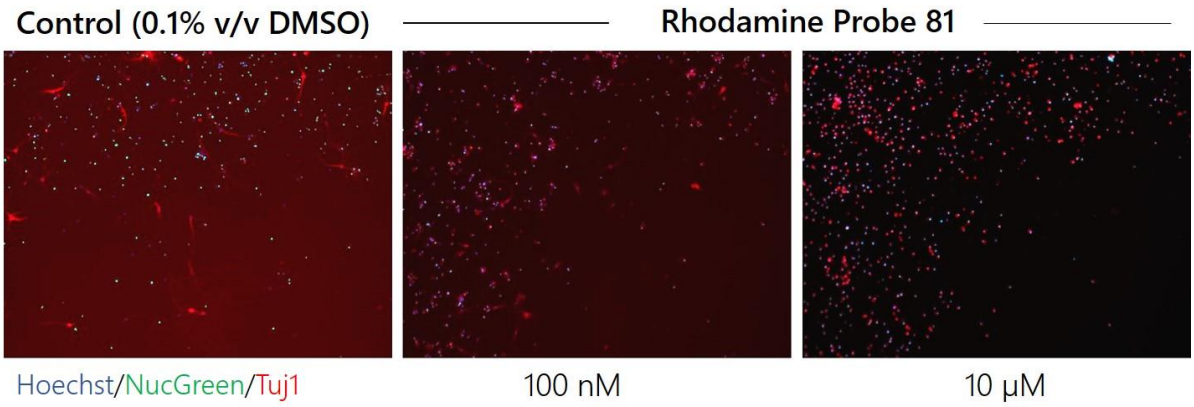


*Figure 27. Images of cells after 5 days treatment with DMSO control, and rhodamine B-tagged probe **81** (100 nM and 10 μM). Hoechst (blue) was used to stain for nuclei, NucGreen Dead (green) was used to stain for unviable cells and β3-tubulin (tuj1) antibody (red) was used to stain for neurons. Death of neurons was observed with increasing concentration of **81**, leading to changes in cell morphology.*

The cationic charge on the *N*,*N*,*N*',*N*'-tetraethylamino substituents has been reported to contribute to the accumulation of rhodamine in the mitochondrial membrane.[232] The prolonged exposure of the rhodamine derivative to the cells could have caused toxicity resulting from its

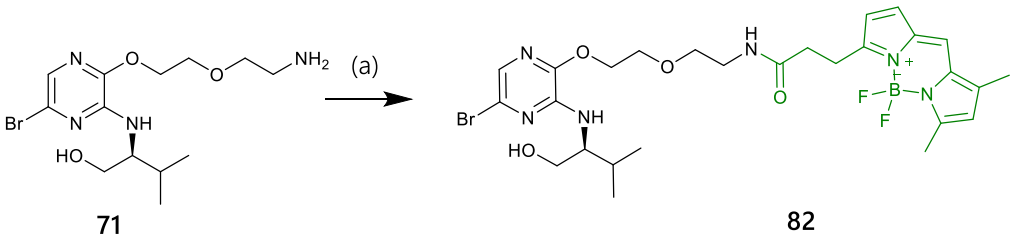
inhibitory effect on mitochondria. The cytotoxicity of the rhodamine probe **81** limits the concentration and the incubation time of the probe when treated in the cells. A low concentration (< 100 nM) is unlikely to achieve a high degree of subcellular labelling. The synthesis of other probes using different fluorophore tags was hence explored.

3.3 BODIPY-tagged Derivatives

BODIPY (4-bora-3a,4a-diaza-s-indacene) is another good candidate for a fluorophore label due to its high photostability, molar absorption coefficient and fluorescence quantum yield.[233] It has a zwitterionic core, with a localised anionic charge on a tetra-substituted boron atom, and a cationic charge delocalised through its tricyclic aromatic ring system. BODIPY probes are cell-permeable and have been used to target proteins and specific organelles in cells.[234]

3.3.1 Synthesis and Testing of BODIPY-tagged OXS-N1

BODIPY-FL was appended onto intermediate **71** through amide coupling. The BODIPY-tagged probe **82** was obtained with 68% yield (Scheme 12).



*Scheme 12. Synthesis of BODIPY-labelled derivative **82**. Reagents and conditions: (a) BODIPY-FL, HATU, DMF, rt, 16 h, 68%.*

This probe was tested *in vitro* in the neurosphere differentiation assay, and its activity is shown in Figure 28. It was confirmed to retain biological activity, which correlates well with previous observations that modifications at the 2-hydroxyl position of the pyrazine are tolerated. The biological activity of the BODIPY probe may suggest that it binds to a similar target as OXS-N1.

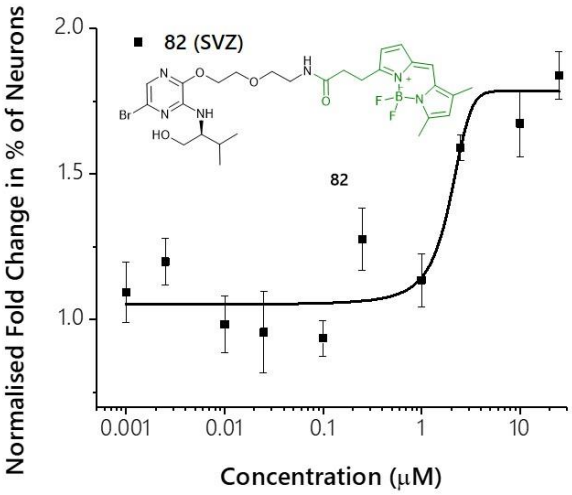


*Figure 28. Concentration-response curves of probe **82** when tested in vitro in SVZ-derived NSCs. EC_{50} ~3 μM. Error bars indicate standard error of the mean; biological replicates, n = 2.*

3.4 Cellular Imaging

3.4.1 *In vitro* Cellular Uptake of Fluorescent Probe

BODIPY-tagged derivative **82** was used to probe the subcellular localisation of OXS-N1. As BODIPY dyes are lipophilic and generally tend to accumulate in subcellular membranes, a control probe **83**, containing only BODIPY-FL modified with a similar PEG chain linker, was used as a negative control (Figure 29). This probe is important for identifying non-specific background signals due to the BODIPY-FL moiety. LysoTracker Red, a BODIPY-based dye that labels the lysosomes in the cells, was also used as a positive control for indicating cellular uptake. Co-staining with LysoTracker Red can also highlight any non-specific accumulation of the BODIPY probe in lysosomes.

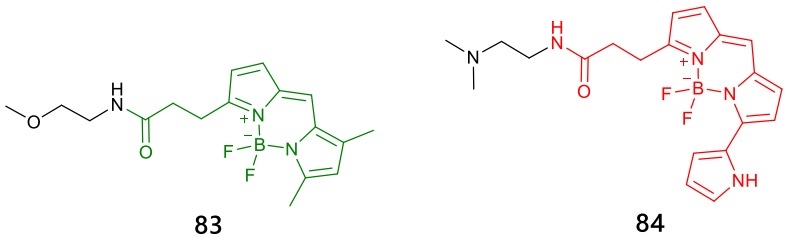


*Figure 29. Structures of BODIPY-FL control **83** (kindly provided by Dr Aini Vuorinen, University of Oxford) and LysoTracker Red **84**.*

SVZ-derived NSCs were incubated with the probes for 2 hours. After incubation, the cells were washed twice with PBS to remove any excess unincorporated probe, before fixing and imaging. The cells were then visualised with a fluorescence microscope, and the images obtained are shown in Figure 30.

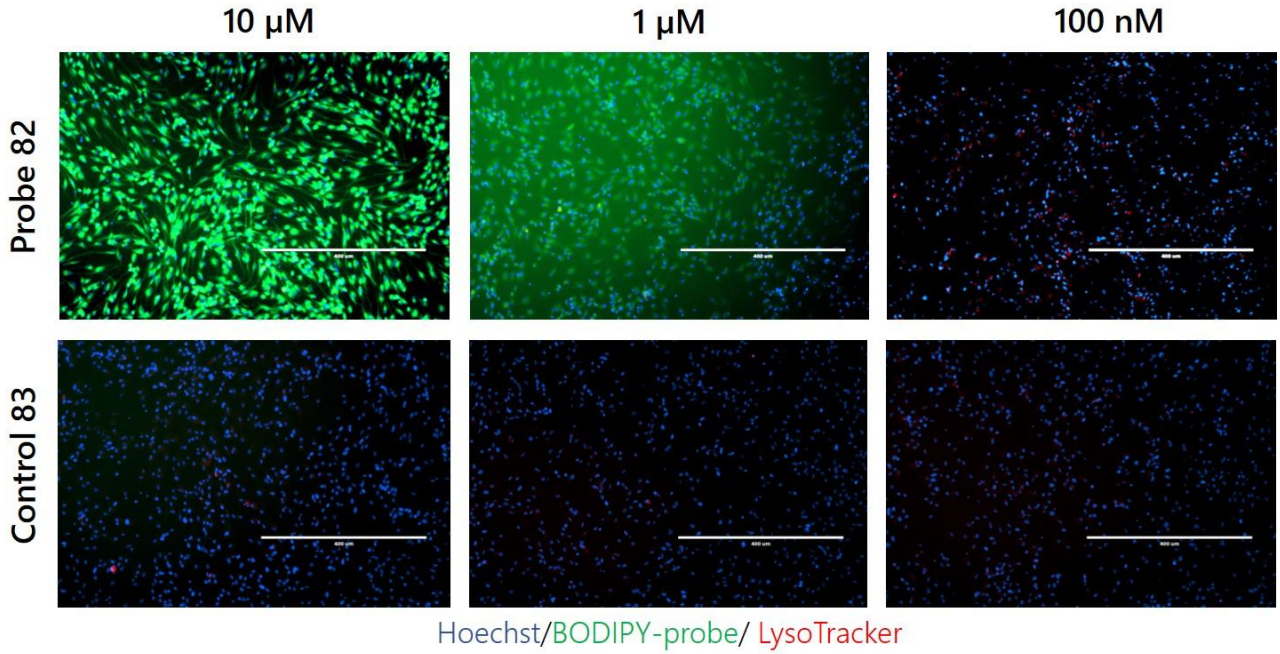


*Figure 30. Fluorescence images (merged channels) taken after 2 h treatment with BODIPY-tagged probe **82** and negative control **83**.*

A bright green fluorescent signal was observed in cells after 2 h treatment with BODIPY probe **82**, confirming that **82** is taken up into the cells. A decrease in fluorescence labelling with decreasing concentrations of **82** shows that this cellular labelling is concentration-dependent. Labelling of the cells was observed with 1 µM and 10 µM of **82**. This corresponds to the activity data of **82** in the neurosphere differentiation assay, which indicated that the EC_{50} of the probe was around 3 µM. The background labelling by control probe **83** was insignificant, showing that the BODIPY-FL moiety does not interact non-specifically with cellular targets or accumulate in specific organelles in the cell. The BODIPY probe **82** did not localise to lysosomes labelled by LysoTracker Red, suggesting that it does not accumulate in lysosomes and could be binding to other molecular targets in the cells.

3.4.2 Confocal Imaging

Confocal microscopy was used for imaging of the cells at a higher resolution, to better visualise the subcellular localisation of the fluorescent probe. The Z-axis scanning also provides a clearer examination at a specific depth of field. Confocal images of the stained SVZ-derived NSCs are shown in Figure 31.

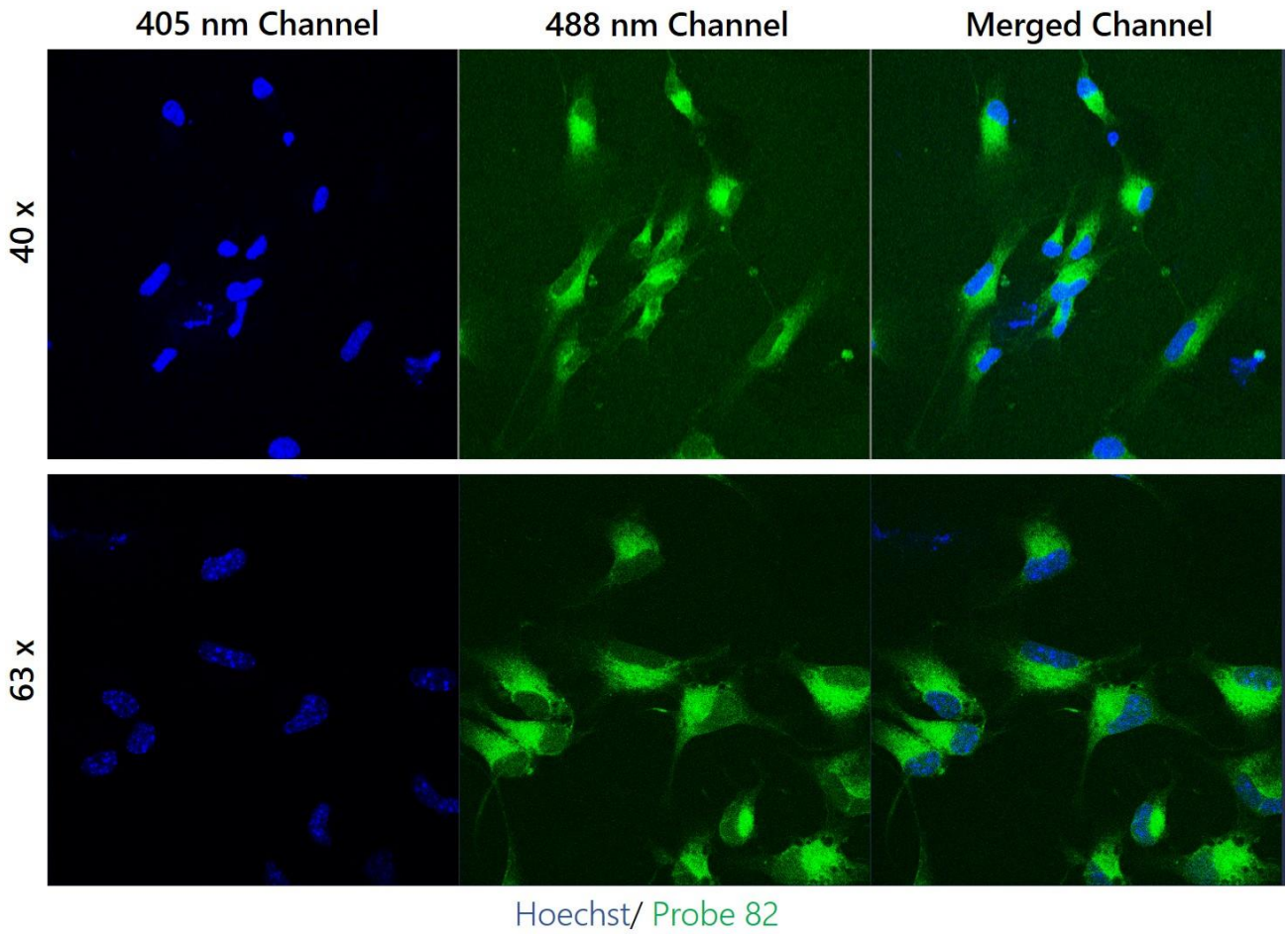


*Figure 31. Confocal images showing SVZ-derived NSCs stained with Hoechst (blue) and BODIPY probe **82** (green).*

As observed in the 488 nm channel, the BODIPY probe was found to accumulate in the cytoplasm of the cells. A lack of staining in the nucleus of the cells (Hoechst) indicated that the probe was not taken up into the nucleus. This suggests that the molecular target of OXS-N1 is localised in the cytoplasm, and not in the nucleus or the membranes.

3.4.3 Competition Study with Parent Compound

To determine the specificity of the labelling of the BODIPY probe, cells were treated with a fixed concentration of **82** (5 μM) and increasing concentrations of OXS-N1. The cells were imaged after 2 hours of treatment and shown in Figure 32.

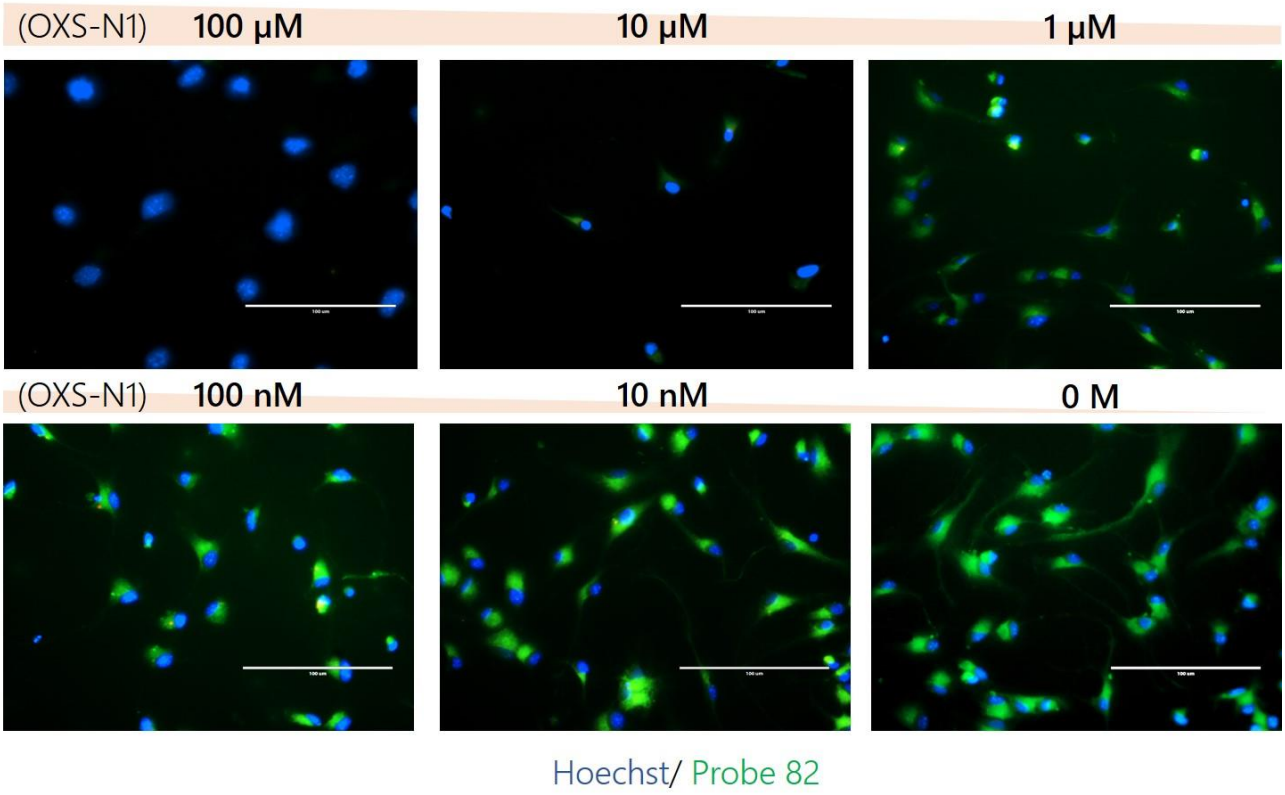


*Figure 32. Fluorescence images showing labelling of the cells by BODIPY probe **82** (5 μM) in the presence of varying concentrations of OXS-N1 (0 to 100 μM).*

As the concentration of OXS-N1 was increased from 10 nM to 100 μM, the green fluorescence signal observed from **82** decreased. When OXS-N1 was treated in 20x excess over the fluorescent probe, no fluorescence labelling was observed in the GFP channel, indicating the parent compound outcompeted the probe for binding to the molecular target(s) in the cells. This also provides evidence that the probe is labelling the molecular target(s) of OXS-N1 specifically.

3.4.4 Quantification of Fluorescence Signal

Using a fluorescence microplate reader, the green fluorescence signal from the cells can be quantified. A concentration-dependent increase in fluorescence intensity was observed with

increasing concentration of BODIPY probe **82** (Figure 33A). A baseline fluorescence of around 50000 R.F.U was observed for the cells treated with the control probe **83**, indicating low levels of background labelling.

The outcompetition of the fluorescence signal can be also be quantified by measuring the fluorescence intensity after different treatment conditions (Figure 33B). In the SVZ-derived cells, when OXS-N1 (**15**) was treated in 40x excess of the BODIPY probe, the fluorescence intensity decreased from 114370 R.F.U to 79400 R.F.U, indicating displacement of the BODIPY probe from the molecular target(s) in the cells. When the inactive analogue **29** was treated at the same concentration, there was no significant change in fluorescence intensity in the SVZ-derived cells. The same experiment was conducted without cells to ascertain that the decrease in fluorescence intensity was not related to fluorescence quenching. The fluorescence intensity of the BODIPY probe was measured after OXS-N1 and **29** were added in 40x excess concentration. No significant changes in the fluorescence intensity were observed, indicating that both OXS-N1 and **29** did not have fluorescence quenching effects on the BODIPY probe.

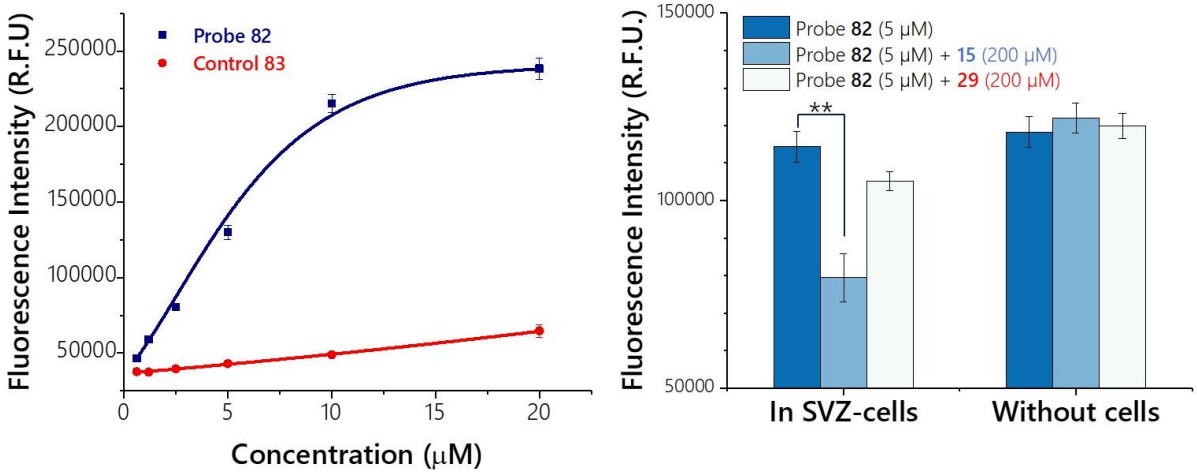


*Figure 33. Graphs showing fluorescence intensity of BODIPY probes measured using a fluorescence microplate reader. (A) Graph shows fluorescence intensity measured in SVZ-derived cells after 2h treatment with varying concentrations of BODIPY-tagged probe **82** and BODIPY control **83**. (B) Graph showing changes in fluorescence intensity of BODIPY probe **82** after addition of OXS-N1 (**15**) and inactive analogue (**29**), in SVZ-derived cells, and without cells respectively. Biological replicates, n = 2; Error bars represent standard error; ** $p < 0.005$.*

3.5 Slice Culture Imaging

3.5.1 Organotypic Slice Cultures

To investigate if similar uptake and specific localisation of the BODIPY probe in neuronal cells was likely to occur *in vivo*, organotypic slice cultures were explored. Organotypic slice cultures of the brain provide a physiologically relevant three-dimensional model for *ex vivo* studies.[235] The slice cultures preserve aspects of anatomical and synaptic connectivity, and may be useful to identify specific areas where the small molecule accumulates in the tissues among the heterogeneous mixture of cells. To probe the uptake and accumulation of OXS-N1 in brain tissues, mouse brains were used for organotypic slice culture imaging with BODIPY-tagged probe **82**.

The brains of wild-type postnatal mice were dissected and manually sliced (by Dr Anna Hoerder-Suabedissen, DPAG, Oxford). The slices were then incubated with **82** (10 μM) for 4 hours and washed with incubation in PBS for 1 hour before imaging with an epifluorescence microscope (Figure 34).

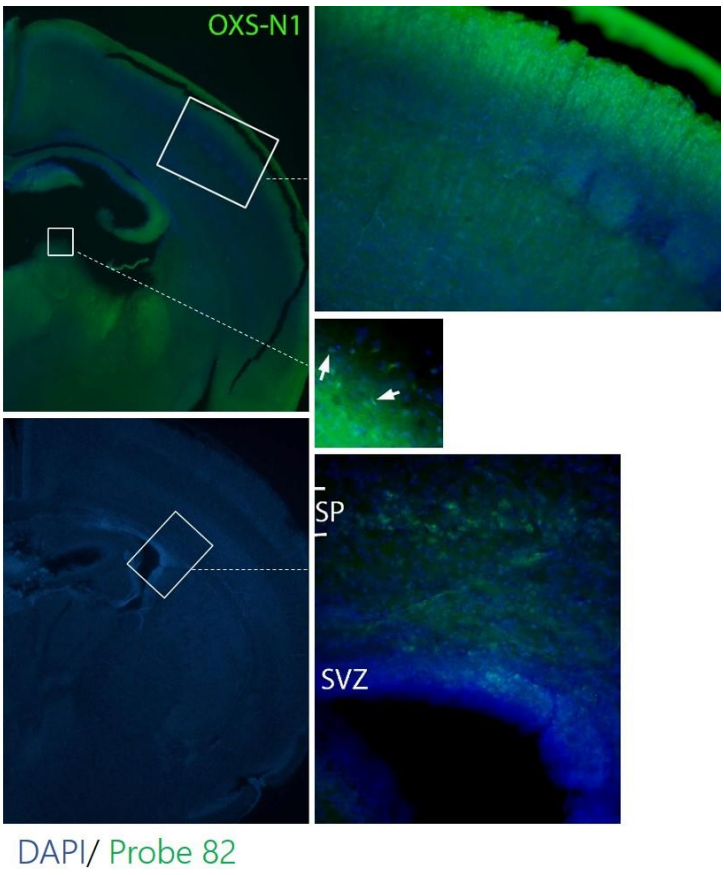


*Figure 34. Fluorescence images of tissue slices after treatment with BODIPY-tagged probe **82** (green) for 4h. Nuclei are stained with DAPI (blue). Magnified images of the boxed regions are on the right.*

As seen in the top right panel, there is a gradient of green intensity from the pial surface (edge of tissue slice) into the cortex, indicating uptake of the BODIPY probe **82** into the tissue slices. The observed gradient suggested that the probe did not fully penetrate the organotypic slice in 4 h. In regions near the surface of the cultured slice, and near a 'hole' or other conduit in the tissue, some cellular labelling, mostly cytoplasmic, is visible (indicated by the arrowheads). The brighter green fluorescence in the subplate (SP) layer (bottom right panel) could be indicative of some accumulation of the BODIPY probe in the SP.

The slices were re-sectioned using a vibratome to obtain thinner sections for use in confocal imaging (Figure 35).

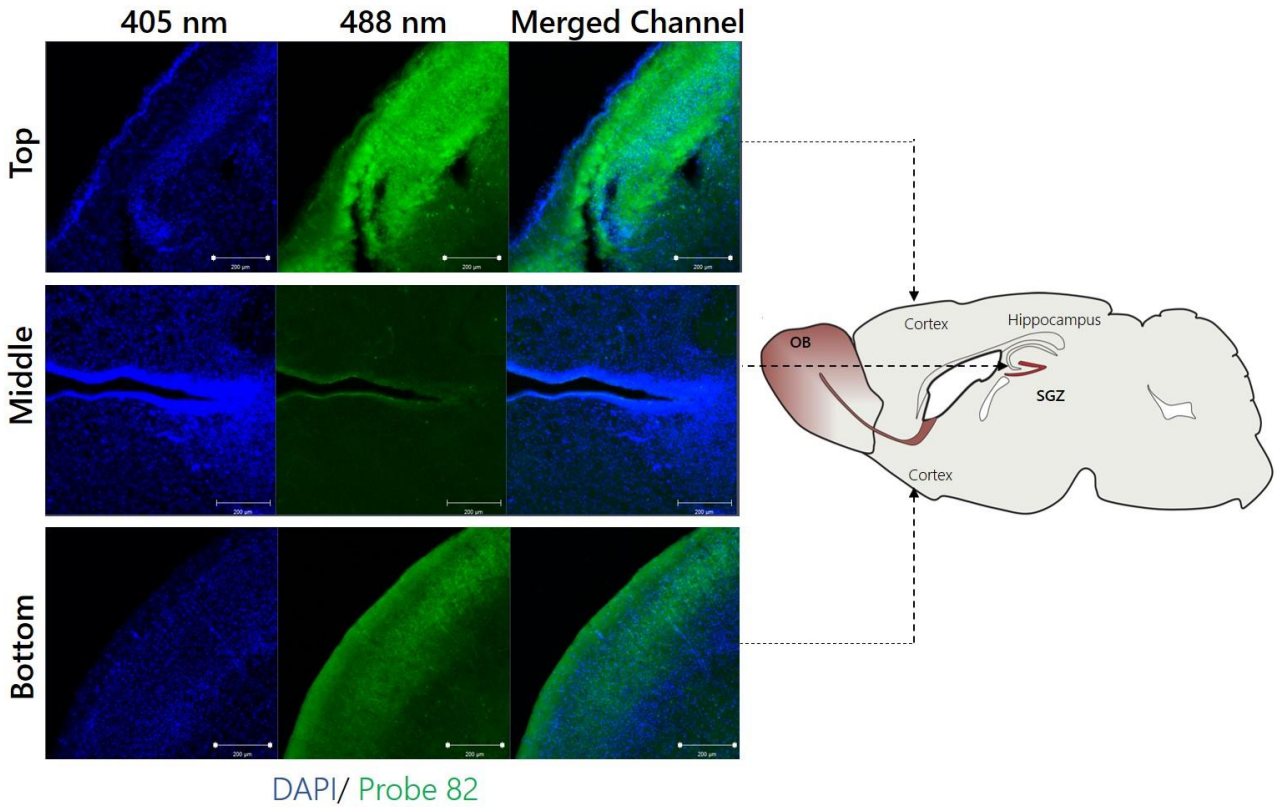


*Figure 35. Confocal images of the top, middle and bottom sections of a re-sectioned tissue slice. Nuclei stained with DAPI (blue), tissues stained with BODIPY-tagged **82** (green). Schematic on the right shows the corresponding regions of the brain.*

The top and bottom sections show labelling of the tissue by BODIPY probe **82**, while the middle section shows very little labelling. This is consistent with previous observations that **82** did not achieve full penetration through the tissue slice within 4h. The labelling in the top and bottom sections were mainly localised in the cortex. In the middle section, there was no significant labelling observed in the DG, but this was most likely due to the low penetration of the probe into the middle section during the short incubation time. A longer incubation time could have resulted in more accumulation of the probe in tissue regions which are further away from the surface. The BODIPY control **83** could have also been used to determine background labelling from the fluorophore. However, due to time and materials constraints, this experiment was not pursued further.

3.6 Summary

Fluorescent probes were designed to visualise the subcellular localisation of OXS-N1. Rhodamine probes were found to be cytotoxic to the NSCs, hence BODIPY probes were developed. BODIPY-tagged probe **82** retained biological activity while having minimal cytotoxicity. Treatment of SVZ-derived NSCs with **82** gave good subcellular labelling, which was concentration-dependent. The fluorescence signal from the probe was outcompeted by increasing concentrations of OXS-N1, indicating specific labelling. OXS-N1 most likely binds to a molecular target in the cytoplasm of the cells, as the BODIPY-tagged probe was not present in the nucleus nor in the membranes. Target identification studies described in Chapter 4 will give further details on how the target is deconvoluted using mass spectrometry methods. Cellular imaging studies in Chapter 5 will elaborate on co-localisation experiments carried out by immunostaining the putative target and labelling with the BODIPY probe.

Chapter 4 Target Identification

4.1 Overview

Target identification of OXS-N1 was carried out using various sets of active and inactive probes. This chapter aims to describe the affinity-based proteomic profiling (AfBPP) workflow to identify target proteins pulled down by the probes. In-gel and in-solution tryptic digest approaches are compared and hit proteins are shortlisted for further validation.

4.2 AfBPP using Biotinylated Probes

4.2.1 Chemoproteomics Workflow

Biotinylated probes **72** and **73** were used to pull down proteins from the SVZ-derived cells using the workflow as outlined in Figure 36. Biotinylated probes are commonly used in cell lysates instead of live cells, due to their low cell permeability.[236] However, the molecular interactions in the cell lysates may differ from the cellular context, especially as protein-protein interactions, downstream events in signal transduction pathways, cellular organisation and compartmentalisation are disrupted in cell lysates.[168] The activity of **72** in the *in vitro* neurosphere differentiation assay suggested that at high concentrations, there was sufficient cellular uptake of the biotinylated probe to result in an increase in neuronal differentiation. As pull-down studies done in live cells are likely to give more physiologically relevant results as compared to those done in cell lysates, we opted to attempt the pull-down workflow using live SVZ-derived cells. A high concentration (25 μM) was chosen to maximise the cellular uptake of the probe and subsequently the probe labelling in the cells.

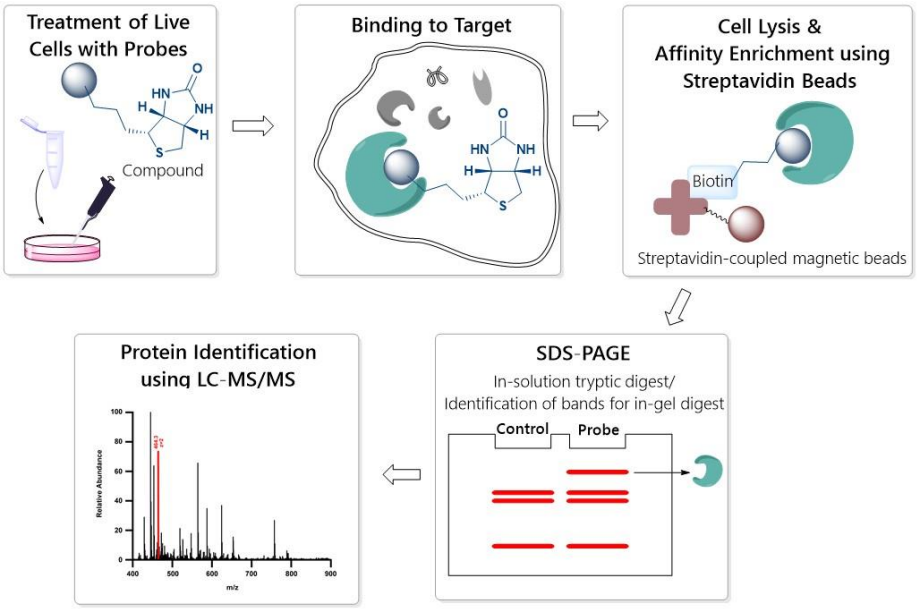


Figure 36. Schematic showing the AfBPP workflow using biotinylated probes.

The cells were incubated with the biotinylated probes for 2 hours. A 2-hour incubation time was chosen as it was previously found to be sufficient for the fluorescent probes to achieve cellular penetration (Section 3.4.1). After compound treatment, the cells were washed twice with PBS and lysed with 0.1% (v/v) SDS in PBS. The cell lysates were then incubated with magnetic streptavidin beads for 1 hour, to capture biotinylated probe-protein complexes. To remove unbound proteins, the beads were washed multiple times. Washing conditions were kept mild so as not to disrupt the probe binding to the target. Bound proteins were eluted by heating the beads in the presence of NuPAGE Sample Buffer for 5 min at 95°C. The proteins were separated using SDS-PAGE and visualised by staining. Silver staining using silver nitrate was chosen as the method to visualise the eluted proteins as it is much more sensitive than Coomassie Blue staining and can detect proteins on the gel in the nanomolar range.[237] Bands were compared between the control and probe-treated samples to identify bands of interest. In-gel tryptic digest and mass spectrometry analysis were used to identify proteins enriched by the active probe.

4.2.2 Protein Identification from In-gel Digest

The proteins eluted from the beads were visualised by silver staining as shown in Figure 37A. DMSO was used as a negative control to identify non-specific interactions and endogenously biotinylated proteins in cells. Active probe **72** (25 μM) was used to pull-down target proteins and inactive probe **73** (25 μM) was used to rule out interactions that did not contribute to biological activity. A large excess of the parent compound **15** (250 μM) was treated together with **72** (25 μM) as a competition control. A band at around 50 kDa (highlighted by the red box) was observed to be enriched by the active biotinylated probe **72** and not by the inactive probe **73** and competition control. This band was excised and subjected to tryptic digest for subsequent protein identification. To serve as a control for identifying non-specific proteins or possible contaminants, a gel section corresponding to the same molecular weight of the selected band was also excised from the DMSO-treated pull-down sample. The proteins identified in these two gel bands were identified by mass spectrometry and the abundance of the proteins found are compared in Figure 37B.

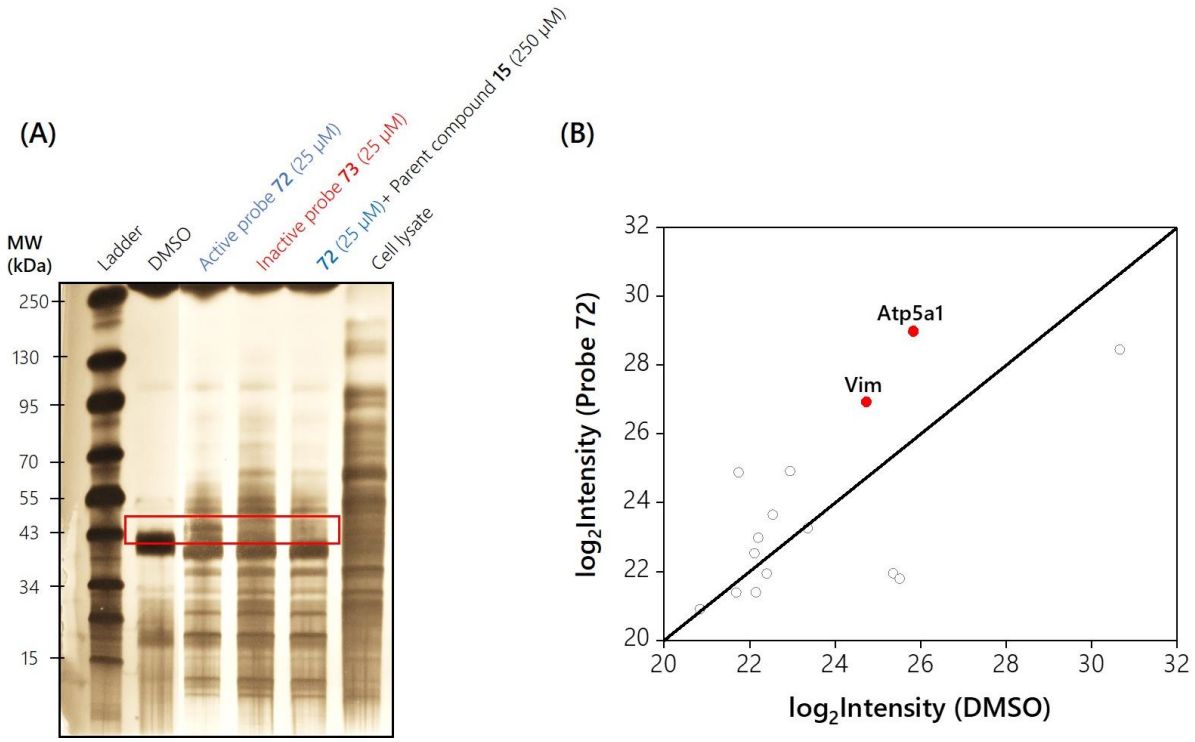


*Figure 37. (A) Silver-stained SDS-PAGE gel showing the proteins eluted from the pull-down experiment with the biotinylated probes **72** and **73**; (B) Protein identification of the excised gel bands of interest by LC-MS/MS analysis.*

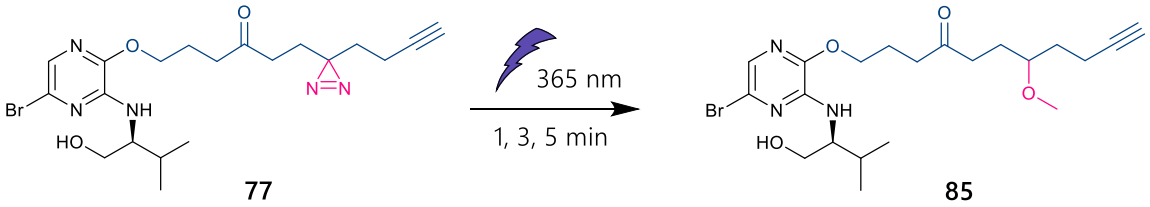
The log_2 intensities of peptides found in the DMSO sample and active biotinylated probe **72** samples were compared. ATP synthase subunit alpha (Atp5a1) and vimentin (Vim) were found to be enriched by at least 4-fold in the gel band excised from the biotinylated probe pull-down over the corresponding gel band from DMSO pull-down. These putative targets will be further discussed in Section 4.4.

4.3 AfBPP using Dual-Tagged Probes

4.3.1 Chemoproteomics Workflow

To improve the detection of weakly-bound or less abundant protein targets in the cell, photoaffinity labelling was attempted. Dual-tagged probes **77** and **78**, which incorporated both a diazirine group and an alkyne handle, were employed. Preliminary irradiation studies were conducted to determine the irradiation time required for activation of the diazirine probes. An irradiation time that is too short would be insufficient for activating the photoaffinity group and result in sub-optimal labelling. On the other hand, irradiating the cells for too long would cause heat damage to the cells and would likely increase the background labelling, making it more difficult to identify relevant targets. Diazirine-tagged probe **77** was dissolved in methanol and irradiated on ice for 1, 3 and 5 min. The presence of **77** was monitored by LCMS (Table 6). As the irradiation time increased, the peak corresponding to **77** decreased, indicating activation of the diazirine probe. After 5 min of irradiation, the starting material **77** was completely lost, and the major product formed had a *m/z* value consistent with methyl ether **85** (*m/z* 469.6, 471.6). An irradiation time of 5 min was hence chosen for use in the chemoproteomics workflow.

Table 6. Monitoring the activation of 77 by LCMS with different irradiation times.



Irradiation Time (min)	Compound 77, Area (%)	Compound 85, Area (%)
0	99.7	0
1	26.3	51.8
3	10.2	64.3
5	0	76.6

The chemoproteomics workflow for pull-down experiments using dual-tagged probes is illustrated in Figure 38. The addition of photocrosslinking and click reaction steps makes this workflow longer than that previously described for the biotinylated probes.

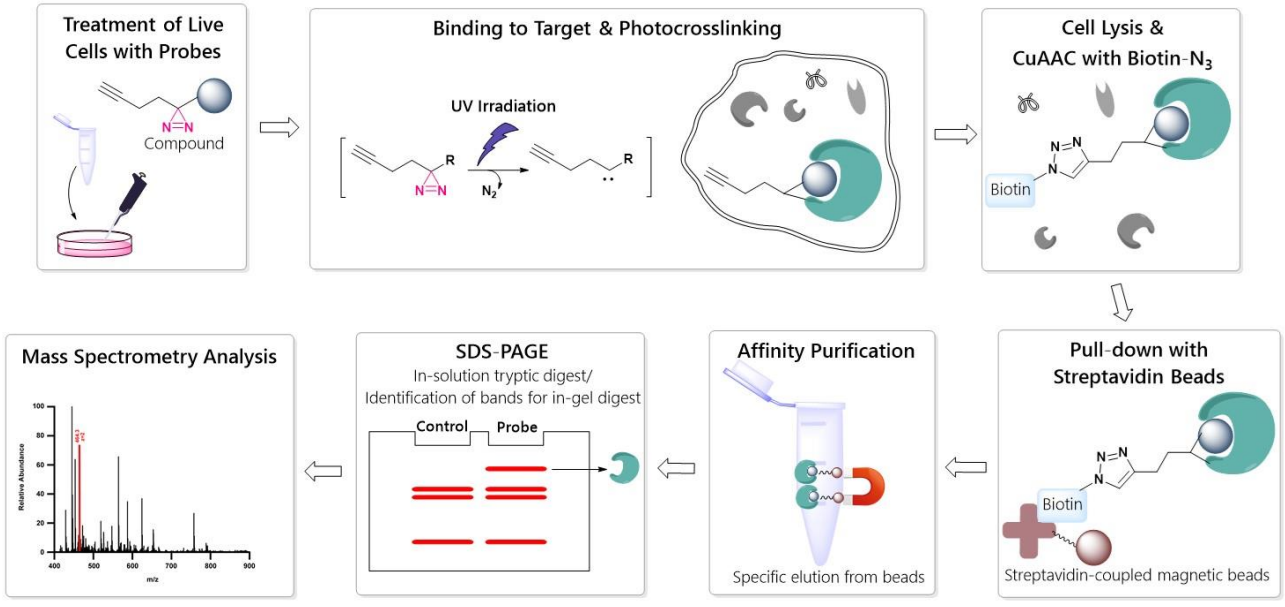


Figure 38. Schematic showing the AfBPP workflow using dual-tagged probes.

The dual-tagged probes were incubated with the live cells for 2 hours. The cells were then subjected to UV irradiation at 365 nm for 5 min to activate the diazirine group to a carbene. Irradiation was done with the cells cooled on ice to minimise heat damage from the UV lamp. The activated carbene can insert into neighbouring bonds and this induces a covalent linkage

between the probe and protein targets in the cell. The cells were lysed and a click reaction was performed to append the biotin tag onto the probe-protein conjugates. Protein precipitation with chloroform/methanol was used to remove the excess click reagents. The probe-protein complexes were captured by magnetic streptavidin beads and purified by affinity enrichment. More stringent washing of the beads was carried out by using 4M and 6M urea to remove non-specifically bound proteins. The proteins were eluted from the beads with heating and identified by mass spectrometry.

4.3.2 Protein Identification from In-gel Digest

The proteins eluted from the beads were visualised by silver staining as shown in Figure 39A. Active diazirine probe **77** (25 μM) was used to pull-down protein targets of interest. To distinguish between background labelling from crosslinking to non-specific protein targets, inactive diazirine probe **78** (25 μM) was important as a negative control. A large excess of the parent compound **15** (250 μM) was treated together with **77** (25 μM) as a competition control. A band at around 70 kDa (highlighted by the red box) was observed to be enriched by the active probe and not in the other conditions. It was excised and subjected to tryptic digest for subsequent protein identification. Similarly, a gel section corresponding to the same molecular weight of the selected band was excised from the DMSO-treated pull-down sample. The proteins identified in these two gel bands were identified by mass spectrometry and the abundance of the proteins found are compared in Figure 39B.

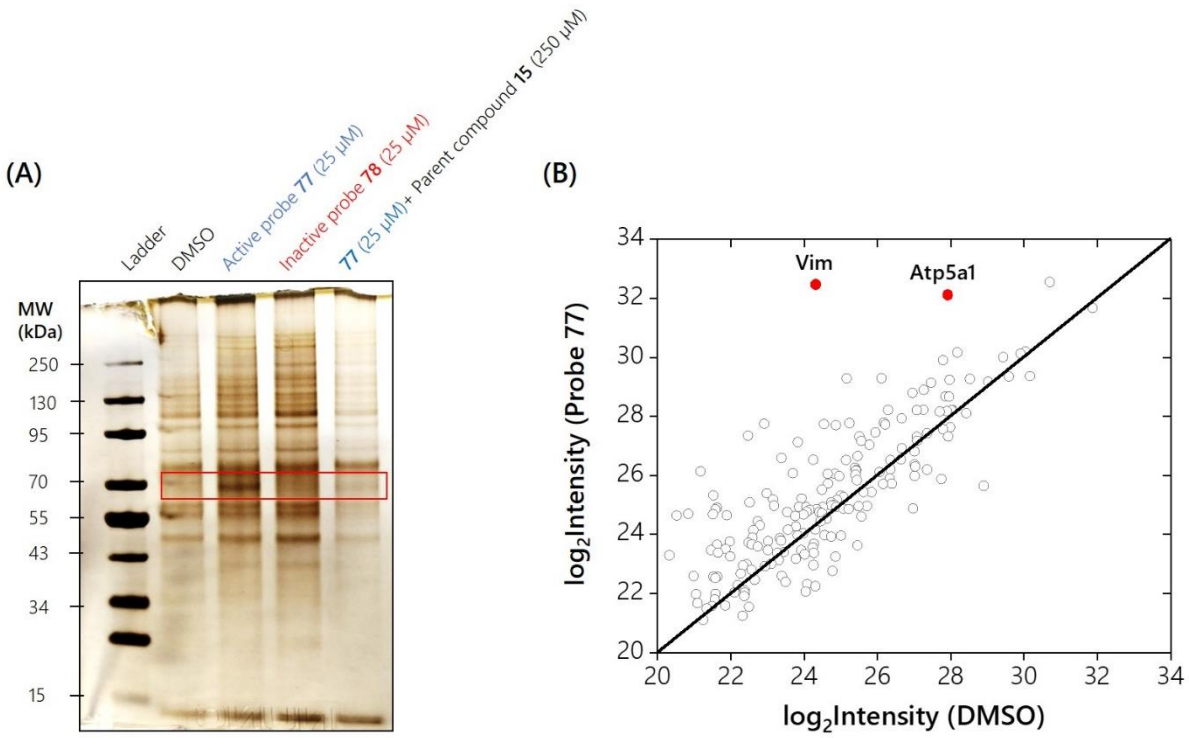


*Figure 39. (A) Silver-stained SDS-PAGE gel showing the proteins eluted from the pull-down experiment with the dual-tagged probes **77** and **78**; (B) Protein identification of the excised gel bands of interest by LC-MS/MS analysis.*

More proteins were identified from the gel bands, possibly due to an increase in background labelling. Interestingly, while the excised band was of a different approximate molecular weight (70 kDa) compared to the band excised from the biotinylated probes pull-down experiment (55 kDa) in Section 4.2.2, the two most significantly enriched proteins were found to be the same - vimentin (Vim) and ATP synthase subunit alpha (Atp5a1). The difference in the washing conditions could have caused changes to the structure and folding of the proteins, resulting in the enriched band being observed at slightly different molecular weights. A high concentration of urea (6 M) was used in the washing of the streptavidin beads in the diazirine probe pull-down procedure. Urea acts as a denaturing agent and disrupts the intermolecular hydrogen bonding and the tertiary structures of proteins. This could have led to changes in how SDS binds to the proteins, and how the proteins migrate on the gel.[238] The two enriched proteins pulled down by the active diazirine probe **77** matched those that were pulled down by the active biotinylated probe **72**.

4.3.3 Protein Identification from In-solution Digest

To further support the findings from the in-gel protein identification, in-solution protein identification from the entire pull-down elutes was carried out. This would allow for a proteome-wide search for enriched protein targets. The high sensitivity of mass spectrometry analysis would improve the detection of protein targets that are less abundant and potentially missed in gel staining methods of visualisation.

The proteomics experiments were conducted at Imperial College London under the guidance of Dr Dan Conole (Professor Ed Tate group). The dual-tagged diazirine probes were used in both SVZ- and DG-derived NSCs. Due to the higher sensitivity of mass spectrometry, a lower probe concentration of (10 μM) was used in the pull-down experiments. For the competition control, parent compound **15** was treated at the same concentration (10 μM) as active probe **77**. As **15** has a lower EC_{50} than probe **77**, it is predicted to have higher binding affinity to the molecular target(s) in the cells compared to **77**.

The conditions tested in each cell type were: (i) DMSO (0.2% v/v), (ii) active probe **77** (10 μM), (iii) inactive probe **78** (10 μM) and (iv) active probe **77** (10 μM) with parent compound **15** (10 μM). For each condition, three technical replicates were used for the pull-down. Click reaction with azide-arginine-biotin (AzRB) reagent was used to append biotin tags to probe-protein complexes. Streptavidin-coated agarose beads (NeutrAvidin) were used for affinity enrichment and the proteins captured were eluted by on-resin tryptic digest. Proteins were identified by nanoLC-MS/MS analysis. Label free quantification (LFQ) of the intensities of the peptides was used to compare the relative amounts of specific proteins across samples.

Results of the proteome-wide target identification are presented in Figure 40. Comparing the proteins found in the active probe samples with those in the controls ruled out the majority of proteins as non-specific background labelling. More specifically enriched proteins were identified to the right of the curve in the volcano plots shown in Figure 40. The full list of enriched proteins against each condition can be found in Appendix 1. The top protein hits which

were found to be overlapping between the SVZ and DG samples are highlighted in orange. The putative protein targets which were found previously from the in-gel digest experiments are highlighted in red.

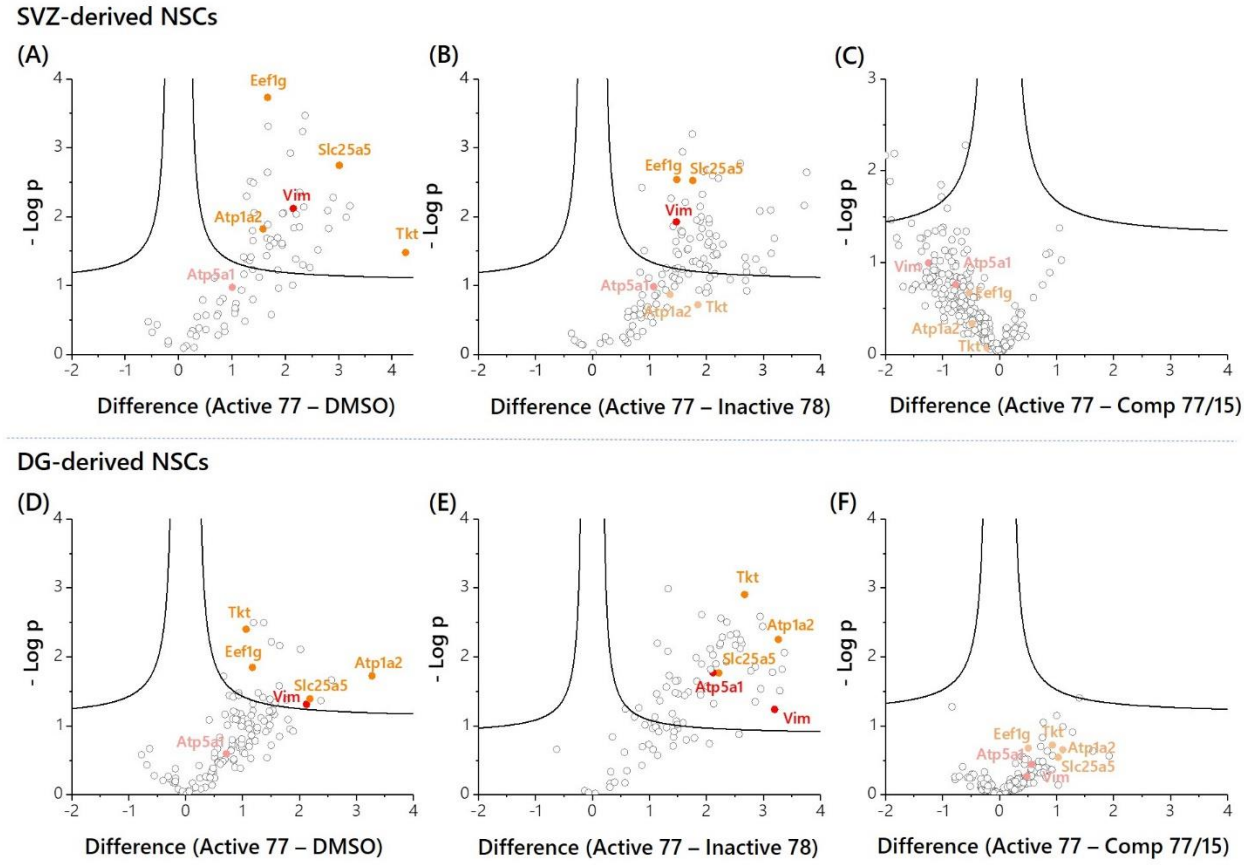


*Figure 40. Volcano plots showing log_2 difference (fold-change) and significance ($-log_{10}$ p-value) between proteins enriched by active probe **77** against (A) DMSO, (B) inactive probe **78** and (C) competition control **15** in SVZ-derived NSCs. Volcano plots showing log_2 difference (fold-change) and significance ($-log_{10}$ p-value) between proteins enriched by active probe **77** against (D) DMSO, (E) inactive probe **78** and (F) competition control **15** in DG-derived NSCs. Technical replicates, n = 3, False Discovery Rate (FDR) = 0.05, S_0 = 1. Top hit proteins enriched by the active probe but not in the other controls are highlighted in orange. Proteins found from the AfBPP in-gel digest experiments are highlighted in red for comparison.*

Vimentin (Vim) was found to be consistently enriched by the active probe against the vehicle and inactive controls in both the SVZ- and DG-derived NSCs. ATP synthase subunit alpha (Atp5a1) was only found to be significantly enriched over the inactive control in the DG-derived NSCs. By comparing the overlap between the enriched proteins against each condition, 4 more putative hits were identified: Sodium/potassium-transporting ATPase subunit alpha-2 (Atp1a2), elongation factor 1-gamma (Eef1g), transketolase (Tkt) and solute carrier family 25 member 5 (Slc25a5).

However, in both the SVZ- and DG-derived NSCs, the active probe failed to show any significant target enrichment over the competition control (Figure 40C, F). This is most likely due to the low concentration of the parent compound used in the competition experiment, leading to less outcompetition of the probe binding to molecular target(s) in the cell. The difference between the abundance of the identified peptides in the sample could have been small and difficult to quantify accurately by LFQ. Due to a technical problem with the mass spectrometer, some of the technical replicates were ran much later after the peptides were reconstituted. The prolonged storage of the peptides in solution could have caused some degradation, leading to variability in the quantification of peptides abundance in the samples.

To improve the quantification of proteins across samples, tandem mass tag (TMT) labelling was performed on the proteins eluted by on-resin tryptic digest (Figure 41). The digested peptides from each sample are labelled in parallel using 11 tag variants. The samples are then mixed and fractioned, before being analysed using LC-MS/MS. The isobaric tags have the same nominal mass and are chemically identical. Identical peptides with different tag variants would hence have the same elution and ionisation profile, leading to more accurate quantification using the MS^2 spectra.[239]

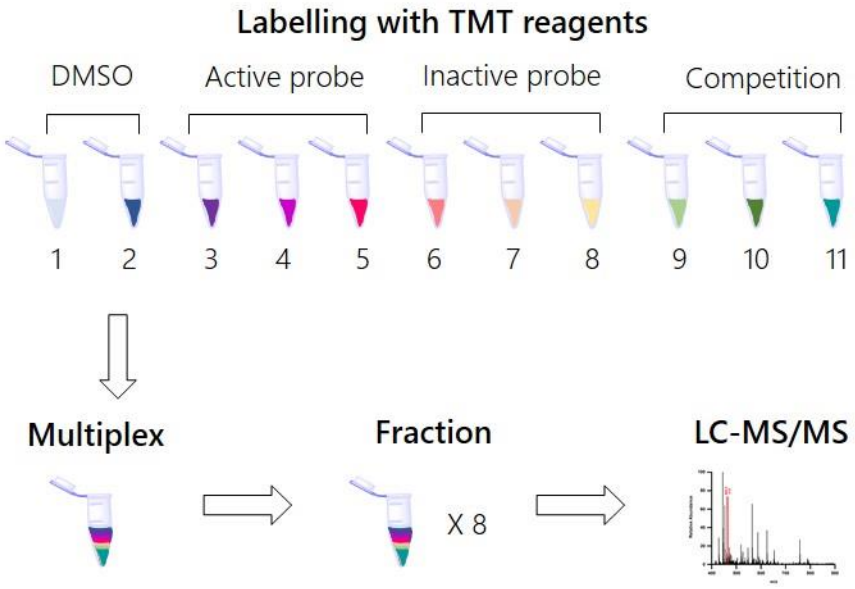


Figure 41. Schematic of the workflow for TMT labelling. The pull-down samples are each labelled with a different mass tag. The samples are then combined and fractioned into 8 fractions. The fractions are separated, and the peptides are identified by LC-MS/MS analysis.

Proteins found by TMT labelling are shown in the volcano plots in Figure 42. The full list of enriched proteins against each condition can be found in Appendix 2. The top protein hits which were found to be enriched by the active probe against other controls are highlighted in blue. The putative protein targets which were found from previous experiments are highlighted in red and orange.

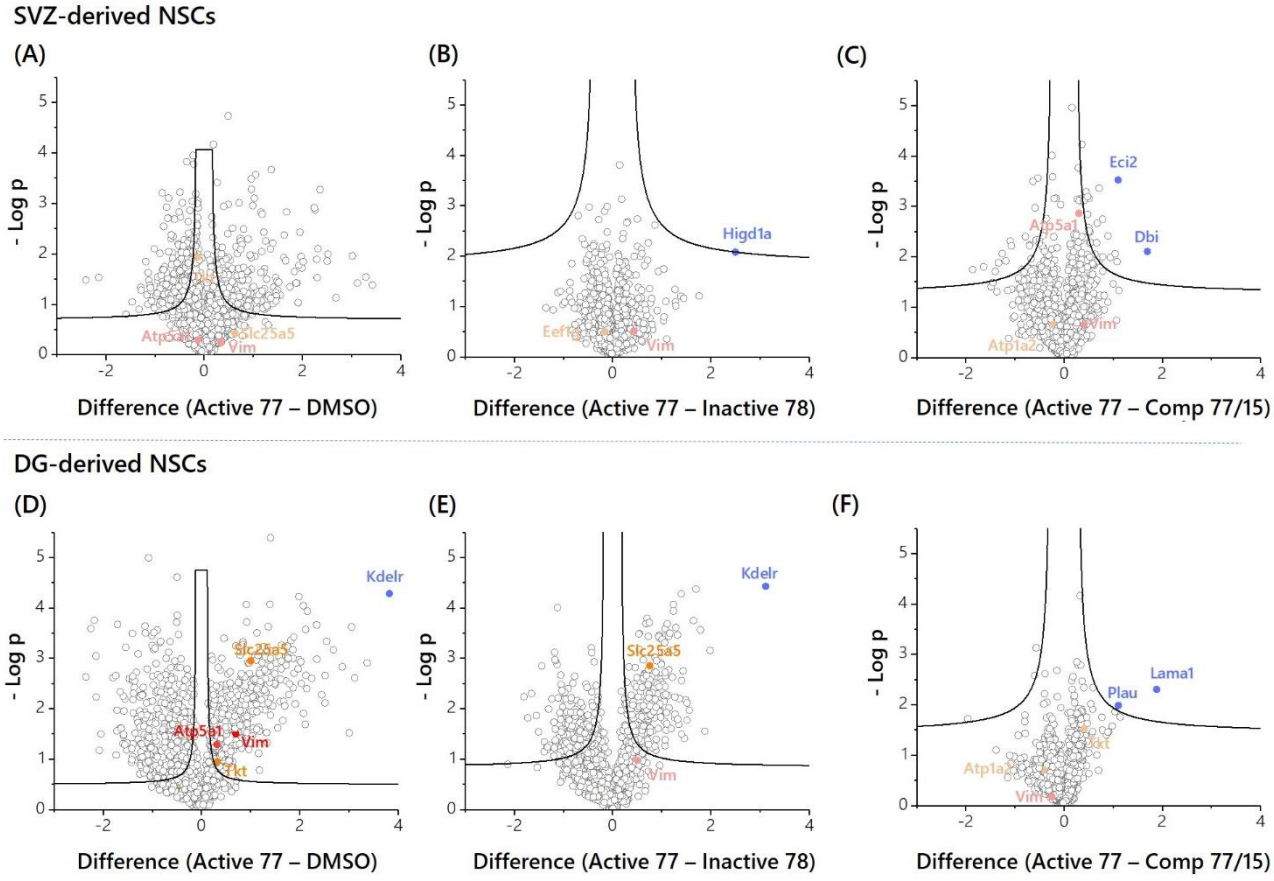


*Figure 42. Volcano plots showing log_2 difference quantified by TMT (fold-change) and significance ($-log_{10}$ p-value) between proteins enriched by active probe **77** against (A) DMSO, (B) inactive probe **78** and (C) competition control **15** in SVZ-derived NSCs. Volcano plots showing log_2 difference quantified by TMT (fold-change) and significance ($-log_{10}$ p-value) between proteins enriched by active probe **77** against (D) DMSO, (E) inactive probe **78** and (F) competition control **15** in DG-derived NSCs. Technical replicates, n = 3, False Discovery Rate (FDR) = 0.05, S_0 = 1. Top hit proteins enriched by the active probe but not in the other controls are highlighted in blue. Proteins found from AfBPP LFQ experiments are highlighted in orange and proteins found from the AfBPP in-gel digest experiments are highlighted in red for comparison.*

There are significantly more proteins identified in the TMT experiment (1600 to 1800 proteins per condition) as compared to the LFQ experiments. The improved coverage of the proteome led to the identification of many proteins which were enriched by the active probe compared to the DMSO vehicle control. Disappointingly, there was poor overlap of proteins enriched by **77** among the DMSO, inactive and competition controls. A few protein targets such as enoyl-CoA delta isomerase 2 (Eci2), diazepam binding inhibitor (Dbi), plasminogen activator urokinase (Plau) and laminin subunit alpha-1 (Lama1) found to be significantly enriched compared to the competition control. However, these proteins were not found in the other controls, and hence were not pursued further as hits. The putative targets found in previous AfBPP experiments were also not significantly enriched in most of the conditions in the TMT experiments. There was poor

concordance with previous data from the LFQ experiment, which indicated that some optimisation might be necessary to use TMT labelling in the AfBPP experiments. As there were already some putative hits from previous AfBPP experiments, the focus was shifted to validate the putative hits instead of pursuing the TMT labelling experiments further.

4.4 Protein Hits from AfBPP

A summary of the putative targets found to be enriched by active probes **72** and **77** over various controls, in separate AfBPP experiments, is shown in Table 7.

*Table 7. Enrichment of putative targets by active probes over various controls: DMSO (vehicle), inactive control (either probes **73** or **78**) and competition control with parent compound **15** (comp). Significant enrichment under each condition is indicated with a tick.*

Protein	In-gel digest (SVZ)		In-solution digest (SVZ)			In-solution digest (DG)		
	72 vs DMSO	*77 vs DMSO*	*77 vs DMSO*	*77 vs inactive*	*77 Vs comp*	*77 Vs DMSO*	*77 Vs inactive*	*77 Vs comp*
Atp5a1	✓	✓					✓	
Vim	✓	✓	✓	✓		✓	✓	
Atp1a2			✓			✓	✓	
Eef1g			✓	✓		✓		
Slc25a5			✓	✓		✓	✓	
Tkt			✓			✓	✓	

Vimentin was the most promising hit, as it was enriched in 6 out of 8 conditions across the different experiments. A brief literature search on the shortlisted putative targets was conducted to examine if there were any known links to neurogenesis and neuronal differentiation.

4.4.1 Vimentin (Vim)

Vimentin is an intermediate filament protein which is involved in a range of cellular processes such as regulation of cell morphology, plasticity, cytoskeletal structure, migration, signalling and differentiation.[240] It induces changes in cell motility and adhesion during epithelial-to-mesenchymal transition (EMT).[241] Vimentin has also been found to play a cellular repair role by

regulating the movement of lens epithelium in response to an injury. [242] Chen *et al.* reported that mutation of serine sites in vimentin in mice led to an increase in the percentage of newly born neurons.[243] This suggests that modulating vimentin could lead to changes in the neuronal differentiation of neural progenitor cells. Vimentin is localised in the cytoplasm, which is consistent with the subcellular localisation of the BODIPY-tagged OXS-N1 probe previously described in confocal imaging experiments (Section 3.4.2).

4.4.2 Mitochondrial proteins (Atp5a1, Atp1a2, Slc25a5)

Atp5a1 and Atp1a2 are alpha subunits of the catalytic core of mitochondrial ATP synthase. Mitochondrial ATP synthase catalyses ATP synthesis from ADP by using an electrochemical proton gradient generated across the inner membrane during oxidative phosphorylation.[244] Slc25a5 (Solute carrier family 25 member 5) is a mitochondrial carrier protein which catalyses the exchange of cytoplasmic ADP with mitochondrial ATP across the mitochondrial inner membrane.[245] It is highly expressed in the cortex and hippocampus.

Mitochondrial dysfunction has been linked to neurodegenerative diseases such AD and amyotrophic lateral sclerosis.[246] Mitochondria plays an important role in energy production for the cell through respiration and regulation of metabolism. It is also involved in neuronal differentiation, release of neurotransmitters and the formation of synapses.[247] Neuronal activity and plasticity are dependent on the maintenance of membrane potentials and a tight regulation on cellular metabolism. Beckervordersandforth *et al.* highlighted evidence that enhancement of mitochondrial function promoted hippocampal neurogenesis in aged mice.[248] Defects in mitochondrial carriers were also reported to result in defective energy production and changes in synaptic plasticity and neurogenesis.[249] Babenko *et al.* showed that the altered gene expression of Slc25 family genes was associated with changes in neurogenesis in male mice subjected to periods of social conflict.[250]

These mitochondrial proteins identified as putative hits could indicate modulation of metabolic events in the cells relating to neurogenesis and could be interesting targets of OXS-N1. However,

based on subcellular localisation studies described in Section 3.4.2, the BODIPY-tagged OXS-N1 probe did not specifically localise in the mitochondrial membranes. This indicates that the binding to these mitochondrial proteins in the AfBPP experiments could also be non-specific.

4.4.3 Transketolase (Tkt)

Transketolase is a key enzyme of the non-oxidative pentose-phosphate pathway (PPP). It catalyses the transformation of phosphate sugars to substrates required for glycolysis.[251] It is highly expressed in rapidly proliferating cells and differentiating cells. Impaired mice and rat hippocampal neurogenesis induced by thiamine deficiency was linked to a decrease in transketolase activity, which resulted in dysregulation of the pentose-phosphate pathway (PPP).[252] Zhao et al. also reported that specific inhibition of transketolase activity by oxythiamine resulted in a significant decrease in proliferation of rat hippocampal progenitor cells.[253] This suggests that modulation of transketolase activity could modulate proliferation and differentiation of neural progenitor cells.

4.4.4 Elongation factor 1-gamma (Eef1g)

Eef1g is a subunit of the elongation factor 1 complex, which plays a key role in the elongation step during translation. Overexpression of Eef1g has been linked to tumorigenesis and poor prognosis in certain cancer types.[254] However, the role of Eef1g in stem cell differentiation has not yet been explored.

4.5 Validation of Pull-down Hits

4.5.1 Immunoblotting of Putative Targets

To validate target engagement by probe 77, immunoblotting using antibodies specific to the putative targets were carried out. SVZ- and DG-derived cells were treated for 2 h, followed by lysis and click reaction to append biotin. After affinity enrichment, the eluted proteins were separated by SDS-PAGE and identified by immunoblotting. The western blots for vimentin and

Atp5a1 were imaged on separate channels on a LI-COR Odyssey imager and shown in Figure 43.

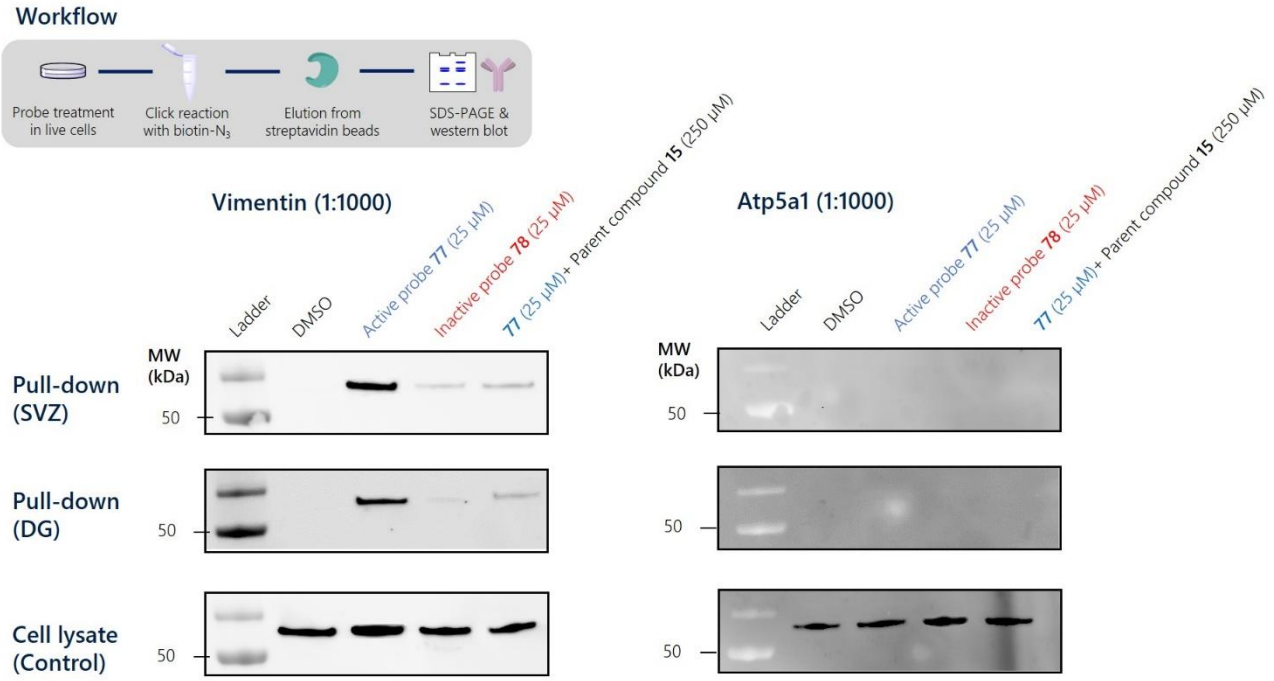


Figure 43. Western blots stained with vimentin antibody (1:1000) and Atp5a1 antibody (1:1000) in pull-down samples from SVZ- and DG-derived NSCs. Cell lysates were used as a control to show relatively similar abundances of the protein in the cell lysates.

Both vimentin and Atp5a1 were found in the cell lysates, indicating they are expressed in the SVZ- and DG- derived NSCs. The cell lysates serve as positive controls to indicate that the antibodies used were able to stain the specific proteins. In the pull-down samples, vimentin was found to be significantly enriched by the active probe, with minimal enrichment by the inactive probe. When parent compound **15** was treated in 10-fold excess (250 μM), the binding of the probe to vimentin was outcompeted, leading to an a much weaker band corresponding to vimentin in the pull-down sample. Specific enrichment of vimentin by diazirine-tagged **77** was demonstrated in both SVZ- and DG-derived NSCs.

While Atp5a1 was found to be very abundant in the cell lysates, it was not found in the pull-down samples under the conditions tested. This indicates that active probe **77** did not bind to Atp5a1 specifically. As Atp5a1 (59 kDa) has a similar molecular weight as vimentin (54 kDa),

trace amounts of Atp5a1 in the pull-down samples could have co-migrated with vimentin, leading to Atp5a1 being identified in the MS analysis of the excised bands.

Antibodies against other putative targets, Atp1a2, Eef1g, Tkt and Slc25a5, were also used to stain western blots of the pull-down samples. While the antibodies were validated in the cell lysates samples, no specific staining of these targets was identified in the pull-down samples. The individual western blots for each target are presented in Appendix 3.

4.5.2 Competition with Parent Compound

Out of the 6 putative targets, vimentin was validated through western blotting to be the most likely protein target of OXS-N1. As proteome-wide target identification studies did not identify vimentin as an enriched target in the competition control, further competition studies were carried out using parent compound OXS-N1 (**15**). A range of concentrations of **15** was titrated against a fixed concentration of active probe **77** (5 µM), and the pull-down samples were subjected to immunoblotting against vimentin. The western blots are presented in Figure 44.

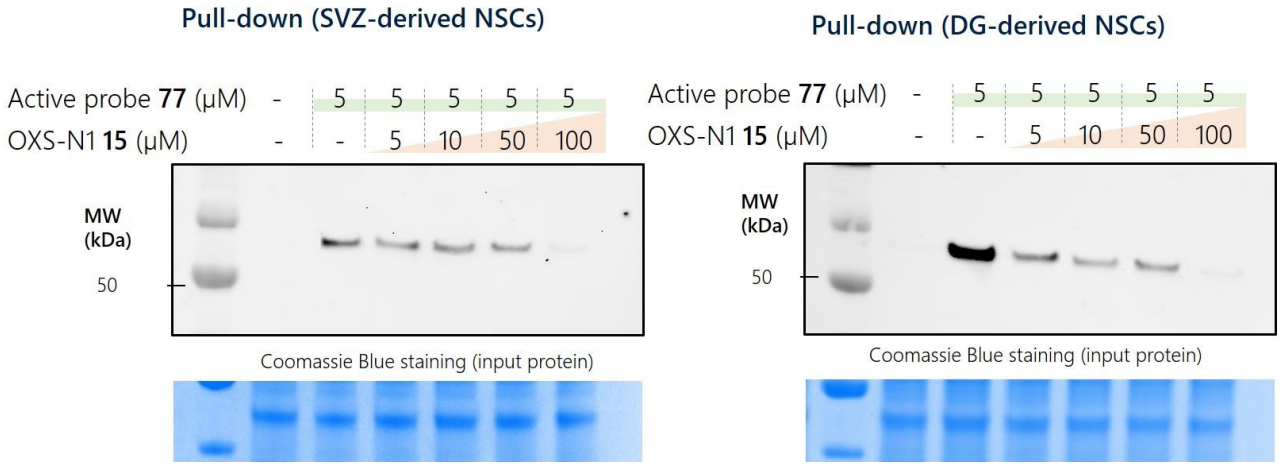


*Figure 44. Immunoblots of pull-down samples against vimentin. SVZ- and DG-derived NSCs were treated with a fixed concentration of active diazirine probe 77 (5 µM) and increasing concentrations of parent compound **15** from 5 to 100 µM. Coomassie Blue staining was used to show equal protein loading across the pull-down samples.*

Active probe **77** (5 µM) specifically enriched for vimentin over the DMSO control. This band decreased in intensity as the concentration of parent compound **15** was increased from 0 to 100 µM. At 20x excess of the parent compound, the binding of vimentin by the active probe was

completely outcompeted, leading to an absence of the vimentin band in the pull-down samples. This shows that a relatively high concentration of the competitor was needed to observe a decrease in labelling by the active probe. This could be attributed to high abundance of vimentin in the cells. A high compound concentration would be required to achieve saturation of target binding. To further validate the outcompetition of the binding to the target in the proteome-wide target identification studies, the parent compound could be titrated and the intensities of peptides could be quantified by TMT labelling.

4.6 Summary

Biotinylated probes and diazirine-tagged probes were used in affinity-based proteome profiling to identify putative hits. Enriched protein bands were excised and identified by mass spectrometry analysis after in-gel digest. There was good agreement between the enriched proteins found by the active biotinylated probe and the active diazirine probe. 2 putative hits, vimentin and Atp5a1, were identified. Proteome-wide profiling was performed to expand the search in both SVZ- and DG-derived NSCs and 4 more putative hits were identified from label-free quantification MS analysis. TMT-labelling was unsuccessful in identifying further potential hits, due to the poor overlap of enriched proteins found for each condition, making it difficult to identify specific hits from the background. The 6 putative hits identified across separate AfBPP experiments were validated using specific antibodies in immunoblotting. Vimentin was validated as a pull-down target of active probe **77**, and not of inactive probe **78**. The binding to vimentin could be outcompeted by increasing concentrations of the parent compound, indicating that it is likely to be the molecular target of OXS-N1. More detailed validation studies to probe the mode of binding to OXS-N1 and implications of modulating this molecular target will be discussed further in Chapter 5.

Chapter 5 Target Validation

5.1 Overview

Vimentin was identified as a protein target of OXS-N1 by a direct chemoproteomics approach. This chapter aims to describe the steps taken to validate vimentin as a therapeutically-relevant target and elucidate its role in the neurogenic activity of OXS-N1. Various biophysical methods were employed to probe the direct binding of the parent compound to the protein. Modulation of the protein in response to OXS-N1 treatment through post-translational modifications (PTMs) and filament assembly was also studied.

5.2 Vimentin as a Molecular Target

Vimentin is a type III intermediate filament (IF) protein, with a molecular weight of 54 kDa. It is made up of a coiled-coil rod domain flanked by head and tail domains (Figure 45). The central α-helical rod domain comprises of coil 1 and coil 2 motifs. The head and rod domains are known to play crucial roles in filament structure and assembly.[255]

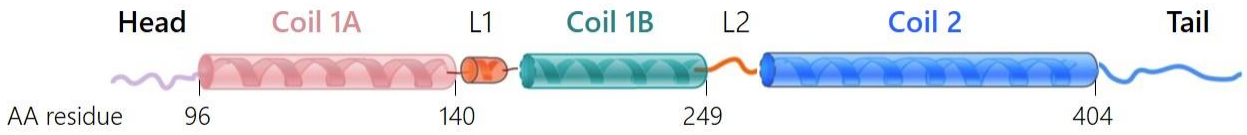


Figure 45. Structure of vimentin protein, showing the head region, coils 1A, 1B and 2 linked by linkers 1 and 2 (L1 & L2), and the tail region.[256]

5.2.1 Expression of Vimentin in Cells and Tissues

Vimentin is highly expressed in mesenchymal cells, including neural precursor cells, fibroblasts, macrophages and metastatic tumour cells.[257,258] Tissue expression of vimentin based on expression data from the Genotype-Tissue Expression (GTEx) project, BioGPS and CGAP databases is shown in Figure 46A.[259,260] It was found to be widely expressed across the tissues in the body, including the nervous, secretory and reproductive systems. In a multiregional

proteomic survey of human brains, Carlyle *et al.* found that vimentin was most highly expressed in the hippocampus (Figure 46B).[261]

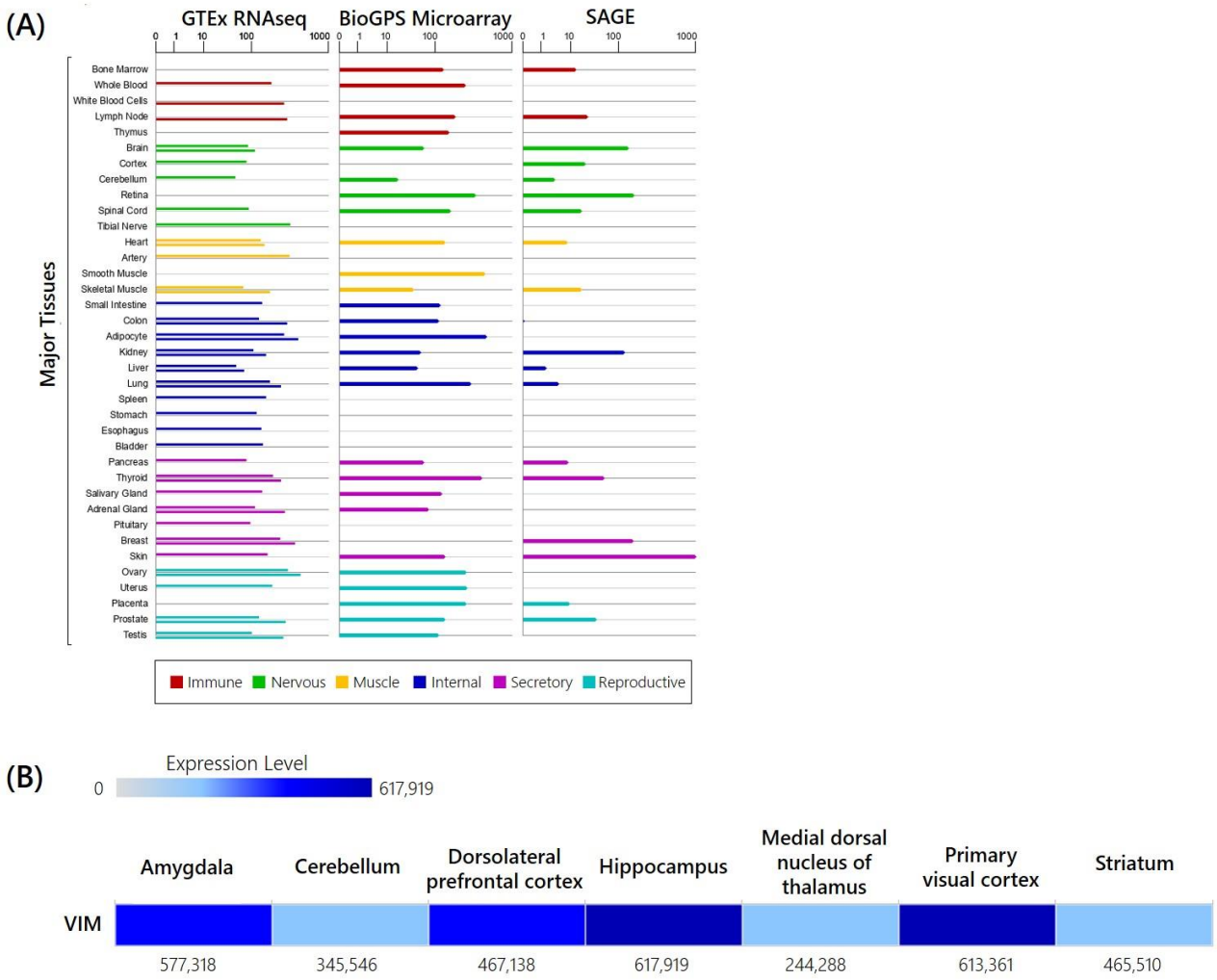


Figure 46. Expression of vimentin in human tissues. (A) Expression levels of vimentin in major tissues ranging from the immune system to the reproductive system. For GTEx RNA-seq, relative expression values were obtained from RNA sequencing of 51 normal human tissues. For BioGPS microarray, relative expression values were obtained from 76 normal human tissues hybridised against HG-U133A. For SAGE (Serial Analysis of Gene Expression), relative expression values were obtained from 19 normal human tissues.[259] (B) Expression levels of vimentin in various regions of the brain, data by Carlyle et al.[261]

Vimentin is highly abundant in the SVZ- and DG-derived murine NSCs. Immunostaining of vimentin in Figure 47 shows that the expression of vimentin is maintained throughout the proliferating and differentiating stages of the cells. However, there are changes in the morphology and distribution of vimentin among cells after 5 days of differentiation. Notably, vimentin is not found in mature neurons marked by beta-III tubulin (Tuj1). This corresponds with literature findings which indicated high expression of vimentin in neural precursor cells *in*

vivo.[262,263] In differentiating cells, vimentin and neurofilament subunits co-exist for some time, before vimentin is replaced completely by neurofilaments in mature neurons.[264]

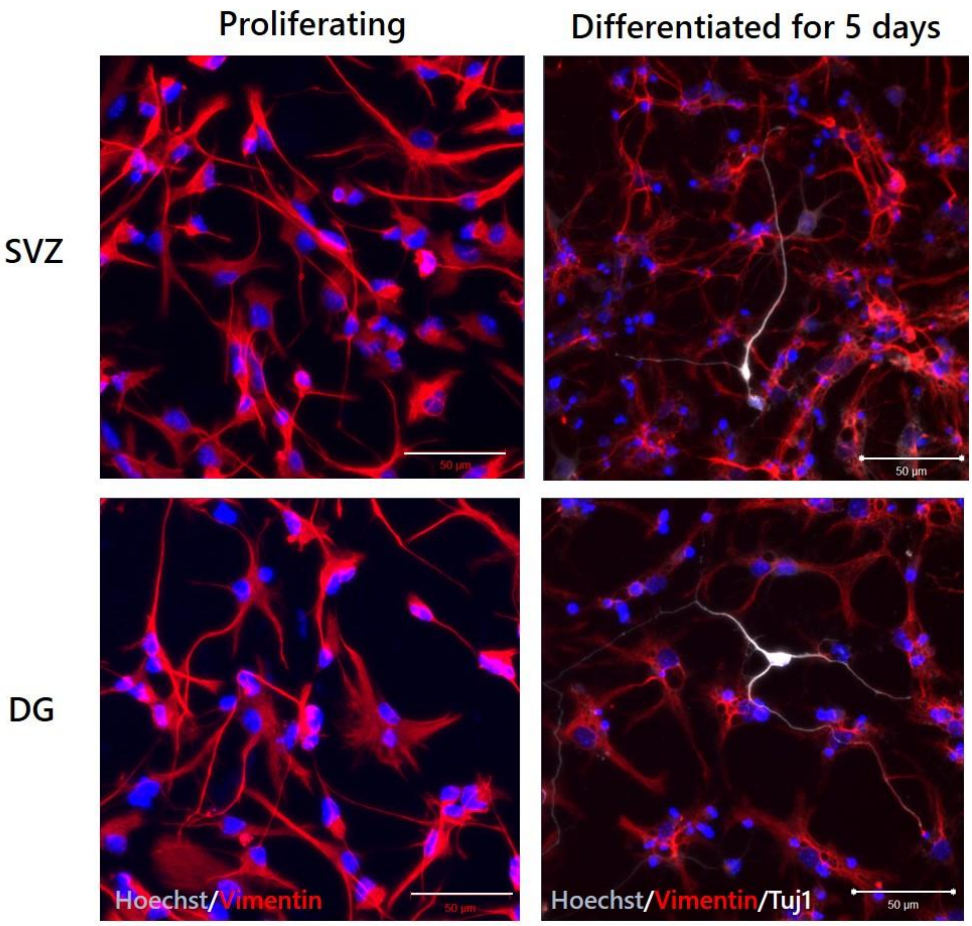


Figure 47. Immunohistochemical staining of vimentin (red), Hoechst (blue) and Tuj1 (white) in the SVZ- and DG- cells in the proliferating and the differentiated (5 days) stages. Scale bar indicates 50 µm.

5.2.2 Structure of Vimentin Filaments

Vimentin assembles into a network of filaments that spans across the cytoplasm, radiating from the juxtanuclear region to the cell periphery. Shorter filaments and non-filamentous units localise in the cytoplasm and in the extracellular matrix (ECM). The vimentin structure can be altered by subunit exchange,[265] cleavage into different sizes, post-translational modifications and interacting proteins.[266] The network of vimentin filaments undergoes significant reorganisation during cell division, cell spreading and motility.[267]

Vimentin assembly occurs in a stepwise manner, starting from dimers rapidly formed by the parallel alignment of 2 vimentin monomers. 2 dimers interact in an anti-parallel fashion to form soluble tetrameric complexes (Figure 48).[268] The spontaneous self-assembly can be induced *in vitro* by increasing the salt concentration. Lateral association of eight tetramers gives rise to a unit-length filament (ULF). Local activation of an ATP-dependent cofactor maintains the equilibrium between the tetrameric and ULF forms of vimentin in cells. ULFs anneal longitudinally via the coil 2 domains to form loosely packed, longer filaments. After further elongation, they compact radially to give rise to mature intermediate filaments (IFs) with a diameter of approximately 10 nm.[269]

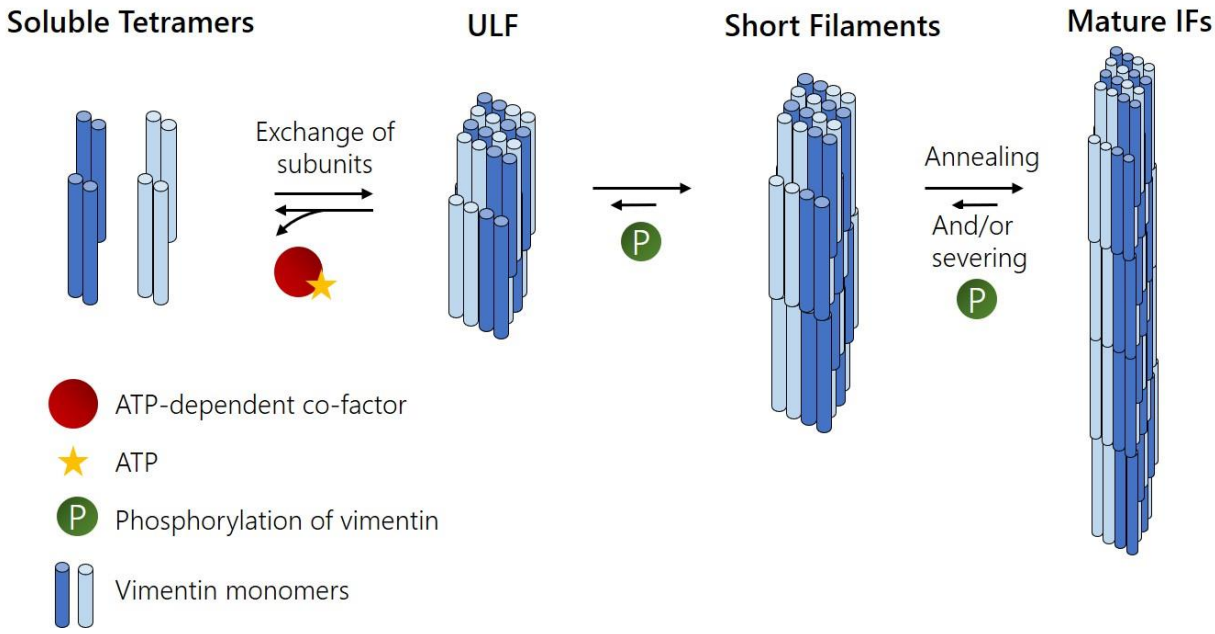


Figure 48. Schematic illustrating the assembly of vimentin filaments in cells.[265] Tetramers are formed by the assembly of 4 vimentin monomer units. The tetramers further assemble into ULFs, short filaments and mature IFs.

In cells, the vimentin filament network is highly dynamic and responds to changes in the cell environment. Filament assembly and reorganisation during mitosis are regulated by the phosphorylation of specific serine residues, mainly in the head domain of vimentin.[270] Key phosphorylation sites are further discussed in Section 5.5.1.

5.2.3 Functions of Vimentin

Vimentin has many diverse cellular roles, ranging from maintaining cell shape and integrity to regulating signalling pathways.[271] It is also involved in processes related to cell migration and adhesion, contributing to tissue regeneration and immune responses.[272] Upregulation of vimentin is required for the induction of epithelial-to-mesenchymal transition (EMT), a process in which epithelial cells acquire a mesenchymal phenotype along with a significant alteration in cell shape and motility.[273]

Vimentin also plays an important role in neuritogenesis. During initial neurite outgrowth in neural precursor cells, there is a transient increase in axonal vimentin filaments followed by increasing accumulation of phosphorylated neurofilaments.[274] Shea *et al.* found that an intracellular delivery of vimentin antisense oligonucleotides depleted vimentin synthesis and inhibited neurite initiation.[275]

5.2.4 Links to Diseases

Vimentin has been linked to various conditions including rheumatoid arthritis (RA), cataracts and cancer. Mutations and citrullinations of vimentin trigger the abnormal production of autoantibodies and result in sustained inflammation in RA patients.[276,277] Elevated levels of citrullinated vimentin contribute to the pathogenesis of RA and are associated with the severity of clinical phenotypes observed in patients.[278]

Among 90 patients diagnosed with congenital cataract, a common missense mutation in the coil 1B region of vimentin was found. The mutation resulted in a severe disruption of vimentin assembly and upregulation of proteasome activity *in vivo*. While this mutation led to the misfolding of vimentin in most mesenchymal cells, its disease phenotype was only restricted to cataract formation in the lens of human and mice.[279] Expression of phosphorylation-compromised mutant vimentin in mice was also found to accelerate the formation of age-related cataracts.[280]

Vimentin has been implicated in various aspects of cancer progression, including tumorigenesis, EMT, invasion and metastatic spread.[258] Overexpression of vimentin has been reported in various cancer types including breast cancer, pancreatic cancer and malignant melanoma.[281,282] This has been linked to an increase in motility and invasiveness of cancer cells, contributing to the metastasis of the cancer.[283]

5.2.5 Links to Neurogenesis

Vimentin plays a significant role in regulating proteostasis during the activation of quiescent NSCs. Morrow *et al.* used CRISPR/Cas9 to add a fluorophore to intracellular vimentin in primary murine hippocampal NSCs and found that vimentin cages surround misfolded and polyubiquitinated proteins in an aggresome structure.[284] In vimentin knockout (KO) mice, the lack of vimentin disrupted the recruitment of proteasomes to the aggresomes and inhibited protein degradation. Reduced clearance of aggregated proteins in NSCs hindered their exit from quiescence, leading to a decrease in proliferation and neurogenesis in vimentin KO mice.

Vimentin and glial fibrillary acidic protein (GFAP) are related intermediate filament proteins with similar functions linked to neural plasticity in health and disease. They are both upregulated during astrocyte activation in response to injury or neurodegeneration.[285] Larsson *et al.* found that hippocampal cell proliferation in 18-month-old GFAP- and vimentin-deficient ($GFAP^{-/-}Vim^{-/-}$) mice was 34% higher than wildtype controls.[286] The absence of intermediate filaments in astrocytes increased neurogenesis by promoting the proliferation and survival of NSCs in aged mice. Wilhelmsson *et al.* also demonstrated that hippocampal neurogenesis under basal conditions and after traumatic injury was increased in $GFAP^{-/-}Vim^{-/-}$ mice.[287] There was a reduction in endocytosis of Notch ligand Jagged1 in the $GFAP^{-/-}Vim^{-/-}$ astrocytes. This inhibited Notch signalling and subsequently increased neuronal differentiation in neurosphere cultures. While $GFAP^{-/-}Vim^{-/-}$ mice exhibited increased adult hippocampal neurogenesis, they showed normal locomotor behaviour and memory retrieval as compared to the wild-type controls.[285] Due to the functional redundancy between the related intermediate filament proteins, these

studies were done on mice lacking both GFAP and vimentin. It is hence difficult to conclude that modulating vimentin alone would be sufficient to affect neurogenesis.

Mutation of mitotic phosphorylation sites in vimentin ($VIM^{SA/SA}$) was found to increase the fraction of newly born and surviving neurons in the hippocampus of adult mice.[243] There was no significant difference in the appearance and distribution of the intermediate filament network in $VIM^{SA/SA}$ astrocytes, but the increased expression of GFAP was thought to compensate for the potential dysfunction of vimentin. 6 weeks after BrdU labelling, the percentage of newly born neurons (NeuN+BrdU+) in $VIM^{SA/SA}$ mice increased by 8% compared to the wild-type controls. This shows that the deficiency of phosphorylated vimentin increased the percentage of neurons formed and suggests that modulation of vimentin could affect neurogenesis.

While vimentin has been linked to neurogenesis in literature, there is some disagreement about whether vimentin deficiency increases or decreases neurogenesis. Discrepancies in the different studies could be due to the way they were performed and could also be indicative of the complex nature of neurogenesis. Neurogenesis is a combination of different processes, and the effects of vimentin knockout could be varied among the heterogeneous mix of NSCs, progenitor cells and differentiated cells in the neurogenic niche. This highlights the importance of elaborate target validation of vimentin to elucidate how modulation of this target affects neurogenesis in detail.

5.2.6 Vimentin-binding Small Molecules

Small molecule vimentin binders have been reported in literature, highlighting vimentin as a potential therapeutic target. Withaferin A (WFA, **86**) is an angiogenic natural product that covalently binds to vimentin through modification of cysteine-327 in the coiled coil 2B domain.[288] The covalent modification of vimentin by WFA disrupts the disulphide cross-linking between vimentin dimers and causes aggregation of vimentin filaments *in vitro* and *in vivo*. At concentrations above 2 μM, WFA caused significant perturbations in the IF assembly of vimentin and induced apoptosis.[289] Due to its inhibitive effects of cell motility and invasion in cancer cells, WFA also reduced angiogenesis and tumour growth *in vivo*.[290]

Bollong *et al.* discovered another vimentin-binding small molecule, FiVe1 (**87**), through a high throughput screen to find selective growth-inhibitors of FOXC2-positive cells.[291] Using a photoactivable FiVe1-PAP probe (**88**), the molecular target of FiVe1 was identified as vimentin. FiVe1 was found to promote vimentin disorganisation and phosphorylation, leading to mitotic disruption and growth inhibition of breast cancer cells and soft tissue sarcomas of various histological subtypes.

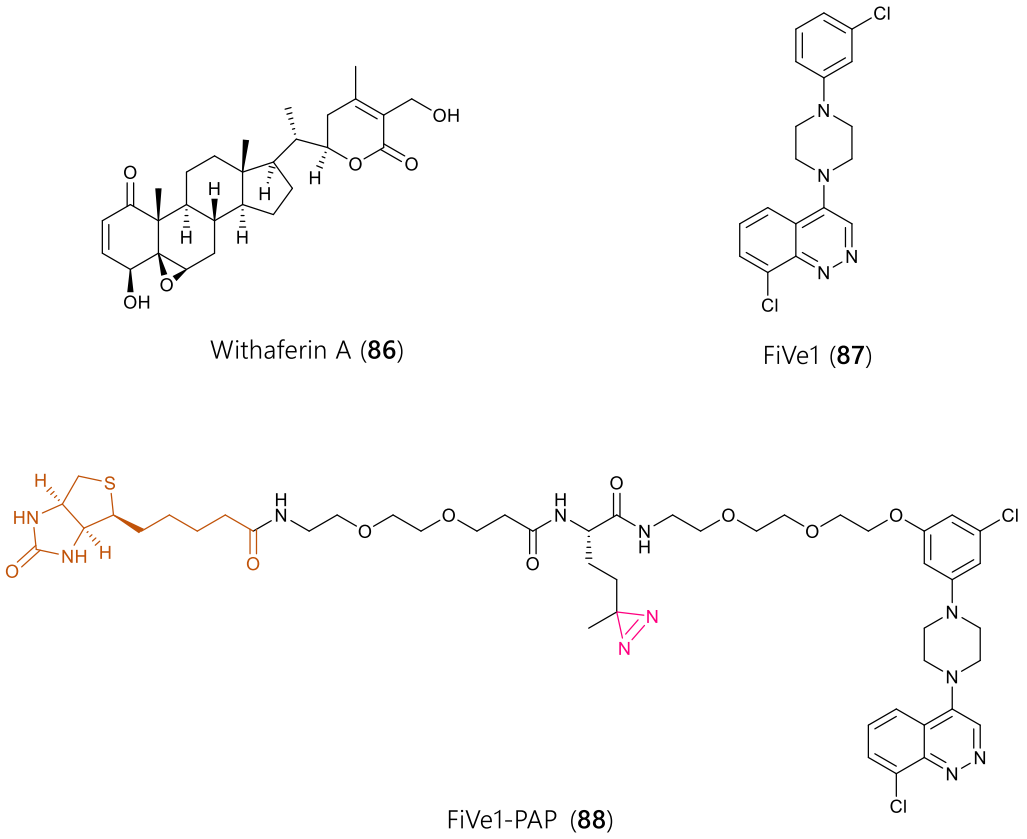


Figure 49. Structures of vimentin-binding small molecules reported in literature.

The two literature small molecules interact with vimentin in different ways but have similar effects in affecting vimentin filament assembly. To investigate if they had neurogenic effects, WFA (**86**) and FiVe1 (**87**) were tested in the neurosphere differentiation assay using SVZ- and DG-derived cells (Figure 50).

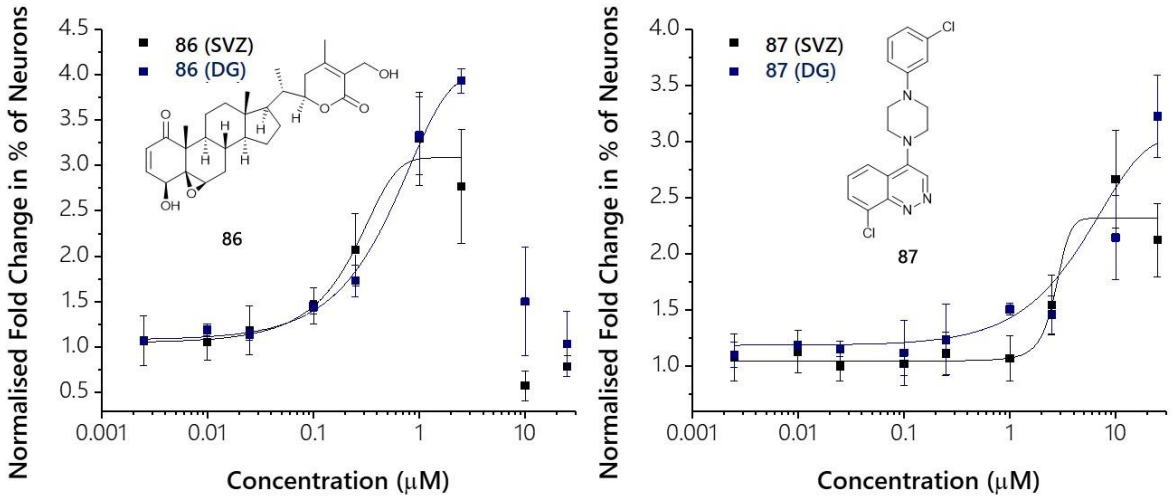


*Figure 50. Concentration-response curves for vimentin-binding compounds **86** and **87** when tested in vitro in SVZ- and DG- derived NSCs. Biological replicates, n = 2; Error bars indicate standard error of the mean.*

Both **86** and **87** showed neurogenic activity in the assay, resulting in at least a 2.5-fold increase in the percentage of neurons formed. **86** and **87** reduced the total cell count at high concentrations, which corresponded to their antiproliferative effects reported in literature. High levels of cell death were observed with covalent inhibitor **86** at concentrations above 2.5 μM, hence points above that concentration was not included in the concentration-response curve. The neurogenic activity of the vimentin-binding small molecules suggests that modulation of vimentin in the murine NSCs could affect the cell fate of NSCs and increase neurogenesis. This supports further target validation studies on vimentin as the molecular target of OXS-N1.

5.2.7 Related Intermediate Filament Proteins

Intermediate filament (IF) proteins related to vimentin were studied to determine if there is any non-specific interaction of OXS-N1 with structurally similar proteins. GFAP and nestin are related IF proteins which are expressed in NSCs residing in the SVZ and DG. GFAP and vimentin have a high sequence homology of 80% and can form heteropolymers with each other.[292] GFAP is highly expressed in mature astrocytes and upregulated during reactive gliosis along with vimentin.[293]

Nestin has a molecular weight of 170 kDa and an extremely long C-terminus of more than 1200 amino acids. It can only form filaments by co-assembling with type III proteins such as vimentin. Nestin promotes the disassembly of the IFs during mitosis when vimentin is phosphorylated at the Ser-55 position.[294]

To probe the specificity of OXS-N1 to related IF proteins which co-assemble with vimentin, proteins pulled down by active diazirine probe **77** were subjected to immunostaining by GFAP and nestin antibodies. Increasing concentrations of **15** was titrated against a fixed concentration of active probe **77** (5 μM), to identify any specific labelling of the related IF proteins (Figure 51).

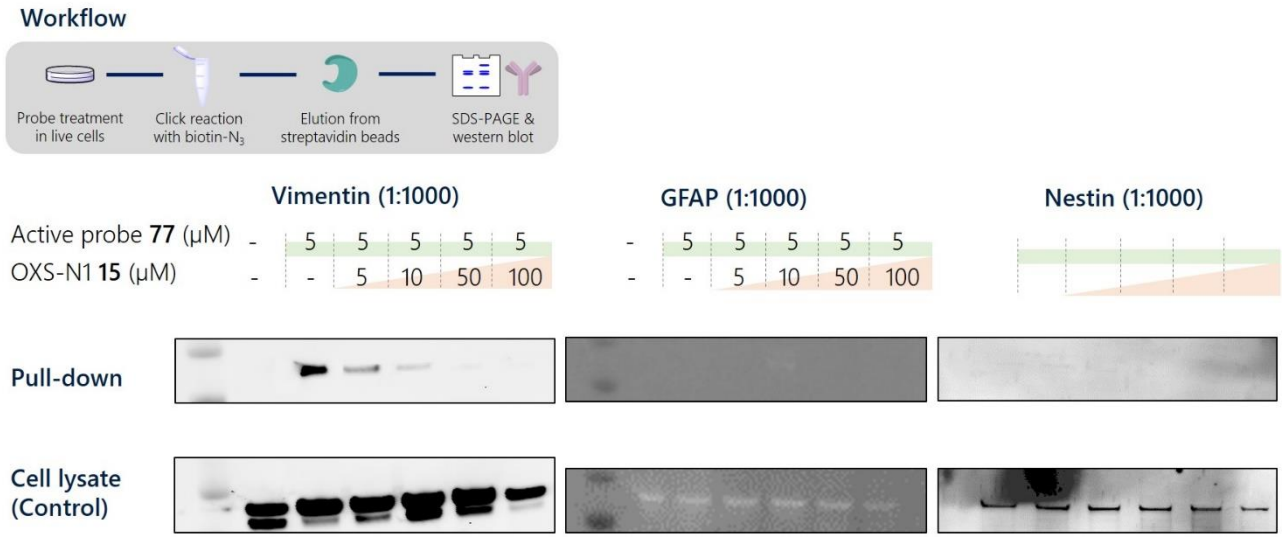


Figure 51. Western blot against related IF proteins, vimentin, GFAP and nestin, in pull-down samples from SVZ-derived NSCs.

GFAP and nestin were found to be expressed in the SVZ-derived NSCs, as the bands corresponding to the proteins were identified in the cell lysates by western blot. There was no specific labelling of GFAP and nestin by the active diazirine probe in the pull-down samples. This indicates that the probe was likely to be interacting with vimentin in a specific manner.

5.3 Biophysical Methods for Probing Protein-Ligand Interaction

To probe the protein-ligand interaction between vimentin and OXS-N1 *in vitro*, biophysical methods were employed. Recombinant human vimentin was obtained commercially in a

lyophilised form and reconstituted in 4 mM HCl before use. The protein was expressed in *Escherichia coli*, purified by HPLC and validated to be >95% in purity by SDS-PAGE. The recombinant vimentin protein was assumed to have minimal post-translational modifications as *E. coli* expression systems are typically unable to process eukaryotic post-translational modifications such as glycosylation and phosphorylation.[295] This was later confirmed using intact protein mass spectrometry (Section 5.3.2).

5.3.1 WaterLOGSY

Water-ligand observed via gradient spectroscopy (waterLOGSY) has been previously described in Section 1.7.1.4 as an NMR method to probe protein-ligand interaction. WaterLOGSY allows for identification of binders and non-binders of protein through the nuclear Overhauser effect (NOE). Small molecules which are non-binders of the protein only interact with the bulk water and undergo very rapid tumbling in water, resulting in positive NOEs with water. Small molecules which bind to the protein interact with the water via water-ligand-protein or protein-ligand complexes. The ligand-protein complexes are much larger in size and rotate more slowly, resulting in negative NOEs with water. WaterLOGSY spectra of OXS-N1 (**15**) and inactive analogue **29** were acquired on a Bruker AVIII 600 instrument (Figure 52).

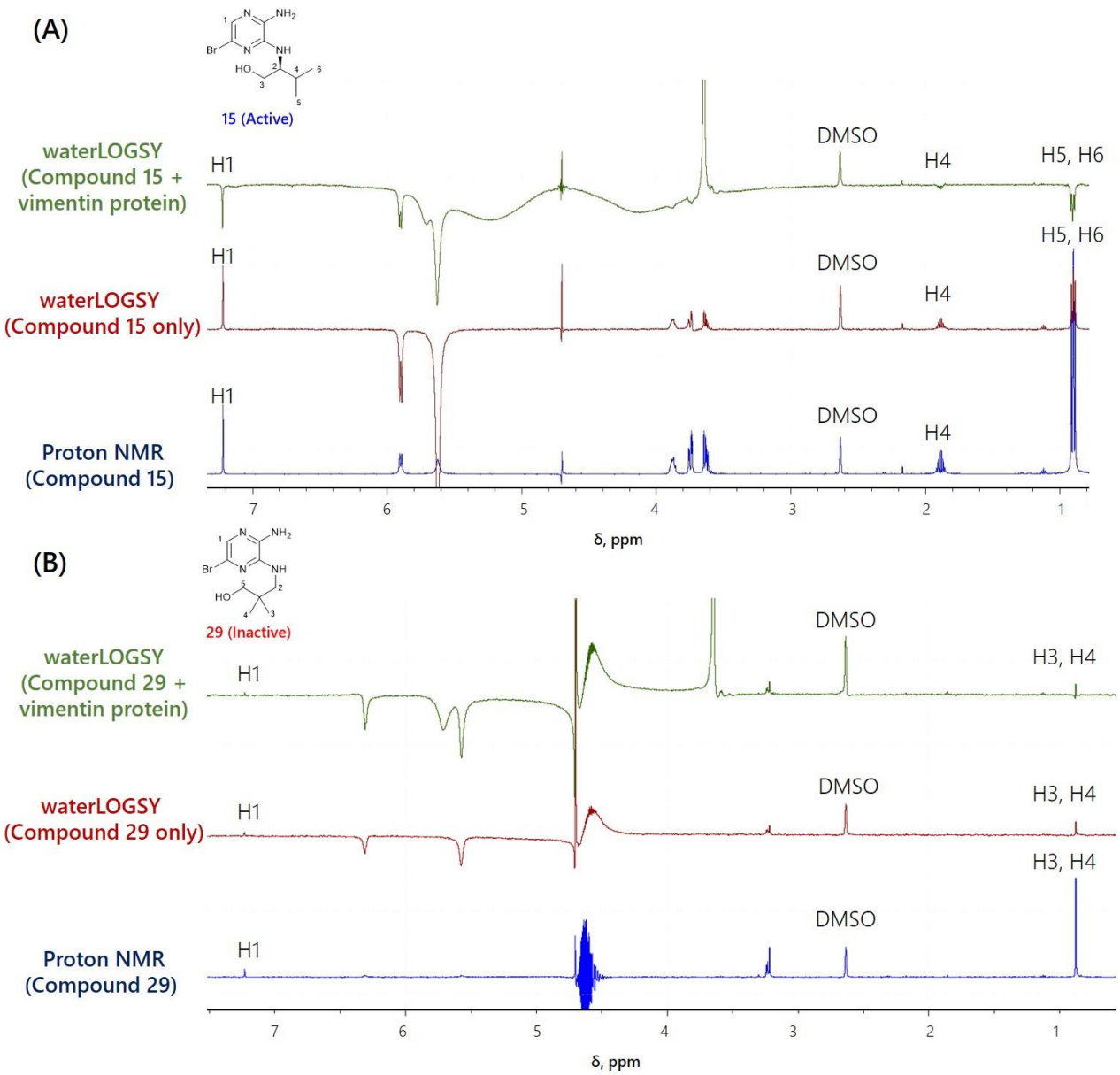


*Figure 52. WaterLOGSY and proton NMR spectra of (A) active compound OXS-N1 (**15**) in presence and absence of recombinant vimentin protein and (B) inactive compound **29** in presence and absence of recombinant vimentin protein. The spectra were kindly acquired and processed by Dr Carole Bataille (Prof Angela Russell group, University of Oxford).*

WaterLOGSY spectra of the compounds in absence of the protein shows the degree of compound aggregation and the suitability of the technique to probe ligand-protein interaction. Compounds which aggregate in aqueous buffer tend to give rise to false positives.[296] Both compounds **15** and **29** were water soluble and showed very little aggregation in the buffer (D_2O:PBS 1:10). Most of the protons had positive signals in absence of the protein. The protons which exhibited negative signals are the labile protons from the amino and hydroxyl groups. WaterLOGSY was deemed as a suitable technique to probe ligand-protein interactions for compounds **15** and **29**.

The compounds were added to the solubilised vimentin protein in 25x excess. The waterLOGSY spectrum for **15** showed that the protons (H1, H4, H5 and H6) exhibited negative signals, indicating binding to protein. This provides evidence that vimentin is a direct binding partner of OXS-N1. Comparable protons from the inactive analogue (H1, H3 and H4) showed positive signals, indicating that inactive compound **29** is a non-binder of vimentin. The enantiomer **28**, which showed neurogenic activity in the neurosphere differentiation assay, also exhibited positive binding through waterLOGSY (Appendix 4). The positive correlation of compound activity to ligand-protein binding supports the hypothesis that vimentin is a potential molecular target that contributes to the biological activity of the compounds.

5.3.2 In-gel Fluorescence & Protein Mass Spectrometry (MS)

Mass spectrometry of intact protein was explored to further characterise the ligand-protein complexes. Diazirine probes **77** and **78** were incubated with the recombinant protein and irradiated with UV to induce covalent crosslinking. A click reaction was performed with TAMRA-azide and in-gel fluorescence was used to visualise the binding (Figure 53).

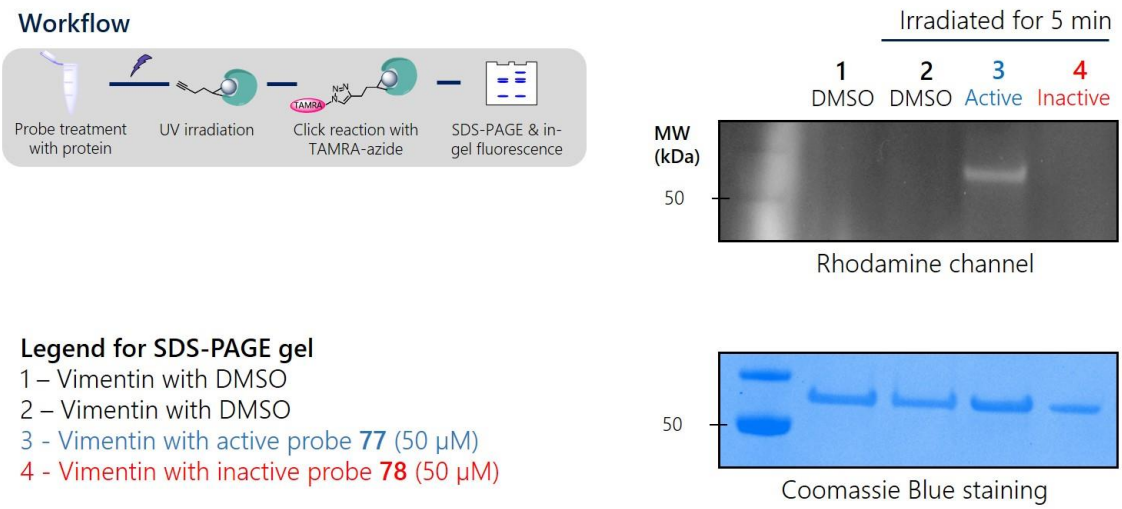


*Figure 53. SDS-PAGE gel of probe-protein conjugates labelled with TAMRA-azide. Vimentin recombinant protein (10 µM) was treated with diazirine probe **77** or **78** (50 µM). After UV irradiation, the probe-protein conjugates were subjected to click reaction with TAMRA-azide. In-gel fluorescence shows protein labelled with TAMRA, and Coomassie Blue staining shows equal amounts of protein loading.*

A fluorescent band in the samples treated with diazirine probe **77** indicates binding of the active probe to vimentin. No fluorescence labelling was observed with inactive probe **78**, showing that the inactive probe does not bind to the recombinant protein non-specifically. This corresponds to the results observed in the waterLOGSY experiments, which indicated that the inactive gem-dimethyl analogue (**29**) did not interact with vimentin. LC-MS/MS of the intact protein was acquired on a Waters Xevo G2-XS spectrometer to characterise the probe-protein conjugates (Figure 54).

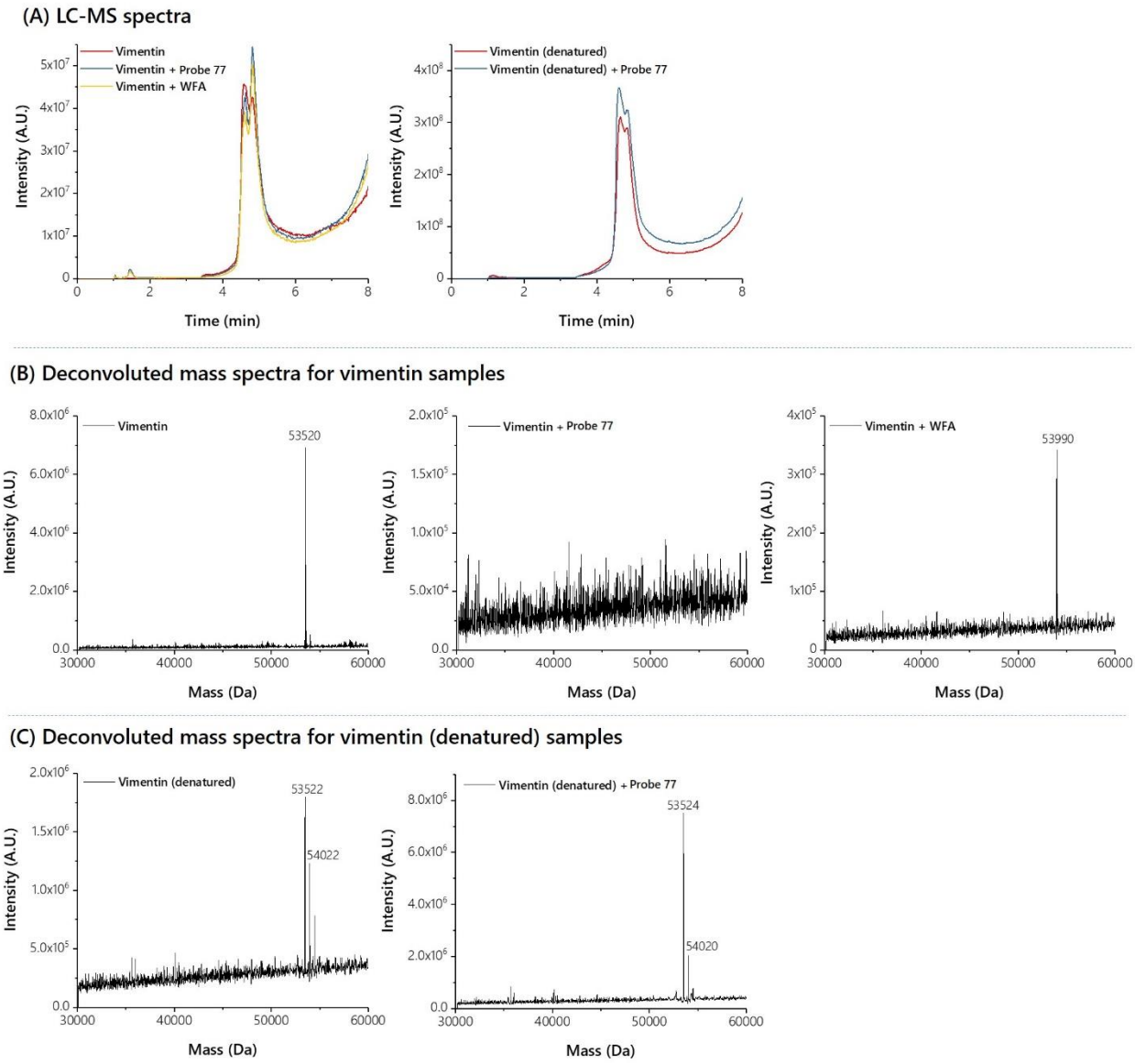


*Figure 54. LC-MS spectra of vimentin protein and ligand-protein conjugates. (A) LC-MS spectra obtained for the vimentin samples. (B) Deconvoluted mass spectra (between 30000 and 60000 Da) for vimentin samples: unmodified, probe **77**-modified and WFA-modified. (C) Deconvoluted mass spectra for vimentin samples in denaturing solvent: unmodified and probe **77**-modified.*

The LC-MS chromatogram of vimentin in PBS showed a main peak at 4.5 min followed by a shoulder peak. LC-MS chromatograms of vimentin samples treated with probe **77** and WFA (**86**) showed a main peak that is slightly shifted at 4.9 min (Figure 54A), indicating some modifications to the protein. The deconvoluted mass spectrum of vimentin had a main peak of 53520 Da, which corresponds to the mass of the primary protein sequence of human vimentin with no post-translational modifications. WFA was used as a positive control for covalent modification of vimentin. The mass of the WFA-vimentin conjugate was found to be 53990 Da, with a mass change of 470 Da corresponding to the molecular weight of WFA. However, the mass of the probe-modified vimentin conjugate could not be deconvoluted and the expected mass change could not be visualised. This was possibly due to multiple modifications on the protein, leading to a noisy spectrum that could not be easily deconvoluted by the algorithm.[297]

Vimentin was solubilised in a denaturing solvent containing 50% methanol and 0.1% trifluoroacetic acid.[298] When treated with diazirine probe **77**, there was no change in the main peak observed in the LC-MS spectrum. The deconvoluted mass spectrum for the probe-treated sample indicated the presence of the unmodified protein, with no modified protein observed. This demonstrates that the probe cannot bind to vimentin in its denatured form and does not interact non-specifically with the protein. Taken together with the waterLOGSY and in-gel fluorescence analysis, this supports the 3D structure of vimentin being important for the binding of the probe.

As the mass of the probe-vimentin conjugate could not be determined by LC-MS/MS, another MS technique was explored. Matrix-assisted laser desorption/ionisation-time of flight (MALDI-TOF) MS was chosen as an alternative for intact protein analysis as its performance is less affected by the presence of contaminants, salts and detergents and the heterogeneity of the sample.[299]

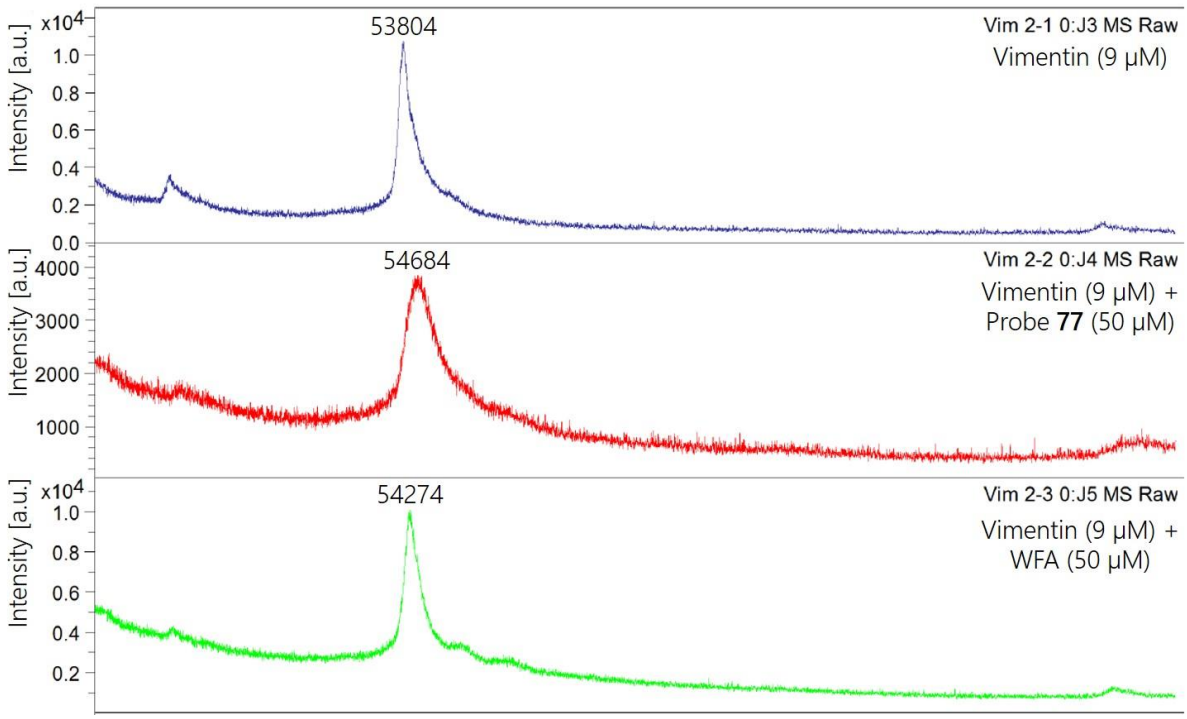


Figure 55. MALDI-TOF mass spectra of vimentin and modified vimentin conjugates obtained.

In the MALDI mass spectrum of the probe-vimentin sample, a mass peak was observed at 54864 Da, indicating a modification on the vimentin protein (Figure 55). The observed mass change of 880 Da corresponded to 2 molecules of the probe. This could suggest double modification on the protein. The broad mass peak could also suggest a mixture of mono- and di-substituted conjugates in the sample. As the probe was treated in 5x excess of the recombinant protein, a lower probe to protein ratio could be used to observe mono-substitution on the protein.

To determine the binding site of the probe, the probe-protein conjugates were subjected to tryptic digest and the peptides were identified by mass spectrometry. The predicted modification was calculated according to the mass of the probe with a loss of the diazirine group. PEAKS software was used to search for the potential probe modification of 438.13 Da among the peptides identified corresponding to vimentin (Figure 56).

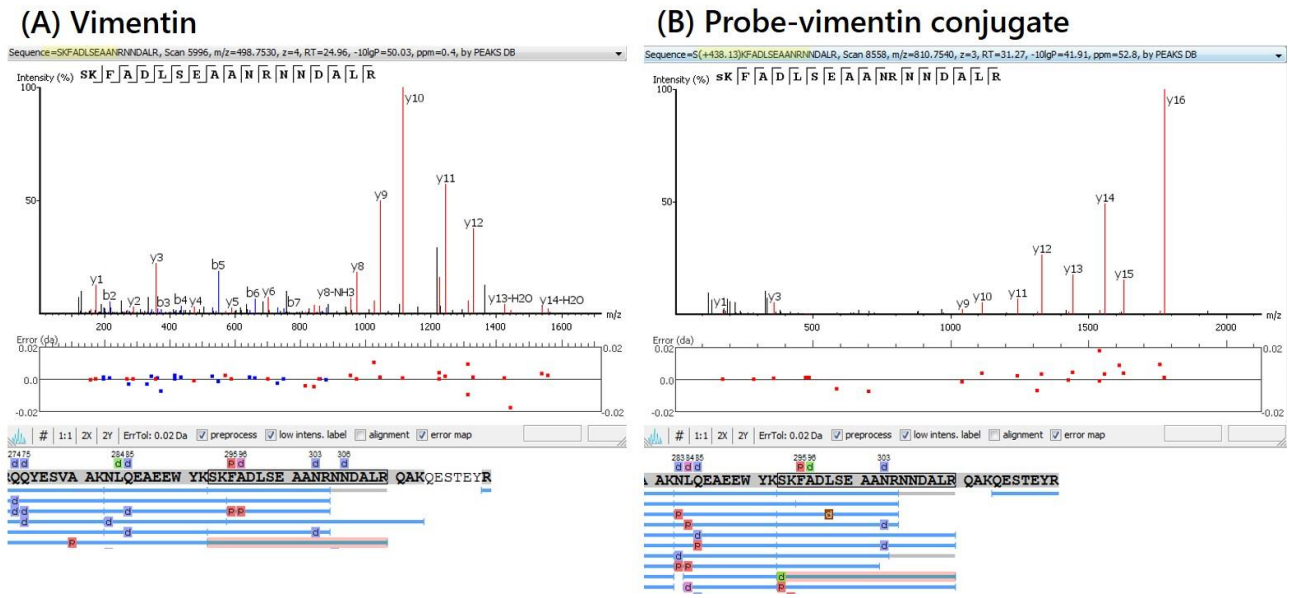


Figure 56. PEAKS analysis of peptide SKFADLSEAANRNNDALR in (A) vimentin only and (B) probe-vimentin conjugate.

Among all three replicates of the probe-vimentin conjugate samples, a potential site of modification was observed at serine residue 293. The peptide sequence SKFADLSEANRNNDALR was found to have a modification of 438.13 Da only in the probe-vimentin samples, corresponding to the addition of the probe with a loss of N_2. The photoaffinity-labelled peptide was identified with a -10logP value of 41.91, which is above the threshold value of 20 for a high confidence peptide match.[300]

The modified sequence is part of the coil 2 domain of the vimentin protein. The coil 2 domain contains a rigid coiled coil structure that is important for the mechanical properties of vimentin.[301] The MS analysis suggests that the contact region of the probe is at the coil 2 domain of vimentin. However, whether the contact region corresponds to the binding site of OXS-N1 would depend on the proximity and the orientation of the photoaffinity group when the probe binds to the binding site.[302]

Other spectroscopic methods could be used to characterise the ligand-protein binding domain. The binding epitope of the ligand bound to the protein could be determined using saturation transfer difference (STD) NMR spectroscopy.[303] Ligand protons in close contact to the protein would exhibit strong STD signals, and identification of these important binding epitopes would

provide information on the ligand binding orientation. Differential hydrogen/deuterium exchange (HDX) coupled with mass spectrometry could be used to further study the ligand-protein interactions and characterise the ligand-binding pocket.[304] It could provide more information on changes in dynamics upon ligand binding, which may contribute to the understanding of the downstream effects of OXS-N1 treatment. X-ray crystallography could also be employed to further validate the ligand-protein binding interactions at an atomic resolution.[305]

5.3.3 Surface Plasmon Resonance (SPR)

While waterLOGSY and mass spectrometry techniques were very useful to probe the ligand-protein interaction, it was difficult to quantify the binding affinity using these techniques. To determine the dissociation constant (K_D) of OXS-N1 binding to vimentin, surface plasmon resonance (SPR) was explored. His-tagged human recombinant vimentin was immobilised on the surface of a sensor chip (CM5) using amide coupling. Compound solutions were passed over the immobilised protein and ligand-protein interactions are recorded as response units (RU) (Figure 57).

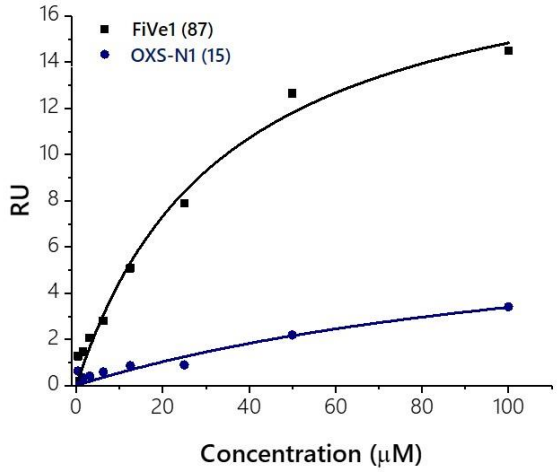


Figure 57. Concentration curves of FiVe1 and OXS-N1 when tested in SPR experiments with immobilised vimentin. RU: Response units. SPR experiments were kindly run by Dr Mikhail Kutuzov (Sir William Dunn School of Pathology, University of Oxford), and samples prepared by Dr Sébastien Galan (Prof Russell group, University of Oxford).

FiVe1 was chosen as a positive control and tested at 9 concentrations from 390 nM to 100 μM. The K_D of FiVe1 was determined to be 33.7±8.2 μM. This was surprisingly high as the IC_{50} of FiVe1 was reported to be 0.44 to 1.33 μM in various cancer cell lines.[291] The K_D of OXS-N1 was determined to be 133.1±9.3 μM. This K_D value was also much higher than expected and exceeds the active concentration range of OXS-N1 in the biological assays. This suggests poor binding of the ligands to the immobilised monomeric vimentin on the chip.

The high K_D values indicate a potential limitation of using SPR to probe ligand-protein interactions for vimentin. The native conformation of vimentin might have changed upon immobilisation on the sensor chip. The immobilisation process might have also obscured the binding domains of vimentin, hindering the access of the ligands to the binding site. To address this problem, the ligands could be immobilised on the sensor chip instead. The biotinylated probes could be used for immobilising the ligand in a specific orientation on the chip. The filament structure of the vimentin protein is also uncharacterised in the buffer used for the SPR experiments, and variations in the assembly state of vimentin in the buffer could lead to changes in the binding responses at the sensor surface. More optimisation would have to be done on the buffer and immobilisation strategies to further pursue SPR as a method for determining K_D values of ligands binding to vimentin.

5.3.4 Thermal Shift Assay (TSA)

Thermal shift assay (TSA) is described as a method to characterise ligand binding by observing shifts in the protein melting curves in Section 1.7.1.1. SYPRO orange was used as a fluorescence dye that binds to hydrophobic surfaces. In solution, its fluorescence is quenched by water. As the temperature is increased, more of the protein unfolds to expose hydrophobic regions which SYPRO orange can bind to. This results in an increase in dye fluorescence which drops off as the temperature is raised further due to protein aggregation (Figure 58A). The melt temperature (T_m) is determined from the inflexion point on the melt curve. Ligand binding typically increases protein stability and causes an increase in the T_m value.

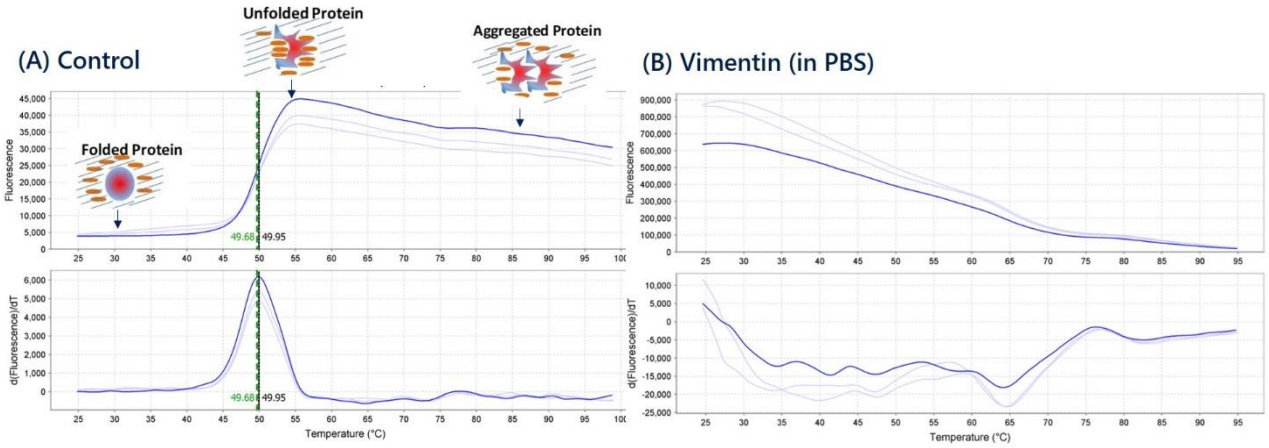


Figure 58. Thermal melt curves and derivative curves of the control protein (ThermoFisher TSA kit) and vimentin (in PBS).

The thermal melt curve of vimentin in PBS buffer (Figure 58B) showed an initially high fluorescence signal that decreased as the temperature was increased to 95 °C. The high fluorescence suggests that the SYPRO orange fluorescence dye is bound to exposed hydrophobic sections of the protein. There was a high degree of aggregation as the protein was heated, causing the dye to be displaced.

Buffer conditions are known to affect protein stabilisation in the TSAs. The lower than expected stability of vimentin could be due to the poor suitability of PBS as the buffer. Vimentin was likely to be present in PBS as a mixture of monomers, dimers and tetramers. The *in vitro* assembly of

vimentin filaments can be initiated by increasing the ionic strength of the solution.[255] The assembly of vimentin filaments would lower the exposure of hydrophobic sections in the rod domain of the monomers and improve the stability of the protein.

2 buffer systems were explored: (i) tetramer buffer (2 mM sodium phosphate) and (ii) IF assembly buffer (2 mM sodium phosphate, 200 mM potassium chloride). The structures of vimentin in these buffer systems have been characterised extensively by Mücke *et al.*[306] Vimentin in 2 mM sodium phosphate solution was a homogenous tetramer species of approximately 202,000 Da. When the ionic strength of the solution was increased with the addition of 200 mM potassium chloride, vimentin ULFs are formed with an average diameter of 9.4 nm. The melt curve of vimentin in these buffers showed a lower initial fluorescence intensity, allowing for the melt temperature (T_m) of vimentin to be determined (Table 8).

Table 8. T_m values of vimentin (1 μM) in the tetramer and IF assembly buffers when incubated with vimentin-binding compounds OXS-N1, WFA and FiVe1 (500 μM).

Compound	T_m in tetramer buffer (°C)	T_m in IF assembly buffer (°C)
DMSO (vehicle control)	51.15	57.99
OXS-N1 (**15**)	52.04	58.14
WFA (**86**)	52.34	57.84
FiVe1 (**87**)	38.81	40.59

The T_m of vimentin increased from 51.15 to 57.99 °C in the IF assembly buffer, which corresponds to an increase in protein stability as the vimentin tetramers assemble into well-packed filaments. There was a slight increase in T_m (~ 1 °C) when vimentin was incubated with OXS-N1 and WFA, possibly indicating some stabilisation of the protein with the ligand binding. However, as the increase was modest even with a high concentration of the compound (500 μM), it would be difficult to determine the binding affinity by varying the concentration. The TSA method was found to be unsuitable to determine the binding affinity of OXS-N1 to vimentin.

Interestingly, the T_m of vimentin showed a drastic decrease with FiVe1 incubation, dropping to 38.81 and 40.59 °C in the tetramer and IF assembly buffers respectively. This indicates

destabilisation of the protein,[307] which corresponds with the effects of the compound on disrupting vimentin filament assembly. As OXS-N1 did not show such effects, it is likely to be binding to vimentin differently compared to FiVe1.

As the T_m of vimentin is quite high, the TSA method was unsuitable for determining the K_D of ligand binding. The association of the ligand to the protein could be measured using a fluorescence polarisation (FP) assay instead. Advantages of the FP method include the measurement of the ligand-protein interaction in solution without significant perturbation and the ease of quantification using a microplate reader.[207] BODIPY-tagged OXS-N1 derivative **82** could be used as the fluorescently-labelled ligand required for the assay. The K_D of OXS-N1 could be determined through ligand competition with the fluorescent probe in the FP assay.

5.4 Target Visualisation

5.4.1 Co-localisation with Fluorescent Probe

Immunostaining was used to visualise vimentin in the SVZ- and DG-derived NSCs by confocal imaging. Fluorescence labelling by the BODIPY-tagged derivative **82** was used to identify the localisation of OXS-N1 for comparison (Figure 59).

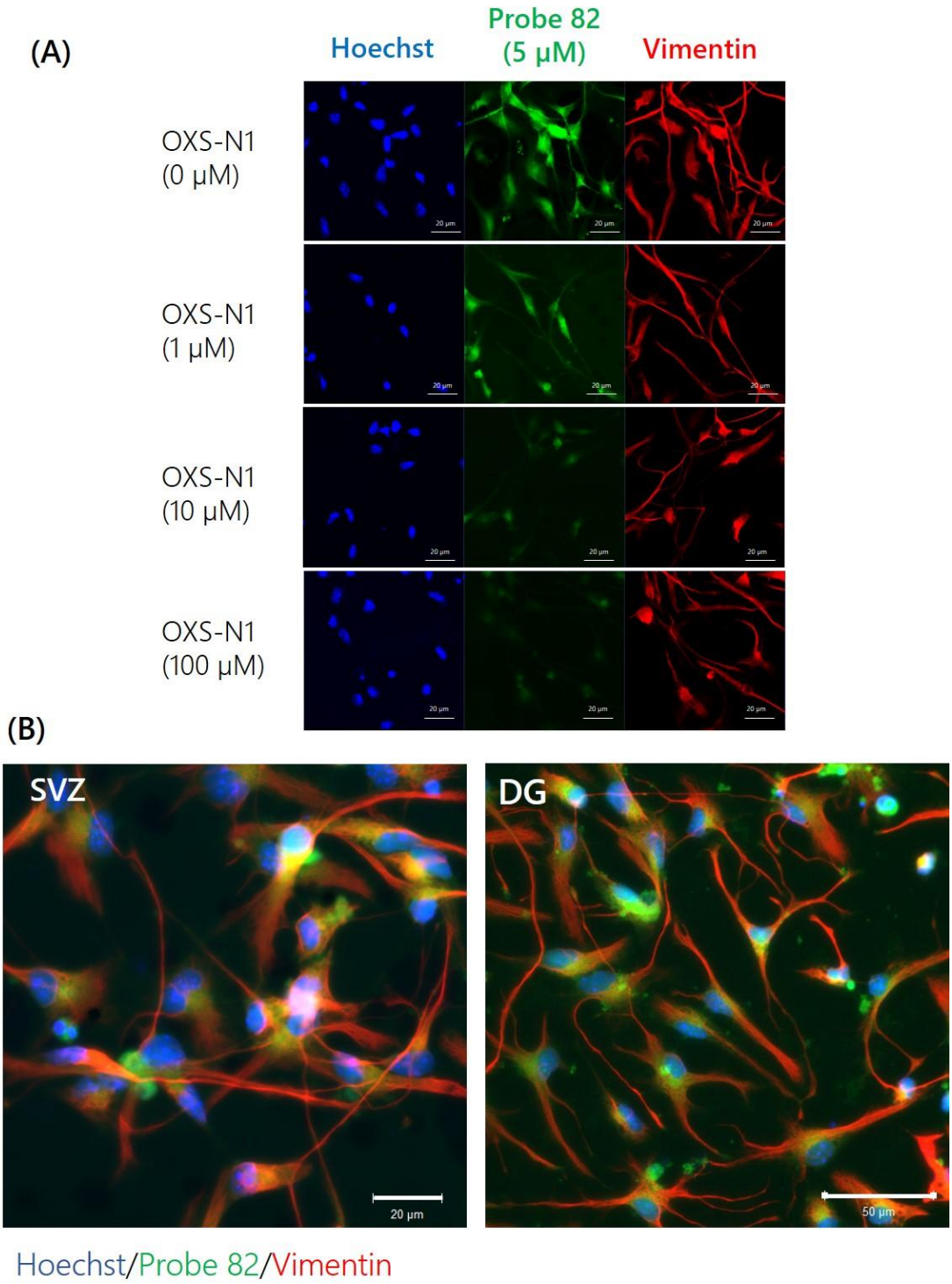


*Figure 59. Confocal images of NSCs stained with hoechst (blue), BODIPY probe **82** (green) and vimentin (red). (A) Images showing the localisation of the BODIPY-probe corresponds with the staining of the vimentin filaments in the SVZ-derived NSCs. With increasing concentrations of OXS-N1, the fluorescence labelling by **82** is outcompeted. (B) Higher magnification images showing the co-localisation of probe **82** with stained vimentin filaments in SVZ- and DG-derived NSCs.*

Vimentin was found to be primarily localised in the cytoplasm, exhibiting a perinuclear distribution which extends towards the cell periphery. Probe **82** shows a similar localisation in the cells, with some accumulation in the perinuclear area, which can be outcompeted by increasing concentrations of the parent compound OXS-N1 (Figure 59A). Higher magnification

images of the SVZ- and DG-derived cells show good overlap of the BODIPY probe with the stained vimentin filaments (Figure 59B).

5.4.2 Effects of Compound Treatment on Assembly of Vimentin Filaments

As the literature vimentin-binding compounds were reported to have effects on the structure of vimentin filaments, a time-course imaging of vimentin filaments after treatment with various vimentin-binding compounds was carried out (Figure 60 (SVZ), Appendix 5 (DG)).

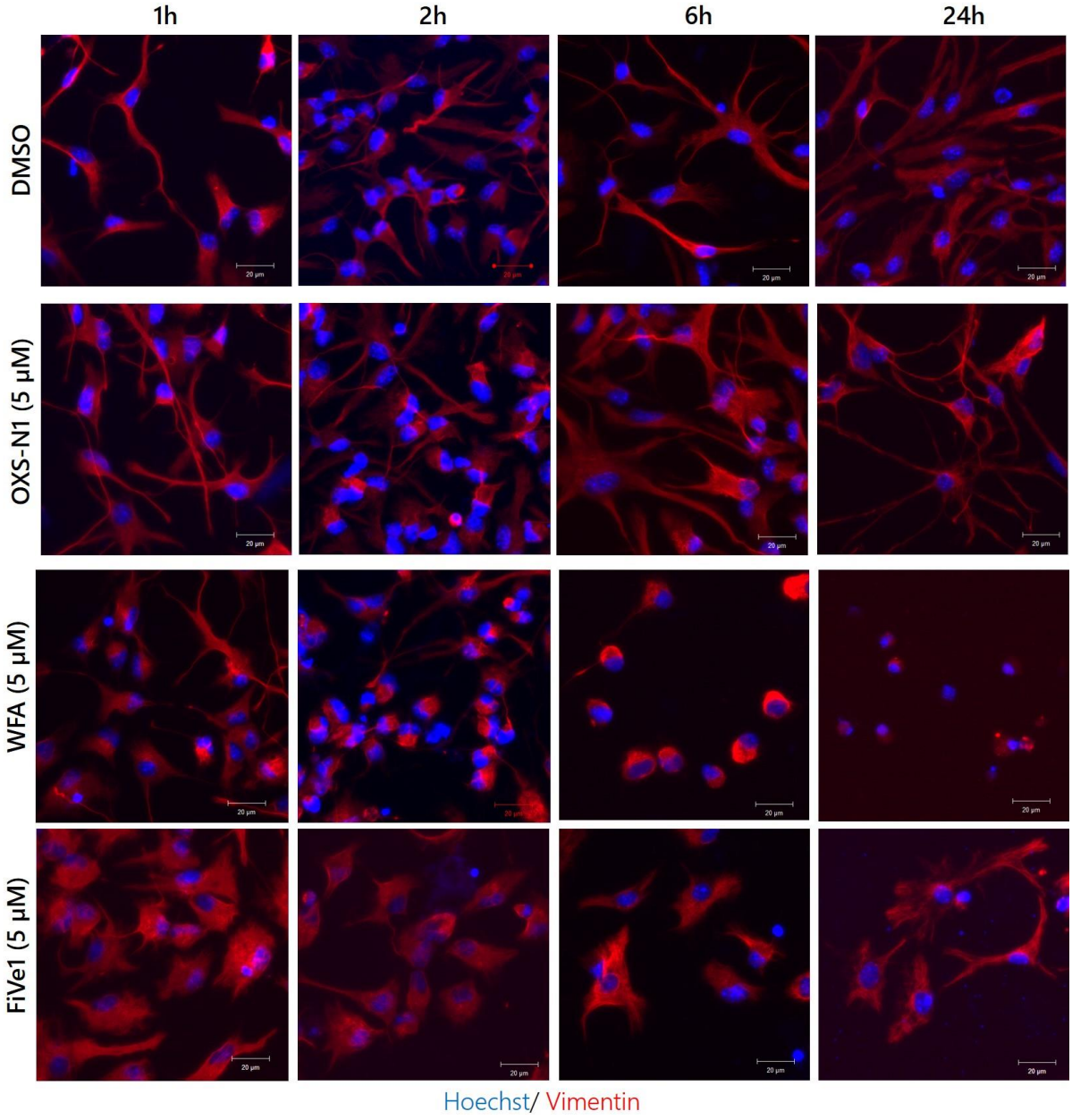


Figure 60. Immunostaining of vimentin in SVZ-derived NSCs at various timepoints after treatment with DMSO (0.1%v/v), OXS-N1, WFA and Five1. Staining: Hoeschst (blue), vimentin (red).

Cells treated with WFA showed an aggregation of vimentin filaments in the perinuclear region after 2 h. This is consistent with literature reports that WFA binding caused polymeric forms of vimentin to condense in the perinuclear region and resulted in changes to cell shape and behaviour.[308,309] Cells treated with FiVe1 showed a drastic disassembly of vimentin filaments after 1 h. The collapse of the filamentous structure of vimentin with FiVe1 treatment was associated with the loss of mesenchymal morphology and mitotic defects.[291]

OXS-N1 treatment did not affect the assembly of vimentin filaments in both the SVZ- and DG-NSCs as compared to the vehicle control (DMSO). The mechanism in which OXS-N1 binds to vimentin and modulates its structure and function differs from the other vimentin-binders tested. WFA and FiVe1 resulted in major disruption of vimentin filaments, which contributed to the cytotoxic effects observed in the neurosphere differentiation assay. In contrast, the structure and organisation of vimentin filaments were largely unaffected with OXS-N1 treatment.

5.5 Investigation of Vimentin Post-Translational Modifications

5.5.1 Phosphorylation of Vimentin

Phosphorylation is a key post-translational modification (PTM) that contributes to the assembly and disassembly of vimentin filaments, and subsequent downstream signalling events. Disassembly of vimentin filaments is crucial for cytokinesis. Phosphorylation of vimentin at specific residues during mitosis causes filament disassembly and subsequent segregation of vimentin between the newly formed daughter cells.[310] Major serine phosphorylation sites have been identified on vimentin (Table 9). Phosphorylation of vimentin by protein kinase A (PKA) at Ser-38 and Ser-72 was found to decrease filament formation *in vivo*.[311] Aurora B, rhoA kinase (ROCK) and cyclic-dependent kinase 1 (Cdk1) regulate vimentin filament separation during mitosis through cleavage furrow-specific phosphorylation.[312,313] In contrast to other protein kinases, phosphorylation of vimentin by mitogen-activated protein kinase-activated protein kinase-2 (MAPKAP-K2) at Ser-38, Ser-55 and Ser-82 was found to serve as a phosphate reservoir and had no effects on filament assembly.[314]

Table 9. Major phosphorylation sites in vimentin, modified by protein kinases: protein kinase A (PKA), protein kinase C (PKC), mitogen-activated protein kinase-activated protein kinase-2 (MAPKAP-K2), RhoA kinase (ROCK), polo-like kinase (Plk1), aurora B and cyclin-dependent kinase 1 (Cdk1).

Phosphorylation Site	Protein Kinases
Ser-38	PKA,[311] PKC, ROCK,[315] MAPKAP-K2[314]
Ser-55	PKA, Cdk1, MAPKAP-K2[314]
Ser-71	PKA, ROCK[315]
Ser-72	PKA,[311] Aurora B[313]
Ser-82	Plk1, CaMKII, MAPKAP-K2[314]

Commercially available antibodies against phosphorylated vimentin for serine residues 38, 56, 72 and 82 were used for immunoblotting. The levels of phosphorylated vimentin in the cells after 24 h incubation with compounds OXS-N1 (**15**), inactive analogue **29**, WFA (**86**) and FiVe1 (**87**) were quantified by normalising against the beta-actin control.

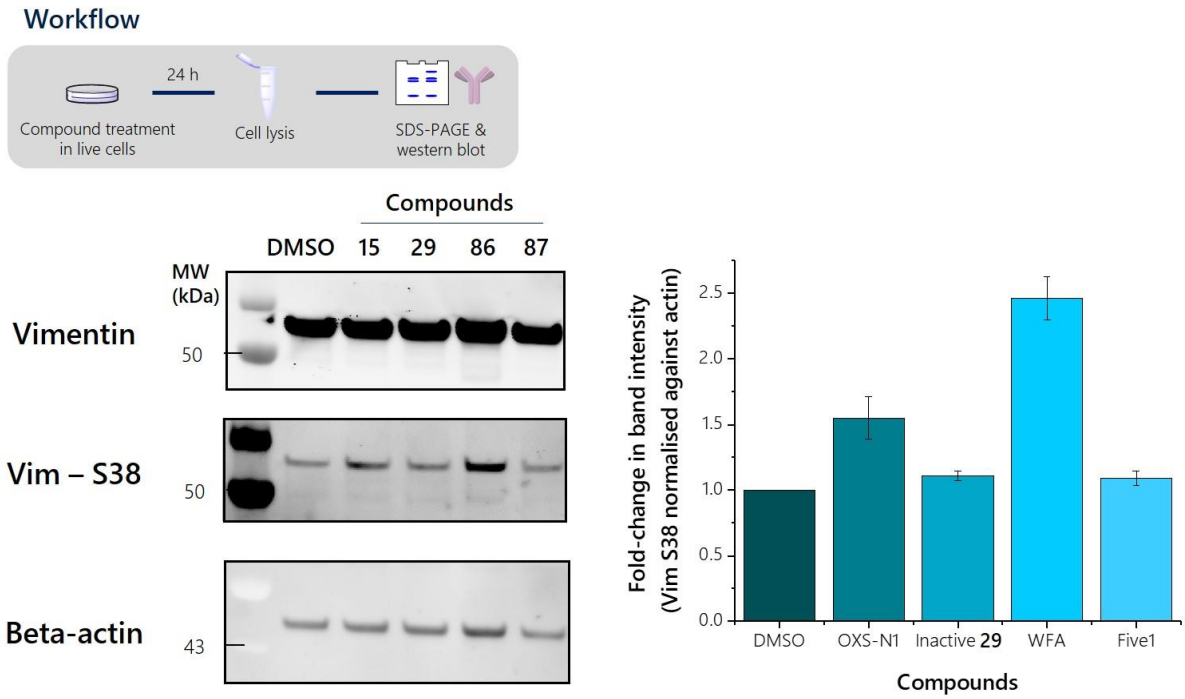


*Figure 61. Western blotting against vimentin, phosphovimentin-S38 and beta-actin. Fold-change in band intensity of phosphovimentin-S38 was normalised against beta-actin and compared across treatment with compounds OXS-N1 (**15**), inactive analogue **29**, WFA (**86**) and FiVe1 (**87**).*

The levels of vimentin after 24 h of compound treatment remained relatively similar. The levels of phosphorylation in Ser-56, 72 and 82 were very low compared to Ser-38 and there were no major changes with compound treatment. Changes in phosphorylation levels of Ser-38 were observed with WFA and OXS-N1 treatment (Figure 61). WFA resulted in a 2.5-fold increase in

phosphorylation of vimentin at Ser-38. OXS-N1 treatment resulted in a 1.5-fold increase in phosphorylated Ser-38, suggesting that its neurogenic activity might be related to phosphorylation of vimentin. Further experiments to link the changes in phosphorylation to downstream molecular effects would help to elucidate the mechanism of action of OXS-N1 in promoting neurogenesis.

5.6 Summary

Vimentin was validated as a direct binding molecular target of OXS-N1 through waterLOGSY and mass spectrometry experiments. Inactive gem-dimethyl analogue **29** did not show binding to vimentin, suggesting that the biological activity was related to vimentin binding. The mass of the probe-protein conjugate was identified by MALDI-TOF MS and the potential binding site of probe **77** was identified to be part of the rod domain of vimentin through LC-MS/MS. Attempts to determine the binding affinity of OXS-N1 to vimentin through SPR and TSA techniques were unsuccessful as the signal from the ligand-protein interaction under these experimental conditions was relatively weak. This was associated with complexity of probing the binding to a filamentous protein. Literature small molecule vimentin-binders, WFA and FiVe1, were found to increase the percentage of neurons formed in SVZ- and DG-derived NSCs after 5 days of differentiation. The activity of these structurally distinct vimentin-binding molecules further supports the hypothesis that modulating vimentin affected neuronal differentiation.

Target visualisation by immunostaining in the SVZ- and DG-derived NSCs was used to characterise the effects of modulating vimentin *in vitro*. WFA and FiVe1 treatment induced a rapid disassembly of vimentin filaments, while OXS-N1 treatment did not affect the organisation and assembly of vimentin filaments. Western blots to quantify the levels of phosphorylation among key serine residues in vimentin showed that OXS-N1 increased the phosphorylation of serine residue 38 after 24 h treatment in SVZ-derived cells. The increase in phosphorylation of vimentin could affect downstream interactions with other proteins and key signalling pathways, contributing to the neurogenic effects of OXS-N1 *in vitro*.

Chapter 6 Conclusion

6.1 Overview

OXS-N1 (**15**) was discovered as a hit neurogenic compound through phenotypic screening and its molecular target(s) were unknown. The aim of this DPhil project was to identify the molecular target(s) of OXS-N1 to elucidate its mechanism of action contributing to the neurogenic activity observed *in vitro* and *in vivo*. This would aid the hit-to-lead optimisation of OXS-N1 and the understanding of pathways contributing to NSC specification and neurogenesis.

6.2 Research Findings

Using the OXS-N1 scaffold, alkyne-tagged, biotinylated and dual-tagged probes were designed and synthesised for use in affinity-based protein profiling experiments (Figure 62). Inactive analogue **29** was used for generating inactive probes as negative controls, to rule out non-specific interactions that do not contribute to the phenotypic outcome. The biological activities of the probes were assessed *in vitro* using the neurosphere differentiation assay.

Alkyne tags were incorporated at various positions around OXS-N1 to explore the SAR. Among the probes synthesised, *O*-alkylated derivative **48** demonstrated the most similar level of biological activity as OXS-N1. The gem-dimethyl analogue **49** was confirmed to be inactive. Preliminary pull-down experiments with the active alkyne-tagged probe **48** demonstrated low levels of protein labelling, hence alternative strategies were explored.

Biotinylated probes were synthesised and while **72** was found to be less potent than OXS-N1, it was sufficiently active at high concentrations. Active probe **72** was used to pull-down target proteins from the SVZ-derived NSCs, with inactive biotinylated probe **73** as the negative control and OXS-N1 as the competition control respectively. The gel band enriched by the active probe was excised for mass spectrometry analysis and putative targets were identified.

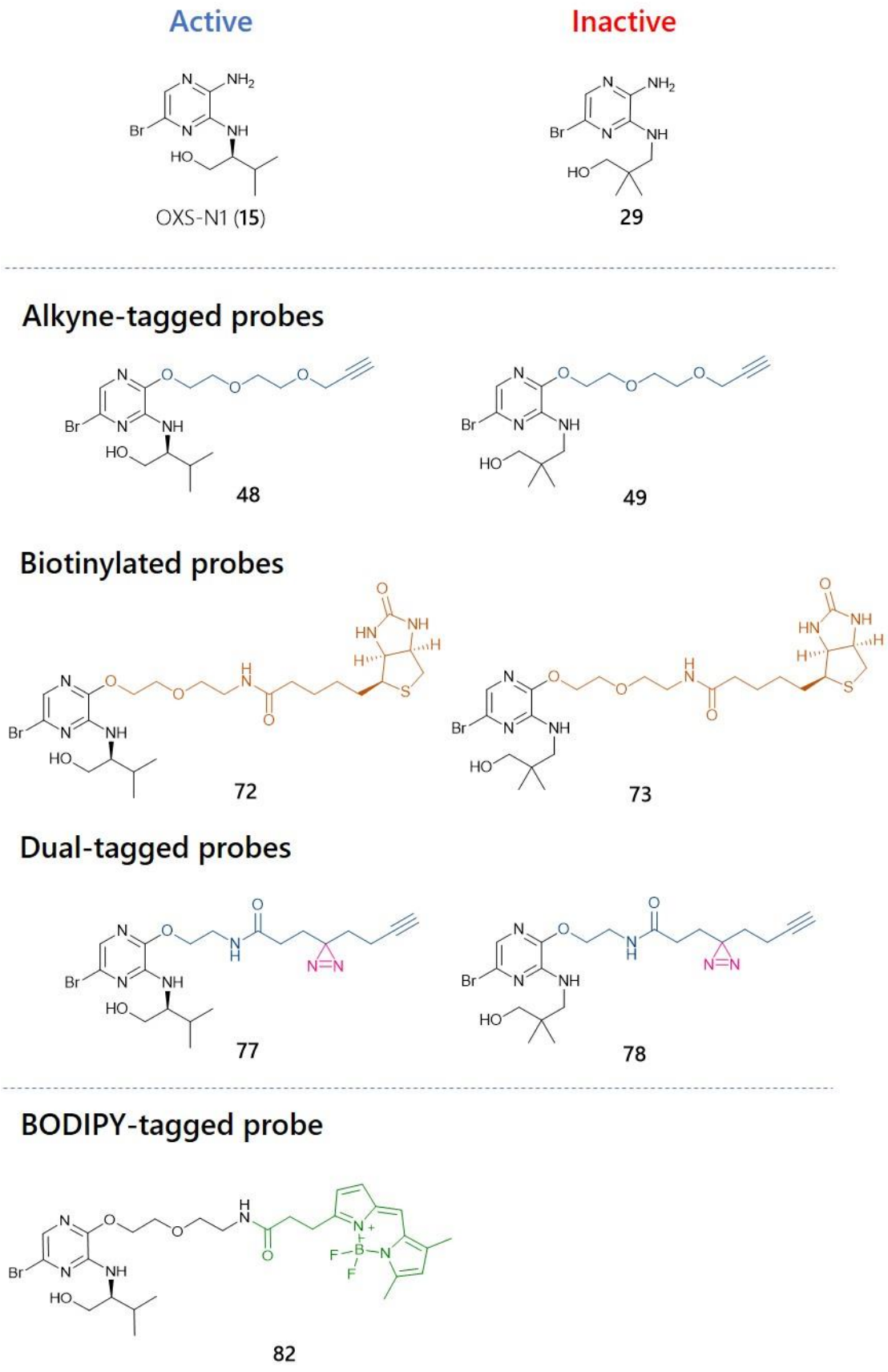


*Figure 62. Structures of OXS-N1 (**15**), inactive gem-dimethyl analogue **29**, and affinity and fluorescent probes.*

Dual-tagged probes, containing an alkyl diazirine moiety as a photoaffinity label and an alkyne moiety as a clickable handle, were also synthesised. The incorporation of photoaffinity labelling allowed for the covalent capture of proteins and improved the labelling of protein targets which were weakly bound or less abundant in the cells. Active diazirine probe **77** and inactive diazirine probe **78** were used to pull-down target proteins from SVZ- and DG-derived NSCs. In-gel digest and in-solution digest were used to identify proteins enriched by the active probe.

Significantly enriched and therapeutically relevant targets were identified by comparing the active probe samples with the inactive and competition controls in the chemoproteomics experiments. A list of putative targets was identified, and the proteins were prioritised through a literature search for relevance to neurogenesis. Of the six putative hits, western blotting confirmed only vimentin as a potential molecular target of OXS-N1.

Cellular imaging was carried out using BODIDY-tagged probe **82** to visualise the subcellular localisation of OXS-N1. The probe was mainly localised in the cytoplasm, which corresponded to the known subcellular localisation of vimentin. Immunostaining with anti-vimentin antibodies showed good co-localisation of the probe and vimentin filaments within the murine NSCs. Treatment with excess OXS-N1 outcompeted the fluorescence signal from BODIPY-tagged probe **82**, showing that the parent compound engages with the same molecular target as the probe in the cells.

Validation of vimentin as the molecular target of OXS-N1 was carried out using a range of biophysical techniques. Western blots of the pull-down samples demonstrated that OXS-N1 competed with the active diazirine probe **77** for binding to vimentin. The ligand-protein interaction of OXS-N1 with human recombinant vimentin protein was confirmed through waterLOGSY experiments. The inactive analogue **29** demonstrated no significant interaction with the protein, indicating that the binding of vimentin was of therapeutic relevance. Intact protein mass spectrometry was used to characterise the probe-protein conjugates, confirming that the active diazirine probe was covalently linked to vimentin *in vitro* after UV irradiation.

Two structurally distinct vimentin inhibitors, WFA and FiVe1, demonstrated neurogenic activity in the neurosphere differentiation assay, suggesting that modulating vimentin was relevant in increasing neurogenesis *in vitro*.

6.3 Future Work

Due to the closure of the departmental labs and travel restrictions arising from the COVID-19 global pandemic, some experiments could not be carried out in the planned timeline. These studies are described as future work that can be done to further validate vimentin as a molecular target of OXS-N1.

6.3.1 Investigation of Vimentin Modulation

To investigate if vimentin modulation is necessary for the biological activity of OXS-N1, knockdown of vimentin can be carried out in the NSCs. RNA interference can be used for vimentin gene-specific RNA degradation. Kumar *et al.* have previously described the depletion of vimentin in cells transfected with short-hairpin RNA (shRNA).[316] The shRNA constructs can be delivered into the murine-derived NSCs through nucleofection. While the transfection efficiency using this method is generally high, a drawback is the decrease in cell viability.[317]

In preliminary transfection experiments, cell viability significantly dropped after transfection. Many of the NSCs exhibited a rounded morphology and did not attach well to the surface of the wells. The decrease in cell viability would lead to difficulties in interpreting the results of the neurosphere differentiation assay. Optimisation of the transfection protocol is required to achieve a balance between the transfection efficiency and the viability of the transfected cells.

Morrow *et al.* have also described the knockout of vimentin in primary mouse hippocampal NSCs using CRISPR-Cas9 gene editing.[284] The effects of complete vimentin deficiency in the SVZ- and DG-derived NSCs can be explored in relation to OXS-N1 treatment. A comparison of the biological activity of OXS-N1 in wild-type and vimentin-knockout mice would also provide insight on the importance of vimentin modulation *in vivo*.

A loss in the biological activity of OXS-N1 in the vimentin-knockdown and knockout models would indicate that the neurogenic potential of OXS-N1 is dependent on the interaction with vimentin in the cells.

6.3.2 Investigation of Protein-protein Interactions & Affected Pathways

The biological effects of literature vimentin binders, WFA and FiVe1, have been attributed to a disassembly of vimentin filaments *in vitro*. In imaging experiments however, OXS-N1 did not induce similar effects on the disruption of vimentin filaments, suggesting that it modulates vimentin in a different manner. A possible mechanism contributing to OXS-N1's activity could be its interaction with one of the proteins associated with vimentin and its modulation of protein-protein interactions relevant to neurogenesis.

Vimentin interacts with a range of proteins to elicit its various cellular functions and serves as a scaffolding protein where complexes for important processes are assembled.[301] Through co-immunoprecipitation studies, Santos *et al.* found that vimentin interacted with inflammasome proteins, caspase-1 and NLRP3, to activate inflammation. Vimentin was also found to interact with membrane glycoprotein, CD44, which contributes to its roles in tumorigenesis and angiogenesis.[318]

As the interactions of vimentin contributing to its role in neuronal differentiation have not been studied in detail, it would be interesting to investigate its protein-protein interactions in relation to OXS-N1 treatment. Co-immunoprecipitation experiments can be used to identify proteins that interact with vimentin using vimentin-specific antibodies. Lysates obtained from cells treated with DMSO or OXS-N1 can be subjected to affinity-enrichment through incubation and washing on the Protein A beads coupled with anti-vimentin antibodies. The immunoprecipitated samples can then be analysed by mass spectrometry and the identified proteins quantified by LFQ or TMT labelling. This could provide a detailed map of the interactions between vimentin and other proteins in NSCs. The upregulation or downregulation of related proteins in response

to OXS-N1 could provide some insight into how the modulation of vimentin leads to downstream changes resulting in the phenotypic outcomes observed.

Signalling pathways affected by OXS-N1 treatment can also be investigated. Certain pathways related to neurogenesis, such as Notch signalling and Wnt signalling pathways, (Section 1.2.3) can be explored. Inhibitors of these key pathways can be treated in combination with OXS-N1. A loss in biological activity of OXS-N1 would indicate that its mechanism of action is dependent on the particular signalling pathways inhibited.

6.3.3 Investigation of Vimentin as a Therapeutic Target

With the protein profiling and preliminary validation studies converging on vimentin as the molecular target of OXS-N1, it is crucial to investigate vimentin as a potential drug target. The phenotypic outcomes of modulating vimentin have been examined mostly in a cellular context. To assess the suitability of vimentin as a drug target for neuroregeneration, more studies are required to characterise its role in disease phenotypes in a clinical context and to determine its therapeutic window.

As the studies of OXS-N1 were mainly performed in wild-type mice, further studies to examine the effects of OXS-N1 in disease models, particularly in relation to vimentin modulation, are needed. Leuvin *et al.* demonstrated that vimentin was expressed in neurons residing in the affected regions of AD transgenic mice brain and in response to mechanical injury.[319] The upregulation of vimentin has also been reported in reactive gliosis during injury or stress.[320] Livne-Bar *et al.* showed that pharmacological inhibition of vimentin in reactive glia using WFA protected retinal neurons from metabolic stress and cell death.[321] The use of OXS-N1 to investigate vimentin modulation in the context of neuronal injury and neurodegeneration could establish if vimentin is a suitable target for regenerative therapy.

A desirable drug target would need an acceptable therapeutic window, such that the drug can be dosed effectively without undesirable toxic effects. Possible negative effects arising from the

modulation of vimentin in mesenchymal tissues should be examined. A way to minimise possible side effects is to increase the drug exposure and accumulation in the target tissue, which in the case of neuroregenerative therapies, is the brain. Pharmacokinetics studies of OXS-N1 have shown that the compound is absorbed well through the blood brain barrier (BBB) and a high concentration of OXS-N1 is maintained in the brain with a thrice-a-day dosing regimen (Section 1.5.2). To increase the uptake of the compound through the BBB, the lipophilicity of the compound could be increased.[322] Other methods of delivery, such as intranasal delivery, can be explored to increase brain exposure and minimise systemic effects.[323]

6.4 Summary

Deconvoluting the mechanism in which OXS-N1 modulates vimentin and its potential downstream interactions could aid the understanding of the complex functions of vimentin and its role in neurogenesis. Studies to characterise the OXS-N1-vimentin binding site and any conformational changes upon binding could be performed using spectroscopic techniques such as HDX and STD NMR. Co-immunoprecipitation studies could help to identify important protein-protein interactions and potential recruitment of factors that lead to changes in neuronal differentiation observed in the NSCs. Studies in vimentin-null models would also determine if vimentin modulation is the key interaction that leads to the phenotypic outcome of OXS-N1 treatment.

Investigation of the role of vimentin in neurodegenerative disease models would further support vimentin as a therapeutic target. As vimentin is widely expressed in tissues throughout the body, the issue of specificity and potential side effects arising from the uptake of the vimentin modulator into different tissues have to be addressed. The therapeutic window of vimentin modulation has to be determined to assess the suitability of vimentin as a drug target for neuroregenerative therapy. Hit-to-lead optimisation of the compound could improve its specificity for uptake into the brain tissue, to minimise potential issues. The rigorous validation of vimentin as a molecular target could pave the way for a target-based drug discovery programme for small molecule modulators of neurogenesis as a therapeutic strategy for neurodegenerative diseases.

Chapter 7 Experimental

7.1 Chemistry Methods

7.1.1 General Experimental

Chemicals were purchased from Sigma-Aldrich UK, TCI UK, Apollo Scientific UK, Alfa Aesar UK, Fluorochem UK or Fisher Scientific UK unless otherwise stated. All reactions involving moisture-sensitive reagents were carried out under a nitrogen or argon atmosphere using oven-dried glassware. Microwave reactions were carried out using Biotage® Initiator Classic microwave synthesiser.

Anhydrous DMF was purchased from Sigma-Aldrich UK in SureSeal™ bottles and other anhydrous solvents were dried following the procedure outlined by Grubbs *et al*. Degassed solvents were purged with nitrogen or argon for at least 10 min. Water was purified by an Elix® UV-10 system. All other solvents and reagents were used as supplied (analytical or HPLC grade) without further purification. Brine refers to a saturated aqueous solution of sodium chloride. Organic layers were dried over Na_2SO_4. *In vacuo* refers to the use of a rotary evaporator attached to a diaphragm pump.

7.1.2 Analytical Procedures

Thin layer chromatography was performed on Merck silica gel 60 F_{254} aluminium-supported thin layer chromatography sheets. Plates were visualised either under UV light (254 nm and 370 nm) or thermal development after dipping in 1% aq. $KMnO_4$ or anisaldehyde. Flash column chromatography was performed on Kieselgel 60 silica in a glass column, unless otherwise stated. Melting points were recorded on a Gallenkamp Hot Stage apparatus and are reported uncorrected. Optical rotations were recorded on a Perkin-Elmer 241 polarimeter with a water-jacketed 10 cm cell at 25 °C. Specific rotations are reported in 10^{-1} deg cm^2 g^{-1} and concentrations in g/100 mL. Infrared spectra were recorded on a Bruker Tensor 27 FT-IR

spectrometer as thin film samples. Selected characteristic peaks are reported in wavenumbers (cm^{-1}).

NMR spectra were recorded on Bruker Avance spectrometers (AVIIIHD 400 or AVII 500) in the deuterated solvent stated. Spectra were recorded at rt unless otherwise stated. The field was locked by external referencing to the relevant deuteron resonance. Chemical shifts (δ) are reported in parts per million (ppm) to the nearest 0.01 ppm for ^{1}H and 0.1 ppm for ^{13}C, ^{19}F and ^{11}B. The multiplicity of each signal is indicated by: s (singlet); br. s (broad singlet); d (doublet); t (triplet); q (quartet); hept (heptet); m (multiplet); app (apparent); or combinations thereof. Coupling constants (*J*) are quoted in Hz and are reported to the nearest 0.1 Hz. Structural assignments were made using COSY, HSQC and HMBC experiments.

Low-resolution mass spectra were recorded on an Agilent 6120 spectrometer operating in positive or negative mode, from solutions of MeOH, unless otherwise stated. Accurate mass measurements were run on either a Bruker MicroTOF internally calibrated with polyalanine, or a Micromass GCT instrument fitted with a Scientific Glass Instruments BPX5 column (15 m × 0.25 mm) using amyl acetate as a lock mass, by the mass spectrometry department of the Chemistry Research Laboratory, University of Oxford, UK. *m/z* values are reported in Daltons and followed by their percentage abundance in parentheses.

7.1.3 General Synthetic Procedures

General procedure 1: Buchwald-Hartwig Coupling

Hydroxyl linker (1.2 eq), caesium carbonate (2 eq), *t*BuXPhos (3 mol%) and palladium (II) acetate (2 mol%) were added to aryl bromide (1 eq) in degassed toluene under an argon atmosphere. The reaction mixture was heated at 90 °C for 16 h. The mixture was diluted with CH_2Cl_2, then washed with water and brine. The organic layer was dried over Na_2SO_4, filtered and concentrated *in vacuo* to obtain the crude product.

General procedure 2: Boc Deprotection

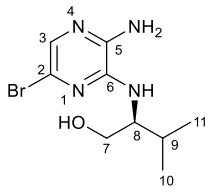
Boc-protected compound was dissolved in CH_2Cl_2 and trifluoroacetic acid (TFA) (1:1 v/v, 20 eq) was added. The reaction mixture was stirred at rt and concentrated *in vacuo*. The residue was diluted with water, neutralised with saturated $NaHCO_3$ and extracted with CH_2Cl_2. The organic layer was dried over Na_2SO_4, filtered and concentrated *in vacuo* to obtain the crude product.

General procedure 3: Amide Coupling

Amine (1 eq) was added to a solution of HATU (1.4 eq) in DMF. DIPEA (4 eq) and carboxylic acid (1.2 eq) was added and the solution was stirred at room temperature for 18 h. The reaction mixture was extracted with EtOAc twice, washed with brine/water (1:1), brine and dried over Na_2SO_4 to obtain the crude product.

7.1.4 Experimental Procedures and Characterisation Data

(S)-2-((3-Amino-6-bromopyrazin-2-yl)amino)-3-methylbutan-1-ol (15)

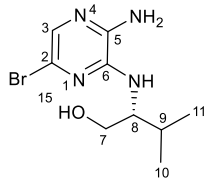


A solution of 2-amino-3,5-dibromopyrazine (17.6 g, 69.6 mmol), L-valinol (7.9 g, 76.6 mmol) and DIPEA (14.5 mL, 83.5 mmol) in *n*BuOH (70 mL) was heated at 160 °C for 120 h. The reaction mixture was concentrated *in vacuo*, diluted with EtOAc, then washed with water and brine. The organic layer was dried over Na_2SO_4, filtered and concentrated *in vacuo*. The crude product was purified by flash column chromatography on silica gel (CH_2Cl_2/EtOAc 80:20 to CH_2Cl_2/MeOH 95:5) to give the desired product (11.9 g, 62%) as a pale brown solid.

$[\alpha]_D^{25}$ –59.5 (*c* = 0.1 in MeOH); mp 124–126 °C; ν_{max} (solid) 3446 (O–H or N–H), 3365 (O–H or N–H), 2902 (C–H), 2845 (C–H), 1637, 1457; ^{1}H NMR (400 MHz, $CDCl_3$) δ 7.40 (1H, s, H3), 4.65 (1H, d, *J* = 7.7 Hz, N*H*), 4.40 (2H, s, NH_2), 4.00–3.89 (1H, m, H8), 3.86–3.69 (2H, m, H7),

1.98–1.94 (1H, m, H9), 0.99 (6H, t_{app}, J = 6.7 Hz, H10, H11); ^{13}C NMR (100 MHz, $CDCl_3$) δ 144.9 (C6), 142.1 (C5), 129.7 (C3), 125.9 (C2), 63.6 (C8), 58.4 (C7), 29.6 (C9), 19.5 (C11 or C10), 19.3 (C11 or C10); *m/z* (ESI$^+$) 277 ([M(^{81}Br)+H]$^+$, 98%), 275 ([M(^{79}Br)+H]$^+$, 100%); HRMS (ESI$^+$) $C_9H_{16}BrN_4O^+$ ([M(^{79}Br)+H]$^+$) requires 275.0502, found 275.0500.

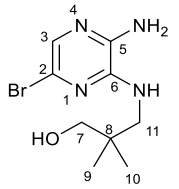
(R)-2-((3-Amino-6-bromopyrazin-2-yl)amino)-3-methylbutan-1-ol (15)



A solution of 2-amino-3,5-dibromopyrazine (635 mg, 2.50 mmol), D-valinol (284 mg, 2.75 mmol) and DIPEA (0.50 mL, 3 mmol) in *n*BuOH (2.5 mL) was heated using MW at 200 °C for 2 h. The reaction mixture was concentrated *in vacuo*, diluted with EtOAc, then washed with water and brine. The organic layer was dried over Na_2SO_4, filtered and concentrated *in vacuo*. The crude product was purified by flash column chromatography on silica gel (CH_2Cl_2/EtOAc 80:20 to CH_2Cl_2/MeOH 95:5) to give the desired product (215 mg, 31%) as a pale brown solid.

$[\alpha]_D^{25}$ +56.5 (*c* = 0.1 in MeOH); mp 120–124 °C; ν_{max} (solid) 3445 (O–H or N–H), 3355 (O–H or N–H), 2912 (C–H), 2844 (C–H), 1640, 1455; ^{1}H NMR (400 MHz, $CDCl_3$) δ 7.45 (1H, s, H3), 4.45 (1H, d, *J* = 7.7 Hz, N*H*), 4.15 (2H, s, NH_2), 4.01–3.90 (1H, m, H8), 3.87–3.70 (2H, m, H7), 2.04–2.02 (1H, m, H9), 1.01 (6H, t_{app}, *J* = 6.7 Hz, H10, H11); ^{13}C NMR (100 MHz, $CDCl_3$) δ 146.8 (C6), 143.1 (C5), 128.7 (C3), 126.1 (C2), 62.9 (C8), 59.0 (C7), 29.8 (C9), 19.6 (C11 or C10), 19.4 (C11 or C10); *m/z* (ESI$^+$) 277 ([M(^{81}Br)+H]$^+$, 99%), 275 ([M(^{79}Br)+H]$^+$, 100%); HRMS (ESI$^+$) $C_9H_{16}BrN_4O^+$ ([M(^{79}Br)+H]$^+$) requires 275.0502, found 275.0500.

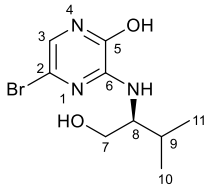
3-((3-Amino-6-bromopyrazin-2-yl)amino)-2,2-dimethylpropan-1-ol (29)



A solution of 2-amino-3,5-dibromopyrazine (635 mg, 2.50 mmol), L-valinol (284 mg, 2.75 mmol) and DIPEA (0.50 mL, 3 mmol) in *n*BuOH (2.5 mL) was heated using MW at 200 °C for 2 h. The reaction mixture was concentrated *in vacuo*, diluted with EtOAc, and washed with water and brine. The organic layer was dried over Na_2SO_4, filtered and concentrated *in vacuo*. The crude product was purified by flash column chromatography on silica gel (CH_2Cl_2/MeOH 98:2 to 90:10) to give the desired product (243 mg, 35%) as a pale orange solid.

mp 105–107 °C; ν_{max} (film) 3250 (O–H or N–H), 2986 (C–H), 1640; ^{1}H NMR (400 MHz, methanol-d_4) δ 7.08 (1H, s, H3), 3.19 (2H, s, H7), 3.09 (2H, s, H11), 0.84 (6H, s, H9, H10); ^{13}C NMR (100 MHz, methanol-d_4) δ 144.4 (C6), 143.0 (C5), 127.0 (C3), 121.6 (C2), 67.6 (C11), 47.6 (C7), 36.7 (C8), 21.6 (C9, C10); *m/z* (ESI$^+$) 277 ([M(^{81}Br)+H]$^+$, 99%), 275 ([M(^{79}Br)+H]$^+$, 100%); *m/z* (ESI$^+$) 277 ([M(^{81}Br)+H]$^+$, 98%), 275 ([M(^{79}Br)+H]$^+$, 100%); HRMS (ESI$^+$) $C_9H_{16}BrN_4O^+$ ([M(^{79}Br)+H]$^+$) requires 275.0502, found 275.0501.

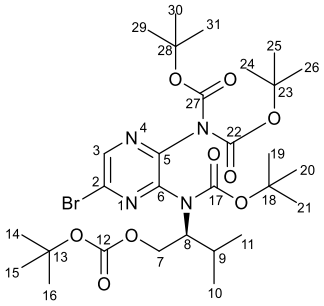
(S)-5-Bromo-3-((1-hydroxy-3-methylbutan-2-yl)amino)pyrazin-2-ol (46)



A solution of 3,5-dibromopyrazin-2-ol (4.6 g, 18.1 mmol), L-valinol (2.06 g, 19.9 mmol) and DIPEA (3.8 mL, 21.7 mmol) in *n*BuOH (18 mL) was heated at 160 °C for 19 h. The reaction mixture was concentrated *in vacuo*, diluted with EtOAc, then washed with water and brine. The organic layer was dried over Na_2SO_4, filtered and concentrated *in vacuo*. The crude product was purified by flash column chromatography on silica gel (CH_2Cl_2/EtOAc 80:20 to CH_2Cl_2/MeOH 95:5) to give the desired product (1.95 g, 39%) as an orange solid.

$[\alpha]_D^{25}$ –56.1 (*c* = 0.1 in MeOH); mp 95–97 °C; ν_{max} (film) 3388 (O–H or N–H), 3306 (O–H or N–H), 2964 (C–H), 1654, 1556; ^{1}H NMR (400 MHz, $CDCl_3$) δ 11.54 (br. s, 1H, O*H*), 6.51 (1H, s, H3), 6.45 (1H, d, *J* = 8.8 Hz, NH), 3.90–3.81 (1H, m, H8), 3.80–3.66 (2H, m, H7), 1.96–1.86 (1H, m, H9), 0.93 (3H, d, *J* = 6.8 Hz, H10), 0.89 (3H, d, *J* = 6.8 Hz, H11); ^{13}C NMR (100 MHz, $CDCl_3$) δ 151.2 (C6), 151.0 (C5), 115.7 (C3), 111.7 (C2), 63.3 (C8), 58.1 (C7), 29.3 (C9), 19.4 (C10), 19.0 (C11); *m/z* (ESI$^+$) 278 ([M(^{81}Br)+H]$^+$, 99%), 276 ([M(^{79}Br)+H]$^+$, 100%); HRMS (ESI$^+$) $C_9H_{15}BrN_3O_2^+$ ([M(^{79}Br)+H]$^+$) requires 276.0342, found 276.0339.

tert-Butyl (S)-(5-bromo-3-((tert-butoxycarbonyl)(1-((tert-butoxycarbonyl)oxy)-3-methylbutan-2-yl)amino)pyrazin-2-yl)(tert-butoxycarbonyl)carbamate (37)

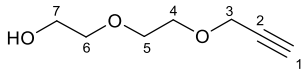


Di-*tert*-butyl dicarbonate (9.6 g, 44.0 mmol) was added to a solution of **15** (1.5 g, 5.5 mmol), DIPEA (7.6 mL, 44.0 mmol) and 4-(dimethylamino)pyridine (DMAP) (67 mg, 0.55 mmol) in THF (55 mL) at 0 °C. The mixture was warmed to rt and stirred for 16 h. The solution was concentrated *in vacuo*, diluted with CH_2Cl_2, and washed with water and brine. The organic layer was dried over Na_2SO_4, filtered and concentrated *in vacuo*. The crude product was purified by flash column chromatography on silica gel (pentane/EtOAc 92:8) to give the desired product (2.39 g, 70%) as a white powder.

$[\alpha]_D^{25}$ –51.3 (*c* = 0.1 in MeOH); mp 102–104 °C; ν_{max} (film) 2980 (C–H), 1803, 1767, 1740 (C=O), 1522, 1473, 1393, 1148; ^{1}H NMR (400 MHz, $CDCl_3$) δ 8.41 (1H, s, H3), 4.41 (2H, d, *J* = 4.8 Hz, H7), 3.67–3.42 (1H, m, H8), 2.44 (1H, dhept, *J* = 9.7, 6.7 Hz, H9), 1.47 (9H, s, H19, H20, H21), 1.39 (18H, s, H24, H25, H26, H29, H30, H31), 1.37 (9H, s, H14, H15, H16), 1.03 (3H, d, *J* = 6.7 Hz, H10), 1.00 (3H, d, *J* = 6.7 Hz, H11); ^{13}C NMR (100 MHz, $CDCl_3$) δ 153.5 (C12), 153.2 (C17), 150.4 (C22, C27), 149.7 (C6), 143.1 (C5), 142.9 (C3), 135.8 (C2), 84.0 (C23, C28), 82.5

(C18), 81.7 (C13), 69.6 (C7), 65.6 (C8), 31.2 (C9), 28.3 (C19, C20, C21), 28.1 (C24, C25, C26, C29, C30, C31), 27.9 (C14, C15, C16), 20.8 (C10), 20.6 (C11); *m/z* (ESI$^+$) 677 ([M(^{81}Br)+H]$^+$, 99%), 675 ([M(^{79}Br)+H]$^+$, 100%); HRMS (ESI$^+$) $C_{29}H_{47}BrN_4O_9Na^+$ ([M(^{79}Br)+Na]$^+$) requires 697.2419, found 697.2413.

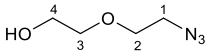
2-(2-(Prop-2-yn-1-yloxy)ethoxy)ethan-1-ol (32)



Ground potassium hydroxide (370 mg, 6.6 mmol) was added to diethylene glycol (1.7 mL, 18.0 mmol) in THF (5 mL). The mixture was heated at 40 °C for 30 min. Propargyl bromide (80% in toluene, 0.57 mL, 6.6 mmol) was added and the reaction mixture was heated at 60 °C for 16 h. Water (10 mL) was added and the solution was acidified to pH 1 using 1M HCl. The mixture was extracted using EtOAc and washed with brine. The organic layer was dried over Na_2SO_4, filtered and concentrated *in vacuo*. The crude product was purified by flash column chromatography on silica gel (pentane/EtOAc 1:1) to give the desired product (316 mg, 37%) as a colourless oil.

ν_{max} (film) 3440 (O–H), 2872 (C–H), 2248 (C≡C), 1351, 1130, 1097, 1066 (C-O), 911; ^{1}H NMR (400 MHz, $CDCl_3$) δ 4.14 (2H, dd_{app}, *J* = 2.4, 0.8 Hz, H3), 3.69–3.57 (6H, m, H5, H6, H7), 3.56–3.49 (2H, m, H4), 3.00 (1H, s, O*H*), 2.43 (1H, t, *J* = 2.4 Hz, H1); ^{13}C NMR (100 MHz, $CDCl_3$) δ 79.5 (C2), 74.8 (C1), 72.54 (C7), 70.1 (C6), 69.1 (C5), 61.5 (C4), 58.3 (C3); HRMS (ESI$^+$) $C_7H_{13}O_3^+$ ([M+H]$^+$) requires 145.0859, found 145.0860.

2-(2-Azidoethoxy)ethan-1-ol (35)

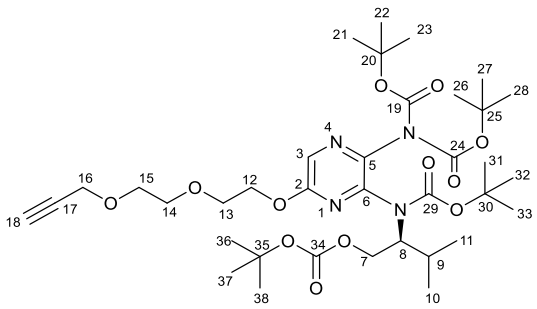


Sodium azide (3.9 g, 60 mmol) was added to a solution of 2-(2-chloro-ethoxy)-ethanol (3.2 mL, 30 mmol) in distilled water (12.5 mL) at 0 °C. The mixture was heated at 90 °C for 16 h. The mixture was extracted with CH_2Cl_2, washed with water and brine. The organic layer was dried over Na_2SO_4, filtered and concentrated *in vacuo*. The crude product was purified by flash column

chromatography on silica gel (pentane/EtOAc 1:1) to give the desired product (2.88 g, 73%) as a colourless oil.

ν_{max} (film) 3410 (O–H), 2928, 2870 (C–H), 2098 (N=N=N), 1345, 1285; ^{1}H NMR (400 MHz, $CDCl_3$) δ 3.82–3.75 (2H, m, H4), 3.74–3.69 (2H, m, H2), 3.67–3.59 (2H, m, H3), 3.43 (2H, t, *J* = 4.9 Hz, H1), 2.15 (1H, br. s, O*H*); ^{13}C NMR (100 MHz, $CDCl_3$) δ 72.5 (C3), 70.0 (C2), 61.8 (C4), 50.7 (C1).

tert-Butyl (S)-(3-(bis(tert-butoxycarbonyl)amino)-6-(2-(2-(prop-2-yn-1-yloxy)ethoxy)ethoxy)pyrazin-2-yl)(1-((tert-butoxycarbonyl)oxy)-3-methylbutan-2-yl)carbamate (89)

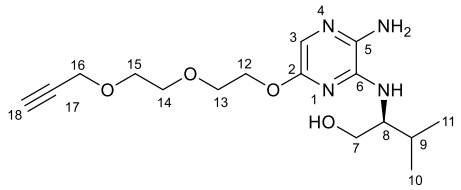


Following *general procedure 1*, tetra-Boc protected **37** (312 mg, 0.50 mmol), alkyne linker **32** (86 mg, 0.6 mmol), *t*BuXPhos (6.37 mg, 0.015 mmol) and Cs_2CO_3 were suspended in degassed anhydrous toluene (1 mL). $Pd(OAc)_2$ (2.25 mg, 0.010 mmol) was added and the reaction mixture was heated in a sealed vial under argon for 18 h. The reaction mixture was diluted with CH_2Cl_2, then washed with water and brine. The organic layer was dried over Na_2SO_4, filtered and concentrated *in vacuo*. The crude product was purified by flash column chromatography on silica gel (pentane/EtOAc 70:30) to give the desired product (190 mg, 51%) as a yellow oil.

$[\alpha]_D^{25}$ –45.6 (*c* = 0.1 in MeOH); ν_{max} (film) 2978 (C–H), 2359 (C≡C), 1799, 1740 (C=O), 1544, 1153, 1116, 1038 (C-O), 911; ^{1}H NMR (400 MHz, $CDCl_3$) δ 7.99 (1H, s, H3), 4.46–4.40 (2H, m, H12), 4.40–4.35 (2H, m, H7), 4.34–4.27 (2H, m, H14), 4.15 (2H, d, *J* = 2.4 Hz, H16), 3.81–3.77 (2H, m, H13), 3.64–3.59 (2H, m, H15), 3.48–3.39 (1H, m, H8), 2.40–2.32 (2H, m, H18, H9), 1.39 (9H, s, H31, H32, H33), 1.38 (18H, s, H21, H22, H23, H26, H27, H28), 1.36 (9H, s, H36, H37, H38), 0.97 (3H, d, *J* = 6.8 Hz, H10), 0.91 (3H, d, *J* = 6.7 Hz, H11); ^{13}C NMR (100

MHz, $CDCl_3$) δ 157.5 (C34), 153.5 (C29), 153.2 (C24, C19), 150.9 (C6), 146.0 (C5), 136.9 (C3), 131.3 (C2), 83.2 (C20, C25), 82.1 (C30), 81.6 (C34), 81.5 (C17), 74.6 (C18), 70.6 (C15), 70.4 (C14), 70.0 (C7), 69.3 (C13), 66.3 (C12), 65.3 (C8), 58.4 (C16), 31.3 (C9), 29.7 (C31, C32, C33), 28.3 (C21, C22, C23), 27.8 (C26, C27, C28), 20.9 (C10), 20.4 (C11); *m/z* (ESI^+) 761 ($[M+Na]^+$, 100%); HRMS (ESI^+) $C_{36}H_{58}N_4O_{12}Na^+$ ($[M+Na]^+$) requires 761.3943, found 761.3939.

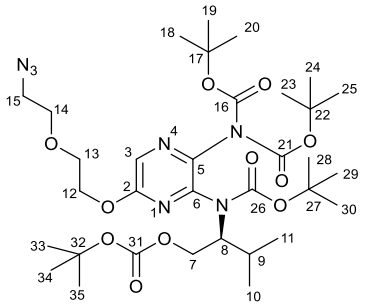
(S)-2-((3-Amino-6-(2-(2-(prop-2-yn-1-yloxy)ethoxy)ethoxy)pyrazin-2-yl)amino)-3-methylbutan-1-ol (40)



Following *general procedure 2*, TFA (2 mL) was added to **89** (190 mg, 0.26 mmol) in CH_2Cl_2 (10 mL) and the reaction was stirred for 16 h. The crude product was purified by flash column chromatography on silica gel (CH_2Cl_2/MeOH 98:2), then reverse phase column chromatography on a C18 column (gradient elution 5% → 60% CH_3CN in water) to give the desired product (20 mg, 23%) as a yellow oil.

$[\alpha]_D^{25}$ –56.8 (*c* = 0.1 in MeOH); ν_{max} (film) 3435 (O–H or N–H), 3258 (O–H or N–H), 2870 (C–H), 2359 (C≡C), 1095 (C-O), 1066; ^1H NMR (400 MHz, $CDCl_3$) δ 6.52 (1H, s, H3), 4.53 (2H, dd, *J* = 9.7, 8.6 Hz, H7), 4.47–4.35 (2H, m, H15), 4.22 (2H, d, *J* = 2.4 Hz, H16), 3.86–3.81 (2H, m, H12), 3.76–3.72 (5H, m, H13, H14, H8), 2.44 (1H, t, *J* = 2.4 Hz, H18), 1.86–1.78 (1H, m, H9), 0.98 (3H, d, *J* = 6.7 Hz, H11), 0.92 (3H, d, *J* = 6.8 Hz, H10); ^{13}C NMR 171.3 (C6), 152.5 (C5), 129.3 (C2), 100.1 (C3), 80.5 (C17), 74.7 (C18), 72.3 (C8), 72.3 (C15), 71.4 (C7), 70.6 (C14), 69.3 (C13), 60.5 (C16), 53.6 (C12), 33.0 (C9), 18.7 (C11), 18.4 (C10); *m/z* (ESI^+) 339 ($[M+H]^+$, 30%); HRMS (ESI^+) $C_{16}H_{27}N_4O_4^+$ ($[M+H]^+$) requires 339.1954, found 339.1960.

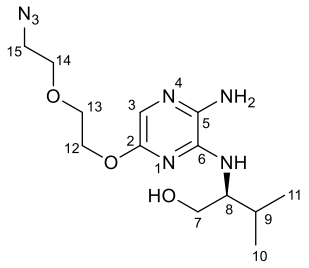
tert-Butyl (S)-(6-(2-(2-azidoethoxy)ethoxy)-3-(bis(tert-butoxycarbonyl)amino)pyrazin-2-yl)(1-hydroxy-3-methylbutan-2-yl)carbamate (90)



Following *general procedure 1*, tetra-Boc protected **37** (312 mg, 0.50 mmol), azide linker **35** (79 mg, 0.6 mmol), *t*BuXPhos (6.37 mg, 0.015 mmol) and Cs_2CO_3 were suspended in degassed anhydrous toluene (1 mL). $Pd(OAc)_2$ (2.25 mg, 0.010 mmol) was added and the reaction mixture was heated in a sealed vial under argon for 18 h. The reaction mixture was diluted with CH_2Cl_2, then washed with water and brine. The organic layer was dried over Na_2SO_4, filtered and concentrated *in vacuo*. The crude product was purified by flash column chromatography on silica gel (pentane/EtOAc 80:20) to give the desired product (200 mg, 55%) as a yellow oil.

$[\alpha]_D^{25}$ –43.5 (*c* = 0.1 in MeOH); ν_{max} (film) 2940 (C–H), 2099 (N=N=N), 1347, 1171; ^{1}H NMR (400 MHz, $CDCl_3$) δ 8.04 (1H, s, H3), 4.48-4.45 (1H, m, H7a), 4.46–4.43 (2H, m, H12), 4.37 (1H, dd, *J* = 11.3, 3.6 Hz, H7b), 3.91–3.80 (2H, m, H13), 3.76–3.69 (2H, m, H14), 3.50 (1H, ddd, *J* = 9.6, 5.6, 3.6 Hz, H8), 3.41 (2H, t, *J* = 5.1 Hz, H15), 2.43 (1H, dhept, *J* = 9.7, 6.7 Hz, H9), 1.45 (9H, s, H28, H29, H30), 1.44 (18H, s, H18, H19, H20, H23, H24, H25), 1.42 (9H, s, H33, H34, H35), 1.04 (3H, d, *J* = 6.7 Hz, H11), 0.97 (3H, d, *J* = 6.7 Hz, H10); ^{13}C NMR (100 MHz, $CDCl_3$) δ 157.5 (C31), 153.7 (C26), 153.3 (C6), 151.0 (C16, C21), 146.1 (C5), 137.1 (C2), 131.5 (C3), 83.4 (C17), 81.6 (C27), 81.6 (C32), 70.3 (C7), 70.1 (C13), 69.3 (C14), 66.3 (C15), 65.5 (C8), 50.8 (C12), 31.4 (C9), 28.4 (C28, C29, C30), 28.1 (C18, C19, C20, C23, C24, C25), 27.9 (C33, C34, C35), 21.0 (C11), 20.7 (C10); *m/z* (ESI$^+$) 748 ([M+Na]$^+$, 100%); HRMS (ESI$^+$) $C_{33}H_{55}N_7O_{11}Na^+$ ([M+Na]$^+$) requires 748.8352, found 748.8337.

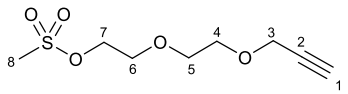
(S)-2-((3-Amino-6-(2-(2-azidoethoxy)ethoxy)pyrazin-2-yl)amino)-3-methylbutan-1-ol (41)



Following *general procedure 2*, TFA (2 mL) was added to **90** (190 mg, 0.26 mmol) in CH_2Cl_2 (10 mL) and the reaction was stirred for 16 h. The crude product was purified by flash column chromatography on silica gel (CH_2Cl_2/MeOH 98:2) to give the desired product (20 mg, 24%) as a yellow oil.

$[\alpha]_D^{25}$ –32.4 (*c* = 0.1 in MeOH); ν_{max} (film) 3155 (N–H or O–H), 2959, 2918 (C–H), 2101 (N=N=N), 1562, 1157; ^{1}H NMR (400 MHz, $CDCl_3$) δ 6.49 (1H, s, H3), 4.50 (d, *J* = 8.6 Hz, N*H*), 4.38 (2H, s, NH_2), 4.24 (2H, d, *J* = 8.7 Hz, H7), 4.15–4.06 (1H, m, H8), 3.79–3.75 (2H, m, H15), 3.74–3.66 (2H, m, H13), 3.65–3.60 (2H, m, H14), 3.39 (2H, t, *J* = 5.9 Hz, H12), 1.86–1.72 (1H, m, H9), 0.93 (3H, d, *J* = 6.7 Hz, H11), 0.87 (3H, d, *J* = 6.9 Hz, H10); ^{13}C NMR (100 MHz, $CDCl_3$) δ 157.1 (C6), 156.5 (C5), 129.3 (C2), 100.0 (C3), 71.9 (C8), 71.3 (C7), 70.2 (C15), 70.0 (C14), 68.9 (C13), 50.9 (C12), 33.0 (C9), 18.7 (C11), 18.4 (C10); HRMS (ESI$^+$) $C_{13}H_{24}N_7O_3^+$ ([M+H]$^+$) requires 326.1862, found 326.1868.

2-(2-(Prop-2-yn-1-yloxy)ethoxy)ethyl methanesulfonate (33)

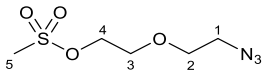


Methanesulfonylchloride (0.35 mL, 4.5 mmol) was added to a solution of **32** (432 mg, 3.0 mmol) and triethylamine (0.50 mL, 3.6 mmol) in anhydrous THF at 0 °C under an argon atmosphere. The reaction mixture was warmed to rt and stirred for 90 min. The reaction was diluted with water (20 mL) and extracted with CH_2Cl_2. The organic layer was washed with 1 M K_2CO_3 and brine, dried over Na_2SO_4, filtered and concentrated *in vacuo*. The crude product was purified by

flash column chromatography on silica gel (pentane/EtOAc 1:1) to give the desired product (610 mg, 92%) as a yellow oil.

ν_{max} (film) 2880 (C–H), 2250 (C≡C), 1070 (C-O); ^{1}H NMR (400 MHz, $CDCl_3$) δ 4.43–4.36 (2H, m, H7), 4.19 (2H, dd_{app}, *J* = 2.4, 0.8 Hz, H3), 3.80–3.75 (2H, m, H6), 3.73–3.68 (4H, m, H5, H4), 3.08 (3H, s, H8), 2.46 (1H, t, *J* = 2.4 Hz, H1); ^{13}C NMR (100 MHz, $CDCl_3$) δ 79.5 (C2), 74.7 (C1), 70.5 (C6), 69.3 (C7), 69.0 (C4, C5), 58.4 (C3), 37.7 (C8); HRMS (ESI$^+$) $C_8H_{14}O_5SNa^+$ ([M+Na]$^+$) requires 245.0454, found 245.0453.

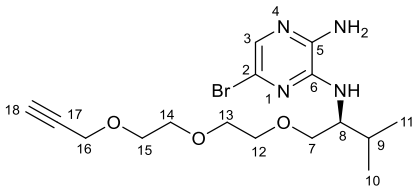
2-(2-Azidoethoxy)ethyl methanesulfonate (36)



Methanesulfonylchloride (0.95 mL, 12.2 mmol) was added to a solution of **35** (1.07 g, 8.16 mmol) and triethylamine (1.4 mL, 9.8 mmol) in anhydrous THF at 0 °C under an argon atmosphere. The reaction mixture was warmed to rt and stirred for 90 min. The reaction was diluted with water (20 mL) and extracted with CH_2Cl_2. The organic layer was washed with 1 M K_2CO_3 and brine, dried over Na_2SO_4, filtered and concentrated *in vacuo*. The crude product was purified by flash column chromatography on silica gel (pentane/EtOAc 1:1) to give the desired product (1.40 g, 82%) as a yellow oil.

ν_{max} (film) 2980, 2884 (C–H), 2100 (N=N=N), 1349, 1173; ^{1}H NMR (400 MHz, $CDCl_3$) δ 4.43–4.36 (2H, m, H4), 3.84–3.76 (2H, m, H3), 3.75–3.67 (2H, m, H2), 3.42 (2H, t, *J* = 4.9 Hz, H1), 3.08 (3H, s, H5); ^{13}C NMR (100 MHz, $CDCl_3$) δ 70.2 (C3), 69.0 (C2), 68.8 (C4), 50.7 (C1), 37.6 (C5); HRMS (ESI$^+$) $C_5H_{11}N_3O_4SNa^+$ ([M+Na]$^+$) requires 232.0363, found 232.0362.

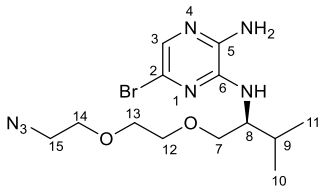
(S)-6-Bromo-N2-(3-methyl-1-(2-(2-(prop-2-yn-1-yloxy)ethoxy)ethoxy)butan-2-yl)pyrazine-2,3-diamine (42)



Ground potassium hydroxide (56 mg, 1.0 mmol) was added to a solution of **15** (138 mg, 0.50 mmol) and **33** (134 mg, 0.60 mmol) in anhydrous DMF (1 mL). The mixture was heated at 35 °C for 16 h. The reaction was diluted with EtOAc (50 mL), and washed with brine/water (1:1) and brine. The organic layer was dried over Na_2SO_4, filtered and concentrated *in vacuo*. The crude product was purified by reverse phase column chromatography on a C18 column (gradient elution 5% → 60% CH_3CN in water) to give the desired product (10 mg, 5%) as a yellow oil.

$[\alpha]_D^{25}$ –18.9 (*c* = 0.1 in MeOH); ν_{max} (film) 3363 (O–H or N–H), 3292 (O–H or N–H), 3250 (O–H or N–H), 2957 (C–H), 2362 (C≡C), 1468, 1102 (C-O); ^{1}H NMR (400 MHz, $CDCl_3$) δ 7.27 (1H, s, H3), 5.09 (1H, d, *J* = 8.6 Hz, N*H*), 4.56 (2H, s, NH_2), 4.13 (2H, d, *J* = 2.6 Hz, H16), 4.01–3.89 (1H, m, H8), 3.78–3.69 (2H, m, H7), 3.67–3.50 (6H, m, H12, H13, H14), 3.49–3.44 (2H, m, H15), 2.38 (1H, t, *J* = 2.4 Hz, H18), 2.02–1.91 (1H, m, H9), 0.92 (3H, d, *J* = 4.7 Hz, H10), 0.90 (3H, d, *J* = 4.8 Hz, H11); ^{13}C NMR (100 MHz, $CDCl_3$) δ 144.1 (C6), 142.2 (C5), 128.6 (C3), 125.4 (C2), 79.3 (C17), 75.2 (C18), 70.7 (C7), 70.6 (C12, C13), 70.1 (C14), 69.1 (C15), 58.4 (C16), 56.0 (C8), 29.7 (C9), 19.7 (C11), 19.4 (C10); *m/z* (ESI$^+$) 403 ([M(^{81}Br)+H]$^+$, 99%), 401 ([M(^{79}Br)+H]$^+$, 100%); HRMS (ESI$^+$) $C_{16}H_{26}BrN_4O_3^+$ ([M(^{79}Br)+H]$^+$) requires 401.1183, found 401.1184.

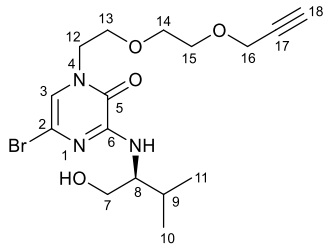
(S)-N2-(1-(2-(2-Azidoethoxy)ethoxy)-3-methylbutan-2-yl)-6-bromopyrazine-2,3-diamine (43)



Ground potassium hydroxide (56 mg, 1.0 mmol) was added to a solution of **15** (138 mg, 0.50 mmol) and **36** (126 mg, 0.60 mmol) in anhydrous DMF (1 mL). The mixture was heated at 35 °C for 16 h. The reaction was diluted with EtOAc (50 mL), and washed with brine/water (1:1) and brine. The organic layer was dried over Na_2SO_4, filtered and concentrated *in vacuo*. The crude product was purified by reverse phase column chromatography on a C18 column (gradient elution 5% → 60% CH_3CN in water) to give the desired product (8 mg, 10%) as a yellow oil.

$[\alpha]_D^{25}$ –12.9 (*c* = 0.1 in MeOH); ν_{max} (film) 3342 (O–H or N–H), 3292 (O–H or N–H), 3234 (O–H or N–H), 2960 (C–H), 2104 (N=N=N), 1470, 1125 (C-O); ^{1}H NMR (400 MHz, $CDCl_3$) δ 7.32 (1H, s, H3), 4.70 (1H, d, *J* = 8.6 Hz, N*H*), 4.25 (2H, s, NH_2), 4.03–3.92 (1H, m, H8), 3.67 (1H, dd, *J* = 10.0, 3.8 Hz, H7a), 3.62–3.53 (6H, m, H12, H13, H14), 3.48 (1H, dd, *J* = 10.0, 3.5 Hz, H7b), 3.37–3.29 (2H, m, H15), 2.04–1.88 (1H, m, H9), 0.92 (6H, t_{app}, *J* = 6.7 Hz, H10, H11); ^{13}C NMR (100 MHz, $CDCl_3$) δ 144.3 (C6), 141.94 (C5), 129.0 (C3), 126.0 (C2), 70.6 (C7, C12), 69.9 (C13, C14), 55.6 (C8), 50.8 (C15), 29.6 (C9), 19.5 (C10), 19.3 (C11); *m/z* (ESI^+) 390 ([M(^{81}Br)+H]$^+$, 99%), 388 ([M(^{79}Br)+H]$^+$, 100%); HRMS (ESI^+) $C_{13}H_{23}BrN_7O_2^+$ ([M(^{79}Br)+H]$^+$) requires 388.1091, found 388.1086.

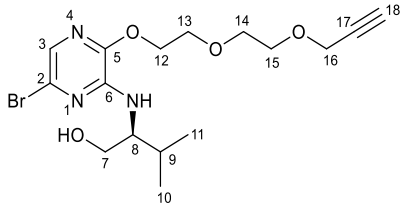
(S)-5-Bromo-3-((1-hydroxy-3-methylbutan-2-yl)amino)-1-(2-(2-(prop-2-yn-1-yloxy)ethoxy)ethyl)pyrazin-2(1H)-one (47)



K_2CO_3 (691 mg, 5.0 mmol) was added to a solution of **46** (276 mg, 1.0 mmol) and **32** (267 mg, 1.2 mmol) in anhydrous DMF (10 mL). The reaction mixture was heated at 80 °C for 3 h. The reaction was diluted with EtOAc (50 mL), and washed with brine/water (1:1) and brine. The organic layer was dried over Na_2SO_4, filtered and concentrated *in vacuo*. The crude product was purified by reverse phase column chromatography on a C18 column (gradient elution 5% → 60% CH_3CN in water) to give the desired product (120 mg, 38%) as a yellow oil.

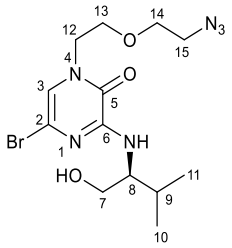
$[\alpha]_D^{25}$ –14.9 (*c* = 0.1 in MeOH); ν_{max} (film) 3392 (O–H or N–H), 3303 (O–H or N–H), 2960 (C–H), 2873, 2128 (C≡C), 1640 (C=O), 1559, 1100; ^{1}H NMR (400 MHz, $CDCl_3$) δ 6.69 (1H, d, *J* = 0.8 Hz, H3), 6.33 (1H, d, *J* = 7.6 Hz, N*H*), 4.14 (dd_{app}, *J* = 2.4, 0.7 Hz, H16), 4.05–3.87 (2H, m, H12), 3.80–3.75 (1H, m, H8), 3.74–3.64 (4H, m, H13, H7), 3.64–3.60 (2H, m, H14), 3.59–3.56 (2H, m, H15), 2.83 (1H, br. s, O*H*), 2.39 (1H, t, *J* = 2.4 Hz, H18), 2.02–1.90 (1H, m, H9), 0.96–0.91 (6H, m, H10, H11); ^{13}C NMR (100 MHz, $CDCl_3$) δ 150.8 (C6), 150.6 (C5), 116.8 (C3), 113.6 (C2), 79.5 (C17), 74.8 (C18), 70.4 (C14), 68.9 (C15), 68.6 (C7), 64.3 (C13), 59.1 (C8), 58.5 (C16), 48.8 (C12), 29.3 (C9), 19.4 (C11 or C10), 18.7 (C11 or C10); *m/z* (ESI^+) 404 ($[M(^{81}Br)+H]^+$, 99%), 402 ($[M(^{79}Br)+H]^+$, 100%); HRMS (ESI^+) $C_{16}H_{25}BrN_3O_4^+$ ($[M(^{79}Br)+H]^+$) requires 402.1023, found 402.1029.

(S)-2-((6-Bromo-3-(2-(2-(prop-2-yn-1-yloxy)ethoxy)ethoxy)pyrazin-2-yl)amino)-3-methylbutan-1-ol (48)



Yellow oil (34 mg, 12%). $[\alpha]_D^{25}$ –26.3 (*c* = 0.1 in MeOH); ν_{max} (film) 3427 (O–H or N–H), 3294 (O–H or N–H), 2959 (C–H), 2873, 2115 (C≡C), 1587, 1516, 1253; ^{1}H NMR (400 MHz, $CDCl_3$) δ 7.22 (1H, s, H3), 5.33 (1H, d, *J* = 8.1 Hz, N*H*), 4.49–4.36 (2H, m, H7), 4.13 (2H, d, *J* = 2.4 Hz, H16), 3.88–3.80 (1H, m, H8), 3.78 (2H, t, *J* = 4.7 Hz, H12), 3.76–3.66 (2H, m, H13), 3.66–3.62 (4H, m, H14, H15), 2.43 (1H, t, *J* = 2.4 Hz, H18), 2.02–1.87 (1H, m, H9), 0.94 (3H, d, *J* = 6.8 Hz, H10), 0.91 (3H, d, *J* = 6.8 Hz, H11); ^{13}C NMR (100 MHz, $CDCl_3$) δ 146.9 (C6), 145.7 (C5), 127.5 (C3), 126.6 (C2), 79.6 (C17), 74.8 (C18), 70.6 (C12), 69.3 (C13), 69.2 (C14), 66.0 (C7), 63.9 (C15), 58.6 (C8), 58.5 (C16), 29.5 (C9), 19.6 (C10), 19.1 (C11); *m/z* (ESI$^+$) 404 ([M(^{81}Br)+H]$^+$, 99%), 402 ([M(^{79}Br)+H]$^+$, 100%); HRMS (ESI$^+$) $C_{16}H_{25}BrN_3O_4^+$ ([M(^{79}Br)+H]$^+$) requires 402.1023, found 402.1023.

(S)-1-(2-(2-Azidoethoxy)ethyl)-5-bromo-3-((1-hydroxy-3-methylbutan-2-yl)amino)pyrazin-2(1H)-one (49)

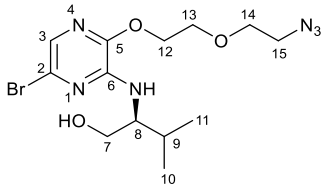


K_2CO_3 (691 mg, 5.0 mmol) was added to a solution of **46** (276 mg, 1.0 mmol) and **35** (209 mg, 1.2 mmol) in andryous DMF (10 mL). The reaction mixture was heated at 80 °C for 3 h. The reaction was diluted with EtOAc (50 mL), and washed with brine/water (1:1) and brine. The organic layer was dried over Na_2SO_4, filtered and concentrated *in vacuo*. The crude product was

purified by reverse phase column chromatography on a C18 column (gradient elution 5% → 60% CH_3CN in water) to give the desired product (131 mg, 34%) as a yellow oil.

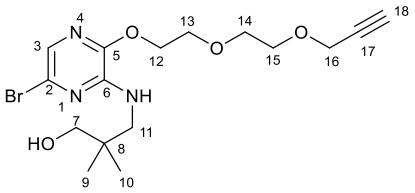
$[\alpha]_D^{25}$ –19.3 (*c* = 0.1 in MeOH); ν_{max} (film) 3390 (O–H or N–H), 2962 (C–H), 2873, 2108 (N=N=N), 1638 (C=O), 1557; ^{1}H NMR (400 MHz, $CDCl_3$) δ 6.64 (1H, s, H3), 6.43 (d, *J* = 8.2 Hz, N*H*), 4.03–3.87 (2H, m, H7), 3.79–3.74 (1H, m, H8), 3.73–3.62 (4H, m, H12, H13), 3.57 (2H, t, *J* = 4.9 Hz, H14), 3.29 (2H, t, *J* = 4.9 Hz, H15), 2.03–1.88 (1H, m, H9), 0.94 (3H, d, *J* = 6.8 Hz, H10), 0.91 (3H, d, *J* = 6.8 Hz, H11); ^{13}C NMR (100 MHz, $CDCl_3$) δ 149.7 (C6), 149.5 (C5), 115.5 (C3), 113.1 (C2), 69.2 (C14), 67.4 (C13), 62.8 (C7), 57.9 (C8), 49.6 (C15), 48.1 (C12), 28.2 (C9), 18.4 (C10), 17.8 (C11); *m/z* (ESI$^+$) 391 ([M(^{81}Br)+H]$^+$, 99%), 389 ([M(^{79}Br)+H]$^+$, 100%); HRMS (ESI$^+$) $C_{13}H_{22}BrN_6O_3^+$ ([M(^{79}Br)+H]$^+$) requires 389.0931, found 389.0921.

(S)-2-((3-(2-(2-Azidoethoxy)ethoxy)-6-bromopyrazin-2-yl)amino)-3-methylbutan-1-ol (50)



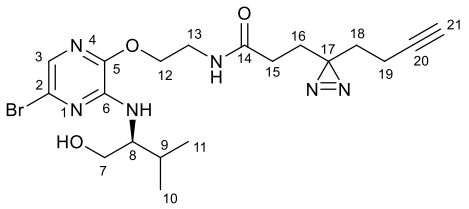
$[\alpha]_D^{25}$ –28.9 (*c* = 0.1 in MeOH); Yellow oil (43 mg, 11%). ν_{max} (film) 3418 (O–H or N–H), 2980 (C–H), 2884, 2109 (N=N=N), 1587, 1253; ^{1}H NMR (400 MHz, $CDCl_3$) δ 7.22 (1H, s, H3), 5.30 (1H, d, *J* = 8.1 Hz, N*H*), 4.50–4.36 (2H, m, H7), 3.87–3.72 (3H, m, H8, H12), 3.69–3.64 (4H, m, H13, H14), 3.31 (2H, t, *J* = 4.8 Hz, H15), 2.01–1.85 (1H, m, H9), 0.94 (3H, d, *J* = 6.7 Hz , H10), 0.91 (3H, d, *J* = 6.8 Hz, H11); ^{13}C NMR (100 MHz, $CDCl_3$) δ 146.7 (C6), 145.5 (C5), 127.4 (C3), 126.4 (C2), 70.3 (C12), 69.1 (C11), 65.7 (C14), 63.9 (C7), 58.4 (C8), 50.5 (C15), 29.3 (C9), 19.4 (C10), 19.0 (C11); *m/z* (ESI$^+$) 391 ([M(^{81}Br)+H]$^+$, 99%), 389 ([M(^{79}Br)+H]$^+$, 100%); HRMS (ESI$^+$) $C_{13}H_{21}BrN_6O_3Na^+$ ([M(^{79}Br)+Na]$^+$) requires 411.0751, found 411.0747.

3-((6-bromo-3-(2-(2-(prop-2-yn-1-yloxy)ethoxy)ethoxy)pyrazin-2-yl)amino)-2,2-dimethylpropan-1-ol (69)



K_2CO_3 (691 mg, 5.0 mmol) was added to a solution of **29** (276 mg, 1.0 mmol) and **32** (267 mg, 1.2 mmol) in anhydrous DMF (10 mL). The reaction mixture was heated at 80 °C for 3 h. The reaction was diluted with EtOAc (50 mL), and washed with brine/water (1:1) and brine. The organic layer was dried over Na_2SO_4, filtered and concentrated *in vacuo*. The crude product was purified by reverse phase column chromatography on a C18 column (gradient elution 5% → 60% CH_3CN in water) to give the desired product (42 mg, 15%) as a yellow oil. ν_{max} (film) 3410 (O–H or N–H), 3300 (O–H or N–H), 2957 (C–H), 2871, 2110 (C≡C), 1586, 1240; ^{1}H NMR (400 MHz, $CDCl_3$) δ 6.70 (1H, s, H3), 6.49 (1H, d, *J* = 8.1 Hz, N*H*), 3.95 (2H, t, *J* = 4.5 Hz, H12), 3.71–3.67 (2H, m, H13), 3.67–3.53 (4H, m, H14, H15), 3.18 (2H, s, H7), 3.10 (2H, s, H11), 0.87 (6H, s, H9, H10); ^{13}C NMR (100 MHz, $CDCl_3$) δ 151.2 (C6), 150.4 (C5), 126.3 (C3), 117.0 (C2), 79.4 (C17), 77.2 (C18), 74.8 (C12), 72.4 (C13), 70.4 (C14), 68.9 (C15), 67.7 (C11), 58.5 (C16), 48.0 (C7), 37.4 (C8), 22.8 (C9, C10); *m/z* (ESI$^+$) 404 ([M(^{81}Br)+H]$^+$, 98%), 402 ([M(^{79}Br)+H]$^+$, 100%); HRMS (ESI$^+$) $C_{16}H_{25}BrN_3O_4^+$ ([M(^{79}Br)+H]$^+$) requires 402.1023, found 402.1018.

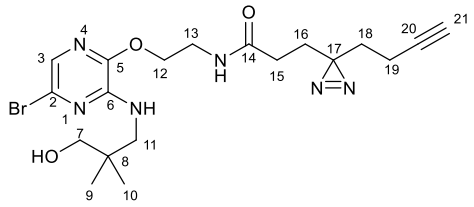
(S)-N-(2-((5-bromo-3-((1-hydroxy-3-methylbutan-2-yl)amino)pyrazin-2-yl)oxy)ethyl)-3-(3-(but-3-yn-1-yl)-3H-diazirin-3-yl)propanamide (77)



Following *general procedure 3*, amide coupling was carried out between amine **75** and linker **76**. The crude product obtained was purified by flash column chromatography on silica gel (CH_2Cl_2/MeOH 98:2) to give the desired product as a yellow oil (10 mg, 15%).

$[\alpha]_D^{25}$ –21.3 (*c* = 0.1 in MeOH); ν_{max} (film) 3414 (O–H or N–H), 3274 (O–H or N–H), 2957 (C–H), 2869, 2119 (C≡C), 1675 (C=O), 1577, 1241; ^{1}H NMR (400 MHz, $CDCl_3$) δ 7.20 (1H, s, H3), 5.95 (1H, s, CON*H*), 5.37 (1H, d, *J* = 8.5 Hz, N*H*), 4.53–4.35 (2H, m, H7), 4.34–4.09 (4H, m, H15, H16), 3.87–3.74 (1H, m, H8), 3.75–3.68 (4H, m, H18, H19), 3.66–3.47 (4H, m, H12, H13), 2.81 (1H, t, *J* = 2.3 Hz, H21), 2.06–1.84 (1H, m, H9), 0.98–0.90 (6H, m, H10, H11); ^{13}C NMR (100 MHz, $CDCl_3$) δ 162.4 (C14), 145.8 (C6), 145.4 (C5), 128.5 (C3), 126.1 (C2), 79.1 (C20), 74.2 (C21), 70.6 (C12), 69.3 (C13), 69.3 (C14), 65.9 (C7), 63.4 (C15), 58.2 (C8), 58.0 (C19), 30.4 (C16), 29.4 (C18), 28.2 (C9), 19.5 (C10), 19.2 (C11); *m/z* (ESI$^+$) 469 ([M(^{81}Br)+H]$^+$, 99%), 467 ([M(^{79}Br)+H]$^+$, 100%); HRMS (ESI$^+$) $C_{19}H_{28}BrN_6O_3^+$ ([M(^{79}Br)+H]$^+$) requires 467.1401, found 467.1402.

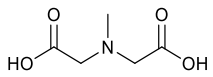
N-(2-((5-bromo-3-((3-hydroxy-2,2-dimethylpropyl)amino)pyrazin-2-yl)oxy)ethyl)-3-(3-(but-3-yn-1-yl)-3H-diazirin-3-yl)propanamide (78)



Following *general procedure 3*, amide coupling was carried out between amine **90** and linker **76**. The crude product obtained was purified by flash column chromatography on silica gel (CH_2Cl_2/MeOH 98:2) to give the desired product as a yellow oil.

ν_{max} (film) 3395 (O–H or N–H), 3310 (O–H or N–H), 2957 (C–H), 2889, 2110 (C≡C), 1682 (C=O), 1515, 1230; ^{1}H NMR (400 MHz, $CDCl_3$) δ 6.80 (1H, s, H3), 5.75 (1H, s, CON*H*), 5.49 (1H, d, *J* = 8.2 Hz, N*H*), 4.01 (2H, t, *J* = 4.5 Hz, H12), 3.75–3.68 (4H, m, H18, H19), 3.67–3.62 (2H, m, H13), 3.65–3.39 (4H, m, H15, H16), 3.22 (2H, s, H7), 3.12 (2H, s, H11), 2.55 (1H, t, *J* = 2.2 Hz, H21), 0.91 (6H, s, H9, H10); ^{13}C NMR (100 MHz, $CDCl_3$) δ 163.1 (C14), 151.3 (C6), 150.9 (C5), 127.0 (C3), 118.2 (C2), 78.8 (C20), 76.2 (C21), 75.2 (C12), 72.0 (C13), 71.4 (C14), 67.9 (C15), 66.5 (C11), 59.5 (C19), 30.8 (C16), 30.4 (C18), 49.0 (C7), 36.4 (C8), 26.8 (C9, C10); *m/z* (ESI$^+$) 469 ([M(^{81}Br)+H]$^+$, 99%), 467 ([M(^{79}Br)+H]$^+$, 100%); HRMS (ESI$^+$) $C_{19}H_{28}BrN_6O_3^+$ ([M(^{79}Br)+H]$^+$) requires 467.1401, found 467.1401.

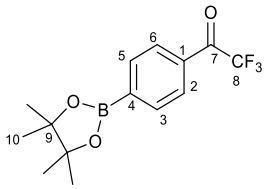
N-Methyliminodiacetic acid (MIDA) (91)



Formalin (21.3 mL, 281.7 mmol) was added to iminodiacetic acid (25 g, 187.8 mmol) in a three-necked flask fitted with a water-cooled condenser and a dropping funnel containing formic acid (14.2 mL, 375.6 mmol). The reaction mixture was heated at 90 °C for 30 min. Formic acid was added dropwise over 20 min and the reaction mixture was observed to turn yellow. The solution was refluxed for 1 h before being cooled to rt over 1 h. Absolute ethanol (190 mL) was added dropwise to the reaction mixture, resulting in the formation of a white precipitate. The mixture was filtered under vacuum to obtain the desired product (24.1 g, 90%) as a white powder.

mp 220–222 °C; ν_{max} (film) 3660 (O–H), 2981 (C–H), 1689 (C=O), 1381, 1251 (C–N); ^{1}H NMR (400 MHz, D_2O) δ 3.86 (4H, s, CH_2), 2.91 (s, 3H, NCH_3); ^{13}C NMR (100 MHz, D_2O) δ 169.3, 57.4 (*C*H_2), 42.5 (*C*H_3); HRMS (ESI$^+$) $C_5H_{10}NO_4^+$ ([M+H]$^+$) requires 148.0604, found 148.0604.

2,2,2-Trifluoro-1-(4-(4,4,5,5-tetramethyl-1,3,2-dioxaborolan-2-yl)phenyl)ethan-1-one (58)

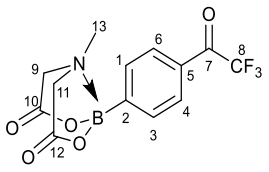


Potassium acetate (9.8 g, 100 mmol), bis(pinacolato)diboron (10.3 g, 40.4 mmol) and Pd(dppf)Cl_2 (731 mg, 1.0 mmol) were added to a solution of 4′-bromo-2,2,2-trifluoroacetophenone, **51** (10.1 g, 40 mmol) in anhydrous DMF (200 mL) under argon. The reaction mixture was heated at 90 °C for 18 h and concentrated *in vacuo*. The reaction mixture was diluted with CH_2Cl_2 (500 mL), washed with 5% LiCl (3 x 200 mL) and brine. The organic layer was dried over Na_2SO_4, filtered and concentrated *in vacuo*. The crude product was purified

by flash column chromatography on silica gel (pentane/EtOAc 90:10) to give the desired product (9.03 g, 75%) as a yellow oil.

ν_{max} (film) 2960 (C–H), 1767 (C=O), 1337 (B–O), 1195, 1180, 1153 (C–F); ^{1}H NMR (400 MHz, $CDCl_3$) δ 8.09–8.02 (2H, m, H2, H6), 7.99–7.92 (2H, m, H3, H5), 1.39 (12H, s, H10); ^{13}C NMR (100 MHz, $CDCl_3$) δ 180.8 (C7), 135.2 (C3, C5), 131.7 (C2, C6), 128.9 (q, J = 210 Hz, C8), 84.5 (C9), 24.8 (C10); ^{19}F NMR (377 MHz, $CDCl_3$) δ –71.5; ^{11}B NMR (128 MHz, $CDCl_3$) δ 22.3; HRMS (APCI$^+$) $C_{14}H_{17}O_3BF_3^+$ ([M+H]$^+$) requires 300.1254, found 300.1255.

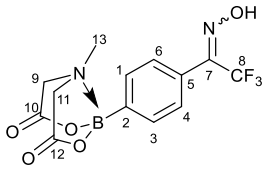
6-Methyl-2-(4-(2,2,2-trifluoroacetyl)phenyl)-1,3,6,2-dioxazaborocane-4,8-dione (59)



$NaIO_4$ (4.3 g, 20.0 mmol) was added to a solution of **91** (3.0 g, 10.0 mmol) in acetone (90 mL) and the reaction mixture was stirred at rt for 2 h. The reaction mixture was concentrated *in vacuo*, diluted with water and neutralised with 1M HCl. The mixture was extracted with CH_2Cl_2, and the organic layer was washed with water and brine and dried over Na_2SO_4. The solution was filtered and concentrated *in vacuo* to give the crude boronic acid as a yellow solid. MIDA (4.4 g, 30.0 mmol) and 3Å MS (3.6 g) was added to a solution of the boronic acid in anhydrous DMF (100 mL). The reaction mixture was heated at 90 °C for 16 h. The mixture was cooled to rt over 1 h then filtered. The filtrate was concentrated *in vacuo*, diluted with EtOAc, and washed with 5% LiCl and brine. The organic layer was dried over Na_2SO_4, filtered and concentrated *in vacuo*. The crude product was purified was purified by flash column chromatography on silica gel (EtOAc/CH_3CN 2:1) to give the desired product as an off-white solid. The product was redissolved in minimal amount of acetone, and addition of Et_2O resulted in a white precipitate. The mixture was filtered under vacuum to obtain the desired product (1.4 g, 42%) as a white solid.

mp 170–174 °C; ν_{max} (film) 2956 (C–H), 1745 (C=O), 1298, 1177, 1040; ^{1}H NMR (400 MHz, acetone-d_6) δ 7.73 (2H, d, *J* = 7.9 Hz, H4, H6), 7.63–7.52 (2H, m, H1, H3), 4.37 (2H, d, *J* = 17.0 Hz, H9a, H11a), 4.19 (2H, d, *J* = 17.0 Hz, H9b, H11b), 2.76 (3H, s, H13); ^{13}C NMR (100 MHz, acetone-d_6) δ 169.3 (C10, C12), 139.8 (C2), 132.9 (C1, C3), 127.7 (C4, C6), 126.0 (C5), 94.1 (q, *J* = 81.9 Hz, C8), 62.9 (C9, C11), 48.3 (C13); ^{19}F NMR (377 MHz, acetone-d$_6$) δ –84.6; ^{11}B NMR (128 MHz, acetone-d$_6$) δ 10.6; HRMS (EI$^-$, in CH_3CN) $C_{13}H_{11}O_5NBF_3^-$ ([M–H]$^-$) requires 328.0713, found 328.0716.

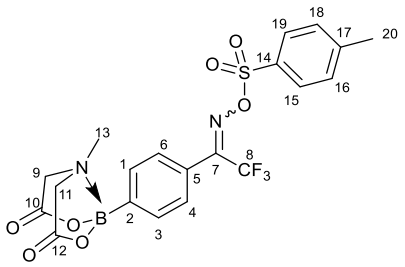
6-Methyl-2-(4-(2,2,2-trifluoro-1-(hydroxyimino)ethyl)phenyl)-1,3,6,2-dioxazaborocane-4,8-dione (60)



Hydroxylamine hydrochloride (243 mg, 3.5 mmol) was added to a solution of **59** (1.0 g, 2.9 mmol) in anhydrous CH_3CN/pyridine (1:2) (18 mL). The reaction mixture was heated at 80 °C for 16 h and concentrated *in vacuo*. The reaction mixture was diluted with EtOAc, washed with water and brine. The organic layer was dried over Na_2SO_4, filtered and concentrated *in vacuo*. The crude product was purified by flash column chromatography on silica gel (EtOAc/CH_3CN 2:1) to give the desired product (320 mg, 32%) as a blue oil.

ν_{max} (film) 3331 (O–H), 2959 (C–H), 1764, 1747 (C=O), 1338 (N–O); ^{1}H NMR (400 MHz, acetonitrile-d_3) δ 10.6 (br. s, O*H*, isomer A), 10.2 (br. s, O*H*, isomer B), 7.68–7.57 (2H, m, Ar*H*), 7.56–7.47 (2H, m, Ar*H*), 4.16–4.04 (2H, m, H9a, H11a), 4.01–3.87 (2H, m, H9b, H11b), 2.56 (s, H13, isomer B), 2.54 (s, H13, isomer A); ^{19}F NMR (377 MHz, acetonitrile-d_3) δ –63.2, –67.0; ^{11}B NMR (128 MHz, CD_3CN) δ 10.5; HRMS (ESI$^+$, in CH_3CN) $C_{13}H_{11}O_5N_2BF_3^+$ ([M+H]$^+$) requires 342.0755, found 342.0754.

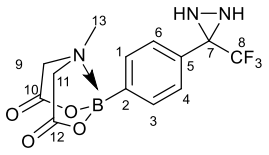
6-Methyl-2-(4-(2,2,2-trifluoro-1-((tosyloxy)imino)ethyl)phenyl)-1,3,6,2-dioxazaborocane-4,8-dione (61)



p-Toulenesulfonyl chloride (191 mg, 1.0 mmol) was added to a solution of oxime **60** (300 mg, 0.87 mmol), DMAP (10.6 mg, 0.09 mmol) and triethylamine (0.15 mL) in anhydrous CH_3CN (9 mL). The reaction mixture was stirred at rt for 3 h and concentrated *in vacuo*. The reaction mixture was diluted with EtOAc, washed with water and brine. The organic layer was dried over Na_2SO_4, filtered and concentrated *in vacuo*. The crude product (350 mg, 71%) was obtained as a green oil.

ν_{max} (film) 2917 (C–H), 1770 (C=O), 1650 (C=N), 1195; ^{1}H NMR (400 MHz, acetonitrile-d_3) δ 7.54 (2H, d, J = 8.3 Hz, H15, H19), 7.45–7.31 (4H, m, H1, H3, H4, H6), 7.09 (2H, d, J = 6.7 Hz, H16, H18), 4.07–3.93 (2H, m, H9a, H11a), 3.90–3.79 (2H, m, H9b, H11b), 2.43 (s, H13, isomer B), 2.38 (s, H13, isomer A), 2.26 (3H, s, H20); ^{19}F NMR (377 MHz, acetonitrile-d_3) δ –62.5, –67.8; ^{11}B NMR (128 MHz, acetonitrile-d_3) δ 11.0; HRMS (EI$^-$, in CH_3CN) $C_{20}H_{17}O_7N_2BF_3S^-$ ([M–H]$^-$) requires 496.0843, found 496.0838.

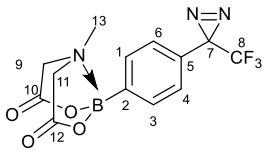
6-Methyl-2-(4-(3-(trifluoromethyl)diaziridin-3-yl)phenyl)-1,3,6,2-dioxazaborocane-4,8-dione (62)



Tosyl oxime **61** (400 mg, 0.80 mmol) was dissolved in anhydrous CH_3CN/CH_2Cl_2 (1:2) (16 mL) and cooled to –78°C. Excess liquid ammonia was condensed into the flask and the reaction was stirred at –78°C for 6 h before being warmed to rt over 16 h. The reaction mixture was concentrated *in vacuo*, diluted with EtOAc and washed with water and brine. The organic layer was dried over Na_2SO_4, filtered and concentrated *in vacuo*. The crude product was purified by flash column chromatography on silica gel (EtOAc/CH_3CN 2:1) to give the desired product (250 mg, 91%) as a yellow oil.

ν_{max} (film) 3259 (N–H), 2929 (C–H), 1768 (C=O), 1636, 1153 (C–N); ^{1}H NMR (400 MHz, acetonitrile-d_3) δ 7.66–7.57 (2H, m, H4, H6), 7.31–7.25 (2H, m, H1, H3), 4.20–4.06 (2H, m, H9a, H11a), 4.02–3.86 (2H, m, H9b, H11b), 2.92 (1H, d, J = 0.4 Hz, N*H*), 2.80 (1H, d, J = 0.7 Hz, N*H*), 2.51 (3H, s, H13); ^{19}F NMR (377 MHz, acetonitrile-d_3) δ –76.0; ^{11}B NMR (128 MHz, acetonitrile-d_3) δ 11.2; HRMS (ESI$^-$, in CH_3CN) $C_{13}H_{12}O_4N_3BF_3^-$ ([M–H]$^-$) requires 341.0915, found 341.0912.

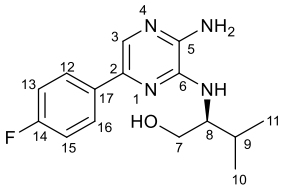
6-Methyl-2-(4-(3-(trifluoromethyl)-3H-diazirin-3-yl)phenyl)-1,3,6,2-dioxazaborocane-4,8-dione (63)



Iodine (220 mg,m 0.88 mmol) in CH_3CN (2.2 mL) was added dropwise to a solution of **62** (250 mg, 0.73 mmol) and NEt_3 in anhydrous CH_3CN (14 mL). The reaction was stirred at rt for 20 min, then concentrated *in vacuo*. The reaction mixture was diluted with EtOAc and washed with 10% $Na_2S_2O_5$, water and brine.. The organic layer was dried over Na_2SO_4, filtered and concentrated *in vacuo*. The crude product was purified by flash column chromatography on silica gel (EtOAc/CH_3CN 2:1) to give the desired product (150 mg, 44%) as a yellow oil.

ν_{max} (film) 2980 (C–H), 1763 (C=O), 1179, 1149 (C–N); ^{1}H NMR (400 MHz, CD_3CN) δ 7.66–7.59 (2H, m, H4, H6), 7.33–7.24 (2H, m, H1, H3), 4.15–4.06 (2H, m, H9a, H11a), 3.97–3.86 (2H, m, H9b, H11b), 2.51 (3H, s, H13); ^{13}C NMR (100 MHz, CD_3CN δ 171.3 (C10, C12), 136.2 (C2), 133.9 (C1, C3), 126.4 (C4, C6), 123.2 (C5), 102.4 (q, J = 95.7 Hz, C8), 62.6 (C9, C11), 48.2 (C13); ^{19}F NMR (377 MHz, CD_3CN) δ –66.1; ^{11}B NMR (128 MHz, CD_3CN) δ 11.0; HRMS (ESI$^-$, in CH_3CN) $C_{13}H_{10}O_4N_3BF_3^-$ ([M–H]$^-$) requires 339.0758, found 339.0754.

(S)-2-((3-Amino-6-(4-fluorophenyl)pyrazin-2-yl)amino)-3-methylbutan-1-ol (66)

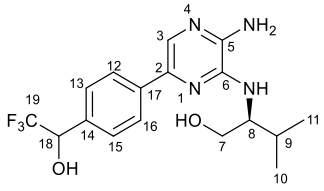


Aryl bromide **1** (50 mg, 0.18 mmol), 4-fluorophenyl boronic acid MIDA ester **65** (60 mg, 0.18 mmol), PPh_3 (7.2 mg, 0.027 mmol) and K_2CO_3 (126 mg, 0.91 mmol) were suspended in degassed DMF/water (2:1, 1.8 mL). $Pd(OAc)_2$ (2.0 mg, 0.010 mmol) was added and the reaction mixture

was heated in a sealed vial at 80 °C for 18 h under argon. The reaction mixture was diluted with EtOAc, then washed with water and brine. The organic layer was dried over Na_2SO_4, filtered and concentrated *in vacuo*. The crude product was purified by flash column chromatography on silica gel (CH_2Cl_2/MeOH 95:5) to give the desired product (50 mg, 95%) as an off-white solid.

mp 120–124 °C; ν_{max} (solid) 3460 (N–H or O–H), 2981 (C–H), 1380; ^{1}H NMR (400 MHz, DMSO-d_6) δ 7.94–7.83 (2H, m, H15, H13), 7.69 (1H, s, H3), 7.24–7.14 (2H, m, H12, H16), 6.20 (2H, s, NH_2), 5.84 (1H, d, J = 8.0 Hz, N*H*), 4.57 (1H, t, J = 5.4 Hz, O*H*), 4.15–4.05 (1H, m, H8), 3.64–3.51 (2H, m, H7), 2.05 (1H, h, J = 6.8 Hz, H9), 0.95 (3H, d, J = 6.8 Hz, H11), 0.94 (3H, d, J = 6.9 Hz, H10); ^{13}C NMR (100 MHz, DMSO-d_6) δ 161.4 (d, J = 243.1 Hz, C14), 143.3 (C6), 142.3 (C5), 135.1 (C2), 134.8 (d, J = 3.1 Hz, C17), 126.3 (d, J = 7.9 Hz, C13, C15), 123.9 (C3), 115.2 (d, J = 21.4 Hz, C12, C16), 60.6 (C7), 56.9 (C8), 28.4 (C9), 19.6 (C11), 18.7 (C10); ^{19}F NMR (377 MHz, DMSO-d_6) δ –112.1; *m/z* (ESI$^+$) 291 ([M+H]$^+$, 100%); HRMS (ESI$^+$) $C_{15}H_{20}ON_4F_3^+$ ([M+H]$^+$) requires 291.1616, found 291.1618.

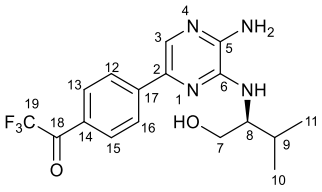
(2S)-2-((3-Amino-6-(4-(2,2,2-trifluoro-1-hydroxyethyl)phenyl)pyrazin-2-yl)amino)-3-methylbutan-1-ol (67)



Aryl bromide **15** (50 mg, 0.18 mmol), trifluoromethyl boronate **59** (46 mg, 0.18 mmol), PPh_3 (7.2 mg, 0.027 mmol) and K_2CO_3 (126 mg, 0.91 mmol) were suspended in degassed DMF/water (2:1, 1.8 mL). $Pd(OAc)_2$ (2.0 mg, 0.010 mmol) was added and the reaction mixture was heated in a sealed vial at 80 °C for 18 h under argon. The reaction mixture was diluted with EtOAc, then washed with water and brine. The organic layer was dried over Na_2SO_4, filtered and concentrated *in vacuo*. The crude product was purified by flash column chromatography on silica gel (CH_2Cl_2/MeOH 95:5) to give the product (58 mg, 87%) as an orange solid.

$[\alpha]_D^{25}$ –51.9 (*c* = 0.1 in MeOH); mp 138–142 °C; ν_{max} (film) 3361 (N–H or O–H), 3246 (N–H or O–H), 2962 (C–H), 1477, 1262, 1169, 1127; ^{1}H NMR (400 MHz, methanol-d_4) δ 7.84–7.75 (2H, m, H12, H16), 7.57 (1H, s, H3), 7.43–7.36 (2H, m, H13, H15), 4.93 (1H, q, *J* = 7.1 Hz, H18), 4.14 (1H, ddd, *J* = 6.8, 5.8, 4.4 Hz, H8), 3.76–3.60 (2H, m, H7), 2.05–1.86 (1H, m, H9), 0.95 (3H, d, *J* = 6.8 Hz, H11), 0.94 (3H, d, *J* = 6.8 Hz, H10); ^{13}C NMR (100 MHz, methanol-d_4) δ 143.2 (C6), 138.8 (C14), 137.6 (C5), 134.3 (C17), 127.5 (C13, C15), 126.6 (C2), 124.6 (C12, C16), 123.4 (C3), 120.1 (q, *J* = 199 Hz, C19), 71.6 (q, *J* = 31.4 Hz, C18), 61.8 (C7), 57.6 (C8), 28.8 (C9), 18.6 (C11), 18.0 (C10); ^{19}F NMR (377 MHz, methanol-d_4) δ –79.6 (d, *J* = 7.1 Hz); *m/z* (ESI$^+$) 371 ([M+H]$^+$, 100%); HRMS (ESI$^+$) $C_{17}H_{22}O_2N_4F_3^+$ ([M+H]$^+$) requires 371.1687, found 371.1686.

(S)-1-(4-(5-Amino-6-((1-hydroxy-3-methylbutan-2-yl)amino)pyrazin-2-yl)phenyl)-2,2,2-trifluoroethan-1-one (68)

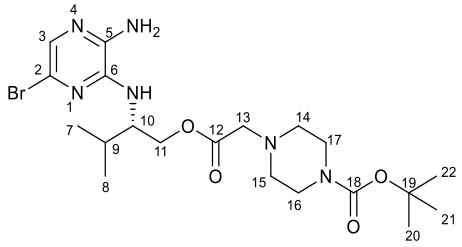


Aryl bromide **15** (40 mg, 0.15 mmol), trifluoromethyl boronate **59** (46 mg, 0.15 mmol), PPh_3 (5.7 mg, 0.021 mmol) and K_2CO_3 (100 mg, 0.72 mmol) were suspended in degassed DME/water (2:1, 1.5 mL). $Pd(OAc)_2$ (1.6 mg, 0.010 mmol) was added and the reaction mixture was heated in a sealed vial at 80 °C for 18 h under argon. The reaction mixture was diluted with EtOAc, then washed with water and brine. The organic layer was dried over Na_2SO_4, filtered and concentrated *in vacuo*. The crude product was purified by flash column chromatography on silica gel (CH_2Cl_2/MeOH 95:5) to give the desired product (38 mg, 70%) as an orange solid.

$[\alpha]_D^{25}$ –12.4 (*c* = 0.1 in MeOH); mp 162–166 °C; ν_{max} (film) 3370 (N–H or O–H), 3244 (N–H or O–H), 2963 (C–H), 1708, 1649 (C=O), 1470, 1175; ^{1}H NMR (400 MHz, acetonitrile-d_3) δ 8.19–8.13 (2H, m, H12, H16), 8.12–8.05 (2H, m, H13, H15), 7.96 (1H, s, H3), 5.22 (2H, s, NH_2), 4.92

(1H, d, *J* = 8.2 Hz, N*H*), 4.20 (1H, ddd, *J* = 8.3, 6.8, 4.1 Hz, H8), 3.76–3.65 (2H, m, H7), 2.12–1.99 (1H, m, H9), 1.03 (3H, d, *J* = 6.8 Hz, H10), 1.02 (3H, d, *J* = 6.8 Hz, H11); ^{13}C NMR (100 MHz, acetonitrile-d_3) δ 179.9 (C18), 149.0 (C14), 146.4 (C17), 145.2 (C6), 143.7 (C5), 136.7 (C2), 131.0 (C13, C15), 128.1 (C3), 126.5 (q, *J* = 210 Hz, C19), 125.9 (C12, C16), 62.3 (C7), 58.4 (C8), 29.7 (C9), 19.4 (C10), 19.0 (C11); ^{19}F NMR (377 MHz, acetonitrile-d_3) δ –72.0; *m/z* (ESI$^+$) 387 ([M+OH+H]$^+$, 100%), 369 ([M+H]$^+$, 10%); HRMS (ESI$^+$) $C_{17}H_{20}O_2N_4F_3^+$ ([M+H]$^+$) requires 369.1533, found 369.1530.

tert-Butyl (S)-4-(2-(2-((3-amino-6-bromopyrazin-2-yl)amino)-3-methylbutoxy)-2-oxoethyl)piperazine-1-carboxylate (92)

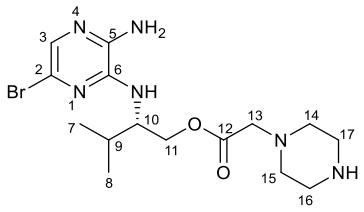


15 (550 mg, 2 mmol) was added to a solution of HATU (1.06 g, 2.8 mmol) in DMF (5 mL). DIPEA (1.4 mL, 8 mmol) was added and the solution was stirred at room temperature for 18 h. The reaction mixture was extracted with EtOAc (50 mL) twice, washed with brine/water (1:1) (2 x 50 mL), brine and dried over Na_2SO_4. The crude product was purified by flash column chromatography on silica gel (CH_2Cl_2/MeOH 98:2) to give the desired product (820 mg, 82%) as an orange solid.

$[\alpha]_D^{25}$ –48.8 (*c* = 0.1 in MeOH); ν_{max} (film) 3246 (N–H), 2935 (C–H), 1690 (C=O), 1423, 1168 (C–O); ^{1}H NMR (400 MHz, $CDCl_3$) δ 7.39 (1H, s, H3), 4.77 (1H, d, *J* = 8.3 Hz, N*H*), 4.43–4.33 (1H, m, H10), 4.30–4.19 (2H, m, H11), 3.43 (4H, t, *J* = 5.1 Hz, H17, H16), 3.27–3.11 (2H, m, H13), 2.47 (4H, t, *J* = 5.1 Hz, H14, H15), 1.94 (1H, h, *J* = 6.8 Hz, H9), 1.45 (9H, s, H20, H21, H22), 1.00 (3H, d, *J* = 6.7 Hz, H8), 0.99 (3H, d, *J* = 6.8 Hz, H7); ^{13}C NMR (101 MHz, $CDCl_3$) δ 170.5 (C12), 154.8 (C18), 144.2 (C6), 141.9 (C5), 129.7 (C3), 126.1 (C2), 80.1 (C19), 65.0 (C11),

59.6 (C13), 55.0 (C10), 52.8 (C14, C15), 43.9 (C16, C17), 29.9 (C9), 28.5 (C20, C21, C22), 19.3 (C8), 19.2 (C7); *m/z* (ESI$^+$) 503 ([M(^{81}Br)+H]$^+$, 99%), 501 ([M(^{79}Br)+H]$^+$, 100%); HRMS (ESI$^+$) $C_{20}H_{34}BrN_6O_4^+$ ([M(^{79}Br)+H]$^+$) requires 501.1819, found 501.1822.

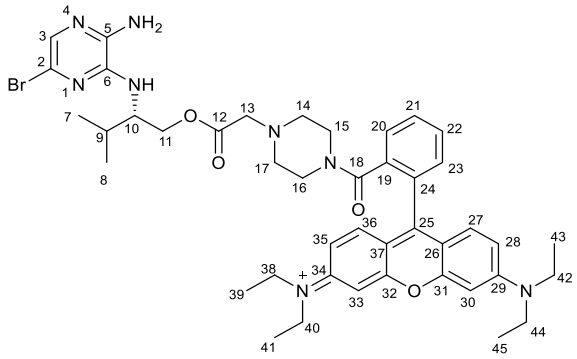
(S)-2-((3-Amino-6-bromopyrazin-2-yl)amino)-3-methylbutyl 2-(piperazin-1-yl)acetate (80)



Following *general procedure 2*, TFA (2 mL) was added to **91** (800 mg, 1.6 mmol) in CH_2Cl_2 (10 mL) and the reaction was stirred for 16 h. The crude product was obtained as an orange solid (556 mg, 87%).

$[\alpha]_D^{25}$ –25.6 (*c* = 0.1 in MeOH); ν_{max} (film) 3364 (N–H), 3242 (N–H), 2965 (C–H), 1674 (C=O), 1463, 1202 (C–O); ^{1}H NMR (400 MHz, $CDCl_3$) δ 7.29 (1H, s, H3), 5.46 (1H, d, *J* = 7.9 Hz, N*H*), 5.21 (2H, s, NH_2), 4.45–4.34 (2H, m, H11), 4.20–4.14 (1H, m, H10), 3.44–3.30 (2H, m, H13), 3.23–3.10 (4H, m, H16, H17), 2.97–2.84 (4H, m, H15, H14), 2.03–1.91 (1H, m, H9), 1.03 (3H, d, *J* = 6.7 Hz, H7), 1.00 (3H, d, *J* = 6.8 Hz, H8); ^{13}C NMR (100 MHz, $CDCl_3$) δ 170.6 (C12), 143.7 (C6), 142.2 (C5), 128.4 (C3), 124.8 (C2), 64.6 (C11), 58.8 (C13), 55.4 (C10), 48.6 (C15, C14), 44.1 (C16, C17), 29.5 (C9), 19.7 (C7), 19.3 (C8); *m/z* (ESI$^+$) 403 ([M(^{81}Br)+H]$^+$, 99%), 401 ([M(^{79}Br)+H]$^+$, 100%); HRMS (ESI$^+$) $C_{15}H_{26}BrN_6O_2^+$ ([M(^{79}Br)+H]$^+$) requires 401.1295, found 401.1299.

(S)-N-(9-(2-(4-(2-(2-((3-Amino-6-bromopyrazin-2-yl)amino)-3-methylbutoxy)-2-oxoethyl)piperazine-1-carbonyl)phenyl)-6-(diethylamino)-3H-xanthen-3-ylidene)-N-ethylethanaminium (81)

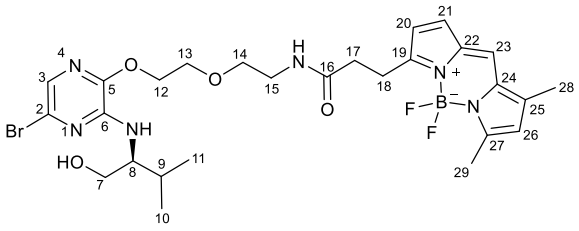


HATU (266 mg, 0.70 mmol) was added to Rhodamine B (288 mg, 0.60 mmol) in DMF (5 mL). DIPEA (0.35 mL) and **80** (200 mg, 0.50 mmol) were added and the reaction mixture was stirred for 19 h. The solution was concentrated *in vacuo*, diluted with CH_2Cl_2, and washed with water and brine. The organic layer was dried over Na_2SO_4, filtered and concentrated *in vacuo*. The crude product was purified by flash column chromatography on silica gel (CH_2Cl_2/MeOH 92:8) to give the desired product (50 mg, 12%) as a dark purple solid.

ν_{max} (film) 3656 (N–H), 2981 (C–H), 1743 (C=O), 1589 (C=O), 1338, 1180 (C–O), 843; ^{1}H NMR (400 MHz, $CDCl_3$) δ 7.69 (1H, dd, *J* = 7.6, 1.4 Hz, H20), 7.64 (1H, td, *J* = 7.6, 1.4 Hz, H21), 7.54 (1H, dd, *J* = 7.7, 1.3 Hz, H22), 7.30 (1H, dd, *J* = 7.5, 0.9 Hz, H23), 7.27 (1H, s, H3), 7.22 (2H, dd, *J* = 9.5, 8.4 Hz, H27, H36), 6.98–6.87 (2H, m, H28, H35), 6.74 (2H, dd, *J* = 2.5, 1.6 Hz, H30, H33), 4.95 (1H, d, *J* = 8.5 Hz, N*H*), 4.65 (2H, s, NH_2), 4.40–4.21 (2H, m, H11), 4.16–4.08 (1H, m, H10), 3.60 (8H, dtd, *J* = 11.8, 7.6, 4.6 Hz, H38, H40, H42, H44), 3.44 (2H, s, H15), 3.34 (2H, s, H16), 3.24–3.11 (2H, m, H13), 2.34 (4H, s, H14, H17), 2.09–1.94 (1H, m, H9), 1.31 (12H, td, *J* = 7.1, 1.8 Hz, H39, H41, H43, H45), 0.98 (3H, d, *J* = 6.7 Hz, H7), 0.96 (3H, d, *J* = 6.8 Hz, H8); ^{13}C NMR (100 MHz, $CDCl_3$) δ 170.0 (C12), 167.4 (C18), 157.9 (C26, C37), 157.8 (C25), 155.8 (C24), 143.8 (C34, C29), 142.4 (C6), 138.8 (C5), 135.6 (C19), 132.2 (C21), 130.8 (C35, C28), 130.3 (C20), 129.9 (C23), 128.1 (C22), 128.0 (C3), 124.4 (C31, C32), 114.2 (C2), 113.9 (C36, C27), 96.3 (C30, C33), 64.5 (C11), 58.7 (C13), 55.2 (C10), 52.5 (C14, C17), 52.4

(C15), 47.3 (C38, C40, C42, C44), 46.2 (C16), 29.3 (C9), 19.7 (C8), 19.5 (C7), 12.7 (C39, C41, C43, C45); *m/z* (ESI$^+$) 827 ([M(^{81}Br)]$^+$, 99%), 825 ([M(^{79}Br)]$^+$, 100%); HRMS (ESI$^+$) $C_{45}H_{54}BrN_8O_4^+$ ([M(^{79}Br)]$^+$) requires 825.3446, found 825.3453.

(S)-N-(2-(2-((5-bromo-3-((1-hydroxy-3-methylbutan-2-yl)amino)pyrazin-2-yl)oxy)ethoxy)ethyl)-3-(5,5-difluoro-7,9-dimethyl-5H-4',5'-dipyrrolo[1,2-c:2",1"-f][1,3,2]diazaborinin-3-yl)propenamide (82)



Following *general procedure 3*, amide coupling was carried out between amine **71** and BODIPY-FL. The crude product obtained was purified by flash column chromatography on silica gel (CH_2Cl_2/MeOH 98:2) to give the desired product (24 mg, 68%) as a purple-green oil.

ν_{max} (film) 3420 (O–H or N–H), 3225 (O–H or N–H), 2984 (C–H), 1665 (C=O), 1550, 1231; ^{1}H NMR (400 MHz, $CDCl_3$) δ 8.04 (1H, s, CON*H*), 7.29 (1H, s, H3), 6.91 (1H, d, *J* = 4.2 Hz, H20), 6.87 (1H, d, *J* = 4.0 Hz, H21), 6.30 (1H, dd, *J* = 9.8, 4.1 Hz, H26), 6.14 (1H, s, H23), 4.51 (1H, d, *J* = 8.5 Hz, N*H*), 4.42-4.35 (2H, m, H7), 3.91-3.83 (1H, m, H8), 3.81-3.74 (4H, m, H14, H15), 3.72-3.66 (2H, m, H17), 3.64-3.51 (2H, m, H18), 3.36-3.24 (4H, m, H12, H13), 2.28 (3H, s, H29), 2.19 (3H, s, H28), 2.07–1.94 (1H, m, H9), 1.03–0.94 (6H, m, H10, H11); ^{13}C NMR (100 MHz, $CDCl_3$) δ 170.3 (C16), 158.3 (C24), 154.6 (C22), 151.2 (C6), 146.4 (C5), 138.5 (C27), 133.1 (C25), 127.3 (C3), 125.6 (C2), 122.1 (C23), 191.1 (C20), 140.5 (C21), 138.7 (C26), 70.2 (C12), 69.8 (C13), 67.5 (C14), 67.2 (C15), 32.2 (C17), 30.4 (C18), 29.8 (C9), 19.9 (C10), 19.7 (C11), 15.5 (C29), 14.1 (C28); *m/z* (ESI$^+$) 638 ([M(^{81}Br)+H]$^+$, 98%), 636 ([M(^{79}Br)+H]$^+$, 100%); HRMS (ESI$^+$) $C_{27}H_{36}BrN_6O_4^+$ ([M(^{79}Br)+H]$^+$) requires 636.2043, found 636.2041.

7.2 Biology Methods

7.2.1 Materials

The following materials were obtained from commercial sources: P7C3-A20 (Cayman Chemical #24201), Biotin-PEG-azide (Sigma-Aldrich #762024), TBTA (Cayman Chemical #18816), TCEP (Sigma-Aldrich #C4706), TAMRA-biotin-azide (DC Biosciences #CCR-1048), Withaferin A (Abcam #ab120644), FiVe1 (Glixx Laboratories Inc #11119), recombinant human vimentin protein (Bio-Techne #NBP2-35139).

7.2.2 Experimental Procedures

7.2.2.1 Primary Neurosphere Culture

Primary neurospheres were obtained by culturing SVZ and DG cells isolated from postnatal day (P)3-6 C57BL/6 mice using 2-3 animals per culture. Animals were administered an overdose of pentobarbital and death was confirmed by cervical dislocation. The brains were removed and transferred to a petri dish containing cold neurobasal-A media (NB-A, GiBCO #10888022). The brains were sliced in 450 µm coronal sections using a McIlwain tissue chopper. Sections containing the SVZ and DG were microdissected separately in NB-A media under a dissection microscope (Leica) and stored in 15ml tubes on ice. 1 mL of accutase solution (Sigma-Aldrich #A6964) was added to the pooled tissue in each tube, and the tissue mixture was incubated for 15 min at 37 °C. Mechanical dissociation via trituration with a 200 µL Pipetteman was carried out to obtain a single cell suspension. NB-A+ media was prepared by adding B27 supplement (GiBCO #17504), glutamax (GiBCO #35050061), 100 U/mL Penicillin-Streptomycin (GiBCO #15140122) and growth factors hEGF (20 ng/mL, Sigma-Aldrich #E9644) and hFGF2 (20 ng/mL, R&D systems #233-FB-025). 12 mL of NB-A+ media was added to the single cell suspension. 2 mL of cell suspension was plated in each well of a 6-well non-treated plate (Corning #351146) and incubated at 37 °C with 5% CO_2. The media was changed after 24 h and the cells were left to grow in the incubator. On day 6, the neurospheres were passaged using accutase, re-suspended in NB-A+ supplemented with hEGF & hFGF2 and plated in ultra-low

attachment cell culture T75 flasks (Corning #CLS3814) at 5 x 10^4 cells/mL. The following passages were carried out every 4 days and cells were always used for experiments as tertiary neurospheres, i.e. after the second passage.

7.2.2.2 Neurosphere Differentiation Assay

For compound screening, 96-well CellCarrier Ultra plates (Perkin Elmer #6055302) were coated with 15 µg/mL poly-ornithine (Sigma-Aldrich #P3655-50MG) in PBS overnight at 4°C, then washed once with PBS and incubated with 10 µg/mL of laminin (Sigma-Aldrich #L2020) in PBS for 1 h at 37 °C. Cells were dissociated with accutase, re-suspended in NB-A+ and seeded as monolayer in 96 well plates (25,000 cells/well). The plates were incubated for overnight before adding the compounds diluted in NB-A+ without growth factors. The compounds were diluted to the following concentrations from a 10 mM stock in DMSO: 25 µM, 10 µM, 2.5 µM, 1 µM, 250 nM, 100 nM, 25 nM, 10 nM, 2.5 nM. The final assay concentration of DMSO was 0.1%. P7C3-A20 was used as a positive control. After compound addition, the cells were left in the incubator to differentiate for 5 days without any media change. 5 µL of NucGreen-488 probe (ThermoFisher #R37109) was added to each well and incubated for 15 min at 37 °C. The cells were washed once with PBS and fixed in 4% paraformaldehyde (PFA, Santa Cruz Biotechnology #sc-281692) for 15 min at rt. The cells were then immunostained and analysed on a high content imaging system (GE InCell 1000 High Content Imager, Target Discovery Institute, Oxford).

7.2.2.3 Immunohistochemical Staining

After fixation, cells were washed once with PBS for 10 min followed by a blocking-permeabilization step for 1 h at rt in PBS+ blocking buffer (PBS with 5% donkey serum and 0.1% Triton-X100). Primary antibodies diluted in blocking buffer were added to the cells (DCX, 1:400) and incubated at 4°C overnight in a rocking shaker. The cells were washed once in PBS for 10 min and incubated with Alexa Fluor secondary antibodies in PBS+ (1:1000) for 1 h at rt. The cells were washed in PBS for 10 min, incubated with Hoechst (1:1000, Thermo Scientific #H3570) for 15 min at rt to label cell nuclei and washed again for 10 min. The cells were kept in

PBS at 4 °C until they are used for imaging. Antibodies used for immunohistochemical staining are presented in Table 10.

Table 10. List of antibodies used for immunohistochemical staining.

Antigen	Dilution	Host	Source	Product No.
DCX	1:400	Goat	Santa Cruz	Sc-8066
βIII-tubulin	1:1000	Rabbit	Covance	MRB-435P-100
Vimentin	1:1000	Mouse	Abcam	Ab8978

7.2.2.4 Cellular Imaging

SVZ- and DG-derived NSCs were seeded in 4-well chamber slides (Thermo Fisher #154461) and left to grow overnight. NB-A media containing the test compound are added to the cells at various concentrations, and incubated for 2 h at 37 °C. The cells were washed once with PBS and fixed in 4% paraformaldehyde for 15 min at rt. The cells were incubated with Hoechst (1:1000, Thermo Scientific #H3570) for 15 min at rt to label cell nuclei and washed again for 10 min. The plastic chambers were removed and drops of FluorSave (Merck #345789) were added to the slide. The slides were stored at 4 °C until they are used for imaging. Fluorescence imaging was done using an EVOS digital inverted microscope equipped with 20X and 40X objectives. Confocal imaging was done on a Zeiss LSM 710 laser scanning confocal microscope.

7.2.2.5 Affinity-based Protein Profiling (AfBPP) with LC-MS/MS Analysis

SVZ- and DG-derived NSCs were plated in 10 cm dishes (Corning #430167) and left to grow overnight. NB-A media containing the test compounds are added to the cells at concentration of 10 µM. The cells were incubated with probes for 2 h at 37°C. The dishes were irradiated on ice for 5 min with a UV lamp (365 nm 100 W lamp, VWR #36595-021). The cells were then washed with PBS three times and lysed in a PBS buffer (250 µL) containing 1 % Triton X-100 (Sigma-Aldrich #X100), 0.1% SDS (Sigma-Aldrich #71736) and EDTA-free protease inhibitor (Thermo Scientific #A32955). The lysates were sonicated thrice (2 s on, 3 s off, 20% amplitude) and centrifuged to remove cell debris. Protein concentration of each lysate sample was determined using a bicinchoninic acid protein assay (Thermo Scientific #23225) and adjusted to 2.5 mg/mL.

400 µL of each protein lysate in lysis buffer (1000 µg, 2.5 mg/mL) was treated with a click reaction master mix (24 µL per sample), which was prepared freshly as follows: biotin capture reagent (AzRB, 50 µL, 10 mM DMSO stock concentration; 100 µM final concentration), $CuSO_4$ (100 µL, 50 mM stock concentration; 1 mM final concentration), TCEP (100 µL, 50 mM stock concentration; 1 mM final concentration) and TBTA (50 µL, 10 mM DMSO stock concentration; 0.1 mM final concentration). 24 µL of master mix was added to each sample and the sample vortexed for 1 h at room temperature. The reaction was quenched by addition of EDTA (8 µL per sample, 500mM stock, final concentration 10 mM).

The proteins were precipitated by addition of methanol (800 µL), chloroform (200 µL) and water (400 µL), followed by centrifugation (6000 × g, 4 min). The upper liquid phase was discarded before addition of methanol (1.6 mL), vortexing, sonication and centrifugation (8000 × g, 4 min). The resulting protein pellet was washed twice with methanol (1.6 mL), with vortexing, sonication and centrifugation (8000 × g, 4 min). The pellet was air dried for 10 min before being resuspended in 40 µL of HEPES buffer (50 mM, pH 8.0) with 2% SDS.

Avidin agarose beads (100 µL, Thermo Scientific #20225) were washed with 0.2% SDS/HEPES buffer thrice. Resuspended protein samples were added to the derivatised beads and incubated for 2 h at rt with mild shaking. The samples were centrifuged (2000 x g, 1 min) and the supernatant was removed. The beads were washed with 0.2% SDS/HEPES buffer three times and HEPES buffer three times. TCEP (15 µL of 50 mM stock) and CAA (15 µL of 150 mM stock) were added for the reduction and alkylation of samples. The samples were incubated for 10 min with gentle shaking at rt. 7.5 µL of Trypsin (20 µg/100 µL, Thermo Scientific #90057) was added to each sample and incubated overnight at 37 °C.

EDTA-free protease inhibitor (4 µL) was added to quench the trypsin reaction. Samples were centrifuged (6000 x g, 2 min) and supernatant was collected. Supernatant was dried on a SpeedVac concentrator at 45 °C for 2 h to dryness. Samples were resuspended in 0.5% TFA, 1% acetonitrile in proteomic grade H_2O. The samples were desalted using stage-tips prepared with

polystyrene-divinylbenzene co-polymer (SDB-XC) discs and resuspended in 60% ACN in H_2O. The samples were dried overnight using a SpeedVac at 45 °C. Samples were resuspended in 2% ACN, 0.5 % TFA in proteomic grade H_2O. The samples were filtered through 3 layers of PVDF Durapore filter discs on a stage-tip before loading onto the LC-MS.

Peptide identification and quantification were performed using MaxQuant (Version 1.6.3.4). MS spectra were searched against the *Mus musculus* UniProt Reference proteome. Protein intensities were transformed and normalised across samples using Perseus (Version 1.6.6.0).

7.2.2.6 AfBPP with Immunoblotting

The same sample preparation for cell lysates was carried out as in described in Section 7.2.2.5. 300 µL of each protein lysate in lysis buffer (600 µg, 2 mg/mL) was treated with a click reaction master mix (18 µL per sample), which was prepared freshly as follows: biotin capture reagent (biotin-PEG-azide, 50 µL, 10 mM DMSO stock concentration; 100 µM final concentration), $CuSO_4$ (100 µL, 50 mM stock concentration; 1 mM final concentration), TCEP (100 µL, 50 mM stock concentration; 1 mM final concentration) and TBTA (50 µL, 10 mM DMSO stock concentration; 0.1 mM final concentration). 18 µL of master mix was added to each sample and the sample vortexed for 1 h at room temperature. The reaction was quenched by addition of EDTA (6 µL per sample, 500mM stock, final concentration 10 mM).

Excess click reagents were removed by methanol/chloroform precipitation as described previously. The protein pellet was resuspended in PBS buffer (300 µL) with 0.2% SDS. Magnetic streptavidin beads (15 µL per sample, Thermo Scientific #65601) were washed three times with 0.2% SDS/PBS before addition of the resuspended protein samples. The samples were incubated for 2 h at rt with mild shaking. The beads were washed with 0.2% SDS/PBS three times and eluted with heating at 95 °C for 10 min in NuPAGE LDS sample buffer (30 µL, Thermo Scientific #NP0008).

The eluted proteins were separated by NuPAGE 4-12% Bis-Tris protein gel electrophoresis and transferred to a PVDF membrane. 2% BLOT-QuickBlocker (Merck #WB57) in PBST (PBS with 0.05% Tween-20) was used as blocking buffer. Vimentin protein was detected with an anti-vimentin antibody (1:1000, Abcam #ab92547) and anti-rabbit secondary antibody (Alexa Fluor 647, #A31573). The membrane was washed with PBST three times before imaging on an Odyssey Li-Cor imager.

7.2.2.7 MS Analysis for Site of Probe Modification

The vimentin recombinant protein (1 mg, Bio-Techne #NBP2-35139) was dissolved in 4 mM HCl (1 mL) to give a 1 mg/mL solution, then diluted with PBS buffer (1 mL) to give a 9 µM stock solution. Compounds were diluted 10-fold from the 10 mM DMSO stock solution. 1 µL of each diluted compound was added to 9 µL of protein solution. The tubes were irradiated with a UV lamp for 5 min on ice. The probe-protein solution was transferred to a 10 kDa MWCO Vivaspin 500 concentrator and centrifuged (10000 x g, 5 min) to remove the excess probe. TCEP (2 µL of 50 mM stock) and CAA (5 µL of 300 mM) was added for reduction and alkylation of samples. The samples were incubated in the dark for 10 min with shaking. The Vivaspin concentrators were washed three times with PBS (100 µL), with centrifugation each time (10000 x g, 3 min) to remove excess liquid. Trypsin (0.5 µg) was added to each sample and the samples were incubated overnight at 37 °C on a heat block. The digested peptides were eluted from the concentrator with PBS (40 µL) and NaCl (0.5 M, 40 µL), by centrifugation (17000 x g, 5 min). Protease inhibitor (2 µL) was added to quench the digestion. The digested peptides were desalted using stage-tips prepared with polystyrene-divinylbenzene co-polymer (SDB-XC) discs and resuspended in 80% ACN in H_2O. The samples were dried overnight using a SpeedVac at 45 °C. Samples were resuspended in 2% ACN, 0.5 % TFA in proteomic grade H_2O. The samples were filtered through 3 layers of PVDF Durapore filter discs on a stage-tip before loading onto the LC-MS.

Peptide identification and quantification were performed using PEAKS X software. MS spectra were searched against the *Homo sapiens* UniProt Reference vimentin sequence (P08670).

7.2.2.8 WaterLOGSY

WaterLOGSY experiments were conducted by Dr Carole Bataille. They were conducted at a ^{1}H frequency of 600 MHz using a Bruker Avance spectrometer equipped with a BBI probe. The vimentin recombinant protein (1 mg, Bio-Techne #NBP2-35139) was dissolved in 4 mM HCl (500 µL) to give a 2 mg/mL solution, then diluted with H_2O PBS buffer (500 µL) to give the 18.2 µM stock solution. The compound (10 µL of a 10 mM solution in DMSO-d6) was added to an eppendorf tube before sequential addition of the H_2O PBS buffer (60 µL), D_2O (20 µL), and protein (110 µL, 18.2 µM) to get a final volume of 200 µL. The resulting solution was spun to ensure well mixing and transferred to a 3 mm NMR tube for the waterLOGSY run.

7.2.2.9 Thermal Shift Assay

Two buffer systems were prepared as follows: Tetramer buffer (2 mM phosphate, pH 7.5) and IF assembly buffer (2 mM phosphate, pH 7.5, 200 mM KCl). Vimentin recombinant protein (1 mg, Bio-Techne #NBP2-35139) was dissolved in 4 mM HCl (500 µL) to give a 2 mg/mL solution. Compounds in 10 mM DMSO stock solutions were diluted with selected buffer system. Protein Thermal Shift Dye (Thermo Scientific #4461146) was diluted 1:125 in selected buffer system. To each well of a 96-well plate (Thermo Scientific #N8010560), protein (15 µL), ligand (2.5 µL) and diluted dye (2.5 µL) were added to give a total volume of 20 µL. Fluorescence readings were taken between 25 °C and 90 °C, with the temperature increasing 1 °C every min, on a thermocycler. Protein Thermal Shift Software (version 1.4) was used to determine T_m values from the melt curves.

Chapter 8 References

(1) Fuentealba, L. C.; Obernier, K.; Alvarez-Buylla, A. *Cell Stem Cell* **2012**, *10*, 698.

(2) Zhao, C.; Deng, W.; Gage, F. H. *Cell* **2008**, *132*, 645.

(3) Bonaguidi, M. A.; Wheeler, M. A.; Shapiro, J. S.; Stadel, R. P.; Sun, G. J.; Ming, G.-l.; Song, H. *Cell* **2011**, *145*, 1142.

(4) Goncalves, J. T.; Schafer, S. T.; Gage, F. H. *Cell* **2016**, *167*, 897.

(5) Seri, B.; García-Verdugo, J. M.; Collado-Morente, L.; McEwen, B. S.; Alvarez-Buylla, A. *Journal of Comparative Neurology* **2004**, *478*, 359.

(6) Sorrells, S. F.; Paredes, M. F.; Cebrian-Silla, A.; Sandoval, K.; Qi, D.; Kelley, K. W.; James, D.; Mayer, S.; Chang, J.; Auguste, K. I.; Chang, E. F.; Gutierrez, A. J.; Kriegstein, A. R.; Mathern, G. W.; Oldham, M. C.; Huang, E. J.; Garcia-Verdugo, J. M.; Yang, Z.; Alvarez-Buylla, A. *Nature* **2018**, *555*, 377.

(7) Kempermann, G. *Cold Spring Harbor Perspectives in Biology* **2015**, *7*.

(8) Boldrini, M.; Fulmore, C. A.; Tartt, A. N.; Simeon, L. R.; Pavlova, I.; Poposka, V.; Rosoklija, G. B.; Stankov, A.; Arango, V.; Dwork, A. J.; Hen, R.; Mann, J. J. *Cell Stem Cell* **2018**, *22*, 589.

(9) Moreno-Jiménez, E. P.; Flor-García, M.; Terreros-Roncal, J.; Rábano, A.; Cafini, F.; Pallas-Bazarra, N.; Ávila, J.; Llorens-Martín, M. *Nature Medicine* **2019**, *25*, 554.

(10) Eriksson, P. S.; Perfilieva, E.; Björk-Eriksson, T.; Alborn, A.-M.; Nordborg, C.; Peterson, D. A.; Gage, F. H. *Nature Medicine* **1998**, *4*, 1313.

(11) Spalding, K. L.; Bergmann, O.; Alkass, K.; Bernard, S.; Salehpour, M.; Huttner, H. B.; Bostrom, E.; Westerlund, I.; Vial, C.; Buchholz, B. A.; Possnert, G.; Mash, D. C.; Druid, H.; Frisen, J. *Cell* **2013**, *153*, 1219.

(12) Roy, N. S.; Wang, S.; Jiang, L.; Kang, J.; Benraiss, A.; Harrison-Restelli, C.; Fraser, R. A. R.; Couldwell, W. T.; Kawaguchi, A.; Okano, H.; Nedergaard, M.; Goldman, S. A. *Nature Medicine* **2000**, *6*, 271.

(13) Lazarini, F.; Lledo, P.-M. *Trends in Neurosciences* **2011**, *34*, 20.

(14) Trouche, S.; Bontempi, B.; Roullet, P.; Rampon, C. *Proceedings of the National Academy of Sciences* **2009**, *106*, 5919.

(15) Schmidt-Hieber, C.; Jonas, P.; Bischofberger, J. *Nature* **2004**, *429*, 184.

(16) Wojtowicz, J. M. *Hippocampus* **2006**, *16*, 261.

(17) Wojtowicz, J. M.; Askew, M. L.; Winocur, G. *European Journal of Neuroscience* **2008**, *27*, 1494.

(18) Egeland, M.; Zunszain, P. A.; Pariante, C. M. *Nat Rev Neurosci* **2015**, *16*, 189.

(19) Kempermann, G.; Kuhn, H. G.; Gage, F. H. *Nature* **1997**, *386*, 493.

(20) Fitzsimons, C. P.; Herbert, J.; Schouten, M.; Meijer, O. C.; Lucassen, P. J.; Lightman, S. *Frontiers in Neuroendocrinology* **2016**, *41*, 44.

(21) Planchez, B.; Surget, A.; Belzung, C. *Current Opinion in Pharmacology* **2020**, *50*, 88.

(22) Shimazu, K.; Zhao, M.; Sakata, K.; Akbarian, S.; Bates, B.; Jaenisch, R.; Lu, B. *Learning & Memory* **2006**, *13*, 307.

(23) Zhang, C.-L.; Zou, Y.; He, W.; Gage, F. H.; Evans, R. M. *Nature* **2008**, *451*, 1004.

(24) Naylor, A. S.; Persson, A. I.; Eriksson, P. S.; Jonsdottir, I. H.; Thorlin, T. *Journal of Neurophysiology* **2005**, *93*, 2406.

(25) Kim, Y.-P.; Kim, H.; Shin, M.-S.; Chang, H.-K.; Jang, M.-H.; Shin, M.-C.; Lee, S.-J.; Lee, H.-H.; Yoon, J.-H.; Jeong, I.-G.; Kim, C.-J. *Neuroscience Letters* **2004**, *355*, 152.

(26) Santarelli, L.; Saxe, M.; Gross, C.; Surget, A.; Battaglia, F.; Dulawa, S.; Weisstaub, N.; Lee, J.; Duman, R.; Arancio, O.; Belzung, C.; Hen, R. *Science* **2003**, *301*, 805.

(27) Arvidsson, A.; Collin, T.; Kirik, D.; Kokaia, Z.; Lindvall, O. *Nature Medicine* **2002**, *8*, 963.

(28) Chen, X.-H.; Iwata, A.; Nonaka, M.; Browne, K. D.; Smith, D. H. *Journal of Neurotrauma* **2003**, *20*, 623.

(29) Dash, P. K.; Mach, S. A.; Moore, A. N. *Journal of Neuroscience Research* **2001**, *63*, 313.

(30) Sun, D.; McGinn, M. J.; Zhou, Z.; Harvey, H. B.; Bullock, M. R.; Colello, R. J. *Experimental Neurology* **2007**, *204*, 264.
(31) Zheng, W.; ZhuGe, Q.; Zhong, M.; Chen, G.; Shao, B.; Wang, H.; Mao, X.; Xie, L.; Jin, K. *Journal of neurotrauma* **2013**, *30*, 1872.
(32) Ihunwo, A. O.; Tembo, L. H.; Dzamalala, C. *Neural Regen Res* **2016**, *11*, 1869.
(33) Ma, D. K.; Kim, W. R.; Ming, G.-l.; Song, H. *Ann N Y Acad Sci* **2009**, *1170*, 664.
(34) Seidenfaden, R.; Desoeuvre, A.; Bosio, A.; Virard, I.; Cremer, H. *Molecular and Cellular Neuroscience* **2006**, *32*, 187.
(35) Hack, M. A.; Saghatelyan, A.; de Chevigny, A.; Pfeifer, A.; Ashery-Padan, R.; Lledo, P.-M.; Götz, M. *Nature Neuroscience* **2005**, *8*, 865.
(36) Fujimoto, M.; Takagi, Y.; Muraki, K.; Nozaki, K.; Yamamoto, N.; Tsuji, M.; Hashimoto, N.; Honjo, T.; Tanigaki, K. *Developmental Biology* **2009**, *332*, 339.
(37) Fujioka, T.; Fujioka, A.; Duman, R. S. *The Journal of neuroscience : the official journal of the Society for Neuroscience* **2004**, *24*, 319.
(38) Herold, S.; Jagasia, R.; Merz, K.; Wassmer, K.; Lie, D. C. *Molecular and Cellular Neuroscience* **2011**, *46*, 79.
(39) Ferri, A. L. M.; Cavallaro, M.; Braida, D.; Di Cristofano, A.; Canta, A.; Vezzani, A.; Ottolenghi, S.; Pandolfi, P. P.; Sala, M.; DeBiasi, S.; Nicolis, S. K. *Development* **2004**, *131*, 3805.
(40) Amador-Arjona, A.; Cimadamore, F.; Huang, C.-T.; Wright, R.; Lewis, S.; Gage, F. H.; Terskikh, A. V. *Proceedings of the National Academy of Sciences of the United States of America* **2015**, *112*, E1936.
(41) Petrik, D.; Latchney, S. E.; Masiulis, I.; Yun, S.; Zhang, Z.; Wu, J. I.; Eisch, A. J. *Stem cells (Dayton, Ohio)* **2015**, *33*, 3655.
(42) Wu, H.; Coskun, V.; Tao, J.; Xie, W.; Ge, W.; Yoshikawa, K.; Li, E.; Zhang, Y.; Sun, Y. E. *Science* **2010**, *329*, 444.
(43) Oliver, R. J.; Mandyam, C. D. *Front Neurosci* **2018**, *12*, 849.
(44) Djuranovic, S.; Nahvi, A.; Green, R. *Science (New York, N.Y.)* **2012**, *336*, 237.
(45) Tsan, Y.-c.; Morell, M. H.; O'Shea, K. S. *Stem Cell Research* **2016**, *17*, 238.
(46) Åkerblom, M.; Sachdeva, R.; Barde, I.; Verp, S.; Gentner, B.; Trono, D.; Jakobsson, J. *The Journal of neuroscience : the official journal of the Society for Neuroscience* **2012**, *32*, 8879.
(47) Ramos, Alexander D.; Diaz, A.; Nellore, A.; Delgado, Ryan N.; Park, K.-Y.; Gonzales-Roybal, G.; Oldham, Michael C.; Song, Jun S.; Lim, Daniel A. *Cell Stem Cell* **2013**, *12*, 616.
(48) Vilar, M.; Mira, H. *Front Neurosci* **2016**, *10*, 26.
(49) Huang, E. J.; Reichardt, L. F. *Annual Review of Biochemistry* **2003**, *72*, 609.
(50) Chao, M. V. *Nature Reviews Neuroscience* **2003**, *4*, 299.
(51) Bagley, J. A.; Belluscio, L. *Neuroscience* **2010**, *169*, 1449.
(52) Wang, L.; Chang, X.; She, L.; Xu, D.; Huang, W.; Poo, M.-m. *The Journal of neuroscience : the official journal of the Society for Neuroscience* **2015**, *35*, 8384.
(53) Taliaz, D.; Stall, N.; Dar, D. E.; Zangen, A. *Molecular Psychiatry* **2010**, *15*, 80.
(54) Liu, P. Z.; Nusslock, R. *Front Neurosci* **2018**, *12*, 52.
(55) Delgado, Ana C.; Ferrón, Sacri R.; Vicente, D.; Porlan, E.; Perez-Villalba, A.; Trujillo, Carmen M.; D′Ocón, P.; Fariñas, I. *Neuron* **2014**, *83*, 572.
(56) Wang, B.; Gao, Y.; Xiao, Z.; Chen, B.; Han, J.; Zhang, J.; Wang, X.; Dai, J. *Neuroscience Letters* **2009**, *461*, 252.
(57) Frielingsdorf, H.; Simpson, D. R.; Thal, L. J.; Pizzo, D. P. *Neurobiology of Disease* **2007**, *26*, 47.
(58) Fantacci, C.; Capozzi, D.; Ferrara, P.; Chiaretti, A. *Brain Sci* **2013**, *3*, 1013.
(59) Pallotto, M.; Deprez, F. *Frontiers in cellular neuroscience* **2014**, *8*, 166.
(60) Ge, S.; Goh, E. L.; Sailor, K. A.; Kitabatake, Y.; Ming, G. L.; Song, H. *Nature* **2006**, *439*, 589.
(61) Owens, D. F.; Kriegstein, A. R. *Nat Rev Neurosci* **2002**, *3*, 715.
(62) Tozuka, Y.; Fukuda, S.; Namba, T.; Seki, T.; Hisatsune, T. *Neuron* **2005**, *47*, 803.
(63) Earnheart, J. C.; Schweizer, C.; Crestani, F.; Iwasato, T.; Itohara, S.; Mohler, H.; Luscher, B. *J Neurosci* **2007**, *27*, 3845.
(64) Zhou, Y.; Danbolt, N. C. *J Neural Transm (Vienna)* **2014**, *121*, 799.
(65) Tashiro, A.; Sandler, V. M.; Toni, N.; Zhao, C.; Gage, F. H. *Nature* **2006**, *442*, 929.
(66) Ge, S.; Pradhan, D. A.; Ming, G.-l.; Song, H. *Trends in Neurosciences* **2007**, *30*, 1.
(67) Guillemot, F.; Zimmer, C. *Neuron* **2011**, *71*, 574.

(68) Woodbury, M. E.; Ikezu, T. *J Neuroimmune Pharmacol* **2014**, *9*, 92.
(69) Zheng, W.; Nowakowski, R. S.; Vaccarino, F. M. *Developmental Neuroscience* **2004**, *26*, 181.
(70) Keeffe, G. C.; Tyers, P.; Aarsland, D.; Dalley, J. W.; Barker, R. A.; Caldwell, M. A. *Proceedings of the National Academy of Sciences* **2009**, *106*, 8754.
(71) Doetsch, F.; Petreanu, L.; Caille, I.; Garcia-Verdugo, J.-M.; Alvarez-Buylla, A. *Neuron* **2002**, *36*, 1021.
(72) Gritti, A.; Parati, E. A.; Cova, L.; Frolichsthal, P.; Galli, R.; Wanke, E.; Faravelli, L.; Morassutti, D. J.; Roisen, F.; Nickel, D. D.; Vescovi, A. L. *The Journal of Neuroscience* **1996**, *16*, 1091.
(73) Baldauf, K.; Reymann, K. G. *Brain Research* **2005**, *1056*, 158.
(74) Jin, K.; Zhu, Y.; Sun, Y.; Mao, X. O.; Xie, L.; Greenberg, D. A. *Proceedings of the National Academy of Sciences* **2002**, *99*, 11946.
(75) Palmer, T. D.; Willhoite, A. R.; Gage, F. H. *Journal of Comparative Neurology* **2000**, *425*, 479.
(76) Fabel, K.; Fabel, K.; Tam, B.; Kaufer, D.; Baiker, A.; Simmons, N.; Kuo, C. J.; Palmer, T. D. *European Journal of Neuroscience* **2003**, *18*, 2803.
(77) Guo, H.; Zhou, H.; Lu, J.; Qu, Y.; Yu, D.; Tong, Y. *Neural Regen Res* **2016**, *11*, 174.
(78) Johnson, M. A.; Ables, J. L.; Eisch, A. J. *BMB Rep* **2009**, *42*, 245.
(79) Varela-Nallar, L.; Inestrosa, N. C. *Front Cell Neurosci* **2013**, *7*, 100.
(80) Lie, D. C.; Colamarino, S. A.; Song, H. J.; Desire, L.; Mira, H.; Consiglio, A.; Lein, E. S.; Jessberger, S.; Lansford, H.; Dearie, A. R.; Gage, F. H. *Nature* **2005**, *437*, 1370.
(81) Qu, Q.; Sun, G.; Murai, K.; Ye, P.; Li, W.; Asuelime, G.; Cheung, Y.-T.; Shi, Y. *Mol Cell Biol* **2013**, *33*, 2551.
(82) Chapouton, P.; Skupien, P.; Hesl, B.; Coolen, M.; Moore, J. C.; Madelaine, R.; Kremmer, E.; Faus-Kessler, T.; Blader, P.; Lawson, N. D.; Bally-Cuif, L. *The Journal of neuroscience : the official journal of the Society for Neuroscience* **2010**, *30*, 7961.
(83) Schroeter, E. H.; Kisslinger, J. A.; Kopan, R. *Nature* **1998**, *393*, 382.
(84) Imayoshi, I.; Shimojo, H.; Sakamoto, M.; Ohtsuka, T.; Kageyama, R. *Cell Mol Life Sci* **2013**, *70*, 2045.
(85) Breunig, J. J.; Silbereis, J.; Vaccarino, F. M.; Šestan, N.; Rakic, P. *Proceedings of the National Academy of Sciences* **2007**, *104*, 20558.
(86) Borghese, L.; Dolezalova, D.; Opitz, T.; Haupt, S.; Leinhaas, A.; Steinfarz, B.; Koch, P.; Edenhofer, F.; Hampl, A.; Brüstle, O. *STEM CELLS* **2010**, *28*, 955.
(87) Álvarez-Buylla, A.; Ihrie, R. A. *Semin Cell Dev Biol* **2014**, *33*, 105.
(88) Traiffort, E.; Charytoniuk, D. A.; Faure, H.; Ruat, M. *Journal of Neurochemistry* **1998**, *70*, 1327.
(89) Yao, P. J.; Petralia, R. S.; Mattson, M. P. *Trends in neurosciences* **2016**, *39*, 840.
(90) Balordi, F.; Fishell, G. *The Journal of neuroscience : the official journal of the Society for Neuroscience* **2007**, *27*, 5936.
(91) Pitter, K. L.; Tamagno, I.; Feng, X.; Ghosal, K.; Amankulor, N.; Holland, E. C.; Hambardzumyan, D. *Glia* **2014**, *62*, 1595.
(92) Akazawa, C.; Tsuzuki, H.; Nakamura, Y.; Sasaki, Y.; Ohsaki, K.; Nakamura, S.; Arakawa, Y.; Kohsaka, S. *The Journal of Neuroscience* **2004**, *24*, 7923.
(93) Liu, A.; Niswander, L. A. *Nature Reviews Neuroscience* **2005**, *6*, 945.
(94) Bond, A. M.; Bhalala, O. G.; Kessler, J. A. *Dev Neurobiol* **2012**, *72*, 1068.
(95) Gross, R. E.; Mehler, M. F.; Mabie, P. C.; Zang, Z.; Santschi, L.; Kessler, J. A. *Neuron* **1996**, *17*, 595.
(96) Guo, J.; Wu, G. *Cytokine & Growth Factor Reviews* **2012**, *23*, 61.
(97) Bonaguidi, M. A.; Peng, C.-Y.; McGuire, T.; Falciglia, G.; Gobeske, K. T.; Czeisler, C.; Kessler, J. A. *The Journal of neuroscience : the official journal of the Society for Neuroscience* **2008**, *28*, 9194.
(98) Yousef, H.; Morgenthaler, A.; Schlesinger, C.; Bugaj, L.; Conboy, I. M.; Schaffer, D. V. *STEM CELLS* **2015**, *33*, 1577.
(99) Hardy, J.; Selkoe, D. J. *Science* **2002**, *297*, 353.
(100) Pini, L.; Pievani, M.; Bocchetta, M.; Altomare, D.; Bosco, P.; Cavedo, E.; Galluzzi, S.; Marizzoni, M.; Frisoni, G. B. *Ageing Research Reviews* **2016**, *30*, 25.

(101) Scopa, C.; Marrocco, F.; Latina, V.; Ruggeri, F.; Corvaglia, V.; La Regina, F.; Ammassari-Teule, M.; Middei, S.; Amadoro, G.; Meli, G.; Scardigli, R.; Cattaneo, A. *Cell Death & Differentiation* **2020**, *27*, 934.

(102) Sun, B.; Halabisky, B.; Zhou, Y.; Palop, J. J.; Yu, G.; Mucke, L.; Gan, L. *Cell Stem Cell* **2009**, *5*, 624.

(103) Albers, M. W.; Tabert, M. H.; Devanand, D. P. *Current Neurology and Neuroscience Reports* **2006**, *6*, 379.

(104) Ziabreva, I.; Perry, E.; Perry, R.; Minger, S. L.; Ekonomou, A.; Przyborski, S.; Ballard, C. *Journal of Psychosomatic Research* **2006**, *61*, 311.

(105) Unger, M. S.; Marschallinger, J.; Kaindl, J.; Höfling, C.; Rossner, S.; Heneka, M. T.; Van der Linden, A.; Aigner, L. *Molecular neurobiology* **2016**, *53*, 5796.

(106) Kohl, Z.; Ben Abdallah, N.; Vogelgsang, J.; Tischer, L.; Deusser, J.; Amato, D.; Anderson, S.; Müller, C. P.; Riess, O.; Masliah, E.; Nuber, S.; Winkler, J. *Neurobiology of Disease* **2016**, *85*, 206.

(107) Carlesimo, G. A.; Piras, F.; Assogna, F.; Pontieri, F. E.; Caltagirone, C.; Spalletta, G. *Neurology* **2012**, *78*, 1939.

(108) Bano, D.; Zanetti, F.; Mende, Y.; Nicotera, P. *Cell Death Dis* **2011**, *2*, e228.

(109) Ernst, A.; Alkass, K.; Bernard, S.; Salehpour, M.; Perl, S.; Tisdale, J.; Possnert, G.; Druid, H.; Frisen, J. *Cell* **2014**, *156*, 1072.

(110) Gil, J. M. A. C.; Mohapel, P.; Araújo, I. M.; Popovic, N.; Li, J.-Y.; Brundin, P.; Petersén, Å. *Neurobiology of Disease* **2005**, *20*, 744.

(111) Kohl, Z.; Regensburger, M.; Aigner, R.; Kandasamy, M.; Winner, B.; Aigner, L.; Winkler, J. *BMC Neurosci* **2010**, *11*, 114.

(112) Simpson, J. M.; Gil-Mohapel, J.; Pouladi, M. A.; Ghilan, M.; Xie, Y.; Hayden, M. R.; Christie, B. R. *Neurobiology of Disease* **2011**, *41*, 249.

(113) Mendiola-Precoma, J.; Berumen, L. C.; Padilla, K.; Garcia-Alcocer, G. *Biomed Res Int* **2016**, *2016*, 2589276.

(114) Bonuccelli, U.; Del Dotto, P.; Rascol, O. *Parkinsonism & Related Disorders* **2009**, *15*, S44.

(115) Fox, S. H.; Lang, A. E. In *Handbook of Clinical Neurology*; Koller, W. C., Melamed, E., Eds.; Elsevier: 2007; Vol. 84, p 159.

(116) Frank, S. *Neurotherapeutics* **2014**, *11*, 153.

(117) Murphy, M. P.; LeVine, H., 3rd *J Alzheimers Dis* **2010**, *19*, 311.

(118) Cummings, J.; Lee, G.; Ritter, A.; Sabbagh, M.; Zhong, K. *Alzheimers Dement (N Y)* **2019**, *5*, 272.

(119) Imbimbo, B. P.; Watling, M. *Expert Opin Investig Drugs* **2019**, *28*, 967.

(120) Panza, F.; Lozupone, M.; Watling, M.; Imbimbo, B. P. *Expert Review of Neurotherapeutics* **2019**, *19*, 599.

(121) Panza, F.; Lozupone, M.; Logroscino, G.; Imbimbo, B. P. *Nature Reviews Neurology* **2019**, *15*, 73.

(122) Honig, L. S.; Vellas, B.; Woodward, M.; Boada, M.; Bullock, R.; Borrie, M.; Hager, K.; Andreasen, N.; Scarpini, E.; Liu-Seifert, H.; Case, M.; Dean, R. A.; Hake, A.; Sundell, K.; Poole Hoffmann, V.; Carlson, C.; Khanna, R.; Mintun, M.; DeMattos, R.; Selzler, K. J.; Siemers, E. *New England Journal of Medicine* **2018**, *378*, 321.

(123) Lang, A. E.; Espay, A. J. *Movement Disorders* **2018**, *33*, 660.

(124) AlDakheel, A.; Kalia, L. V.; Lang, A. E. *Neurotherapeutics* **2014**, *11*, 6.

(125) Mittal, S.; Bjørnevik, K.; Im, D. S.; Flierl, A.; Dong, X.; Locascio, J. J.; Abo, K. M.; Long, E.; Jin, M.; Xu, B.; Xiang, Y. K.; Rochet, J.-C.; Engeland, A.; Rizzu, P.; Heutink, P.; Bartels, T.; Selkoe, D. J.; Caldarone, B. J.; Glicksman, M. A.; Khurana, V.; Schüle, B.; Park, D. S.; Riise, T.; Scherzer, C. R. *Science (New York, N.Y.)* **2017**, *357*, 891.

(126) Dickey, A. S.; La Spada, A. R. *Am J Med Genet A* **2018**, *176*, 842.

(127) Hayashi, Y.; Lin, H.-T.; Lee, C.-C.; Tsai, K.-J. *J Biomed Sci* **2020**, *27*, 29.

(128) Grealish, S.; Diguet, E.; Kirkeby, A.; Mattsson, B.; Heuer, A.; Bramoulle, Y.; Van Camp, N.; Perrier, Anselme L.; Hantraye, P.; Björklund, A.; Parmar, M. *Cell Stem Cell* **2014**, *15*, 653.

(129) Malberg, J. E. *J Psychiatry Neurosci* **2004**, *29*, 196.

(130) Malberg, J. E.; Eisch, A. J.; Nestler, E. J.; Duman, R. S. *The Journal of Neuroscience* **2000**, *20*, 9104.

(131) Kajitani, N.; Hisaoka-Nakashima, K.; Morioka, N.; Okada-Tsuchioka, M.; Kaneko, M.; Kasai, M.; Shibasaki, C.; Nakata, Y.; Takebayashi, M. *PLoS One* **2012**, *7*, e51197.

(132) Morales-Garcia, J. A.; Luna-Medina, R.; Alonso-Gil, S.; Sanz-SanCristobal, M.; Palomo, V.; Gil, C.; Santos, A.; Martinez, A.; Perez-Castillo, A. *ACS Chemical Neuroscience* **2012**, *3*, 963.

(133) Morales-Garcia, J. A.; Echeverry-Alzate, V.; Alonso-Gil, S.; Sanz-SanCristobal, M.; Lopez-Moreno, J. A.; Gil, C.; Martinez, A.; Santos, A.; Perez-Castillo, A. *STEM CELLS* **2017**, *35*, 458.

(134) Kim, S. H.; Steele, J. W.; Lee, S. W.; Clemenson, G. D.; Carter, T. A.; Treuner, K.; Gadient, R.; Wedel, P.; Glabe, C.; Barlow, C.; Ehrlich, M. E.; Gage, F. H.; Gandy, S. *Molecular psychiatry* **2014**, *19*, 1235.

(135) Sasaki, T.; Kitagawa, K.; Omura-Matsuoka, E.; Todo, K.; Terasaki, Y.; Sugiura, S.; Hatazawa, J.; Yagita, Y.; Hori, M. *Stroke* **2007**, *38*, 1597.

(136) Tanaka, Y.; Tanaka, R.; Liu, M.; Hattori, N.; Urabe, T. *Neuroscience* **2010**, *171*, 1367.

(137) Kitayama, T.; Yoneyama, M.; Yoneda, Y. *Journal of Neurochemistry* **2003**, *84*, 767.

(138) Gruden, M. A.; Ratmirov, A. M.; Storozheva, Z. I.; Solovieva, O. A.; Sherstnev, V. V.; Sewell, R. D. E. *J Mol Neurosci* **2018**, *65*, 167.

(139) Di Giorgi-Gerevini, V.; Melchiorri, D.; Battaglia, G.; Ricci-Vitiani, L.; Ciceroni, C.; Busceti, C. L.; Biagioni, F.; Iacovelli, L.; Canudas, A. M.; Parati, E.; De Maria, R.; Nicoletti, F. *Cell Death & Differentiation* **2005**, *12*, 1124.

(140) Zhang, M.; Luo, G.; Zhou, Y.; Wang, S.; Zhong, Z. *J Biomol Screen* **2014**, *19*, 1.

(141) Pieper, A. A.; Xie, S.; Capota, E.; Estill, S. J.; Zhong, J.; Long, J. M.; Becker, G. L.; Huntington, P.; Goldman, S. E.; Shen, C.-H.; Capota, M.; Britt, J. K.; Kotti, T.; Ure, K.; Brat, D. J.; Williams, N. S.; MacMillan, K. S.; Naidoo, J.; Melito, L.; Hsieh, J.; De Brabander, J.; Ready, J. M.; McKnight, S. L. *Cell* **2010**, *142*, 39.

(142) Barrett, D. A.; Munjal, M. A.; Celine, L.; Erich, G.; Nicole, N. C.; David, Q.; Mike, H.; Karl, K. J.; Charles, L. L. *Radiation Research* **2018**, *189*, 345.

(143) Chakravarty, S.; Maitra, S.; Reddy, R. G.; Das, T.; Jhelum, P.; Kootar, S.; Rajan, W. D.; Samanta, A.; Samineni, R.; Pabbaraja, S.; Kernie, S. G.; Mehta, G.; Kumar, A. *Sci Rep* **2015**, *5*, 14134.

(144) Li, J.; Ma, J.; Meng, G.; Lin, H.; Wu, S.; Wang, J.; Luo, J.; Xu, X.; Tough, D.; Lindon, M.; Rioja, I.; Zhao, J.; Mei, H.; Prinjha, R.; Zhong, Z. *Stem Cell Research* **2016**, *17*, 212.

(145) MacMillan, K. S.; Naidoo, J.; Liang, J.; Melito, L.; Williams, N. S.; Morlock, L.; Huntington, P. J.; Estill, S. J.; Longgood, J.; Becker, G. L.; McKnight, S. L.; Pieper, A. A.; De Brabander, J. K.; Ready, J. M. *Journal of the American Chemical Society* **2011**, *133*, 1428.

(146) Yoon, H. J.; Kong, S.-Y.; Park, M.-H.; Cho, Y.; Kim, S.-E.; Shin, J.-Y.; Jung, S.; Lee, J.; Farhanullah; Kim, H.-J.; Lee, J. *Bioorganic & Medicinal Chemistry* **2013**, *21*, 7165.

(147) Wang, G.; Han, T.; Nijhawan, D.; Theodoropoulos, P.; Naidoo, J.; Yadavalli, S.; Mirzaei, H.; Pieper, Andrew A.; Ready, Joseph M.; McKnight, Steven L. *Cell* **2014**, *158*, 1324.

(148) De Jesús-Cortés, H.; Miller, A. D.; Britt, J. K.; DeMarco, A. J.; De Jesús-Cortés, M.; Stuebing, E.; Naidoo, J.; Vázquez-Rosa, E.; Morlock, L.; Williams, N. S.; Ready, J. M.; Narayanan, N. S.; Pieper, A. A. *NPJ Parkinsons Dis* **2015**, *1*, 15010.

(149) Voorhees, J. R.; Remy, M. T.; Cintrón-Pérez, C. J.; El Rassi, E.; Khan, M. Z.; Dutca, L. M.; Yin, T. C.; McDaniel, L. N.; Williams, N. S.; Brat, D. J.; Pieper, A. A. *Biol Psychiatry* **2018**, *84*, 488.

(150) Loris, Z. B.; Pieper, A. A.; Dietrich, W. D. *Experimental Neurology* **2017**, *290*, 63.

(151) Blaya, M. O.; Wasserman, J. M.; Pieper, A. A.; Sick, T. J.; Bramlett, H. M.; Dietrich, W. D. *Neuropharmacology* **2019**, *145*, 268.

(152) Kelleher-Andersson, J.; Johe, K. K.; Neuralstem, Inc. : 2012.

(153) Fava, M.; Johe, K.; Ereshefsky, L.; Gertsik, L. G.; English, B. A.; Bilello, J. A.; Thurmond, L. M.; Johnstone, J.; Dickerson, B. C.; Makris, N.; Hoeppner, B. B.; Flynn, M.; Mischoulon, D.; Kinrys, G.; Freeman, M. P. *Molecular Psychiatry* **2016**, *21*, 1372.

(154) Papakostas, G. I.; Johe, K.; Hand, H.; Drouillard, A.; Russo, P.; Kay, G.; Kashambwa, R.; Hoeppner, B.; Flynn, M.; Yeung, A.; Martinson, M. A.; Fava, M. *Molecular Psychiatry* **2019**.

(155) Joshi, P. C.; Samineni, R.; Bhattacharya, D.; Reddy, B. R.; Veeraval, L.; Das, T.; Maitra, S.; Wahul, A. B.; Karri, S.; Pabbaraja, S.; Mehta, G.; Kumar, A.; Chakravarty, S. *Sci Rep* **2017**, *7*, 1492.

(156) Benito, E.; Ramachandran, B.; Schroeder, H.; Schmidt, G.; Urbanke, H.; Burkhardt, S.; Capece, V.; Dean, C.; Fischer, A. *Translational Psychiatry* **2017**, *7*, e1239.
(157) Lee, J. A.; Uhlik, M. T.; Moxham, C. M.; Tomandl, D.; Sall, D. J. *Journal of Medicinal Chemistry* **2012**, *55*, 4527.
(158) Koroleva, E. V.; Ignatovich, Z. I.; Sinyutich, Y. V.; Gusak, K. N. *Russian Journal of Organic Chemistry* **2016**, *52*, 139.
(159) Lin, S.; Malkani, S.; Lombardo, M.; Yang, L.; Mills, S. G.; Chapman, K.; Thompson, J. E.; Zhang, W. X.; Wang, R.; Cubbon, R. M.; O'Neill, E. A.; Hale, J. J. *Bioorganic & Medicinal Chemistry Letters* **2015**, *25*, 5402.
(160) Takahashi, S. *J Hematol Oncol* **2011**, *4*, 13.
(161) Mackarehtschian, K.; Hardin, J. D.; Moore, K. A.; Boast, S.; Goff, S. P.; Lemischka, I. R. *Immunity* **1995**, *3*, 147.
(162) Brazel, C. Y.; Ducceschi, M. H.; Pytowski, B.; Levison, S. W. *Molecular and Cellular Neuroscience* **2001**, *18*, 381.
(163) Maffezzini, C.; Calvo-Garrido, J.; Wredenberg, A.; Freyer, C. *Cellular and Molecular Life Sciences* **2020**.
(164) Blair, J. D.; Hockemeyer, D.; Doudna, J. A.; Bateup, H. S.; Floor, S. N. *Cell Rep* **2017**, *21*, 2005.
(165) Cong, F.; Cheung, A. K.; Huang, S.-M. A. *Annual Review of Pharmacology and Toxicology* **2012**, *52*, 57.
(166) Sun, H.; Shen, Y.; Luo, G.; Cai, Y.; Xiang, Z. *BMC Bioinformatics* **2018**, *19*, 315.
(167) Sato, S.-i.; Murata, A.; Shirakawa, T.; Uesugi, M. *Chemistry & Biology* **2010**, *17*, 616.
(168) Wright, M. H.; Sieber, S. A. *Natural Product Reports* **2016**, *33*, 681.
(169) Zheng, M.; Zheng, L.; Zhang, P.; Li, J.; Zhang, Y. *Molecules* **2015**, *20*, 3190.
(170) Tornøe, C. W.; Christensen, C.; Meldal, M. *The Journal of Organic Chemistry* **2002**, *67*, 3057.
(171) Rostovtsev, V. V.; Green, L. G.; Fokin, V. V.; Sharpless, K. B. *Angewandte Chemie International Edition* **2002**, *41*, 2596.
(172) Chan, T. R.; Hilgraf, R.; Sharpless, K. B.; Fokin, V. V. *Organic Letters* **2004**, *6*, 2853.
(173) Cravatt, B. F.; Wright, A. T.; Kozarich, J. W. *Annual Review of Biochemistry* **2008**, *77*, 383.
(174) Speers, A. E.; Cravatt, B. F. *Chemistry & Biology* **2004**, *11*, 535.
(175) Jewett, J. C.; Bertozzi, C. R. *Chem Soc Rev* **2010**, *39*, 1272.
(176) Agard, N. J.; Prescher, J. A.; Bertozzi, C. R. *Journal of the American Chemical Society* **2004**, *126*, 15046.
(177) Agard, N. J.; Baskin, J. M.; Prescher, J. A.; Lo, A.; Bertozzi, C. R. *ACS Chemical Biology* **2006**, *1*, 644.
(178) Li, S.; Zhu, H.; Wang, J.; Wang, X.; Li, X.; Ma, C.; Wen, L.; Yu, B.; Wang, Y.; Li, J.; Wang, P. G. *Electrophoresis* **2016**, *37*, 1431.
(179) Wang, S.; Tian, Y.; Wang, M.; Wang, M.; Sun, G.-B.; Sun, X.-B. *Front Pharmacol* **2018**, *9*, 353.
(180) Ekkebus, R.; van Kasteren, S. I.; Kulathu, Y.; Scholten, A.; Berlin, I.; Geurink, P. P.; de Jong, A.; Goerdayal, S.; Neefjes, J.; Heck, A. J. R.; Komander, D.; Ovaa, H. *Journal of the American Chemical Society* **2013**, *135*, 2867.
(181) Sadakane, Y.; Hatanaka, Y. *Analytical Sciences* **2006**, *22*, 209.
(182) Geurink, P. P.; Prely, L. M.; van der Marel, G. A.; Bischoff, R.; Overkleeft, H. S. In *Activity-Based Protein Profiling*; Sieber, S. A., Ed.; Springer Berlin Heidelberg: Berlin, Heidelberg, 2012, p 85.
(183) Preston, G. W.; Wilson, A. J. *Chem Soc Rev* **2013**, *42*, 3289.
(184) Smith, E.; Collins, I. *Future Med Chem* **2015**, *7*, 159.
(185) Wittelsberger, A.; Thomas, B. E.; Mierke, D. F.; Rosenblatt, M. *FEBS Letters* **2006**, *580*, 1872.
(186) Ge, S.-S.; Chen, B.; Wu, Y.-Y.; Long, Q.-S.; Zhao, Y.-L.; Wang, P.-Y.; Yang, S. *RSC Advances* **2018**, *8*, 29428.
(187) Li, Z.; Hao, P.; Li, L.; Tan, C. Y. J.; Cheng, X.; Chen, G. Y. J.; Sze, S. K.; Shen, H.-M.; Yao, S. Q. *Angewandte Chemie International Edition* **2013**, *52*, 8551.
(188) Wakahara, T.; Niino, Y.; Kato, T.; Maeda, Y.; Akasaka, T.; Liu, M. T. H.; Kobayashi, K.; Nagase, S. *Journal of the American Chemical Society* **2002**, *124*, 9465.

(189) Ong, S.-E.; Blagoev, B.; Kratchmarova, I.; Kristensen, D. B.; Steen, H.; Pandey, A.; Mann, M. *Molecular & Cellular Proteomics* **2002**, *1*, 376.

(190) Ong, S.-E.; Schenone, M.; Margolin, A. A.; Li, X.; Do, K.; Doud, M. K.; Mani, D. R.; Kuai, L.; Wang, X.; Wood, J. L.; Tolliday, N. J.; Koehler, A. N.; Marcaurelle, L. A.; Golub, T. R.; Gould, R. J.; Schreiber, S. L.; Carr, S. A. *Proceedings of the National Academy of Sciences* **2009**, *106*, 4617.

(191) Lomenick, B.; Hao, R.; Jonai, N.; Chin, R. M.; Aghajan, M.; Warburton, S.; Wang, J.; Wu, R. P.; Gomez, F.; Loo, J. A.; Wohlschlegel, J. A.; Vondriska, T. M.; Pelletier, J.; Herschman, H. R.; Clardy, J.; Clarke, C. F.; Huang, J. *Proceedings of the National Academy of Sciences* **2009**, *106*, 21984.

(192) West, G. M.; Tucker, C. L.; Xu, T.; Park, S. K.; Han, X.; Yates, J. R.; Fitzgerald, M. C. *Proceedings of the National Academy of Sciences* **2010**, *107*, 9078.

(193) Dittmann, A.; Werner, T.; Chung, C.-W.; Savitski, M. M.; Fälth Savitski, M.; Grandi, P.; Hopf, C.; Lindon, M.; Neubauer, G.; Prinjha, R. K.; Bantscheff, M.; Drewes, G. *ACS Chemical Biology* **2014**, *9*, 495.

(194) Low, W. K.; Dang, Y.; Schneider-Poetsch, T.; Shi, Z.; Choi, N. S.; Rzasa, R. M.; Shea, H. A.; Li, S.; Park, K.; Ma, G.; Romo, D.; Liu, J. O. In *Methods in Enzymology*; Academic Press: 2007; Vol. 431, p 303.

(195) Wirth, T.; Schmuck, K.; Tietze, L. F.; Sieber, S. A. *Angewandte Chemie International Edition* **2012**, *51*, 2874.

(196) Heydenreuter, W.; Kunold, E.; Sieber, S. A. *Chemical Communications* **2015**, *51*, 15784.

(197) Wilkinson, I. V. L.; Perkins, K. J.; Dugdale, H.; Moir, L.; Vuorinen, A.; Chatzopoulou, M.; Squire, S. E.; Monecke, S.; Lomow, A.; Geese, M.; Charles, P. D.; Burch, P.; Tinsley, J. M.; Wynne, G. M.; Davies, S. G.; Wilson, F. X.; Rastinejad, F.; Mohammed, S.; Davies, K. E.; Russell, A. J. *Angewandte Chemie International Edition* **2020**, *59*, 2420.

(198) Vanhaesebroeck, B.; Guillermet-Guibert, J.; Graupera, M.; Bilanges, B. *Nature Reviews Molecular Cell Biology* **2010**, *11*, 329.

(199) Walker, E. H.; Pacold, M. E.; Perisic, O.; Stephens, L.; Hawkins, P. T.; Wymann, M. P.; Williams, R. L. *Molecular Cell* **2000**, *6*, 909.

(200) Hu, L.; Zaloudek, C.; Mills, G. B.; Gray, J.; Jaffe, R. B. *Clinical Cancer Research* **2000**, *6*, 880.

(201) Kong, D.; Yamori, T. *Cancer Science* **2008**, *99*, 1734.

(202) Molina, D. M.; Jafari, R.; Ignatushchenko, M.; Seki, T.; Larsson, E. A.; Dan, C.; Sreekumar, L.; Cao, Y.; Nordlund, P. *Science* **2013**, *341*, 84.

(203) Vedadi, M.; Niesen, F. H.; Allali-Hassani, A.; Fedorov, O. Y.; Finerty, P. J., Jr.; Wasney, G. A.; Yeung, R.; Arrowsmith, C.; Ball, L. J.; Berglund, H.; Hui, R.; Marsden, B. D.; Nordlund, P.; Sundstrom, M.; Weigelt, J.; Edwards, A. M. *Proceedings of the National Academy of Sciences of the United States of America* **2006**, *103*, 15835.

(204) Huynh, K.; Partch, C. L. *Curr Protoc Protein Sci* **2015**, *79*, 28.9.1.

(205) Senisterra, G. A.; Ghanei, H.; Khutoreskaya, G.; Dobrovetsky, E.; Edwards, A. M.; Privé, G. G.; Vedadi, M. *Journal of Biomolecular Screening* **2010**, *15*, 314.

(206) Shaw, J.; Dale, I.; Hemsley, P.; Leach, L.; Dekki, N.; Orme, J. P.; Talbot, V.; Narvaez, A. J.; Bista, M.; Martinez Molina, D.; Dabrowski, M.; Main, M. J.; Gianni, D. *SLAS Discov* **2019**, *24*, 121.

(207) Rossi, A. M.; Taylor, C. W. *Nat Protoc* **2011**, *6*, 365.

(208) Maynard, J. A.; Lindquist, N. C.; Sutherland, J. N.; Lesuffleur, A.; Warrington, A. E.; Rodriguez, M.; Oh, S.-H. *Biotechnol J* **2009**, *4*, 1542.

(209) Khan, S. H.; Farkas, K.; Kumar, R.; Ling, J. *Analytical Biochemistry* **2012**, *421*, 385.

(210) Harner, M. J.; Frank, A. O.; Fesik, S. W. *Journal of biomolecular NMR* **2013**, *56*, 65.

(211) Huang, R.; Leung, I. K. H. In *Methods in Enzymology*; Wand, A. J., Ed.; Academic Press: 2019; Vol. 615, p 477.

(212) Ludwig, C.; Michiels, P. J. A.; Wu, X.; Kavanagh, K. L.; Pilka, E.; Jansson, A.; Oppermann, U.; Günther, U. L. *Journal of Medicinal Chemistry* **2008**, *51*, 1.

(213) Dalvit, C.; Fogliatto, G.; Stewart, A.; Veronesi, M.; Stockman, B. *Journal of Biomolecular NMR* **2001**, *21*, 349.

(214) Elbashir, S. M.; Harborth, J.; Lendeckel, W.; Yalcin, A.; Weber, K.; Tuschl, T. *Nature* **2001**, *411*, 494.

(215) McManus, M. T.; Sharp, P. A. *Nature Reviews Genetics* **2002**, *3*, 737.
(216) Chicaybam, L.; Barcelos, C.; Peixoto, B.; Carneiro, M.; Limia, C. G.; Redondo, P.; Lira, C.; Paraguassú-Braga, F.; Vasconcelos, Z. F. M. D.; Barros, L.; Bonamino, M. H. *Frontiers in Bioengineering and Biotechnology* **2017**, *4*, 99.
(217) Mali, P.; Yang, L.; Esvelt, K. M.; Aach, J.; Guell, M.; DiCarlo, J. E.; Norville, J. E.; Church, G. M. *Science* **2013**, *339*, 823.
(218) Hendel, A.; Bak, R. O.; Clark, J. T.; Kennedy, A. B.; Ryan, D. E.; Roy, S.; Steinfeld, I.; Lunstad, B. D.; Kaiser, R. J.; Wilkens, A. B.; Bacchetta, R.; Tsalenko, A.; Dellinger, D.; Bruhn, L.; Porteus, M. H. *Nature Biotechnology* **2015**, *33*, 985.
(219) Dow, L. E. *Trends in Molecular Medicine* **2015**, *21*, 609.
(220) Ahmed, S. *Journal of Cellular Biochemistry* **2009**, *106*, 1.
(221) Yu, S.; Levi, L.; Siegel, R.; Noy, N. *The Journal of biological chemistry* **2012**, *287*, 42195.
(222) Feng, B.; Li, Y.; Li, H.; Zhang, X.; Xie, H.; Cao, H.; Yu, L.; Xu, Q. *The Journal of Organic Chemistry* **2018**, *83*, 6769.
(223) E. Hartung, R.; C. Wall, M.; Lebreton, S.; Smrcina, M.; Patek, M. *HETEROCYCLES* **2017**, *94*, 1305.
(224) Knapp, D. M.; Gillis, E. P.; Burke, M. D. *Journal of the American Chemical Society* **2009**, *131*, 6961.
(225) Gillis, E. P.; Burke, M. D. *Journal of the American Chemical Society* **2008**, *130*, 14084.
(226) Liu, M. T. H.; Tencer, M.; Stevens, I. D. R. *Journal of the Chemical Society, Perkin Transactions 2* **1986**, 211.
(227) Pastoriza-Santos, I.; Liz-Marzán, L. M. *Advanced Functional Materials* **2009**, *19*, 679.
(228) Livnah, O.; Bayer, E. A.; Wilchek, M.; Sussman, J. L. *Proceedings of the National Academy of Sciences* **1993**, *90*, 5076.
(229) Beija, M.; Afonso, C. A. M.; Martinho, J. M. G. *Chem Soc Rev* **2009**, *38*, 2410.
(230) Nguyen, T.; Francis, M. B. *Organic Letters* **2003**, *5*, 3245.
(231) Perfetto, S. P.; Chattopadhyay, P. K.; Lamoreaux, L.; Nguyen, R.; Ambrozak, D.; Koup, R. A.; Roederer, M. *J Immunol Methods* **2006**, *313*, 199.
(232) Krag, D. N.; Theon, A. P.; Gan, L.; Wardell, J.; Tao, S. Z. *J Surg Res* **1989**, *46*, 361.
(233) Boens, N.; Leen, V.; Dehaen, W. *Chem Soc Rev* **2012**, *41*, 1130.
(234) Kowada, T.; Maeda, H.; Kikuchi, K. *Chem Soc Rev* **2015**, *44*, 4953.
(235) Croft, C. L.; Futch, H. S.; Moore, B. D.; Golde, T. E. *Molecular Neurodegeneration* **2019**, *14*, 45.
(236) Kawatani, M.; Osada, H. *MedChemComm* **2014**, *5*, 277.
(237) Chevallet, M.; Luche, S.; Rabilloud, T. *Nat Protoc* **2006**, *1*, 1852.
(238) Morr, C. V. *Journal of Dairy Science* **1967**, *50*, 1752.
(239) Zhang, L.; Elias, J. E. In *Proteomics: Methods and Protocols*; Comai, L., Katz, J. E., Mallick, P., Eds.; Springer New York: New York, NY, 2017, p 185.
(240) Ivaska, J.; Pallari, H.-M.; Nevo, J.; Eriksson, J. E. *Experimental Cell Research* **2007**, *313*, 2050.
(241) Mendez, M. G.; Kojima, S.-I.; Goldman, R. D. *FASEB J* **2010**, *24*, 1838.
(242) Menko, A. S.; Bleaken, B. M.; Libowitz, A. A.; Zhang, L.; Stepp, M. A.; Walker, J. L. *Molecular Biology of the Cell* **2014**, *25*, 776.
(243) Chen, M.; Puschmann, T. B.; Marasek, P.; Inagaki, M.; Pekna, M.; Wilhelmsson, U.; Pekny, M. *Mol Neurobiol* **2018**, *55*, 5478.
(244) Song, J.; Pfanner, N.; Becker, T. *Proceedings of the National Academy of Sciences* **2018**, *115*, 2850.
(245) Vandewalle, J.; Bauters, M.; Van Esch, H.; Belet, S.; Verbeeck, J.; Fieremans, N.; Holvoet, M.; Vento, J.; Spreiz, A.; Kotzot, D.; Haberlandt, E.; Rosenfeld, J.; Andrieux, J.; Delobel, B.; Dehouck, M.-B.; Devriendt, K.; Fryns, J.-P.; Marynen, P.; Goldstein, A.; Froyen, G. *Human Genetics* **2013**, *132*, 1177.
(246) Wang, Y.; Xu, E.; Musich, P. R.; Lin, F. *CNS Neuroscience & Therapeutics* **2019**, *25*, 816.
(247) Beckervordersandforth, R. *Brain Plast* **2017**, *3*, 73.

(248) Beckervordersandforth, R.; Ebert, B.; Schäffner, I.; Moss, J.; Fiebig, C.; Shin, J.; Moore, D. L.; Ghosh, L.; Trinchero, M. F.; Stockburger, C.; Friedland, K.; Steib, K.; von Wittgenstein, J.; Keiner, S.; Redecker, C.; Hölter, S. M.; Xiang, W.; Wurst, W.; Jagasia, R.; Schinder, A. F.; Ming, G.-l.; Toni, N.; Jessberger, S.; Song, H.; Lie, D. C. *Neuron* **2017**, *93*, 560.

(249) Palmieri, F. *Biochimica et Biophysica Acta (BBA) - Bioenergetics* **2008**, *1777*, 564.

(250) Babenko, V. N.; Smagin, D. A.; Galyamina, A. G.; Kovalenko, I. L.; Kudryavtseva, N. N. *BMC Neurosci* **2018**, *19*, 79.

(251) Saha, A.; Connelly, S.; Jiang, J.; Zhuang, S.; Amador, Deron T.; Phan, T.; Pilz, Renate B.; Boss, Gerry R. *Molecular Cell* **2014**, *55*, 264.

(252) Zhao, Y.; Pan, X.; Zhao, J.; Wang, Y.; Peng, Y.; Zhong, C. *Journal of Neurochemistry* **2009**, *111*, 537.

(253) Zhao, Y.; Wu, Y.; Hu, H.; Cai, J.; Ning, M.; Ni, X.; Zhong, C. *Biomed Res Int* **2014**, *2014*, 572915.

(254) Hassan, M. K.; Kumar, D.; Naik, M.; Dixit, M. *PLoS One* **2018**, *13*, e0191377.

(255) Aziz, A.; Hess, J. F.; Budamagunta, M. S.; FitzGerald, P. G.; Voss, J. C. *Journal of Biological Chemistry* **2009**, *284*, 7330.

(256) Danielsson, F.; Peterson, M. K.; Caldeira Araujo, H.; Lautenschlager, F.; Gad, A. K. B. *Cells* **2018**, *7*.

(257) Kidd, M. E.; Shumaker, D. K.; Ridge, K. M. *Am J Respir Cell Mol Biol* **2014**, *50*, 1.

(258) Satelli, A.; Li, S. *Cell Mol Life Sci* **2011**, *68*, 3033.

(259) Wu, C.; Jin, X.; Tsueng, G.; Afrasiabi, C.; Su, A. I. *Nucleic Acids Res* **2016**, *44*, D313.

(260) Su, A. I.; Wiltshire, T.; Batalov, S.; Lapp, H.; Ching, K. A.; Block, D.; Zhang, J.; Soden, R.; Hayakawa, M.; Kreiman, G.; Cooke, M. P.; Walker, J. R.; Hogenesch, J. B. *Proceedings of the National Academy of Sciences of the United States of America* **2004**, *101*, 6062.

(261) Carlyle, B. C.; Kitchen, R. R.; Kanyo, J. E.; Voss, E. Z.; Pletikos, M.; Sousa, A. M. M.; Lam, T. T.; Gerstein, M. B.; Sestan, N.; Nairn, A. C. *Nature Neuroscience* **2017**, *20*, 1787.

(262) Vinci, L.; Ravarino, A.; Fanos, V.; Naccarato, A. G.; Senes, G.; Gerosa, C.; Bevilacqua, G.; Faa, G.; Ambu, R. *Eur J Histochem* **2016**, *60*, 2563.

(263) Tang, C.; Zhu, L.; Gan, W.; Liang, H.; Li, J.; Zhang, J.; Zhang, X.; Lu, Y.; Xu, R. *Int J Biol Sci* **2016**, *12*, 1405.

(264) Yabe, J. T.; Chan, W. K.; Wang, F. S.; Pimenta, A.; Ortiz, D. D.; Shea, T. B. *Cell Motil Cytoskeleton* **2003**, *56*, 193.

(265) Robert, A.; Rossow, M. J.; Hookway, C.; Adam, S. A.; Gelfand, V. I. *Proceedings of the National Academy of Sciences* **2015**, *112*, E3505.

(266) Snider, N. T.; Omary, M. B. *Nature Reviews Molecular Cell Biology* **2014**, *15*, 163.

(267) Helfand, B. T.; Mendez, M. G.; Murthy, S. N. P.; Shumaker, D. K.; Grin, B.; Mahammad, S.; Aebi, U.; Wedig, T.; Wu, Y. I.; Hahn, K. M.; Inagaki, M.; Herrmann, H.; Goldman, R. D. *Molecular biology of the cell* **2011**, *22*, 1274.

(268) Mücke, N.; Kämmerer, L.; Winheim, S.; Kirmse, R.; Krieger, J.; Mildenberger, M.; Baßler, J.; Hurt, E.; Goldmann, W. H.; Aebi, U.; Toth, K.; Langowski, J.; Herrmann, H. *Biophysical Journal* **2018**, *114*, 2408.

(269) Wickert, U.; Mücke, N.; Wedig, T.; Müller, S. A.; Aebi, U.; Herrmann, H. *European Journal of Cell Biology* **2005**, *84*, 379.

(270) Izawa, I.; Inagaki, M. *Cancer Sci* **2006**, *97*, 167.

(271) Goldman, R. D.; Khuon, S.; Chou, Y. H.; Opal, P.; Steinert, P. M. *J Cell Biol* **1996**, *134*, 971.

(272) Cheng, F.; Eriksson, J. E. *Cold Spring Harbor perspectives in biology* **2017**, *9*, a022046.

(273) Ivaska, J. *Small GTPases* **2011**, *2*, 51.

(274) Boyne, L. J.; Fischer, I.; Shea, T. B. *International Journal of Developmental Neuroscience* **1996**, *14*, 739.

(275) Shea, T. B.; Beermann, M. L.; Fischer, I. *Journal of Neuroscience Research* **1993**, *36*, 66.

(276) Van Steendam, K.; Tilleman, K.; Deforce, D. *Rheumatology (Oxford)* **2011**, *50*, 830.

(277) Bang, H.; Egerer, K.; Gauliard, A.; Lüthke, K.; Rudolph, P. E.; Fredenhagen, G.; Berg, W.; Feist, E.; Burmester, G. R. *Arthritis Rheum* **2007**, *56*, 2503.

(278) Van Steendam, K.; Tilleman, K.; De Ceuleneer, M.; De Keyser, F.; Elewaut, D.; Deforce, D. *Arthritis Research & Therapy* **2010**, *12*, R132.

(279) Müller, M.; Bhattacharya, S. S.; Moore, T.; Prescott, Q.; Wedig, T.; Herrmann, H.; Magin, T. M. *Human Molecular Genetics* **2009**, *18*, 1052.

(280) Matsuyama, M.; Tanaka, H.; Inoko, A.; Goto, H.; Yonemura, S.; Kobori, K.; Hayashi, Y.; Kondo, E.; Itohara, S.; Izawa, I.; Inagaki, M. *The Journal of biological chemistry* **2013**, *288*, 35626.

(281) Li, M.; Zhang, B.; Sun, B.; Wang, X.; Ban, X.; Sun, T.; Liu, Z.; Zhao, X. *J Exp Clin Cancer Res* **2010**, *29*, 109.

(282) Bhardwaj, M.; Sen, S.; Chosdol, K.; Bakhshi, S.; Pushker, N.; Sharma, A.; Kashyap, S.; Bajaj, M. S.; Singh, V. K. *British Journal of Ophthalmology* **2020**, *104*, 879.

(283) Hendrix, M. J. C.; Seftor, E. A.; Chu, Y.-W.; Trevor, K. T.; Seftor, R. E. B. *Cancer and Metastasis Reviews* **1996**, *15*, 507.

(284) Morrow, C. S.; Porter, T. J.; Xu, N.; Arndt, Z. P.; Ako-Asare, K.; Heo, H. J.; Thompson, E. A. N.; Moore, D. L. *Cell Stem Cell* **2020**, *26*, 558.

(285) Wilhelmsson, U.; Pozo-Rodrigalvarez, A.; Kalm, M.; de Pablo, Y.; Widestrand, A.; Pekna, M.; Pekny, M. *Biol Chem* **2019**, *400*, 1147.

(286) Larsson, A.; Wilhelmsson, U.; Pekna, M.; Pekny, M. *Neurochem Res*. **2004**, *29*, 2069.

(287) Wilhelmsson, U.; Faiz, M.; de Pablo, Y.; Sjoqvist, M.; Andersson, D.; Widestrand, A.; Potokar, M.; Stenovec, M.; Smith, P. L.; Shinjyo, N.; Pekny, T.; Zorec, R.; Stahlberg, A.; Pekna, M.; Sahlgren, C.; Pekny, M. *Stem Cells* **2012**, *30*, 2320.

(288) Thaiparambil, J. T.; Bender, L.; Ganesh, T.; Kline, E.; Patel, P.; Liu, Y.; Tighiouart, M.; Vertino, P. M.; Harvey, R. D.; Garcia, A.; Marcus, A. I. *International Journal of Cancer* **2011**, *129*, 2744.

(289) Bargagna-Mohan, P.; Deokule, S. P.; Thompson, K.; Wizeman, J.; Srinivasan, C.; Vooturi, S.; Kompella, U. B.; Mohan, R. *PLoS One* **2013**, *8*, e63881.

(290) Bargagna-Mohan, P.; Hamza, A.; Kim, Y. E.; Khuan Abby Ho, Y.; Mor-Vaknin, N.; Wendschlag, N.; Liu, J.; Evans, R. M.; Markovitz, D. M.; Zhan, C. G.; Kim, K. B.; Mohan, R. *Chem Biol* **2007**, *14*, 623.

(291) Bollong, M. J.; Pietila, M.; Pearson, A. D.; Sarkar, T. R.; Ahmad, I.; Soundararajan, R.; Lyssiotis, C. A.; Mani, S. A.; Schultz, P. G.; Lairson, L. L. *Proc Natl Acad Sci U S A* **2017**, *114*, E9903.

(292) Quinlan, R. A.; Franke, W. W. *European Journal of Biochemistry* **1983**, *132*, 477.

(293) Middeldorp, J.; Hol, E. M. *Progress in Neurobiology* **2011**, *93*, 421.

(294) Chou, Y.-H.; Khuon, S.; Herrmann, H.; Goldman, R. D. *Molecular biology of the cell* **2003**, *14*, 1468.

(295) Rosano, G. L.; Ceccarelli, E. A. *Front Microbiol* **2014**, *5*, 172.

(296) Zega, A. *Journal of Medicinal Chemistry* **2017**, *60*, 9437.

(297) Hallenbeck, K. K.; Davies, J. L.; Merron, C.; Ogden, P.; Sijbesma, E.; Ottmann, C.; Renslo, A. R.; Wilson, C.; Arkin, M. R. *SLAS Discov* **2018**, *23*, 183.

(298) Fernández, A.; Sinanoğlu, O. *Biophysical Chemistry* **1985**, *21*, 163.

(299) Signor, L.; Boeri Erba, E. *J Vis Exp* **2013**, 50635.

(300) Tran, N. H.; Qiao, R.; Xin, L.; Chen, X.; Liu, C.; Zhang, X.; Shan, B.; Ghodsi, A.; Li, M. *Nature Methods* **2019**, *16*, 63.

(301) Herrmann, H.; Aebi, U. *Annual Review of Biochemistry* **2004**, *73*, 749.

(302) Murale, D. P.; Hong, S. C.; Haque, M. M.; Lee, J.-S. *Proteome Science* **2017**, *15*, 14.

(303) Haselhorst, T.; Lamerz, A.-C.; Itzstein, M. v. In *Glycomics: Methods and Protocols*; Packer, N. H., Karlsson, N. G., Eds.; Humana Press: Totowa, NJ, 2009, p 375.

(304) Chalmers, M. J.; Busby, S. A.; Pascal, B. D.; West, G. M.; Griffin, P. R. *Expert Rev Proteomics* **2011**, *8*, 43.

(305) Schlichting, I. In *Protein-Ligand Interactions: Methods and Applications*; Ulrich Nienhaus, G., Ed.; Humana Press: Totowa, NJ, 2005, p 155.

(306) Mucke, N.; Wedig, T.; Burer, A.; Marekov, L. N.; Steinert, P. M.; Langowski, J.; Aebi, U.; Herrmann, H. *J Mol Biol* **2004**, *340*, 97.

(307) Cimmperman, P.; Baranauskiene, L.; Jachimoviciūte, S.; Jachno, J.; Torresan, J.; Michailoviene, V.; Matuliene, J.; Sereikaite, J.; Bumelis, V.; Matulis, D. *Biophysical journal* **2008**, *95*, 3222.

(308) Grin, B.; Mahammad, S.; Wedig, T.; Cleland, M. M.; Tsai, L.; Herrmann, H.; Goldman, R. D. *PLoS One* **2012**, *7*, e39065.

(309) Lynch, C. D.; Lazar, A. M.; Iskratsch, T.; Zhang, X.; Sheetz, M. P. *Mol Biol Cell* **2013**, *24*, 21.
(310) Yasui, Y.; Goto, H.; Matsui, S.; Manser, E.; Lim, L.; Nagata, K.-i.; Inagaki, M. *Oncogene* **2001**, *20*, 2868.
(311) Eriksson, J. E.; He, T.; Trejo-Skalli, A. V.; Härmälä-Braskén, A.-S.; Hellman, J.; Chou, Y.-H.; Goldman, R. D. *Journal of Cell Science* **2004**, *117*, 919.
(312) Yamaguchi, T.; Goto, H.; Yokoyama, T.; Silljé, H.; Hanisch, A.; Uldschmid, A.; Takai, Y.; Oguri, T.; Nigg, E. A.; Inagaki, M. *The Journal of cell biology* **2005**, *171*, 431.
(313) Goto, H.; Yasui, Y.; Kawajiri, A.; Nigg, E. A.; Terada, Y.; Tatsuka, M.; Nagata, K.; Inagaki, M. *J Biol Chem* **2003**, *278*, 8526.
(314) Cheng, T.-J.; Tseng, Y.-F.; Chang, W.-m.; Chang, M. D.-T.; Lai, Y.-K. *Journal of Cellular Biochemistry* **2003**, *89*, 589.
(315) Goto, H.; Kosako, H.; Tanabe, K.; Yanagida, M.; Sakurai, M.; Amano, M.; Kaibuchi, K.; Inagaki, M. *Journal of Biological Chemistry* **1998**, *273*, 11728.
(316) Kumar, N.; Robidoux, J.; Daniel, K. W.; Guzman, G.; Floering, L. M.; Collins, S. *J Biol Chem* **2007**, *282*, 9244.
(317) Mullins, C. S.; Wegner, T.; Klar, E.; Classen, C.-F.; Linnebacher, M. *BMC Res Notes* **2015**, *8*, 472.
(318) Päll, T.; Pink, A.; Kasak, L.; Turkina, M.; Anderson, W.; Valkna, A.; Kogerman, P. *PLoS One* **2011**, *6*, e29305.
(319) Levin, E. C.; Acharya, N. K.; Sedeyn, J. C.; Venkataraman, V.; D'Andrea, M. R.; Wang, H. Y.; Nagele, R. G. *Brain Res* **2009**, *1298*, 194.
(320) Lin, J.; Cai, W. *J Neurotrauma* **2004**, *21*, 1671.
(321) Livne-Bar, I.; Lam, S.; Chan, D.; Guo, X.; Askar, I.; Nahirnyj, A.; Flanagan, J. G.; Sivak, J. M. *Cell Death Dis* **2016**, *7*, e2386.
(322) Banks, W. A. *BMC Neurology* **2009**, *9*, S3.
(323) Erdő, F.; Bors, L. A.; Farkas, D.; Bajza, Á.; Gizurarson, S. *Brain Research Bulletin* **2018**, *143*, 155.

Appendices

Appendix 1: List of Enriched Proteins in LFQ Experiments

Table A 1. Table showing proteins enriched by active probe 77 over DMSO vehicle control in SVZ-derived NSCs in LFQ experiments. Biological replicates per condition, n = 3.

Gene Name	Protein Name	-Log p Value	Difference (Active 77 – DMSO)
Rps3a	40S ribosomal protein S3a	4.42318	2.38831
Acly	ATP-citrate synthase	4.37976	2.47036
Eef1g	Elongation factor 1-gamma	3.54919	1.80060
Rpl4	60S ribosomal protein L4	3.18137	1.80979
Fabp7	Fatty acid-binding protein, brain	3.13908	2.45586
Rps11	40S ribosomal protein S11	3.02352	2.22692
Rpl13	60S ribosomal protein L13	2.94047	1.47835
Eno1	Alpha-enolase	2.92404	1.79782
Slc25a5	ADP/ATP translocase 2; ADP/ATP translocase 2, N-terminally processed	2.77853	3.14609
Ckb	Creatine kinase B-type	2.44168	1.53328
Aldoa;Aldoart1	Fructose-bisphosphate aldolase A; Fructose-bisphosphate aldolase	2.32787	3.02808
Vdac2	Voltage-dependent anion-selective channel protein 2	2.28425	7.95278
Pgk1	Phosphoglycerate kinase 1	2.28120	2.37471
Hspa8	Heat shock cognate 71 kDa protein	2.23167	1.40893
Ldha	L-lactate dehydrogenase A chain	2.20718	3.34446
Pdia3	Protein disulfide-isomerase A3	2.16438	2.03109
Aldh1l1	Cytosolic 10-formyltetrahydrofolate dehydrogenase	2.14679	2.47746
Actb	Actin, cytoplasmic 1;Actin, cytoplasmic 1, N-terminally processed	2.12682	1.54945
Hsp90ab1	Heat shock protein HSP 90-beta	2.09326	2.09834
Tubb4b; Tubb4a	Tubulin beta-4B chain;Tubulin beta-4A chain	2.08798	2.92595
Vim	Vimentin	2.06327	2.28205
Ywhae	14-3-3 protein epsilon	2.01286	1.68170
Kpnb1	Importin subunit beta-1	1.97961	2.24419
Gapdh; Gm3839	Glyceraldehyde-3-phosphate dehydrogenase	1.97577	3.22362
Cs;Csl	Citrate synthase, mitochondrial;Citrate synthase	1.97029	1.75501
Gnb2l1	Guanine nucleotide-binding protein subunit beta-2-like 1; Guanine nucleotide-binding protein subunit beta-2-like 1, N-terminally processed	1.95882	2.30548
Slc25a3	Phosphate carrier protein, mitochondrial	1.93769	2.96156
Hmgcs1	Hydroxymethylglutaryl-CoA synthase, cytoplasmic	1.91407	2.39974

Rpl12	60S ribosomal protein L12	1.80619	1.98846
Pebp1	Phosphatidylethanolamine-binding protein 1;Hippocampal cholinergic neurostimulating peptide	1.74276	1.47670
Ppia	Peptidyl-prolyl cis-trans isomerase A;Peptidyl-prolyl cis-trans isomerase A, N-terminally processed	1.69244	1.53700
Eef2	Elongation factor 2	1.69229	1.79326
Tuba1a; Tuba1c; Tuba3a	Tubulin alpha-1A chain; Tubulin alpha-1C chain; Tubulin alpha-3 chain	1.65200	1.85690
Ywhaz	14-3-3 protein zeta/delta	1.60083	2.07525
Rrbp1	Ribosome-binding protein 1	1.59057	2.02262
Aco2	Aconitate hydratase, mitochondrial	1.55450	1.94237
Pgam1	Phosphoglycerate mutase 1	1.53484	1.78674
Mdh2	Malate dehydrogenase, mitochondrial	1.50406	2.74366
Tkt	Transketolase	1.47603	4.38840
Hnrnpa1	Heterogeneous nuclear ribonucleoprotein A1; Heterogeneous nuclear ribonucleoprotein A1, N-terminally processed	1.47489	1.52122
Pkm	Pyruvate kinase PKM	1.46459	1.77955
Eef1a1	Elongation factor 1-alpha 1	1.44929	1.46421
Hspa5	78 kDa glucose-regulated protein	1.43244	1.30207
Cct8	T-complex protein 1 subunit theta	1.42771	2.36218
H3f3a; Hist1h3b; Hist1h3a; H3f3c	Histone H3.3; Histone H3.2; Histone H3.1; Histone H3.3C	1.36145	1.36099
Slc25a4	ADP/ATP translocase 1	1.29908	2.41238
Rps20	40S ribosomal protein S20	1.28817	1.52026
Phgdh	D-3-phosphoglycerate dehydrogenase	1.26335	2.54296
Mdh1	Malate dehydrogenase, cytoplasmic	1.25510	1.99121
Hspd1	60 kDa heat shock protein, mitochondrial	1.21354	1.35705
Hspa9	Stress-70 protein, mitochondrial	1.17251	1.64292
Hsp90b1	Endoplasmin	1.10406	2.05607
Tubb5	Tubulin beta-5 chain	1.02280	2.27008

*Table A 2. Table showing proteins enriched by active probe **77** over inactive probe **78** in SVZ-derived NSCs in LFQ experiments. Biological replicates per condition, n = 3.*

Gene Name	Protein Name	-Log p Value	Difference (Active 77 – Inactive 78)
Rpl13a	60S ribosomal protein L13a	2.88460	1.79079
Rpl4	60S ribosomal protein L4	2.85688	1.63798
Dhrs1	Dehydrogenase/reductase SDR family member 1	2.70272	2.61393
Tomm22	Mitochondrial import receptor subunit TOM22 homolog	2.56456	3.81438
Vdac2	Voltage-dependent anion-selective channel protein 2	2.48482	2.26864
Tpi1	Triosephosphate isomerase	2.44081	2.12725
Ran	GTP-binding nuclear protein Ran	2.41391	2.02459

Eef1g	Elongation factor 1-gamma	2.38846	1.53732
Slc25a5	ADP/ATP translocase 2; ADP/ATP translocase 2, N-terminally processed	2.28522	1.98992
Rpl13	60S ribosomal protein L13	2.18883	1.43649
Hsd17b12	Very-long-chain 3-oxoacyl-CoA reductase	2.16971	3.77290
Vdac1	Voltage-dependent anion-selective channel protein 1	2.13940	1.94745
Rps3	40S ribosomal protein S3	2.05596	1.83913
Dhcr7	7-dehydrocholesterol reductase	2.03023	3.20044
Hsp90b1	Endoplasmin	2.00794	1.66606
Fabp7	Fatty acid-binding protein, brain	2.00303	2.99574
Ipo5	Importin-5	1.93516	2.12322
Cs;Csl	Citrate synthase, mitochondrial; Citrate synthase	1.92788	1.85086
Eno1	Alpha-enolase	1.90916	2.10703
Ywhaq	14-3-3 protein theta	1.85142	1.94256
Aco2	Aconitate hydratase, mitochondrial	1.84342	1.64835
Atp1a1	Sodium/potassium-transporting ATPase subunit alpha-1	1.83500	1.62600
Aldoa; Aldoart1	Fructose-bisphosphate aldolase A;Fructose-bisphosphate aldolase	1.83391	1.94008
Kpnb1	Importin subunit beta-1	1.81814	2.06951
Hspa8	Heat shock cognate 71 kDa protein	1.81306	1.52948
Actb	Actin, cytoplasmic 1; Actin, cytoplasmic 1, N-terminally processed	1.79987	1.47315
Ckb	Creatine kinase B-type	1.74281	1.62062
Flna	Filamin-A	1.73582	1.99562
Tubb4b; Tubb4a	Tubulin beta-4B chain; Tubulin beta-4A chain	1.67840	2.22619
Atp2a2	Sarcoplasmic/endoplasmic reticulum calcium ATPase 2	1.67747	3.24979
Gapdh; Gm3839	Glyceraldehyde-3-phosphate dehydrogenase	1.65803	1.94655
Vim	Vimentin	1.63381	1.52197
Hspa5	78 kDa glucose-regulated protein	1.63326	1.77073
Pgk1	Phosphoglycerate kinase 1	1.56297	1.70340
Ldha	L-lactate dehydrogenase A chain	1.54628	2.34517
Rps11	40S ribosomal protein S11	1.54129	2.07919
Ywhae	14-3-3 protein epsilon	1.52808	2.18818
Hmox2	Heme oxygenase 2	1.46991	3.19519
Pgam1	Phosphoglycerate mutase 1	1.44570	1.74021
Hsp90ab1	Heat shock protein HSP 90-beta	1.42810	2.17997
Vdac3	Voltage-dependent anion-selective channel protein 3	1.41367	2.24108
Atp1a2; Atp1a3	Sodium/potassium-transporting ATPase subunit alpha-2; Sodium/potassium-transporting ATPase subunit alpha-3	1.39429	2.01114
Atp5a1	ATP synthase subunit alpha, mitochondrial	1.39411	1.56733
Pcbp1	Poly(rC)-binding protein 1	1.38569	2.73633
Ctsd	Cathepsin D	1.37755	2.92432
Tubb2b	Tubulin beta-2B chain	1.23960	1.55755
Pcyox1	Prenylcysteine oxidase	1.23943	2.75620
H3f3a; Hist1h3b; Hist1h3a; H3f3c	Histone H3.3; Histone H3.2; Histone H3.1; Histone H3.3C	1.22935	1.62766

Aldh1l1	Cytosolic 10-formyltetrahydrofolate dehydrogenase	1.19079	2.76372
Uqcrc1	Cytochrome b-c1 complex subunit 1, mitochondrial	1.16719	3.07457
Ywhaz	14-3-3 protein zeta/delta	1.06559	2.47531
Tubb5	Tubulin beta-5 chain	1.06230	2.74358

*Table A 3. Table showing proteins enriched by active probe **77** over competition control **15** in SVZ-derived NSCs in LFQ experiments. Biological replicates per condition, n = 3.*

Gene Name	Protein Name	-Log p Value	Difference (Active 77 – Active 77/Comp 15)
Fasn	Fatty acid synthase	1.37450	1.05439
Sec61a1	Protein transport protein Sec61 subunit alpha isoform 1	1.10447	0.87910
Ube2v1; Gm20431	Ubiquitin-conjugating enzyme E2 variant 1	1.02475	1.08740
Eprs	Bifunctional glutamate/proline--tRNA ligase; Glutamate--tRNA ligase	1.08805	0.81768
Mybbp1a	Myb-binding protein 1A	0.88887	0.88356
Sptan1	Spectrin alpha chain, non-erythrocytic 1	0.75550	0.75750
Dhcr7	7-dehydrocholesterol reductase	0.61723	0.59720

*Table A 4. Table showing proteins enriched by active probe **77** over DMSO vehicle control in DG-derived NSCs in LFQ experiments. Biological replicates per condition, n = 3.*

Gene Name	Protein Name	-Log p Value	Difference (Active 77 – DMSO)
Vdac1	Voltage-dependent anion-selective channel protein 1	2.66531	6.87723
Cct4	T-complex protein 1 subunit delta	2.49693	1.37211
Rplp1;Gm10073	60S acidic ribosomal protein P1	2.49656	1.19651
Tkt	Transketolase	2.39946	1.06427
Vdac2	Voltage-dependent anion-selective channel protein 2	2.39552	4.59723
Rac1;Rac2;Rac3	Ras-related C3 botulinum toxin substrate 1; Ras-related C3 botulinum toxin substrate 2; Ras-related C3 botulinum toxin substrate 3	2.21688	1.50711
Uba1	Ubiquitin-like modifier-activating enzyme 1	2.16342	1.65527
Hsp90ab1	Heat shock protein HSP 90-beta	2.11050	2.01702
Eef1g	Elongation factor 1-gamma	1.84789	1.17435
Atp1a2;Atp1a3	Sodium/potassium-transporting ATPase subunit alpha-2; Sodium/potassium-transporting ATPase subunit alpha-3	1.72496	3.27531
Atp2a2	Sarcoplasmic/endoplasmic reticulum calcium ATPase 2	1.66520	2.56232
Tubb2b	Tubulin beta-2B chain	1.57950	1.64647
Slc25a5	ADP/ATP translocase 2; ADP/ATP translocase 2, N-terminally processed	1.39237	2.18493
Acat1	Acetyl-CoA acetyltransferase, mitochondrial	1.36434	2.37567
Vim	Vimentin	1.31241	2.12538

*Table A 5. Table showing proteins enriched by active probe **77** over inactive probe **78** in DG-derived NSCs in LFQ experiments. Biological replicates per condition, n = 3.*

Gene Name	Protein Name	-Log p Value	Difference (Active 77 – Inactive 78)
Rps8	40S ribosomal protein S8	2.98719	1.32982
Tkt	Transketolase	2.90385	2.67085
Lgals1	Galectin-1	2.68458	4.26018
Eef1a1;Eef1a2	Elongation factor 1-alpha 1;Elongation factor 1-alpha 2	2.61296	1.9192
Uba1	Ubiquitin-like modifier-activating enzyme 1	2.58407	2.94240
Pccb	Propionyl-CoA carboxylase beta chain, mitochondrial	2.56028	2.25696
Phgdh	D-3-phosphoglycerate dehydrogenase	2.50358	2.36029
Ckb	Creatine kinase B-type	2.43983	2.98779
Rpl18	60S ribosomal protein L18	2.33530	2.5292
Aldh1l1	Cytosolic 10-formyltetrahydrofolate dehydrogenase	2.31469	2.42319
Gapdh; Gm3839	Glyceraldehyde-3-phosphate dehydrogenase	2.28525	2.28046
Atp1a2; Atp1a3	Sodium/potassium-transporting ATPase subunit alpha-2; Sodium/potassium-transporting ATPase subunit alpha-3	2.25145	3.26554
Vcp	Transitional endoplasmic reticulum ATPase	2.24513	2.60097
Ppia	Peptidyl-prolyl cis-trans isomerase A;Peptidyl-prolyl cis-trans isomerase A, N-terminally processed	2.19747	1.14061
Rpl27a	60S ribosomal protein L27a	2.19212	2.62283
Hmgcs1	Hydroxymethylglutaryl-CoA synthase, cytoplasmic	2.19033	2.24596
Hspd1	60 kDa heat shock protein, mitochondrial	2.16996	2.50953
Hsp90b1	Endoplasmin	2.16433	2.23390
Fasn	Fatty acid synthase	2.12205	2.59311
Tuba1a; Tuba1b; Tuba1c; Tuba3a; Tuba4a	Tubulin alpha-1A chain; Tubulin alpha-1B chain; Tubulin alpha-1C chain; Tubulin alpha-3 chain; Tubulin alpha-4A chain	2.11463	2.06876
Uqcrc2	Cytochrome b-c1 complex subunit 2, mitochondrial	2.08034	1.32669
Pkm	Pyruvate kinase PKM	2.06250	3.36797
Tubb2b	Tubulin beta-2B chain	2.02877	2.11558
Rpl7a	60S ribosomal protein L7a	1.98850	1.82090
Hsp90ab1	Heat shock protein HSP 90-beta	1.92993	2.35081
Gstm1	Glutathione S-transferase Mu 1	1.90020	2.16534
Hspa8	Heat shock cognate 71 kDa protein	1.89674	1.91651
Acadl	Long-chain specific acyl-CoA dehydrogenase, mitochondrial	1.85508	2.85666
Atp2a2	Sarcoplasmic/endoplasmic reticulum calcium ATPase 2	1.82108	3.32950
Atp5a1	ATP synthase subunit alpha, mitochondrial	1.81970	2.07426
Vdac2	Voltage-dependent anion-selective channel protein 2	1.79719	2.78118
Vdac1	Voltage-dependent anion-selective channel protein 1	1.77657	3.16163
Tubb5	Tubulin beta-5 chain	1.77015	2.11685

Slc25a5	ADP/ATP translocase 2; ADP/ATP translocase 2, N-terminally processed	1.76538	2.21685
Ran	GTP-binding nuclear protein Ran	1.72689	1.34777
Rps14	40S ribosomal protein S14	1.65746	1.50179
Cct3	T-complex protein 1 subunit gamma	1.65242	1.46064
Pcbp1	Poly(rC)-binding protein 1	1.64777	1.83381
Cct8	T-complex protein 1 subunit theta	1.57637	2.01492
Cfl1	Cofilin-1	1.56518	1.29863
Aco2	Aconitate hydratase, mitochondrial	1.54645	2.08185
Hspa5	78 kDa glucose-regulated protein	1.53817	2.95559
Eno1	Alpha-enolase	1.50941	3.28891
Aldoa; Aldoart1	Fructose-bisphosphate aldolase A;Fructose-bisphosphate aldolase	1.49163	1.68566
Pcca	Propionyl-CoA carboxylase alpha chain, mitochondrial	1.48096	1.45545
Rps3a	40S ribosomal protein S3a	1.46429	1.12925
Actg1	Actin, cytoplasmic 2;Actin, cytoplasmic 2, N-terminally processed	1.46393	1.51084
Rac1; Rac2; Rac3	Ras-related C3 botulinum toxin substrate 1; Ras-related C3 botulinum toxin substrate 2; Ras-related C3 botulinum toxin substrate 3	1.44978	1.89776
Slc25a20	Mitochondrial carnitine/acylcarnitine carrier protein	1.44137	1.61917
Rpl4	60S ribosomal protein L4	1.36382	1.18520
Acaca	Acetyl-CoA carboxylase 1;Biotin carboxylase	1.34970	2.85683
Rrbp1	Ribosome-binding protein 1	1.32045	2.12745
Vim	Vimentin	1.23743	3.19649
Pc	Pyruvate carboxylase, mitochondrial	1.17678	1.40435
Ywhaz	14-3-3 protein zeta/delta	1.12751	1.09941
Eef2	Elongation factor 2	1.06997	1.47323
Rpl6	60S ribosomal protein L6	1.04559	1.09099
Glud1	Glutamate dehydrogenase 1, mitochondrial	1.04490	1.59198

*Table A 6. Table showing proteins enriched by active probe **77** over competition control **15** in DG-derived NSCs in LFQ experiments. Biological replicates per condition, n = 3.*

Gene Name	Protein Name	-Log p value	Difference (Active 77 – Active 77/Comp 15)
Eef1a1; Eef1a2	Elongation factor 1-alpha 1; Elongation factor 1-alpha 2	1.15034	1.00371
Rpl19	60S ribosomal protein L19	1.05132	0.76799
Pcbp1	Poly(rC)-binding protein 1	0.98586	1.11069
Slc25a3	Phosphate carrier protein, mitochondrial	0.90878	1.28305
Rpl6	60S ribosomal protein L6	0.83096	0.75415
Tkt	Transketolase	0.72185	0.92788
Hist1h1e	Histone H1.4	0.70181	0.72168
Eef1g	Elongation factor 1-gamma	0.67773	0.50717
Atp1a2; Atp1a3	Sodium/potassium-transporting ATPase subunit alpha-2; Sodium/potassium-transporting ATPase subunit alpha-3	0.65386	1.10946
Hnrnpu	Heterogeneous nuclear ribonucleoprotein U	0.63690	0.84124

Lgals1	Galectin-1	0.63562	1.63897
Mdh1	Malate dehydrogenase, cytoplasmic	0.56715	0.93308
Uba1	Ubiquitin-like modifier-activating enzyme 1	0.56391	1.92482
Rps2	40S ribosomal protein S2	0.55579	0.38563
Rps14	40S ribosomal protein S14	0.54835	0.41780
Slc25a5	ADP/ATP translocase 2; ADP/ATP translocase 2, N-terminally processed	0.54341	1.02799

Appendix 2: List of Enriched Proteins in TMT Experiments

Table A 7. Table showing proteins enriched by active probe 77 over DMSO vehicle control in SVZ-derived NSCs in TMT experiments. Biological replicates per condition, n = 3.

Gene Name	Protein Name	-Log p Value	Difference (Active 77 – DMSO)
Tfrc	Transferrin receptor protein 1	4.73174	0.48803
Pmpca	Mitochondrial-processing peptidase subunit alpha	4.16528	0.19107
Nucb1	Nucleobindin-1	3.66709	1.36600
Acadl	Long-chain specific acyl-CoA dehydrogenase, mitochondrial	3.56591	1.04643
Dohh	Deoxyhypusine hydroxylase	3.48184	0.95640
Immt	MICOS complex subunit Mic60	3.41247	0.26634
Eif5	Eukaryotic translation initiation factor 5	3.28198	0.95940
Tmem97	Transmembrane protein 97	3.27256	2.35903
Ephx1	Epoxide hydrolase 1	3.10367	1.02165
Rtn4	Reticulon-4	3.01067	0.71307
Ermp1	Endoplasmic reticulum metallopeptidase 1	2.98313	0.49646
Acad9	Acyl-CoA dehydrogenase family member 9, mitochondrial	2.95492	0.98986
Cse1l	Exportin-2	2.94228	0.39861
Gpr107	Protein GPR107	2.91148	2.23924
Abcb1b;Abcb9; Abcb1a;Abcb4	Multidrug resistance protein 1B;ATP-binding cassette sub-family B member 9;Multidrug resistance protein 1A;Multidrug resistance protein 3	2.87070	2.25857
Bsg	Basigin	2.82793	1.67966
Prcp	Lysosomal Pro-X carboxypeptidase	2.82471	1.16013
Echs1	Enoyl-CoA hydratase, mitochondrial	2.78681	1.18053
Atp1a1	Sodium/potassium-transporting ATPase subunit alpha-1	2.50438	0.58044
Mtap	S-methyl-5-thioadenosine phosphorylase	2.48965	0.80158
Tspan7	Tetraspanin-7	2.43139	1.21399
Hmox2	Heme oxygenase 2	2.42752	1.95052
Psmd7	26S proteasome non-ATPase regulatory subunit 7	2.39751	0.47886
Sccpdh	Saccharopine dehydrogenase-like oxidoreductase	2.37201	1.63057
Tmed7		2.30505	0.73306
Ppt1	Palmitoyl-protein thioesterase 1	2.29032	0.89348
Atp5i	ATP synthase subunit e, mitochondrial	2.25676	0.74506
Bcap31	B-cell receptor-associated protein 31	2.25371	1.25467
Tmem245	Transmembrane protein 245	2.22003	0.73946
Mtch2	Mitochondrial carrier homolog 2	2.21287	1.39788
Glg1	Golgi apparatus protein 1	2.17746	0.77280
Naa15	N-alpha-acetyltransferase 15, NatA auxiliary subunit	2.15677	0.24659
Phb2	Prohibitin-2	2.13688	0.64867

Igf2r	Cation-independent mannose-6-phosphate receptor	2.12733	0.36791
Mfsd5	Molybdate-anion transporter	2.09984	2.31547
Zadh2	Zinc-binding alcohol dehydrogenase domain-containing protein 2	2.09331	1.35115
Mtch1	Mitochondrial carrier homolog 1	2.08657	0.73928
Pitpnb	Phosphatidylinositol transfer protein beta isoform	2.04440	1.17232
Taldo1	Transaldolase	2.01394	0.26854
Pitpna	Phosphatidylinositol transfer protein alpha isoform	2.00516	0.67635
Acsl3	Long-chain-fatty-acid--CoA ligase 3	2.00153	0.35600
Hepacam	Hepatocyte cell adhesion molecule	1.99662	2.51716
Cyb5b	Cytochrome b5 type B	1.97714	0.93589
Ccnd2	G1/S-specific cyclin-D2	1.95935	3.01858
Prkcsh	Glucosidase 2 subunit beta	1.95593	0.40177
Slc4a4	Electrogenic sodium bicarbonate cotransporter 1	1.95141	1.03432
Zmpste24	CAAX prenyl protease 1 homolog	1.94422	1.97269
Coq9	Ubiquinone biosynthesis protein COQ9, mitochondrial	1.94140	0.34725
Lnpep	Leucyl-cystinyl aminopeptidase	1.93386	0.49633
Hm13	Minor histocompatibility antigen H13	1.92213	1.62120
Ckap4	Cytoskeleton-associated protein 4	1.92211	0.96100
Nsdhl	Sterol-4-alpha-carboxylate 3-dehydrogenase, decarboxylating	1.89812	0.44948
Acadm	Medium-chain specific acyl-CoA dehydrogenase, mitochondrial	1.89024	2.29129
Sqle	Squalene monooxygenase	1.87761	0.54096
Kcnj10	ATP-sensitive inward rectifier potassium channel 10	1.86446	1.65750
Ap1s1	AP-1 complex subunit sigma-1A	1.85415	2.50470
Ociad2	OCIA domain-containing protein 2	1.84582	0.35700
Tspan3	Tetraspanin-3	1.84472	2.01685
Atp13a1	Manganese-transporting ATPase 13A1	1.83813	0.37362
Nap1l4	Nucleosome assembly protein 1-like 4	1.79937	0.27160
Olig2	Oligodendrocyte transcription factor 2	1.78417	0.27669
Tmx4	Thioredoxin-related transmembrane protein 4	1.77398	1.92619
Ssrp1	FACT complex subunit SSRP1	1.75187	0.25854
Stx7	Syntaxin-7	1.73401	0.36851
Gria3	Glutamate receptor 3	1.73339	0.80596
Vdac1	Voltage-dependent anion-selective channel protein 1	1.71814	1.98790
Akap12	A-kinase anchor protein 12	1.70988	0.70318
Hars	Histidine--tRNA ligase, cytoplasmic	1.70761	0.57330
Npc1	Niemann-Pick C1 protein	1.70380	1.23078
Dcakd	Dephospho-CoA kinase domain-containing protein	1.69315	0.95829
Dhcr7	7-dehydrocholesterol reductase	1.68779	0.66425
Praf2	PRA1 family protein 2	1.67718	0.30907
Dhfr	Dihydrofolate reductase	1.67169	0.52544

Mtx1	Metaxin-1	1.66753	0.40001
Itgav	Integrin alpha-V; Integrin alpha-V heavy chain;Integrin alpha-V light chain	1.65806	0.30768
Gpaa1	Glycosylphosphatidylinositol anchor attachment 1 protein	1.65699	0.87752
Timm17a	Mitochondrial import inner membrane translocase subunit Tim17-A	1.64989	1.83445
Acox1	Peroxisomal acyl-coenzyme A oxidase 1	1.64745	0.89016
Baiap2	Brain-specific angiogenesis inhibitor 1-associated protein 2	1.63805	1.21140
Sec61a1	Protein transport protein Sec61 subunit alpha isoform 1	1.63783	0.47521
Pcyox1	Prenylcysteine oxidase	1.63249	1.15398
Vkorc1	Vitamin K epoxide reductase complex subunit 1	1.61804	0.31462
Scpep1	Retinoid-inducible serine carboxypeptidase	1.59374	0.39480
Golt1b	Vesicle transport protein GOT1B	1.58496	0.76312
Npepps	Puromycin-sensitive aminopeptidase	1.58486	0.49776
Surf4	Surfeit locus protein 4	1.57870	0.35803
Slc35f1	Solute carrier family 35 member F1	1.57124	0.67362
Alg9	Alpha-1,2-mannosyltransferase ALG9	1.53957	3.29081
Gpm6a	Neuronal membrane glycoprotein M6-a	1.53136	1.45639
Nceh1	Neutral cholesterol ester hydrolase 1	1.52828	2.29911
Il1rap	Interleukin-1 receptor accessory protein	1.52593	0.76219
Ttyh3	Protein tweety homolog 3	1.52222	0.77646
Stt3a	Dolichyl-diphosphooligosaccharide--protein glycosyltransferase subunit STT3A	1.50050	1.27109
Gm2a	Ganglioside GM2 activator	1.49693	0.72771
Lpcat3	Lysophospholipid acyltransferase 5	1.49161	0.78224
Kdsr	3-ketodihydrosphingosine reductase	1.48350	0.89640
Tmem199	Transmembrane protein 199	1.46202	0.77121
Vdac2	Voltage-dependent anion-selective channel protein 2	1.45999	1.48417
Letm1	LETM1 and EF-hand domain-containing protein 1, mitochondrial	1.44657	0.57215
Timm17b	Mitochondrial import inner membrane translocase subunit Tim17-B	1.43737	1.51881
Laptm4a	Lysosomal-associated transmembrane protein 4A	1.42298	3.12001
Slc25a20	Mitochondrial carnitine/acylcarnitine carrier protein	1.42250	1.86922
Tnpo1	Transportin-1	1.42053	0.34762
Tmed2	Transmembrane emp24 domain-containing protein 2	1.41936	1.88875
Yes1; Fyn; Src	Tyrosine-protein kinase Yes; Tyrosine-protein kinase Fyn;Neuronal proto-oncogene tyrosine-protein kinase Src	1.41515	0.55301
Mpv17	Protein Mpv17	1.41224	0.47808
Slc3a2	4F2 cell-surface antigen heavy chain	1.40001	0.29838
Tmem63b	CSC1-like protein 2	1.38361	0.61075
Higd1a	HIG1 domain family member 1A, mitochondrial	1.38340	3.42324
Tomm6	Mitochondrial import receptor subunit TOM6 homolog	1.38228	0.35308
Pspc1	Paraspeckle component 1	1.37471	0.53423
Slc6a11	Sodium- and chloride-dependent GABA transporter 3	1.35258	0.59830

Slc22a17	Solute carrier family 22 member 17	1.34655	1.00849
Atad1	ATPase family AAA domain-containing protein 1	1.34619	1.74588
Ctsd	Cathepsin D	1.33819	1.41210
Chst2	Carbohydrate sulfotransferase 2	1.33318	0.97487
Slc29a1	Equilibrative nucleoside transporter 1	1.33158	0.50894
Hsdl1	Inactive hydroxysteroid dehydrogenase-like protein 1	1.32851	0.53445
Aifm1	Apoptosis-inducing factor 1, mitochondrial	1.32306	0.38964
Hsdl2	Hydroxysteroid dehydrogenase-like protein 2	1.31982	0.54203
Golm1	Golgi membrane protein 1	1.30951	1.22394
Rbx1	E3 ubiquitin-protein ligase RBX1; E3 ubiquitin-protein ligase RBX1, N-terminally processed	1.30461	0.33085
Golim4	Golgi integral membrane protein 4	1.29375	0.55702
Slc35f6	Solute carrier family 35 member F6	1.29295	0.41846
Ept1	Ethanolaminephosphotransferase 1	1.28674	0.65050
Tmem41a	Transmembrane protein 41A	1.28583	1.49437
Emc7	ER membrane protein complex subunit 7	1.26689	1.18059
Tmem43	Transmembrane protein 43	1.26292	0.48573
Mboat7	Lysophospholipid acyltransferase 7	1.26073	0.80900
Tm9sf4	Transmembrane 9 superfamily member 4	1.25963	1.12323
Ptgr2	Prostaglandin reductase 2	1.25729	1.08026
Cdip1	Cell death-inducing p53-target protein 1	1.23624	1.46285
Atp2a2	Sarcoplasmic/endoplasmic reticulum calcium ATPase 2	1.23300	0.74140
Cd9	CD9 antigen	1.22691	1.18259
Pcyox1l	Prenylcysteine oxidase-like	1.21920	0.88327
Uba2	SUMO-activating enzyme subunit 2	1.21674	0.45942
Fdft1	Squalene synthase	1.21590	0.94650
Atp6v0a2	V-type proton ATPase 116 kDa subunit a isoform 2	1.21498	0.52277
Pgrmc2	Membrane-associated progesterone receptor component 2	1.21184	1.15383
Atl3	Atlastin-3	1.19343	0.70120
Ociad1	OCIA domain-containing protein 1	1.19045	1.11129
Canx	Calnexin	1.18933	1.02998
Impad1	Inositol monophosphatase 3	1.18365	0.66331
Gstm1	Glutathione S-transferase Mu 1	1.18284	1.54903
Cd81	CD81 antigen	1.17451	1.31614
Ptrh2	Peptidyl-tRNA hydrolase 2, mitochondrial	1.17137	0.54453
Rtn3	Reticulon-3	1.16829	1.46767
Bri3bp	BRI3-binding protein	1.15949	0.63465
Por	NADPH--cytochrome P450 reductase	1.15770	0.64363
Fundc2	FUN14 domain-containing protein 2	1.15570	0.72047
Etfdh	Electron transfer flavoprotein-ubiquinone oxidoreductase, mitochondrial	1.15386	0.59677
Lemd2	LEM domain-containing protein 2	1.14020	0.61556

Rabgap1	Rab GTPase-activating protein 1	1.13917	0.58656
Scarb2	Lysosome membrane protein 2	1.13561	0.92331
Itgb1	Integrin beta-1	1.13044	0.74294
Slc18b1	MFS-type transporter SLC18B1	1.13037	2.68250
Slc16a1	Monocarboxylate transporter 1	1.12855	0.61966
Apoe	Apolipoprotein E	1.12723	0.5578
Tomm22	Mitochondrial import receptor subunit TOM22 homolog	1.12580	1.46636
Sppl2a	Signal peptide peptidase-like 2A	1.12111	1.35558
Abhd12	Monoacylglycerol lipase ABHD12	1.10676	0.42949
Sec62	Translocation protein SEC62	1.08751	0.50630
Creld1	Cysteine-rich with EGF-like domain protein 1	1.08260	0.92082
Jagn1	Protein jagunal homolog 1	1.07879	1.40210
Saysd1	SAYSvFN domain-containing protein 1	1.07775	1.07930
Cers6	Ceramide synthase 6	1.07705	0.61302
Lmf2	Lipase maturation factor 2	1.07010	1.16105
Pon2	Serum paraoxonase/arylesterase 2	1.06925	1.22118
Sv2a	Synaptic vesicle glycoprotein 2A	1.06868	1.46140
Cyp51a1	Lanosterol 14-alpha demethylase	1.06387	0.79490
P4hb	Protein disulfide-isomerase	1.06267	0.50300
Cers2	Ceramide synthase 2	1.06110	0.90753
Fam114a2	Protein FAM114A2	1.05804	0.66749
Fkbp8	Peptidyl-prolyl cis-trans isomerase FKBP8	1.04560	0.57702
Dhrs1	Dehydrogenase/reductase SDR family member 1	1.04292	0.56937
Dpy19l1	Probable C-mannosyltransferase DPY19L1	1.04127	1.05618
Sgpl1	Sphingosine-1-phosphate lyase 1	1.03812	0.70733
	UPF0729 protein C18orf32 homolog	1.03235	1.91563
Stoml2	Stomatin-like protein 2, mitochondrial	1.02588	0.75588
Acp6	Lysophosphatidic acid phosphatase type 6	1.01729	0.69031
Mfsd1	Major facilitator superfamily domain-containing protein 1	1.01346	1.40144
Hsd17b12	Very-long-chain 3-oxoacyl-CoA reductase	1.01245	1.06270
Rdh11	Retinol dehydrogenase 11	1.01152	0.68415
Tmem87a	Transmembrane protein 87A	1.00858	1.02310
Tram1	Translocating chain-associated membrane protein 1	1.00454	0.58794
Arl3	ADP-ribosylation factor-like protein 3	0.99732	0.51198
Hacd3	Very-long-chain (3R)-3-hydroxyacyl-CoA dehydratase 3	0.99455	0.69782
Psmg1	Proteasome assembly chaperone 1	0.98696	0.68838
Actg1	Actin, cytoplasmic 2; Actin, cytoplasmic 2, N-terminally processed	0.98181	1.24387
Eif3m	Eukaryotic translation initiation factor 3 subunit M	0.97742	0.85273
Ergic3	Endoplasmic reticulum-Golgi intermediate compartment protein 3	0.97604	0.85723
Tm9sf3	Transmembrane 9 superfamily member 3	0.97299	1.27514

Abhd16a	Abhydrolase domain-containing protein 16A	0.96741	0.87974
Sec11a	Signal peptidase complex catalytic subunit SEC11A	0.96533	0.93670
Tmed10	Transmembrane emp24 domain-containing protein 10	0.96063	0.56765
Nptn	Neuroplastin	0.95774	0.93645
Slc7a1	High affinity cationic amino acid transporter 1	0.94807	0.63416
Ankle2	Ankyrin repeat and LEM domain-containing protein 2	0.94466	0.81056
Rtn1	Reticulon-1	0.93727	1.28152
Abcb7	ATP-binding cassette sub-family B member 7, mitochondrial	0.92528	0.74573
Tmem41b	Transmembrane protein 41B	0.92357	1.19214
Reep5	Receptor expression-enhancing protein 5	0.92302	0.66236
Ncam1	Neural cell adhesion molecule 1	0.92227	0.67870
Slc7a5	Large neutral amino acids transporter small subunit 1	0.90190	1.06833
Wls	Protein wntless homolog	0.89603	1.22841
Gdi1	Rab GDP dissociation inhibitor alpha	0.88788	0.78245
Clptm1	Cleft lip and palate transmembrane protein 1 homolog	0.88673	0.91908
Opa3	Optic atrophy 3 protein homolog	0.86349	1.01775

*Table A 8. Table showing protein enriched by active probe **77** over inactive probe **78** in SVZ-derived NSCs in TMT experiments. Biological replicates per condition, n = 3.*

Gene Name	Protein Name	-Log p Value	Difference (Active 77 – Inactive 78)
Higd1a	HIG1 domain family member 1A, mitochondrial	2.07955	2.49809

*Table A 9. Table showing proteins enriched by active probe **77** over competition control **15** in SVZ-derived NSCs in TMT experiments. Biological replicates per condition, n = 3.*

Gene Name	Protein Name	-Log p value	Difference (Active 77 – Active 77/Comp 15)
Pabpc1	Polyadenylate-binding protein 1	1.92009	0.71942
Dbi	Acyl-CoA-binding protein	2.10391	1.69885
Wars	Tryptophan--tRNA ligase, cytoplasmic; T1-TrpRS; T2-TrpRS	3.15959	0.51148
Sec61g	Protein transport protein Sec61 subunit gamma	1.90337	1.08071
Rps27a; Gm8797; Uba52; Ubb; Ubc	Ubiquitin-40S ribosomal protein S27a;Ubiquitin;40S ribosomal protein S27a; Ubiquitin-60S ribosomal protein L40; Ubiquitin; 60S ribosomal protein L40; Polyubiquitin-B;Ubiquitin; Polyubiquitin-C;Ubiquitin;Ubiquitin-related 1; Ubiquitin-related 2	3.36206	0.71635
Dnaja1	DnaJ homolog subfamily A member 1	3.28630	0.44710
Rps12	40S ribosomal protein S12	2.57852	0.49905
Psmb4	Proteasome subunit beta type-4	1.99360	0.68338

Luc7l3	Luc7-like protein 3	2.74607	0.78498
Dek	Protein DEK	2.48858	0.52768
Naa15	N-alpha-acetyltransferase 15, NatA auxiliary subunit	4.22742	0.36502
Armc6	Armadillo repeat-containing protein 6	1.99760	0.78765
Hibch	3-hydroxyisobutyryl-CoA hydrolase, mitochondrial	2.50584	0.50847
Rpe	Ribulose-phosphate 3-epimerase	2.28170	0.54224
Srgap2	SLIT-ROBO Rho GTPase-activating protein 2	2.66417	0.67235
Etfdh	Electron transfer flavoprotein-ubiquinone oxidoreductase, mitochondrial	1.98529	0.94107
Gmfb; Gmfg	Glia maturation factor beta; Glia maturation factor gamma	2.05452	0.62982
Rpl11	60S ribosomal protein L11	3.11497	0.40426
Tbcb	Tubulin-folding cofactor B	2.05995	1.04158
Sec13	Protein SEC13 homolog	2.84180	0.48179
Ube2v2	Ubiquitin-conjugating enzyme E2 variant 2	2.41325	0.89419
Crip2	Cysteine-rich protein 2	3.19277	0.48299
Arpc3	Actin-related protein 2/3 complex subunit 3	2.27447	0.66155
Eci2	Enoyl-CoA delta isomerase 2, mitochondrial	3.52419	1.10031

*Table A 10. Table showing proteins enriched by active probe **77** over DMSO vehicle control in DG-derived NSCs in TMT experiments. Biological replicates per condition, n = 3.*

Gene Name	Protein Name	-Log p Value	Difference (Active 77 – DMSO)
Eif5	Eukaryotic translation initiation factor 5	5.39135	1.40467
Kdelr2; Kdelr1; Kdelr3	ER lumen protein-retaining receptor 2; ER lumen protein-retaining receptor 1; ER lumen protein-retaining receptor 3	4.28226	3.81991
Pcyox1	Prenylcysteine oxidase	4.22443	1.97985
Scamp4	Secretory carrier-associated membrane protein 4	4.07152	1.39282
Nap1l1	Nucleosome assembly protein 1-like 1	4.06698	0.91179
Tomm22	Mitochondrial import receptor subunit TOM22 homolog	4.04345	2.06975
Mtnd5	NADH-ubiquinone oxidoreductase chain 5	3.93308	2.15460
Acox1	Peroxisomal acyl-coenzyme A oxidase 1	3.72068	0.92093
Zmpste24	CAAX prenyl protease 1 homolog	3.66410	2.34149
Npc1	Niemann-Pick C1 protein	3.62755	1.35888
Gstm1	Glutathione S-transferase Mu 1	3.57047	2.11860
Sar1b; Sar1a	GTP-binding protein SAR1b; GTP-binding protein SAR1a	3.50549	1.12611
Canx	Calnexin	3.41974	1.87727
Eif3e	Eukaryotic translation initiation factor 3 subunit E	3.39778	0.46092
Ap3m2	AP-3 complex subunit mu-2	3.33853	2.54681
Nampt	Nicotinamide phosphoribosyltransferase	3.32704	0.84277
Kcnj10	ATP-sensitive inward rectifier potassium channel 10	3.27841	0.84379
Pgrmc2	Membrane-associated progesterone receptor component 2	3.26201	1.62925

Atp5l	ATP synthase subunit g, mitochondrial	3.24573	0.69713
Aldh3a2	Fatty aldehyde dehydrogenase	3.24181	1.74553
Timm17b	Mitochondrial import inner membrane translocase subunit Tim17-B	3.23099	1.26684
Cox4i1	Cytochrome c oxidase subunit 4 isoform 1, mitochondrial	3.19554	1.75351
Dhfr	Dihydrofolate reductase	3.17250	1.29671
Cox6c	Cytochrome c oxidase subunit 6C	3.16995	1.86134
Psap	Prosaposin	3.16808	0.89784
Isoc1	Isochorismatase domain-containing protein 1	3.16677	1.18977
Hmox2	Heme oxygenase 2	3.16676	2.68141
Ociad1	OCIA domain-containing protein 1	3.16261	1.33557
Tmx1	Thioredoxin-related transmembrane protein 1	3.15903	1.32857
Rtn1	Reticulon-1	3.15739	1.39121
Rab1b	Ras-related protein Rab-1B	3.12881	0.79475
Slc25a4	ADP/ATP translocase 1	3.12592	1.30442
P4hb	Protein disulfide-isomerase	3.06921	1.09573
Rab1A	Ras-related protein Rab-1A	3.06007	0.78428
Bcap31	B-cell receptor-associated protein 31	3.05903	1.17777
Tram1	Translocating chain-associated membrane protein 1	3.05536	1.14912
Qil1	Protein QIL1	3.04567	1.57975
Atxn10	Ataxin-10	3.04105	0.20295
Coa3	Cytochrome c oxidase assembly factor 3 homolog, mitochondrial	3.02920	1.30123
Cd9	CD9 antigen	3.02754	1.74848
Pcyox1l	Prenylcysteine oxidase-like	3.02714	1.08232
Fdft1	Squalene synthase	3.02197	1.11541
Cyp51a1	Lanosterol 14-alpha demethylase	3.00031	1.76123
Ogt	UDP-N-acetylglucosamine--peptide N-acetylglucosaminyltransferase 110 kDa subunit	2.99852	0.41328
Acadm	Medium-chain specific acyl-CoA dehydrogenase, mitochondrial	2.99848	1.86584
Tmem35	Transmembrane protein 35	2.99645	1.40460
Slc25a5	ADP/ATP translocase 2; ADP/ATP translocase 2, N-terminally processed	2.98553	1.07814
Por	NADPH--cytochrome P450 reductase	2.98531	1.33795
Vdac1	Voltage-dependent anion-selective channel protein 1	2.98346	2.34476
Vdac2	Voltage-dependent anion-selective channel protein 2	2.97259	1.98855
Slc6a1	Sodium- and chloride-dependent GABA transporter 1	2.96945	1.73631
Tmco1	Transmembrane and coiled-coil domain-containing protein 1	2.96725	0.22288
Saysd1	SAYSvFN domain-containing protein 1	2.95905	1.11091
Creld1	Cysteine-rich with EGF-like domain protein 1	2.95122	1.00125
Ephx1	Epoxide hydrolase 1	2.94388	1.62201
Sec11a	Signal peptidase complex catalytic subunit SEC11A	2.93306	2.02296
Atp5j2	ATP synthase subunit f, mitochondrial	2.91340	1.23236

Zdhhc13	Palmitoyltransferase ZDHHC13	2.90776	3.36839
Npepps	Puromycin-sensitive aminopeptidase	2.90744	0.94541
Cers2	Ceramide synthase 2	2.90446	1.51715
Unc119b	Protein unc-119 homolog B	2.85797	1.72071
Timm17a	Mitochondrial import inner membrane translocase subunit Tim17-A	2.83841	1.40590
Ergic3	Endoplasmic reticulum-Golgi intermediate compartment protein 3	2.83361	2.86589
Lgals1	Galectin-1	2.82117	0.33942
Tm9sf3	Transmembrane 9 superfamily member 3	2.78754	1.96414
Sccpdh	Saccharopine dehydrogenase-like oxidoreductase	2.78744	1.61993
Apoo	Apolipoprotein O	2.76920	1.28490
Slc3a2	4F2 cell-surface antigen heavy chain	2.76529	0.38269
Atp5i	ATP synthase subunit e, mitochondrial	2.76250	1.18846
Gdi2	Rab GDP dissociation inhibitor beta	2.72868	0.58573
Tmem199	Transmembrane protein 199	2.72077	1.34088
Kdsr	3-ketodihydrosphingosine reductase	2.70045	1.87958
Emc7	ER membrane protein complex subunit 7	2.69775	1.17721
Tuba1b; Tuba4a	Tubulin alpha-1B chain; Tubulin alpha-4A chain	2.69648	0.97584
Ndufb3	NADH dehydrogenase [ubiquinone] 1 beta subcomplex subunit 3	2.69263	1.48921
Pgap1	GPI inositol-deacylase	2.69243	1.26867
Nudt5	ADP-sugar pyrophosphatase	2.69193	0.81090
Fabp5	Fatty acid-binding protein, epidermal	2.68805	0.53417
Maoa	Amine oxidase [flavin-containing] A	2.66992	0.84967
Prcp	Lysosomal Pro-X carboxypeptidase	2.66005	2.12575
Laptm4a	Lysosomal-associated transmembrane protein 4A	2.65681	2.51383
Cisd1	CDGSH iron-sulfur domain-containing protein 1	2.64077	1.16647
Tmem19	Transmembrane protein 19	2.63450	0.83970
Mtap	S-methyl-5-thioadenosine phosphorylase	2.63060	1.22221
Cyb5b	Cytochrome b5 type B	2.62915	0.88241
Nudt9	ADP-ribose pyrophosphatase, mitochondrial	2.62400	0.80933
Sgpl1	Sphingosine-1-phosphate lyase 1	2.62214	1.39295
Ctsd	Cathepsin D	2.61294	3.11354
Gpr107	Protein GPR107	2.60342	2.23998
Itgb1	Integrin beta-1	2.59636	1.04233
Rtn3	Reticulon-3	2.59622	1.30471
Atp2a2	Sarcoplasmic/endoplasmic reticulum calcium ATPase 2	2.58318	1.55364
Gria3	Glutamate receptor 3	2.58232	1.60993
Slc25a15	Mitochondrial ornithine transporter 1	2.58205	1.09770
Lnpep	Leucyl-cystinyl aminopeptidase	2.57270	1.05866
Hsd17b12	Very-long-chain 3-oxoacyl-CoA reductase	2.55103	1.71881
Slc25a20	Mitochondrial carnitine/acylcarnitine carrier protein	2.54246	1.19987

Tmx4	Thioredoxin-related transmembrane protein 4	2.52226	1.38542
Tram2	Translocating chain-associated membrane protein 2	2.52030	0.75419
Nptn	Neuroplastin	2.51908	1.20142
Fads2	Fatty acid desaturase 2	2.51161	0.57983
Plin2	Perilipin-2	2.50580	1.09661
Atp5b	ATP synthase subunit beta, mitochondrial	2.50479	0.76915
Vdac3	Voltage-dependent anion-selective channel protein 3	2.50380	1.48691
Snx6	Sorting nexin-6;Sorting nexin-6, N-terminally processed	2.50267	0.76551
Acadl	Long-chain specific acyl-CoA dehydrogenase, mitochondrial	2.50255	1.20985
Tmem87a	Transmembrane protein 87A	2.49815	2.03029
Rab31	Ras-related protein Rab-31	2.49505	0.18841
Cd81	CD81 antigen	2.49408	1.79097
Slc4a4	Electrogenic sodium bicarbonate cotransporter 1	2.49380	1.00766
Atp1a1	Sodium/potassium-transporting ATPase subunit alpha-1	2.49081	0.51042
Impad1	Inositol monophosphatase 3	2.48254	1.20122
Rbp1	Retinol-binding protein 1	2.47820	1.50212
Nucb1	Nucleobindin-1	2.47818	1.10453
Clptm1	Cleft lip and palate transmembrane protein 1 homolog	2.46630	0.39873
Rps15a	40S ribosomal protein S15a	2.46165	0.50107
Mtco2	Cytochrome c oxidase subunit 2	2.45700	1.11452
Ptges2	Prostaglandin E synthase 2; Prostaglandin E synthase 2 truncated form	2.44734	0.48607
Sh3glb1	Endophilin-B1	2.44550	0.30197
Tm9sf4	Transmembrane 9 superfamily member 4	2.43817	1.16454
Rab10	Ras-related protein Rab-10	2.43327	0.53760
Ssr4	Translocon-associated protein subunit delta	2.43073	0.69863
Rab39a	Ras-related protein Rab-39A	2.42667	1.04310
Rab14	Ras-related protein Rab-14	2.42265	1.02344
Cpt1a	Carnitine O-palmitoyltransferase 1, liver isoform	2.42258	0.72337
Pgrmc1	Membrane-associated progesterone receptor component 1	2.41533	1.86313
Slc25a11	Mitochondrial 2-oxoglutarate/malate carrier protein	2.41268	0.35840
Tspan3	Tetraspanin-3	2.39805	2.14106
Fabp7	Fatty acid-binding protein, brain	2.39779	0.70783
Rdh11	Retinol dehydrogenase 11	2.39071	1.12751
Tubb4b;Tubb4a	Tubulin beta-4B chain;Tubulin beta-4A chain	2.38263	0.22935
Phb2	Prohibitin-2	2.37816	0.72327
Gpm6b	Neuronal membrane glycoprotein M6-b	2.37754	1.22351
Asah1	Acid ceramidase; Acid ceramidase subunit alpha; Acid ceramidase subunit beta	2.37604	1.28331
Hacd3	Very-long-chain (3R)-3-hydroxyacyl-CoA dehydratase 3	2.36422	0.99878
Hadha	Trifunctional enzyme subunit alpha, mitochondrial; Long-chain enoyl-CoA hydratase; Long chain 3-hydroxyacyl-CoA dehydrogenase	2.35722	0.77572

Gm10320; Sec61b	Protein transport protein Sec61 subunit beta	2.35303	0.48322
Xpo1	Exportin-1	2.34256	0.50629
Tmem97	Transmembrane protein 97	2.34035	0.70413
Timm44	Mitochondrial import inner membrane translocase subunit TIM44	2.33677	0.85463
Timm23	Mitochondrial import inner membrane translocase subunit Tim23	2.32898	1.31069
Arf4	ADP-ribosylation factor 4	2.31338	0.41113
Nme1	Nucleoside diphosphate kinase A	2.30906	0.51415
Cers1	Ceramide synthase 1	2.30175	1.18921
Gpm6a	Neuronal membrane glycoprotein M6-a	2.28618	0.95111
Dnajc1	DnaJ homolog subfamily C member 1	2.28548	0.91530
Rer1	Protein RER1	2.27948	1.77641
Crip2	Cysteine-rich protein 2	2.27584	0.59878
Ralgapa1	Ral GTPase-activating protein subunit alpha-1	2.27548	2.44392
Sep-05	Septin-5	2.27307	0.24555
Tuba1a; Tuba1c; Tuba3a	Tubulin alpha-1A chain; Tubulin alpha-1C chain;Tubulin alpha-3 chain	2.27108	0.58053
Tomm70a	Mitochondrial import receptor subunit TOM70	2.26581	0.75219
Fam162a	Protein FAM162A	2.25610	0.85521
Ckap4	Cytoskeleton-associated protein 4	2.25408	1.06797
Nup93	Nuclear pore complex protein Nup93	2.25134	0.51577
Rpl9	60S ribosomal protein L9	2.24607	0.35891
Tmed3	Transmembrane emp24 domain-containing protein 3	2.23958	0.60990
Glt8d1	Glycosyltransferase 8 domain-containing protein 1	2.23669	1.09226
Mtch2	Mitochondrial carrier homolog 2	2.23560	1.10221
Tmed10	Transmembrane emp24 domain-containing protein 10	2.23261	1.04377
Kct2	Keratinocyte-associated transmembrane protein 2	2.23163	0.55545
Rab7a	Ras-related protein Rab-7a	2.21269	0.68595
Lpcat3	Lysophospholipid acyltransferase 5	2.21215	1.02675
Cisd2	CDGSH iron-sulfur domain-containing protein 2	2.20930	0.64989
Hccs	Cytochrome c-type heme lyase	2.20783	1.40696
Pmpca	Mitochondrial-processing peptidase subunit alpha	2.19586	0.92132
Lamb1	Laminin subunit beta-1	2.19341	1.03591
Tubb3	Tubulin beta-3 chain	2.18494	0.40216
Ssr1	Translocon-associated protein subunit alpha	2.17980	1.22006
Rtn4	Reticulon-4	2.17954	0.83925
Psma4	Proteasome subunit alpha type-4	2.17550	0.27115
Ykt6	Synaptobrevin homolog YKT6	2.16858	0.35200
Gba	Glucosylceramidase	2.15600	1.09731
Sec62	Translocation protein SEC62	2.14794	1.66754
Ppt1	Palmitoyl-protein thioesterase 1	2.14514	1.59733
Chst2	Carbohydrate sulfotransferase 2	2.14390	0.68949

Slc25a3	Phosphate carrier protein, mitochondrial	2.13886	0.89162
Golim4	Golgi integral membrane protein 4	2.11775	0.56629
Scpep1	Retinoid-inducible serine carboxypeptidase	2.11633	1.36055
Praf2	PRA1 family protein 2	2.11240	2.51064
Ckb	Creatine kinase B-type	2.09768	0.24844
Slc39a1	Zinc transporter ZIP1	2.09346	1.90805
Rpl11	60S ribosomal protein L11	2.08927	0.25336
Tecr	Very-long-chain enoyl-CoA reductase	2.08896	0.47078
Il1rap	Interleukin-1 receptor accessory protein	2.08367	1.12018
Ncam1	Neural cell adhesion molecule 1	2.07925	0.68144
Sdhb	Succinate dehydrogenase [ubiquinone] iron-sulfur subunit, mitochondrial	2.07520	0.88638
Opa3	Optic atrophy 3 protein homolog	2.06747	1.39486
Cops4	COP9 signalosome complex subunit 4	2.06481	0.16081
Uggt1	UDP-glucose:glycoprotein glucosyltransferase 1	2.05989	0.62119
Pon2	Serum paraoxonase/arylesterase 2	2.05509	1.44852
Txndc12	Thioredoxin domain-containing protein 12	2.05469	1.69296
Gnpda1	Glucosamine-6-phosphate isomerase 1	2.05390	0.25097
Pfn1	Profilin-1	2.04221	0.25689
Ndc1	Nucleoporin NDC1	2.03676	0.89262
Sec22b	Vesicle-trafficking protein SEC22b	1.99512	0.41831
Ccdc47	Coiled-coil domain-containing protein 47	1.99282	0.45918
Spcs2	Signal peptidase complex subunit 2	1.98423	1.18442
Ptgr2	Prostaglandin reductase 2	1.97683	0.84411
Scd3; Scd1; Scd2	Acyl-CoA desaturase 1; Acyl-CoA desaturase 2	1.97620	1.29345
Smim4	Small integral membrane protein 4	1.95749	0.58497
Aldh1a3	Aldehyde dehydrogenase family 1 member A3	1.95709	0.78530
Tmem33	Transmembrane protein 33	1.94858	1.04435
Apoe	Apolipoprotein E	1.94469	0.41080
Sppl2a	Signal peptide peptidase-like 2A	1.94215	1.12743
Saraf	Store-operated calcium entry-associated regulatory factor	1.93066	0.87089
Hmox1	Heme oxygenase 1	1.92490	0.86430
Mif	Macrophage migration inhibitory factor	1.91804	0.83755
Agpat5	1-acyl-sn-glycerol-3-phosphate acyltransferase epsilon	1.91407	0.58115
Slc35f1	Solute carrier family 35 member F1	1.90700	2.07372
Ociad2	OCIA domain-containing protein 2	1.90464	0.42294
Rab11a; Rab11b	Ras-related protein Rab-11A;Ras-related protein Rab-11B	1.90085	1.04034
Rps20	40S ribosomal protein S20	1.89860	0.32223
Echs1	Enoyl-CoA hydratase, mitochondrial	1.89740	0.74321
Prdx6; Prdx6b	Peroxiredoxin-6	1.87957	0.44189
Golm1	Golgi membrane protein 1	1.87205	1.40353

Atp6v0a1	V-type proton ATPase 116 kDa subunit a isoform 1	1.86997	0.55369
Rab6a;Rab6b	Ras-related protein Rab-6A;Ras-related protein Rab-6B	1.86670	0.45267
Apmap	Adipocyte plasma membrane-associated protein	1.85212	0.68038
Dhrs1	Dehydrogenase/reductase SDR family member 1	1.85027	0.92535
Phgdh	D-3-phosphoglycerate dehydrogenase	1.84016	0.19270
Ccnd1	G1/S-specific cyclin-D1	1.83543	0.42841
Mpv17l2	Mpv17-like protein 2	1.83184	0.41436
Stt3a	Dolichyl-diphosphooligosaccharide--protein glycosyltransferase subunit STT3A	1.82399	0.60189
Pycr2	Pyrroline-5-carboxylate reductase 2	1.82146	0.54582
Cops2	COP9 signalosome complex subunit 2	1.82075	0.21789
Fech	Ferrochelatase, mitochondrial	1.81739	0.87222
Sep2	Septin-2	1.81025	0.69004
Hsdl1	Inactive hydroxysteroid dehydrogenase-like protein 1	1.80339	0.29404
Akr1b1	Aldose reductase	1.80312	0.31523
Adh5	Alcohol dehydrogenase class-3	1.80068	0.61789
Slc25a25	Calcium-binding mitochondrial carrier protein SCaMC-2	1.78522	0.44900
Acad9	Acyl-CoA dehydrogenase family member 9, mitochondrial	1.77875	0.71941
Rps2	40S ribosomal protein S2	1.77516	0.40506
Gnb2l1	Guanine nucleotide-binding protein subunit beta-2-like 1; Guanine nucleotide-binding protein subunit beta-2-like 1, N-terminally processed	1.76746	0.20666
Acsl3	Long-chain-fatty-acid--CoA ligase 3	1.76690	0.64142
Rps27a; Gm8797; Uba52; Ubb; Ubc	Ubiquitin-40S ribosomal protein S27a; Ubiquitin; 40S ribosomal protein S27a; Ubiquitin-60S ribosomal protein L40; Ubiquitin; 60S ribosomal protein L40; Polyubiquitin-B;Ubiquitin;Polyubiquitin-C;Ubiquitin; Ubiquitin-related 1; Ubiquitin-related 2	1.76643	0.42436
Tmx3	Protein disulfide-isomerase TMX3	1.76612	0.93424
Mtnd2	NADH-ubiquinone oxidoreductase chain 2	1.76604	1.65202
Sfxn1	Sideroflexin-1	1.76377	0.25501
Cpt2	Carnitine O-palmitoyltransferase 2, mitochondrial	1.75796	0.76332
Rpsa	40S ribosomal protein SA	1.73844	0.27885
Mvd	Diphosphomevalonate decarboxylase	1.73562	0.48707
Hsp90aa1	Heat shock protein HSP 90-alpha	1.73109	0.21266
Gnaq; Gna14; Gna11	Guanine nucleotide-binding protein G(q) subunit alpha; Guanine nucleotide-binding protein subunit alpha-14; Guanine nucleotide-binding protein subunit alpha-11	1.72594	0.78848
Glrx3	Glutaredoxin-3	1.72186	0.91873
Mar2	Mitochondrial amidoxime reducing component 2	1.71755	0.56070
Glg1	Golgi apparatus protein 1	1.70081	0.28347
Tmx2	Thioredoxin-related transmembrane protein 2	1.69948	0.93322
Cct8	T-complex protein 1 subunit theta	1.69810	0.23120
Tspan6	Tetraspanin-6	1.68814	2.11187
Hars	Histidine--tRNA ligase, cytoplasmic	1.68528	0.87044

Cdk4	Cyclin-dependent kinase 4	1.67301	0.47676
Itgb6	Integrin beta-6	1.67122	0.78892
Pes1	Pescadillo homolog	1.66890	0.38805
Tubb5	Tubulin beta-5 chain	1.66701	0.51258
Rac1; Rac2; Rac3	Ras-related C3 botulinum toxin substrate 1; Ras-related C3 botulinum toxin substrate 2; Ras-related C3 botulinum toxin substrate 3	1.66530	0.43508
Snx3	Sorting nexin-3	1.64740	0.42464
Ldha	L-lactate dehydrogenase A chain	1.64626	0.28729
Lman1	Protein ERGIC-53	1.63863	0.54803
Reep5	Receptor expression-enhancing protein 5	1.63528	1.16278
Tomm40	Mitochondrial import receptor subunit TOM40 homolog	1.62992	0.48926
Cers5	Ceramide synthase 5	1.62202	1.54926
Psmb5	Proteasome subunit beta type-5	1.61828	0.37800
Pitpnb	Phosphatidylinositol transfer protein beta isoform	1.61540	1.05420
Sv2a	Synaptic vesicle glycoprotein 2A	1.60817	0.68437
Ube2d2b; Ube2d2; Ube2d3	Ubiquitin-conjugating enzyme E2 D2B; Ubiquitin-conjugating enzyme E2 D2;Ubiquitin-conjugating enzyme E2 D3	1.60804	0.74657
Timmdc1	Complex I assembly factor TIMMDC1, mitochondrial	1.60680	0.75340
Bax	Apoptosis regulator BAX	1.60437	0.31041
Psmc6	26S protease regulatory subunit 10B	1.60400	0.63107
Atp6v1a	V-type proton ATPase catalytic subunit A	1.60106	0.44880
Tmem205	Transmembrane protein 205	1.59764	0.70302
Eif5a; Eif5a2	Eukaryotic translation initiation factor 5A-1; Eukaryotic translation initiation factor 5A-2	1.59059	0.32619
Set	Protein SET	1.58937	1.12284
Cyp20a1	Cytochrome P450 20A1	1.58811	0.54935
Abcd3	ATP-binding cassette sub-family D member 3	1.58563	0.62616
Srp68	Signal recognition particle subunit SRP68	1.58208	0.17705
Actr3	Actin-related protein 3	1.57557	0.50533
Dhcr7	7-dehydrocholesterol reductase	1.57520	0.95436
Tm7sf2	Delta(14)-sterol reductase	1.55862	1.18346
Bri3bp	BRI3-binding protein	1.55336	1.17756
Rnf13	E3 ubiquitin-protein ligase RNF13	1.54212	0.74367
Prdx4	Peroxiredoxin-4	1.54027	0.26641
Ankle2	Ankyrin repeat and LEM domain-containing protein 2	1.53537	1.06028
Fam3c	Protein FAM3C	1.53498	0.74200
Eif4a1; Eif4a2	Eukaryotic initiation factor 4A-I;Eukaryotic initiation factor 4A-II; Eukaryotic initiation factor 4A-II, N-terminally processed	1.53272	0.26375
Gpx8	Probable glutathione peroxidase 8	1.53065	0.38857
Tsn	Translin	1.52827	0.52479
Mboat7	Lysophospholipid acyltransferase 7	1.52717	0.92081

Scarb1	Scavenger receptor class B member 1	1.52649	1.32554
Immt	MICOS complex subunit Mic60	1.52621	0.19700
Gm2a	Ganglioside GM2 activator	1.52275	3.00465
Atg3	Ubiquitin-like-conjugating enzyme ATG3	1.49998	0.69602
Hadhb	Trifunctional enzyme subunit beta, mitochondrial; 3-ketoacyl-CoA thiolase	1.48959	0.50875
Galnt16	Polypeptide N-acetylgalactosaminyltransferase 16	1.46103	1.03468
Samm50	Sorting and assembly machinery component 50 homolog	1.44822	0.43464
Fh	Fumarate hydratase, mitochondrial	1.44312	0.31938
Atp1b1	Sodium/potassium-transporting ATPase subunit beta-1	1.44225	0.31187
Gja1	Gap junction alpha-1 protein	1.44207	0.78413
Emd	Emerin	1.43605	0.73513
Rps12	40S ribosomal protein S12	1.42456	0.30928
Slc6a11	Sodium- and chloride-dependent GABA transporter 3	1.41614	0.82218
Uqcrq	Cytochrome b-c1 complex subunit 8	1.40269	0.39117
Ap2a2; Ap2a1	AP-2 complex subunit alpha-2; AP-2 complex subunit alpha-1	1.38855	0.39274
Tdrkh	Tudor and KH domain-containing protein	1.37360	0.70495
Atp2b1; Atp2b4; Atp2b3; Atp2b2	Plasma membrane calcium-transporting ATPase 1; Calcium-transporting ATPase; Plasma membrane calcium-transporting ATPase 2	1.36457	0.36049
Lrrc59	Leucine-rich repeat-containing protein 59	1.36455	0.23524
Naa50	N-alpha-acetyltransferase 50	1.35878	0.18879
Ezr	Ezrin	1.35120	0.37704
Rars	Arginine--tRNA ligase, cytoplasmic	1.34098	0.26538
Pgpep1	Pyroglutamyl-peptidase 1	1.33836	0.25348
Lama1	Laminin subunit alpha-1	1.32476	1.33363
Ran	GTP-binding nuclear protein Ran	1.32380	0.28380
Tmed2	Transmembrane emp24 domain-containing protein 2	1.32044	0.98870
Acp6	Lysophosphatidic acid phosphatase type 6	1.31152	0.92756
Atp5f1	ATP synthase F(0) complex subunit B1, mitochondrial	1.30482	0.77542
Idh3a	Isocitrate dehydrogenase [NAD] subunit alpha, mitochondrial	1.30071	0.33933
Eef1a1	Elongation factor 1-alpha 1	1.29384	0.26718
Atp5g1; Atp5g2	ATP synthase F(0) complex subunit C1, mitochondrial; ATP synthase F(0) complex subunit C3, mitochondrial; ATP synthase F(0) complex subunit C2, mitochondrial	1.28926	0.30969
Vav3	Guanine nucleotide exchange factor VAV3	1.28908	0.31338
Kpnb1	Importin subunit beta-1	1.28887	0.37964
Ppp2r4	Serine/threonine-protein phosphatase 2A activator	1.28381	0.40578
Faf2	FAS-associated factor 2	1.27982	0.71565
Zadh2	Zinc-binding alcohol dehydrogenase domain-containing protein 2	1.27932	0.70613
Prdx2	Peroxiredoxin-2	1.27394	0.29553
Gpi	Glucose-6-phosphate isomerase	1.27261	0.24393

Sppl2b	Signal peptide peptidase-like 2B	1.27000	0.67576
Psat1	Phosphoserine aminotransferase	1.26493	0.19836
Ldhb	L-lactate dehydrogenase B chain	1.26414	0.36380
Wls	Protein wntless homolog	1.26320	0.62610
Etfa	Electron transfer flavoprotein subunit alpha, mitochondrial	1.25621	0.26595
Mapk1	Mitogen-activated protein kinase 1	1.24862	0.25492
Atp5a1	ATP synthase subunit alpha, mitochondrial	1.24621	0.31876
Atad3	ATPase family AAA domain-containing protein 3	1.24571	0.28456
Cdc42	Cell division control protein 42 homolog	1.24017	0.37643
Cct3	T-complex protein 1 subunit gamma	1.22259	0.22128
Vapb	Vesicle-associated membrane protein-associated protein B	1.21759	0.49252
Scamp3	Secretory carrier-associated membrane protein 3	1.21651	0.81805
Drg2	Developmentally-regulated GTP-binding protein 2	1.21505	0.56507
Tmem109	Transmembrane protein 109	1.21437	0.35655
Mdh2	Malate dehydrogenase, mitochondrial	1.20801	0.24369
Tmem245	Transmembrane protein 245	1.20679	0.58982
Dhrs13	Dehydrogenase/reductase SDR family member 13	1.20309	0.52882
Tkt	Transketolase	1.20105	0.19887
Surf4	Surfeit locus protein 4	1.20025	0.33878
Prdx1	Peroxiredoxin-1	1.19011	0.28794
Mmgt1	Membrane magnesium transporter 1	1.18958	0.96282
Camk2b	Calcium/calmodulin-dependent protein kinase type II subunit beta	1.18096	0.65567
Arl6ip6	ADP-ribosylation factor-like protein 6-interacting protein 6	1.16665	0.43898
Vim	Vimentin	1.16552	0.51428
Asrgl1	Isoaspartyl peptidase/L-asparaginase;Isoaspartyl peptidase/L-asparaginase alpha chain;Isoaspartyl peptidase/L-asparaginase beta chain	1.16522	0.43232
Arpc1b	Actin-related protein 2/3 complex subunit 1B	1.15463	0.59518
Pcna	Proliferating cell nuclear antigen	1.13400	0.21214
Ivd	Isovaleryl-CoA dehydrogenase, mitochondrial	1.12359	0.40623
Nutf2	Nuclear transport factor 2	1.12265	0.46737
Tceb1	Transcription elongation factor B polypeptide 1	1.11921	0.25375
Slc18b1	MFS-type transporter SLC18B1	1.11524	1.16131
Prepl	Prolyl endopeptidase-like	1.11278	0.50828
Actg2; Acta1; Actc1; Acta2	Actin, gamma-enteric smooth muscle;Actin, alpha skeletal muscle;Actin, alpha cardiac muscle 1;Actin, aortic smooth muscle	1.10825	0.43687
Rrm1	Ribonucleoside-diphosphate reductase large subunit	1.09520	0.50203
Acaa1a; Acaa1b	3-ketoacyl-CoA thiolase A, peroxisomal;3-ketoacyl-CoA thiolase B, peroxisomal	1.09419	0.24011
Hmgcr	3-hydroxy-3-methylglutaryl-coenzyme A reductase	1.09397	0.57585
Esd	S-formylglutathione hydrolase	1.08910	0.41294
Ahcy	Adenosylhomocysteinase	1.08881	0.42552

Klc1	Kinesin light chain 1	1.08626	0.37499
Lamp2	Lysosome-associated membrane glycoprotein 2	1.08126	0.25350
Letmd1	LETM1 domain-containing protein 1	1.07450	0.38346
Fkbp5	Peptidyl-prolyl cis-trans isomerase FKBP5;Peptidyl-prolyl cis-trans isomerase FKBP5, N-terminally processed	1.07240	0.27044
Pgls	6-phosphogluconolactonase	1.05840	0.24461
Sf3b1	Splicing factor 3B subunit 1	1.05503	0.38573
Tubb2b	Tubulin beta-2B chain	1.04449	0.23553
Atp1a2	Sodium/potassium-transporting ATPase subunit alpha-2	1.03692	0.30112
Ctsc	Dipeptidyl peptidase 1; Dipeptidyl peptidase 1 exclusion domain chain; Dipeptidyl peptidase 1 heavy chain; Dipeptidyl peptidase 1 light chain	1.03592	0.33406
Rpn1	Dolichyl-diphosphooligosaccharide--protein glycosyltransferase subunit 1	1.03432	0.27700
Ano8	Anoctamin-8	1.03112	0.42466
Cct2	T-complex protein 1 subunit beta	1.02306	0.31744
Fkbp4	Peptidyl-prolyl cis-trans isomerase FKBP4;Peptidyl-prolyl cis-trans isomerase FKBP4, N-terminally processed	1.01312	0.34698
Dcakd	Dephospho-CoA kinase domain-containing protein	1.00332	0.33025
Aldoa; Aldoart1	Fructose-bisphosphate aldolase A;Fructose-bisphosphate aldolase	1.00253	0.29695
Vps45	Vacuolar protein sorting-associated protein 45	1.00024	0.39607
Cyc1	Cytochrome c1, heme protein, mitochondrial	0.99978	0.26835
Fth1	Ferritin heavy chain;Ferritin heavy chain, N-terminally processed	0.98674	0.32952
Snrpc	U1 small nuclear ribonucleoprotein C	0.97981	0.43650
Iars2	Isoleucine--tRNA ligase, mitochondrial	0.96527	0.56166
Aldh1a1	Retinal dehydrogenase 1	0.96132	0.57748
Cdk5	Cyclin-dependent-like kinase 5	0.95289	0.52518
Asns	Asparagine synthetase [glutamine-hydrolyzing]	0.95114	0.33152
Pkd2	Polycystin-2	0.94862	0.63100
Elovl1	Elongation of very long chain fatty acids protein 1	0.94640	0.31703
Eif3h	Eukaryotic translation initiation factor 3 subunit H	0.92463	0.32131
Capza2; Capza1	F-actin-capping protein subunit alpha-2;F-actin-capping protein subunit alpha-1	0.92247	0.29834
Akr1e2	1,5-anhydro-D-fructose reductase	0.92109	0.30371
Tpp1	Tripeptidyl-peptidase 1	0.90248	0.28395
Kras; Hras	GTPase KRas; GTPase KRas, N-terminally processed; GTPase HRas; GTPase HRas, N-terminally processed	0.89696	0.32997
Thop1	Thimet oligopeptidase	0.86190	0.33371
Hmgcl	Hydroxymethylglutaryl-CoA lyase, mitochondrial	0.85565	0.49794
Crot	Peroxisomal carnitine O-octanoyltransferase	0.85140	0.37085
Idh3g	Isocitrate dehydrogenase [NAD] subunit gamma 1, mitochondrial	0.84568	0.33708
Mgea5	Protein O-GlcNAcase	0.84265	0.50532
Col4a3bp	Collagen type IV alpha-3-binding protein	0.84062	0.60460
Prdx3	Thioredoxin-dependent peroxide reductase, mitochondrial	0.83340	0.30532

Coq9	Ubiquinone biosynthesis protein COQ9, mitochondrial	0.81034	0.36644
Slc33a1	Acetyl-coenzyme A transporter 1	0.79168	0.43642
Vkorc1l1	Vitamin K epoxide reductase complex subunit 1-like protein 1	0.78007	1.17747
Lbr	Lamin-B receptor	0.71870	0.46529

*Table A 11. Table showing proteins enriched by active probe **77** over inactive probe **78** in DG-derived NSCs in TMT experiments. Biological replicates per condition, n = 3.*

Gene Name	Protein Name	-Log p Value	Difference (Active 77 – Inactive 78)
Tomm22	Mitochondrial import receptor subunit TOM22 homolog	6.22021	1.47348
Kdelr2; Kdelr1; Kdelr3	ER lumen protein-retaining receptor 2; ER lumen protein-retaining receptor 1; ER lumen protein-retaining receptor 3	4.42793	3.11189
Mtnd5	NADH-ubiquinone oxidoreductase chain 5	4.37578	1.69665
Canx	Calnexin	4.27840	1.39923
Saysd1	SAYSvFN domain-containing protein 1	4.06739	1.23963
Rtn1	Reticulon-1	3.93833	1.23760
Rab1A	Ras-related protein Rab-1A	3.79120	0.70171
Cox6c	Cytochrome c oxidase subunit 6C	3.74819	1.64665
Pcyox1l	Prenylcysteine oxidase-like	3.71070	0.74715
Vat1	Synaptic vesicle membrane protein VAT-1 homolog	3.68629	0.68096
Atp5j2	ATP synthase subunit f, mitochondrial	3.68541	1.11151
Pgrmc2	Membrane-associated progesterone receptor component 2	3.61078	1.28932
Gstm1	Glutathione S-transferase Mu 1	3.58187	1.06716
	UPF0729 protein C18orf32 homolog	3.56419	1.78762
Qil1	Protein QIL1	3.49816	1.16642
Hsdl1	Inactive hydroxysteroid dehydrogenase-like protein 1	3.49102	0.54675
Slc25a11	Mitochondrial 2-oxoglutarate/malate carrier protein	3.48423	0.53282
Rbp1	Retinol-binding protein 1	3.45975	1.32128
P4hb	Protein disulfide-isomerase	3.45480	0.94706
Eif5	Eukaryotic translation initiation factor 5	3.43589	0.72891
Cox4i1	Cytochrome c oxidase subunit 4 isoform 1, mitochondrial	3.43516	1.14520
Tmx4	Thioredoxin-related transmembrane protein 4	3.43126	0.94067
Pgrmc1	Membrane-associated progesterone receptor component 1	3.41638	1.06470
Por	NADPH--cytochrome P450 reductase	3.39547	0.95877
Pcyox1	Prenylcysteine oxidase	3.37770	1.00960
Ociad1	OCIA domain-containing protein 1	3.30875	1.05910
Bfar	Bifunctional apoptosis regulator	3.17429	0.54542
Sec11a	Signal peptidase complex catalytic subunit SEC11A	3.16275	1.23075
Cyp51a1	Lanosterol 14-alpha demethylase	3.15940	1.17811
Ralgapa1	Ral GTPase-activating protein subunit alpha-1	3.15187	1.98292

Slc25a4	ADP/ATP translocase 1	3.11459	1.00068
Impad1	Inositol monophosphatase 3	3.02556	0.86168
Tram1	Translocating chain-associated membrane protein 1	2.96822	0.62535
Timm17b	Mitochondrial import inner membrane translocase subunit Tim17-B	2.95461	0.89446
Mtco2	Cytochrome c oxidase subunit 2	2.91093	0.98238
Rtn3	Reticulon-3	2.87703	0.99379
Praf2	PRA1 family protein 2	2.85433	0.75524
Rab7a	Ras-related protein Rab-7a	2.85356	0.75645
Sh3glb1	Endophilin-B1	2.82920	0.33176
Lnpep	Leucyl-cystinyl aminopeptidase	2.81572	0.45923
Rab1b	Ras-related protein Rab-1B	2.77806	0.73045
Hmox2	Heme oxygenase 2	2.77161	1.14120
Tmx1	Thioredoxin-related transmembrane protein 1	2.76367	0.79646
Ergic3	Endoplasmic reticulum-Golgi intermediate compartment protein 3	2.74955	1.43363
Slc25a5	ADP/ATP translocase 2; ADP/ATP translocase 2, N-terminally processed	2.72889	0.74267
Sec62	Translocation protein SEC62	2.72480	1.07236
Cisd1	CDGSH iron-sulfur domain-containing protein 1	2.72394	0.87898
Itgb1	Integrin beta-1	2.69992	0.65171
Fabp7	Fatty acid-binding protein, brain	2.68250	0.65390
Tmem199	Transmembrane protein 199	2.67105	0.78241
Ckap4	Cytoskeleton-associated protein 4	2.66498	0.80646
Timm17a	Mitochondrial import inner membrane translocase subunit Tim17-A	2.65720	0.68939
Sqle	Squalene monooxygenase	2.65371	0.63183
Mtx2	Metaxin-2	2.65051	1.06961
Gpm6b	Neuronal membrane glycoprotein M6-b	2.63617	0.86023
Hsd17b12	Very-long-chain 3-oxoacyl-CoA reductase	2.62262	1.21687
Maoa	Amine oxidase [flavin-containing] A	2.61383	0.49628
Creld1	Cysteine-rich with EGF-like domain protein 1	2.60444	0.62707
Atp2a2	Sarcoplasmic/endoplasmic reticulum calcium ATPase 2	2.58088	0.96420
Fam162a	Protein FAM162A	2.56664	0.75853
Apoo	Apolipoprotein O	2.55821	1.40538
Dhrs13	Dehydrogenase/reductase SDR family member 13	2.55391	0.64498
Ccdc47	Coiled-coil domain-containing protein 47	2.52818	0.29354
Vdac2	Voltage-dependent anion-selective channel protein 2	2.52420	0.98948
Sgpl1	Sphingosine-1-phosphate lyase 1	2.51698	0.87076
Atp5i	ATP synthase subunit e, mitochondrial	2.50457	0.96734
Asah1	Acid ceramidase; Acid ceramidase subunit alpha; Acid ceramidase subunit beta	2.48877	0.90964
Gm10320; Sec61b	Protein transport protein Sec61 subunit beta	2.48838	0.44835
Scamp4	Secretory carrier-associated membrane protein 4	2.47906	0.72640

Unc119b	Protein unc-119 homolog B	2.47865	1.02829
Glt8d1	Glycosyltransferase 8 domain-containing protein 1	2.47578	1.01625
	UPF0554 protein C2orf43 homolog	2.45955	0.67919
Itgb6	Integrin beta-6	2.43702	0.94902
Tm9sf3	Transmembrane 9 superfamily member 3	2.43265	1.06981
Hmox1	Heme oxygenase 1	2.43176	0.48100
Uqcrq	Cytochrome b-c1 complex subunit 8	2.42473	0.59818
Emd	Emerin	2.40413	0.85076
Cd9	CD9 antigen	2.35075	1.00403
Chst2	Carbohydrate sulfotransferase 2	2.34576	0.56999
Atp5l	ATP synthase subunit g, mitochondrial	2.31824	0.80665
Nucb1	Nucleobindin-1	2.31608	0.75938
Tm9sf4	Transmembrane 9 superfamily member 4	2.29454	0.90804
Emc7	ER membrane protein complex subunit 7	2.29130	0.74386
Spcs2	Signal peptidase complex subunit 2	2.28469	1.08186
Lgals1	Galectin-1	2.26594	0.37926
Rer1	Protein RER1	2.26305	1.04849
Vdac3	Voltage-dependent anion-selective channel protein 3	2.25956	1.12706
Gpm6a	Neuronal membrane glycoprotein M6-a	2.24592	0.86704
Nme1	Nucleoside diphosphate kinase A	2.24469	0.57653
Atp5b	ATP synthase subunit beta, mitochondrial	2.23439	0.52308
Ssr1	Translocon-associated protein subunit alpha	2.23240	1.26622
Acox1	Peroxisomal acyl-coenzyme A oxidase 1	2.21223	0.73836
Pgap1	GPI inositol-deacylase	2.19721	1.36194
Tmem87a	Transmembrane protein 87A	2.19112	0.86431
Sar1b; Sar1a	GTP-binding protein SAR1b; GTP-binding protein SAR1a	2.17953	1.48043
Hccs	Cytochrome c-type heme lyase	2.16896	0.76322
Reep5	Receptor expression-enhancing protein 5	2.14484	1.04841
Bcap31	B-cell receptor-associated protein 31	2.14219	0.69913
Dnajc1	DnaJ homolog subfamily C member 1	2.13983	0.42302
Nap1l1	Nucleosome assembly protein 1-like 1	2.11855	0.90683
Zmpste24	CAAX prenyl protease 1 homolog	2.11430	1.51723
Atp6v0a1	V-type proton ATPase 116 kDa subunit a isoform 1	2.10552	0.28163
Slc25a15	Mitochondrial ornithine transporter 1	2.09023	0.96300
Tecr	Very-long-chain enoyl-CoA reductase	2.07020	0.41128
Slc25a20	Mitochondrial carnitine/acylcarnitine carrier protein	2.05703	0.62675
Rdh11	Retinol dehydrogenase 11	2.05453	0.75902
Rab11a; Rab11b	Ras-related protein Rab-11A; Ras-related protein Rab-11B	2.04721	0.75571
Rtn4	Reticulon-4	2.04274	0.54904
Hadha	Trifunctional enzyme subunit alpha, mitochondrial; Long-chain enoyl-CoA hydratase; Long chain 3-hydroxyacyl-CoA dehydrogenase	2.03885	0.56555

Gria3	Glutamate receptor 3	2.02890	0.88368
Pon2	Serum paraoxonase/arylesterase 2	2.02597	0.88042
Gm2a	Ganglioside GM2 activator	2.01645	1.14861
Uggt1	UDP-glucose:glycoprotein glucosyltransferase 1	2.01075	0.91908
Ndc1	Nucleoporin NDC1	2.00956	0.66226
Slc25a3	Phosphate carrier protein, mitochondrial	2.00006	0.63030
Abcd3	ATP-binding cassette sub-family D member 3	2.00001	0.58508
Npepps	Puromycin-sensitive aminopeptidase	1.99996	0.51857
Lpcat3	Lysophospholipid acyltransferase 5	1.99743	0.37137
Nptn	Neuroplastin	1.99183	0.80850
Agpat5	1-acyl-sn-glycerol-3-phosphate acyltransferase epsilon	1.98924	0.69271
Mtap	S-methyl-5-thioadenosine phosphorylase	1.97524	0.66514
Ctsd	Cathepsin D	1.97061	1.56064
Gba	Glucosylceramidase	1.96764	0.97502
Ccnd1	G1/S-specific cyclin-D1	1.95335	0.47596
Lamb1	Laminin subunit beta-1	1.95164	0.56445
Ndufb3	NADH dehydrogenase [ubiquinone] 1 beta subcomplex subunit 3	1.94539	0.95111
Timm23	Mitochondrial import inner membrane translocase subunit Tim23	1.94445	0.83879
Galnt16	Polypeptide N-acetylgalactosaminyltransferase 16	1.92479	1.09340
Bri3bp	BRI3-binding protein	1.91095	0.94946
Kdsr	3-ketodihydrosphingosine reductase	1.89242	0.88201
Actg2; Acta1; Actc1; Acta2	Actin, gamma-enteric smooth muscle; Actin, alpha skeletal muscle; Actin, alpha cardiac muscle 1;Actin, aortic smooth muscle	1.89138	1.27032
Ap3m2	AP-3 complex subunit mu-2	1.88146	0.93549
Tspan3	Tetraspanin-3	1.88123	0.77525
Ephx1	Epoxide hydrolase 1	1.88100	0.39668
Tubb3	Tubulin beta-3 chain	1.86332	0.77444
Slc25a25	Calcium-binding mitochondrial carrier protein SCaMC-2	1.86109	0.33972
Tram2	Translocating chain-associated membrane protein 2	1.84910	0.72250
Isoc1	Isochorismatase domain-containing protein 1	1.83880	0.59647
Sppl2a	Signal peptide peptidase-like 2A	1.83477	0.97960
Tmed10	Transmembrane emp24 domain-containing protein 10	1.81855	0.84607
Mtdh	Protein LYRIC	1.81556	0.41734
Cd81	CD81 antigen	1.81538	1.26877
Eif3e	Eukaryotic translation initiation factor 3 subunit E	1.80465	0.64419
Mar2	Mitochondrial amidoxime reducing component 2	1.79174	0.72576
Zdhhc13	Palmitoyltransferase ZDHHC13	1.78855	1.32541
Scpep1	Retinoid-inducible serine carboxypeptidase	1.77181	1.51492
Ncam1	Neural cell adhesion molecule 1	1.77142	0.67934
Cisd2	CDGSH iron-sulfur domain-containing protein 2	1.74934	1.05711

Tuba1b; Tuba4a	Tubulin alpha-1B chain; Tubulin alpha-4A chain	1.73653	0.71782
Soat1	Sterol O-acyltransferase 1	1.72948	0.52758
Slc39a1	Zinc transporter ZIP1	1.70060	1.10104
Rab10	Ras-related protein Rab-10	1.69392	0.42506
Lama1	Laminin subunit alpha-1	1.69152	1.34558
Atp5c1	ATP synthase subunit gamma, mitochondrial	1.68364	0.46526
Rbm14	RNA-binding protein 14	1.66999	0.52200
Tomm40	Mitochondrial import receptor subunit TOM40 homolog	1.66422	0.41586
Tomm70a	Mitochondrial import receptor subunit TOM70	1.66161	0.65841
Hars	Histidine--tRNA ligase, cytoplasmic	1.65905	0.69181
Gpx8	Probable glutathione peroxidase 8	1.65638	0.63061
Rps12	40S ribosomal protein S12	1.62744	0.57308
Ran	GTP-binding nuclear protein Ran	1.61947	0.38109
Tmx2	Thioredoxin-related transmembrane protein 2	1.61922	0.76730
Set	Protein SET	1.60879	0.93060
Tmem19	Transmembrane protein 19	1.60648	1.19320
Sccpdh	Saccharopine dehydrogenase-like oxidoreductase	1.59407	0.47971
Cpt1a	Carnitine O-palmitoyltransferase 1, liver isoform	1.59071	0.60543
Rps15a	40S ribosomal protein S15a	1.58524	0.69548
Mtnd2	NADH-ubiquinone oxidoreductase chain 2	1.57572	1.09110
Ykt6	Synaptobrevin homolog YKT6	1.57167	0.59920
Snrpc	U1 small nuclear ribonucleoprotein C	1.56919	0.82865
Rab6a; Rab6b	Ras-related protein Rab-6A;Ras-related protein Rab-6B	1.56346	0.46108
Vdac1	Voltage-dependent anion-selective channel protein 1	1.56315	0.52341
Slc25a18; Slc25a22	Mitochondrial glutamate carrier 2; Mitochondrial glutamate carrier 1	1.55710	0.43696
Aldh3a2	Fatty aldehyde dehydrogenase	1.55410	1.87678
Cers2	Ceramide synthase 2	1.54965	0.59919
Pmpca	Mitochondrial-processing peptidase subunit alpha	1.54936	0.46926
Nudt5	ADP-sugar pyrophosphatase	1.53722	0.76808
Tuba1a; Tuba1c; Tuba3a	Tubulin alpha-1A chain; Tubulin alpha-1C chain;Tubulin alpha-3 chain	1.53710	0.44396
Adh5	Alcohol dehydrogenase class-3	1.52025	0.59770
Slc4a4	Electrogenic sodium bicarbonate cotransporter 1	1.51570	0.72889
Acp6	Lysophosphatidic acid phosphatase type 6	1.51521	0.64532
Prdx2	Peroxiredoxin-2	1.51437	0.55241
Txndc12	Thioredoxin domain-containing protein 12	1.50233	0.58900
Laptm4a	Lysosomal-associated transmembrane protein 4A	1.49431	1.40378
Psmb5	Proteasome subunit beta type-5	1.48280	0.51402
Tmem205	Transmembrane protein 205	1.47065	0.48742
Npc1	Niemann-Pick C1 protein	1.45992	0.63313
Slc6a1	Sodium- and chloride-dependent GABA transporter 1	1.42344	0.67345

Mif	Macrophage migration inhibitory factor	1.41173	1.46306
Cers5	Ceramide synthase 5	1.40108	0.53997
Rab39a	Ras-related protein Rab-39A	1.39196	0.88807
Coa3	Cytochrome c oxidase assembly factor 3 homolog, mitochondrial	1.38094	1.07029
Asrgl1	Isoaspartyl peptidase/L-asparaginase; Isoaspartyl peptidase/L-asparaginase alpha chain; Isoaspartyl peptidase/L-asparaginase beta chain	1.37370	0.71583
Dhrs1	Dehydrogenase/reductase SDR family member 1	1.36683	0.48741
Mtch2	Mitochondrial carrier homolog 2	1.36643	0.53243
Rab14	Ras-related protein Rab-14	1.36146	0.46844
Slc25a12	Calcium-binding mitochondrial carrier protein Aralar1	1.36066	0.47624
Cyb5b	Cytochrome b5 type B	1.35879	0.58894
Nudt9	ADP-ribose pyrophosphatase, mitochondrial	1.34980	0.48872
Rpl23	60S ribosomal protein L23	1.34491	0.50666
Il1rap	Interleukin-1 receptor accessory protein	1.32530	0.51701
Tspan31	Tetraspanin-31	1.32332	0.48979
Lamp2	Lysosome-associated membrane glycoprotein 2	1.31327	0.71907
Fh	Fumarate hydratase, mitochondrial	1.30438	0.54044
Srprb	Signal recognition particle receptor subunit beta	1.30005	0.55743
Tmem33	Transmembrane protein 33	1.29247	0.73025
Arf4	ADP-ribosylation factor 4	1.27955	0.58874
Gnaq; Gna14; Gna11	Guanine nucleotide-binding protein G(q) subunit alpha; Guanine nucleotide-binding protein subunit alpha-14; Guanine nucleotide-binding protein subunit alpha-11	1.27376	0.56143
Phb2	Prohibitin-2	1.27373	0.56692
Slc35f1	Solute carrier family 35 member F1	1.26647	1.06632
Apmap	Adipocyte plasma membrane-associated protein	1.25929	0.86167
Tmed3	Transmembrane emp24 domain-containing protein 3	1.22673	0.81438
Txn	Thioredoxin	1.22588	0.57729
Nup93	Nuclear pore complex protein Nup93	1.18747	0.63111
Tspan6	Tetraspanin-6	1.17696	0.88066
Plin2	Perilipin-2	1.17016	0.65163

*Table A 12. Table showing proteins enriched by active probe **77** over competition control **15** in DG-derived NSCs in TMT experiments. Biological replicates per condition, n = 3.*

Gene Name	Protein Name	-Log p Value	Difference (Active 77 – Inactive 78)
Plau	Urokinase-type plasminogen activator; Urokinase-type plasminogen activator long chain A;Urokinase-type plasminogen activator short chain A; Urokinase-type plasminogen activator chain B	1.98539	1.10811
Lama1	Laminin subunit alpha-1	2.30427	1.88646

Appendix 3: Western Blots of Putative Hits

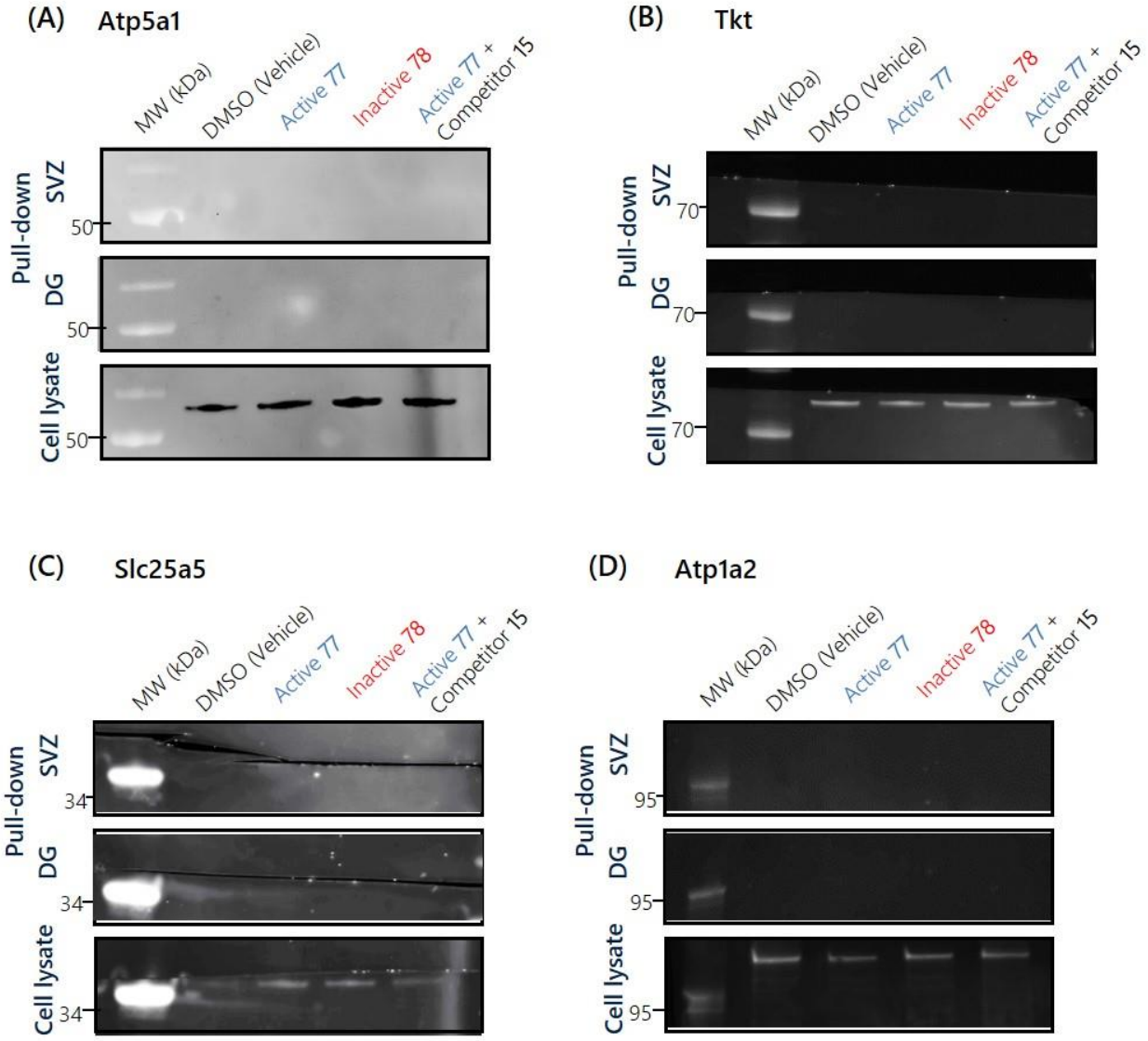


Figure A 1. Western blots of stained with Atp5a1, Tkt, Slc25a5 and Atp1a2 antibodies (1:1000) in pull-down samples from SVZ- and DG-derived NSCs. Cell lysates were used as a control to show relatively similar abundances of the protein in the cell lysates.

Appendix 4: WaterLOGSY Spectra of Compound 28

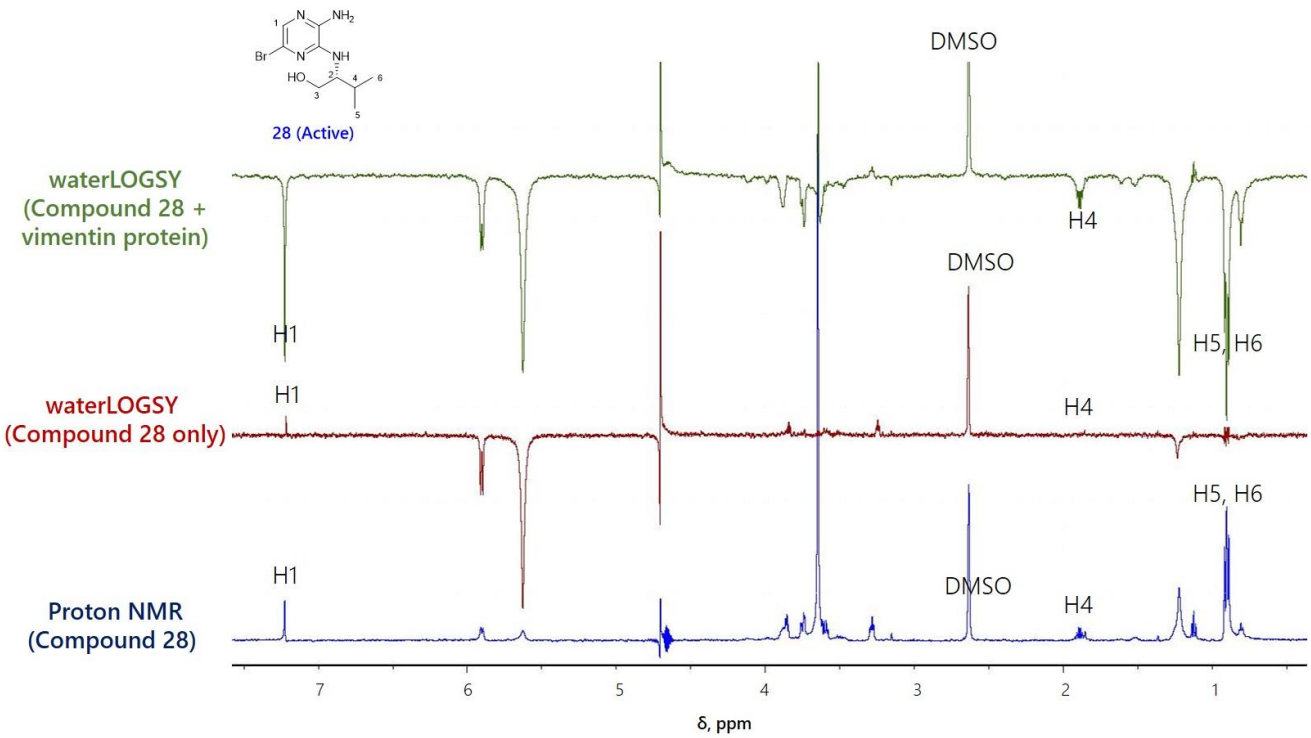


*Figure A 2. WaterLOGSY and proton NMR spectra of (A) active compound **28** in presence and absence of recombinant vimentin protein. The spectra were kindly acquired by Dr Carole Bataille (Prof Angela Russell group, University of Oxford).*

Appendix 5: Confocal Images of Vimentin Filaments in DG-derived NSCs

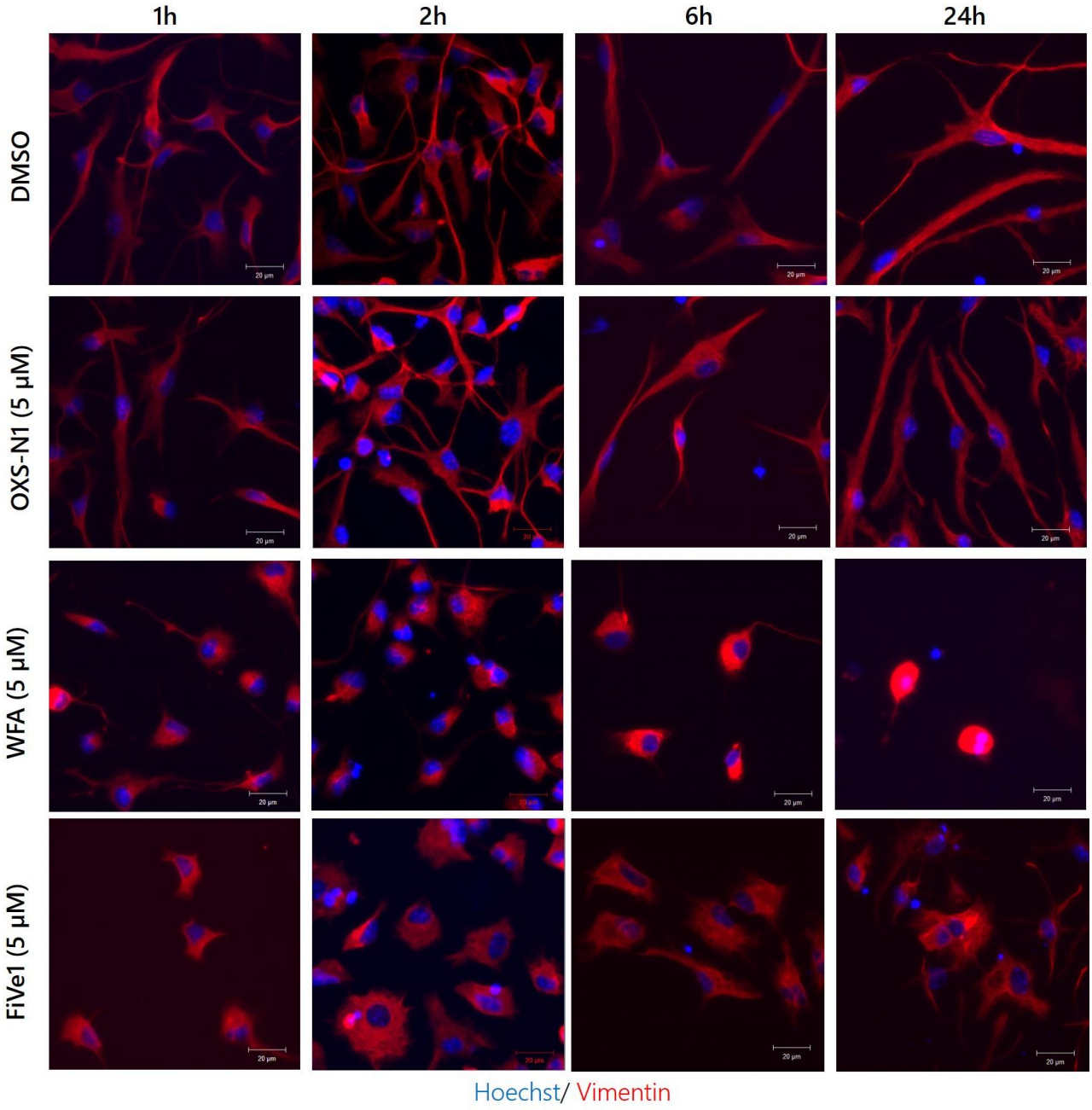


Figure A 3. Immunostaining of vimentin in DG-derived NSCs at various timepoints after treatment with DMSO (0.1%v/v), OXS-N1, WFA and Five1. Staining: Hoeschst (blue), vimentin (red).